COOL'2019

September, 23 - 27, 2019

Novosibirsk
Russia

Preface

The need to develop methods of cooling charged particle beams was realized in connection with the development of colliding-beam techniques. Two high-energy beams collide in the detector and produce a great number of new particles. When beams are cooled, the beam density increases and it becomes possible to study processes with a very small cross-section. Strong synchrotron radiation in the magnetic field of electrons and positrons allows electron-positron colliders to produce strongly compressed beams; however, this technique does not work for heavy particles. Searching for a way to cool proton and antiproton particles G. I. Budker proposed to use an electron beam moving together with a beam of charged heavy particles as a "refrigerator" for heavy beams. This method was proposed in 1967, verified experimentally in 1974 and named the method of electron cooling. Later, van Der Meer proposed to use fast feedback systems for stochastic cooling. This approach has been applied for the first time to cool protons at CERN International Center in 1975. The method based on ionization loss in medium has been promising for cooling muons that do not have strong interaction with target nucleus unlike ions. It was possible to use laser cooling to cool ions with electrons on the shell.

Since the 1960s, the art of cooling and compressing beams has increased the luminosity of storage rings and colliders from 10^{26} to 10^{35} $cm^{-2} \cdot c^{-1}$. The new fundamental particles Z and W bosons were discovered and now many researches are planned for the collider method.

The bi-annual 12th International Workshop COOL'19 was held 23 - 27 September 2019 at the Budker Institute of Nuclear Physics SB RAS. The workshop focused on the various aspects of the cooling methods and techniques of charged particles. 57 physicists from 7 countries (Russia, China, Germany, USA, Switzerland, Japan and England) participated in the conference. 28 oral and 19 poster presentations were made at nine sections of the conference and covered a wide range of issues related to the physics of cooling of charged particles at all energies: from low to relativistic.

The workshop topics: electron cooling, stochastic cooling, muon cooling, cooled beam dynamics, new concepts and theoretical advancements in beam cooling, facility status updates and beam cooling reviews.

Traditionally Dieter Möhl medals are awarded at the conferences. This year’s medals were awarded to Gerard Tranquille and to Rolf Stassen. The Young Researcher Award was given to Lijun Mao.

At the end of the conference the Chairman of the Program Committee V. V. Parkhomchuk informed the participants that the next conference in the series (2021) will be held in the USA, at Stony Brook University by the decision of the Program Committee. The conference at BINP is considered as successful and productive.

V.B. Reva
Chairman of the Organizing Committee

Preface

International Advisory Committee

Yaroslav Derbenev	JLab	USA
Jürgen Dietrich	Uni Dortmund	Germany
Daniel Kaplan	Illinois Institute of Technology	USA
Takeshi Katayama	Nihon University	Japan
Yonehara Katsuya	FNAL	USA
Vladimir Litvinenko	BNL	USA
Igor Meshkov	JINR	Russian Federation
Sergei Nagaitsev	FNAL	USA
Akira Noda	QST	Japan
Vasily Parkhomchuk	BINP	Russian Federation
Dieter Prasuhn	Forschungszentrum Jülich	Germany
Markus Steck	GSI	Germany
Gerard Tranquille	CERN	Switzerland
Grigory Trubnikov	JINR	Russian Federation
Masanori Wakasugi	RIKEN	Japan
Andreas Wolf	MPI Heidelberg	Germany
Xiaodong Yang	IMP Lanzhou	China
Yuhong Zhang	JLab	USA

Local Organizing Committee (LOC)

Vassily Parkhomchuk
Vladimir Reva
Andrey Prokopenko
Maksim Kuzin

Group photo COOL2019 Workshop

Dieter Möhl Award Medals for Rolf Stassen and Gerard Tranquille (not present)

Young Researcher Award for Lijun Mao

Contents

ISBN: 978-3-95450-218-9 ISSN: 2226-0374 doi:10.18429/JACoW-COOL2019-MOX01

COSY EXPERIENCE OF ELECTRON COOLING

V. B. Reva, M. I. Bryzgunov, V. V. Parkhomchuk,
BINP, Novosibirsk, Russia
A. Halama, V. Kamerdzhiev, P. Niedermayer
FZJ, COSY, Jülich, Germany

Abstract

The 2 MeV electron cooling system for COSY-Jülich has highest energy for the electron cooler with strong longitudinal magnetic field. During operation the cooling process was detailed investigated at 908 keV energy of electron beam. The proton beam was cooled at different regimes: RF, barrier bucket RF, cluster target and stochastic cooling. This article deals with the experience of electron cooling at high energy.

INTRODUCTION

In the present time a large experience of using magnetized cooling was collected [1-3]. The first experiments in BINP and further experiments in the other scientific centres show the usefulness of the idea of magnetized cooling. There are many electron cooler devices that operate now at low and middle energy (CSRm, CSRe, LEIR, ESR, e.t.c). The 2 MeV electron cooling system for COSY-Jülich has the highest energy of all coolers based on the idea of magnetized cooling and transport of the electron beam [4-5].

The schematic design of the electron cooler is shown in Fig. 1. The electron beam is generated by an electron gun and accelerated by an electrostatic generator that consists of 33 individual sections connected in series. It is then guided to the cooling sections through the transport line by means of a longitudinal magnetic field. There it will interact with protons. After interaction the electron beam returns to the electrostatic generator where it is decelerated and absorbed in the collector.

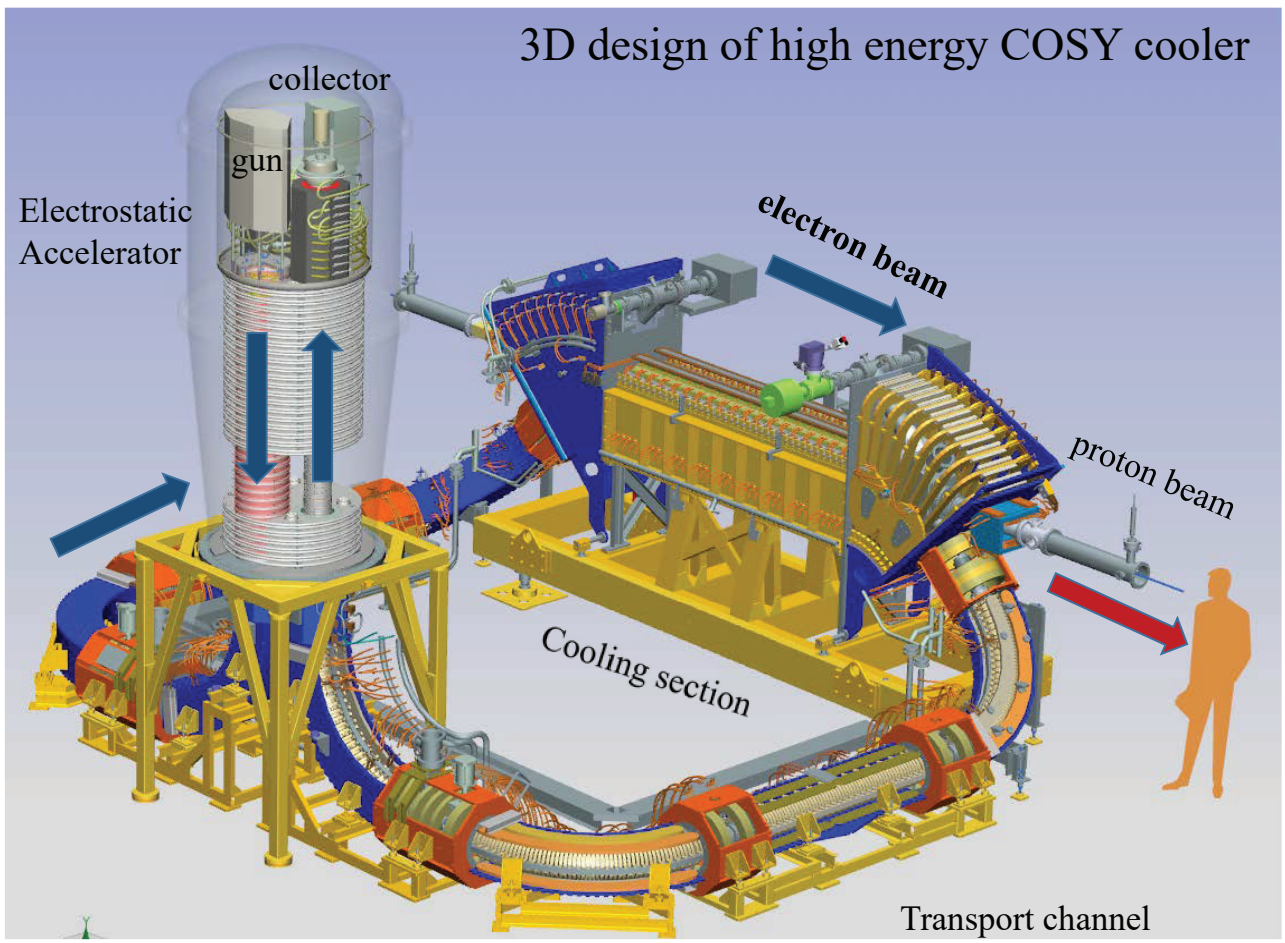

Figure 1: 3D design of 2 MeV COSY cooler.

The optics of the 2 MeV cooler for COSY is designed close to the classical low-energy coolers. The motion of the electron beam is magnetized (or close to magnetized conditions) along the whole trajectory from gun to collector.

ISBN: 978-3-95450-218-9 ISSN: 2226-0374 doi:10.18429/JACoW-COOL2019-MOX01

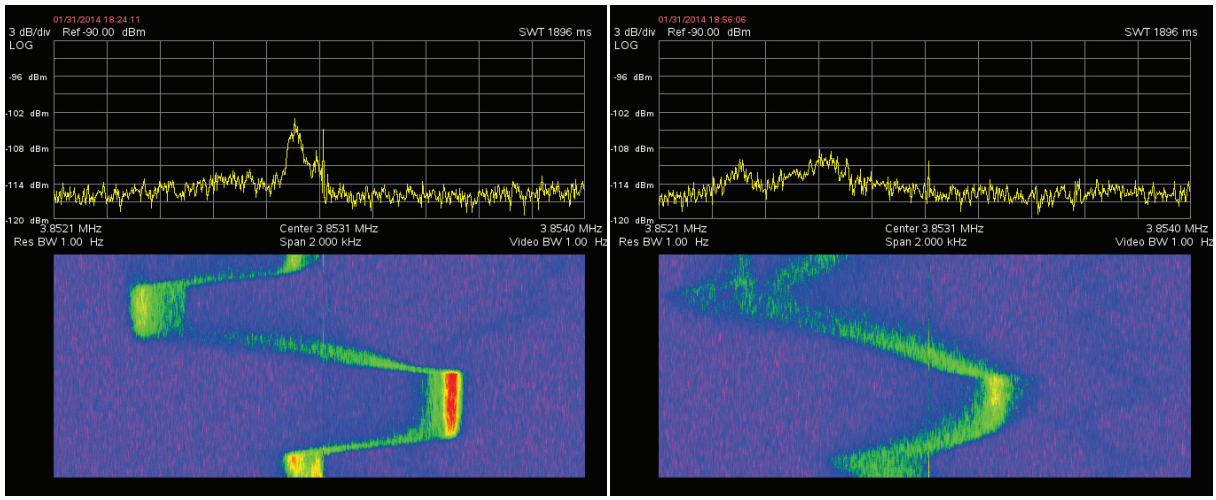

Figure 2: Cooling experiment with different Larmor oscillation of the electron beam in the cooling section. The left picture corresponds to zero oscillations, the right picture corresponds to a Larmor radius about 0.2 mm.

This decision is stimulated by the requirement to operate in a wide energy range from 25 keV to 2 MeV. At low energy the transverse fields is small and the trajectory of electron beam is difficult for the control especially at presents of space-charge effects. Strong longitudinal field helps to determine the electron trajectory. The bend magnets and linear magnets of the cooler are separated by a section with large coils for the location of the BPMs and pumps and comfort of the setup assembling. The length of the linear magnets is defined by the necessity to locate the electrostatic generator outside the shield area of the storage ring. At low electron energies the transverse momentum of the electrons is a less important parameter because the motion is adiabatic and there is no significant excitation of transverse motion. But at high energies the length of the electron's Larmor spiral is comparable with the characteristic lengths of the magnetic elements. Therefore the electron's motion is not adiabatic and strong excitation of transverse momentum is possible. So, the friction force can be reduced significantly compared to the approximation by a strong magnetization process [2].

BEAM COOLING EXPERIMENTS

The first experiments demonstrating the influence of the transverse motion on the electron cooling process was done at an energy of 316 keV. Figure 2 shows the change of the cooling rate due to the influence of the transverse motion. During the experiment, the energy of the electron beam was changed and the longitudinal momentum of the proton beam was changed too. The energy of the electron beam is 315.85 keV. The electron current is 0.26 A. The magnetic field in the cooling section is 1275 G over a length of 2.69 m. Whole duration of one cycle is 600 s. The electron energy was changed by ±300 eV every 100 s. For the measurement shown in the right picture the beam was kicked with a magnetic corrector inducing Larmor oscillations with a radius about $R_L \approx 0.2$ mm. The features of the dynamic of Schottky spectrum during experiment characterize the rate of the cooling process.

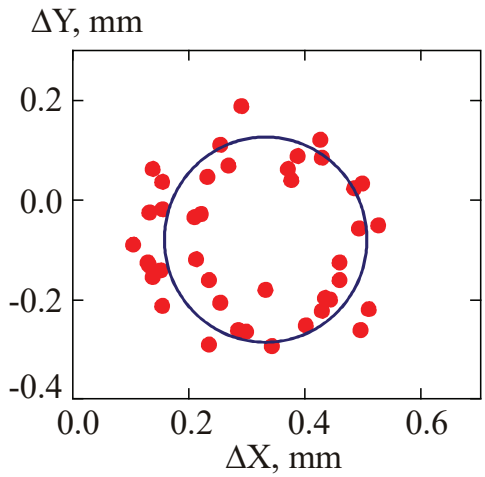

Figure 3: Observation cyclotron rotation of the electron beam with BPM at changing of magnetic field (i.e phase of motion) in the cooling section.

One can see that the cooling process becomes weaker at presence of Larmor oscillation of the electron beam. The area with high density in the Schottky signal disappears from the spectrogram and the motion to the new equilibrium point is slower. The amplitude of the Larmor motion was measured with a BPM because the kick of corrector had dipole component only. Figure 3 shows the transverse position of the electron beam while changing the longitudinal magnetic field strength in the cooling section that produces a phase shift in the Larmor rotation.

The interaction of ions and electrons is realized at different impact parameters. The maximum impact parameter can be estimated as $\rho_{\max} \approx V_i \tau_{cool}$

ISBN: 978-3-95450-218-9 ISSN: 2226-0374 doi:10.18429/JACoW-COOL2019-MOX01

Here V_i is the ion velocity and $\tau_{cool} = L_{cool}/(\gamma\beta c)$ is the interaction time in a co-moving reference system, L_{cool} is the length of the cooling section, γ and β are relativistic factors of the beams. The parameter ρ_{max} corresponds to the path length of an ion in the electron gas in co-moving frame of reference. The comparison of this value with Larmor radius indicates the number of the magnetized collision. If $\rho \approx \rho_L$ than the electron has no time for many Larmor oscillation during collision with ions.

During electron cooling process the size of the proton beam a_i is changed from 4 to 1 mm. Taking the beta function in the cooling section at about $\beta_{x/y} \approx 400$ cm the maximum impact parameter can be estimated as

$$\rho \approx \frac{a_i}{\beta_{x/y}} L_{cool} \approx 0.7 \div 2.7 \text{ mm}.$$

This result gives an initial estimation when Larmor rotations are significant for reducing the amount of magnetized collisions which may be a reason for the decreased cooling rate.

The next experiments were done at high energy 909 keV and the transverse and longitudinal cooling were measured. Main parameters of experiment are following. The electron energy is E_e = 907.7 keV, the proton energy is E_p = 1.67 GeV, the anode and grid voltages are U_{an} = 3.27, U_{grid} = 0.83 kV, the electron current is J_e = 600 mA. The magnetic field in the electron gun is 230 G, acceleration column is 400 G, collector is 500 G. Longitudinal magnetic field in the cooling section is 1300 G, in the toroid section is 1200 G, bend magnet is 860 G. The slip-factor of the proton beam is η = -0.035, the number of protons is N_p = 1.6-1.8·10^9.

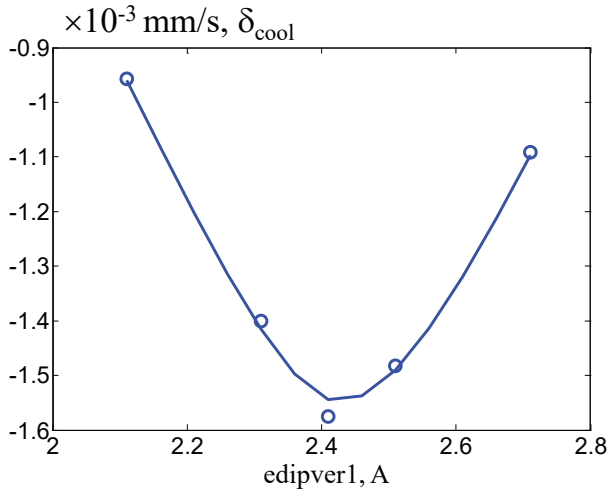

Figure 4: Horizontal increment as function of current of edipver corrector.

The longitudinal cooling was investigated with spectrum analyzer of Schottky signal at 2.438 GHz that corresponds to the 1600 harmonics of the revolution frequency. The transverse cooling was investigated with ion profile monitor (IPM). It measured the profile of the ions generated due to ionization of the residual gas by the proton beam. These ions are accelerated by an electrical field and absorbed by a special detector. This detector contains the microchannel plate, phosphor screen and charge-coupled device (CCD) for amplification, visualization and registration of the beam profile. The IPM contains two such systems allowing to measure horizontal and vertical profiles simultaneously.

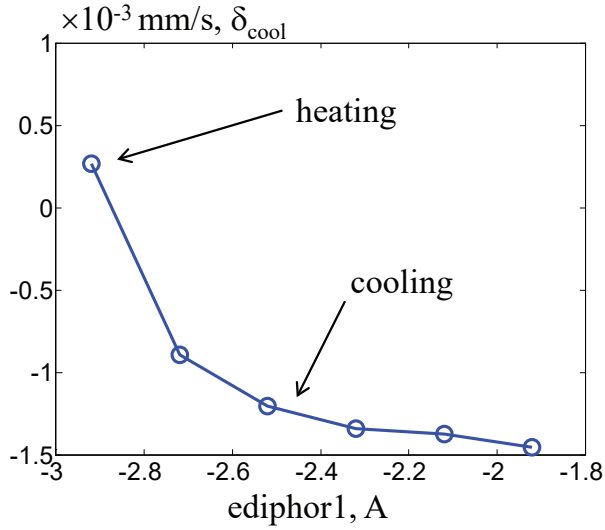

Figure 5: Horizontal increment as function of current of ediphor corrector.

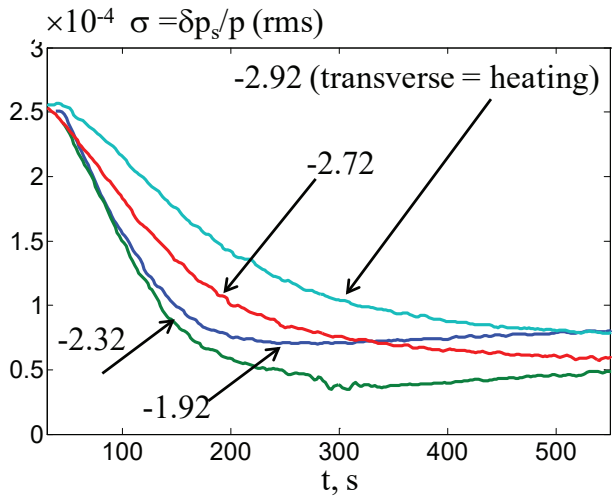

Figure 6: Longitudinal momentum spread as function of time for different values of current in electron dipole corrector ediphor1.

The amplitude of the Larmor rotation was changed with the help of short correctors: ediphor 1 and edipver 1. These correctors have a square shape with a size of about 10 cm and are located about 6.5 cm from the beam axis. There length is small compared to the length of the Larmor spiral.

Figure 4 shows the horizontal cooling rate as function of corrector current. One can see that the cooling rate changes significantly. Another example is shown in Fig. 5. One can see that an unfortunate choice of values of the correctors

ISBN: 978-3-95450-218-9 ISSN: 2226-0374 doi:10.18429/JACoW-COOL2019-MOX01

with short length can eliminate transverse cooling completely.

Despite of the decrease in the transverse cooling rate the longitudinal cooling was good enough. Figure 6 shows the longitudinal cooling rate for experimental parameters corresponding to Fig. 5. The value *ediphor1* = -2.92 A leads to transverse heating. The longitudinal cooling time is increased but cooling is still present.

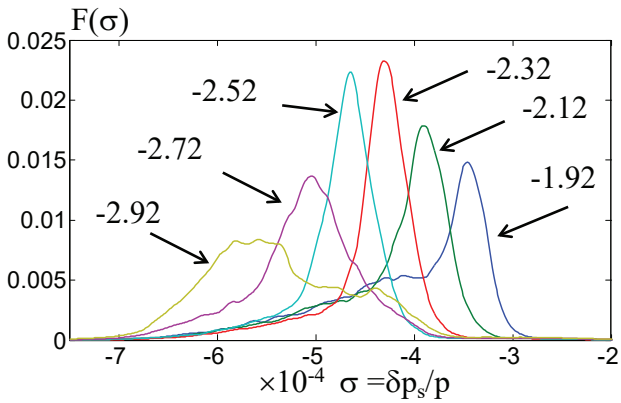

Figure 7: Longitudinal distribution function of the protons in time 500 s for different values of ediphor1 corrector.

Another effect caused by the Larmor oscillation is the connection of the equilibrium momentum distribution of the cooled proton beam to the transverse kick strength. Figure 7 shows the longitudinal distribution function of the protons after the equilibrium was reached. The minimal value of equilibrium momentum and worst longitudinal cooling is observed at *ediphor1*=-2.92 A. The maximum value of equilibrium momentum corresponds to *ediphor1*=-1.92 A when the cooling process is effective. This fact can be explained by decrease of the longitudinal momentum at increase of the transverse one. The estimation of Larmor radius that can be induce by 1 A of current in edip corrector is about $R_L \approx 0.35$ *mm* at electron energy $E_e = 909\,\text{keV}$ (see Fig. 8). It corresponds to change of longitudinal momentum on value

$$\delta\sigma = \frac{\delta p_{II}}{p_0} \approx \frac{1}{2}\left(\frac{R_L}{\rho}\right)^2 = 6\cdot 10^{-5} \qquad (1)$$

where

$$\rho = \frac{\gamma\beta m_e c^2}{eB_{cool}} = 3.2\,cm$$

is the longitudinal Larmor radius and

$$2\pi\rho = 20\ cm$$

is the length of Larmor spiral. One can see that the quality behavior is good. The quantitative difference can be explained by the assumption that the transverse motion already has nonzero amplitude of Lamour oscillation. In this case the change of longitudinal momentum is

$$\delta\sigma = \delta\sigma' - \delta\sigma_0$$

$$\delta\sigma' \approx \frac{1}{2}\frac{\left(\delta\vec{p}_{\perp 0} + \delta\vec{p}_{\perp}\right)^2}{p_0^2}\ ,\ \delta\sigma_0 \approx \frac{1}{2}\frac{\left(\delta\vec{p}_{\perp 0}\right)^2}{p_0^2}$$

where $\delta\vec{p}_{\perp 0}$ is the initial transverse momentum corresponding some Larmor radius R_{L0}, $\delta\vec{p}_{\perp}$ is additional transverse momentum induced by the corrector. One can see that shift of longitudinal momentum may be larger than it describes by equation 1.

CONCLUSION

The physics of electron cooling may contain an open question and this puzzle may have unopened area despite of 50 years of history. Understanding of physics behaviour of the transverse cooling is critical in order to improve transverse electron cooling compared to today's situation. The high-voltage cooler in COSY storage ring is located in the place with low beta function that is unusual for use of electron cooling method. So, the simple way of transverse cooling optimization may be connected with increase of the beta function in the iteration point.

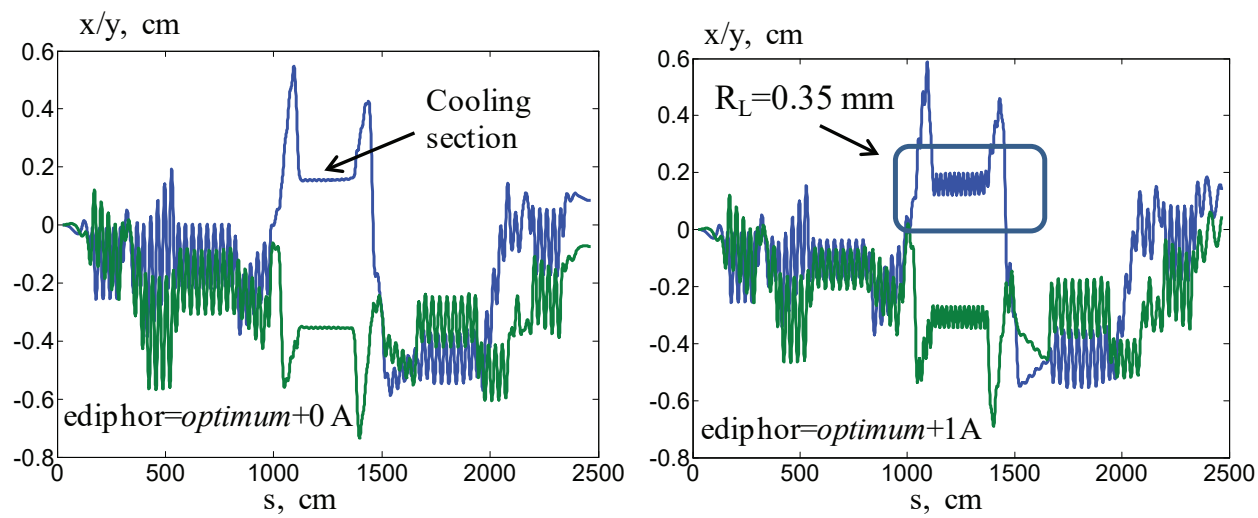

Figure 8: Demonstration of excitation of Larmor oscillation of electron induced by edip corrector.

ISBN: 978-3-95450-218-9 ISSN: 2226-0374 doi:10.18429/JACoW-COOL2019-MOX01

REFERENCES

[1] A.N.Skrinsky, V.V.Parkhomchuk, "The cooling methods of charge particle beams", *Physics of elementary particle and atomic nucleus*, v.12 (1981), N.3, p. 557-613.

[2] N.S. Dikansky, V.I.Kudelainwn, V.A.Lebedev *et al.,* "Ultimate possibilities of electron cooling", BINP, Preprint 88-61.

[3] N. S. Dikanskii, I.N. Meshkov, V.V. Parkhomchuk, A.N. Skrinskiy, "Development of techniques for the cooling of ions", *Phys. Usp.* 61 424–434, 2018.

[4] N. Alinovsky *et al.,* "The first commission results of the high-voltage magnetized cooler for COSY" *in Proc.* of COOL-11, Alushta, Crime, Sept 2011, p. 37-42.

[5] V. B. Reva *et al.*, "Commissioning COSY Cooler with Electron Beam at Novosibirsk", in *Proc. 9th Workshop on Beam Cooling and Related Topics (COOL'13)*, Mürren, Switzerland, Jun. 2013, paper TUPM2HA01, pp. 79-83.

ISBN: 978-3-95450-218-9 ISSN: 2226-0374 doi:10.18429/JACoW-COOL2019-MOY01

FIRST OPERATION FOR STOCHASTIC COOLING OF P-BARS IN THE CERN AD USING OPTICAL DELAY NOTCH FILTER AND PLANS FOR 2021 OPERATION

F. Caspers*, L. Arnaudon, E. Bjørsvik, T. Eriksson, W. Höfle, R. Louwerse, V. Myklebust
CERN, Geneva, Switzerland

Abstract

As part of the consolidation of the stochastic cooling system of the CERN Antiproton Decelerator a notch filter with optical delay lines has been developed. During the 2018 run this new notch filter for the longitudinal cooling at 3.57 GeV/c was successfully tested with beam for the first time. We summarize the hardware implemented including a comparison of hardware transfer functions of the new system and the original system using a coaxial cable plant for the same purpose. Automatic monitoring of the hardware transfer function, being prepared for 2021, will be provided in order to periodically check drifts of the system and send corrections to the control of the system. Integration of this monitoring and feed forward system into the CERN controls environment will be shown.

INTRODUCTION

The CERN antiproton decelerator (AD) has been conceived reusing parts of the former antiproton accelerator complex at CERN which has served to provide antiprotons to the Sp$\bar{p}$ collider from the 1980's onwards [1, 2]. The AD which started operation some 20 years ago in 1998 is designed to provide low energy antiprotons in the range down to 100 MeV/c momentum to a set of experiments located in the AD experimental hall [3].

Antiprotons generated at a target by a primary proton beam from the PS are injected at a momentum of 3.57 GeV/c into the AD ring. Stochastic cooling is applied in all three planes, horizontal, vertical and longitudinal, first at the injection plateau of 3.57 GeV/c and then after deceleration to 2 GeV/c [4].

AD CYCLE AND STOCHASTIC COOLING SYSTEM OVERVIEW

Initially projected for a cycle time of 60 s the AD is today run with a ~100 s long cycle with sufficiently long cooling plateaus in order to provide the nominal emittances with some margin. Ramp rates and idling time at flat-top are limited by magnet cooling and magnet power converters.

Figure 1 shows an overview of the stochastic cooling system. Two pick-ups are used, one horizontal and one vertical. The signal for longitudinal cooling is taken from a combination of the common mode signal from the two transverse pick-ups. The three paths of the signal processing are linked with coaxial 1 5/8" RF lines ($v \simeq c$) to the location of the 48 power amplifiers across the AD hall. These 100 W power amplifiers are installed on top of the shielding of the AD machine gallery. The overall bandwidth of the system ranges from 0.9 GHz to 1.65 GHz with smooth tapering of the gain at the edges of the pass band to minimise changes of delay with frequency that would be detrimental to cooling. The longitudinal signal is combined with the transverse signals at the amplifier platform before signals are split to feed the 24 kicker elements on plunging support structures in each tank through individual feedthroughs. The kicker tank features water cooled loads inside the vacuum tank and the pick-up tank combiner loads are cooled with liquid helium to provide a low noise signal source temperature.

The longitudinal branches of the cooling employ a comb type notch filter with a periodicity equal to the beam revolution frequency at the respective energy. The filter is obtained by combining a directly transmitted longitudinal signal with a signal delayed by one turn. In the original system the delayed branch is realised with coaxial cables with lumped circuits and amplification to match the frequency dependent attenuation, group delay, and the dispersion of the direct path. Part of the direct transmission is realised by a mechanically delicate, ~10 m long thin (< 0.5 mm) coaxial cable to achieve matching of the transmission characteristics. The overall length of the short path is critical at 3.57 GeV/c with a velocity factor of > 98% implemented for the combined length of ~ 40 m of 1 5/8" coaxial line.

In the new system, which was used for the first time with beam in 2018, the transmission for the 1-turn delay has been replaced by an optical fiber cable with low attenuation. Consequently the compensating circuits and the thin coaxial cable of the direct path could be suppressed gaining around 16 ns of delay. Commissioning of this new system is described in more detail further below.

Tables 1,2 shows the performance in cooling as achieved in regular operation and with the classical electric delay line notch filter.

Table 1: Parameters for Cooling at 3.57 GeV/c [4, 5]

Parameter	Design	Achieved
Intensity at 3.57 GeV/c	5×10^7	$\simeq 4 \times 10^7$
Cooling time	20 s	20 s
Hor. emittance (95%)	5π mm mrad	3π mm mrad
Ver. emittance (95%)	5π mm mrad	4π mm mrad
Momentum width	$\pm 0.5 \times 10^{-3}$	$\pm 0.35 \times 10^{-3}$

* Fritz.Caspers@cern.ch

ISBN: 978-3-95450-218-9 ISSN: 2226-0374 doi:10.18429/JACoW-COOL2019-MOY01

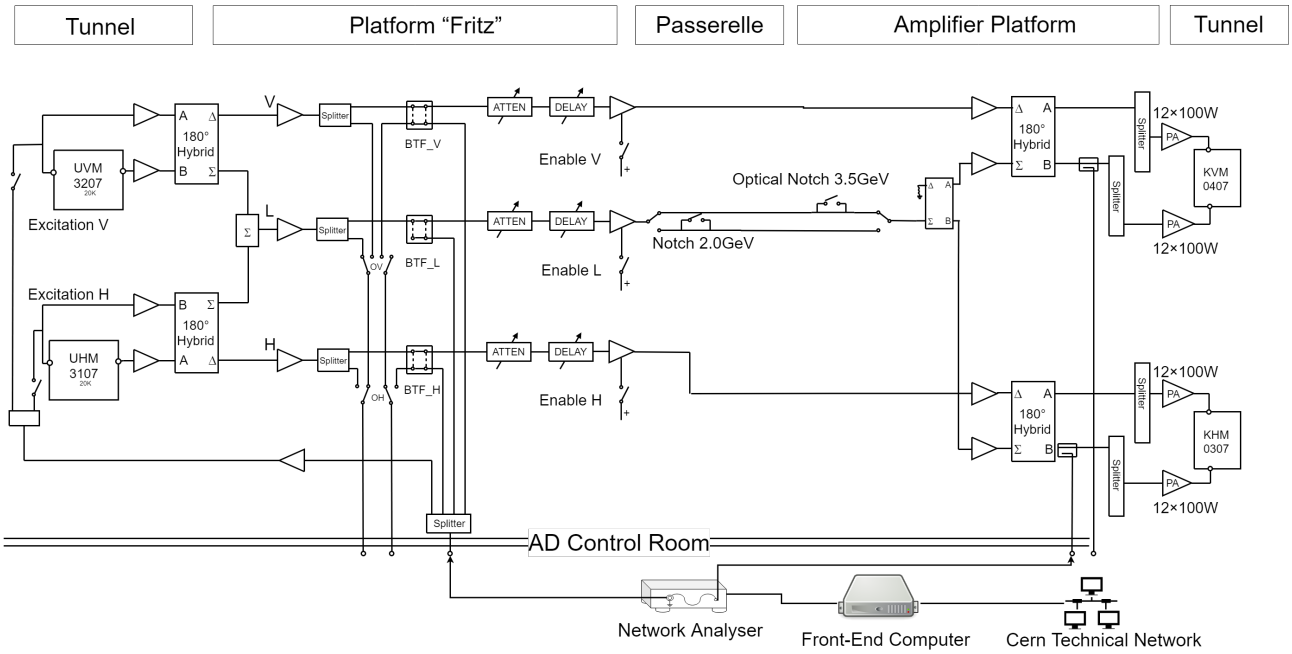

Figure 1: Stochastic cooling System Layout with pickups (PU) UVM 3207 and UHM 3107 and kickers (KI) KVM0407 and KHM0307.

Review of Operation and Faults until 2018

In spring 2000 during the start-up phase a leak was found in one of of the two stochastic cooling kicker tanks in the AD. These tanks are in general difficult to remove, requiring a long intervention in the order of about six months. This would have caused a significant delay of the AD physics program, but was under consideration. However, a closer examination of the situation showed the possibility for an in-situ repair of the problem. The leak was minuscule, leading to an increase in vacuum pressure on the particular tank from about 10^{-8} mbar to around 10^{-5} mbar. A quick calculation showed that it could not be bigger than a few micrometers. Additionally it was confirmed that this leak occurred on the water cooling circuit in this tank which consists of very thin water pipes inside the vacuum. It was decided to blow a special mixture of a four component epoxy glue with very high viscosity through the water cooling circuit followed by continuously blowing hot air through the circuit at about 80° C for two days for the curing process. Everything was done in situ and with the actual tank kept under high vacuum. It was a very delicate operation, and a mistake could have lead to the destruction of the equipment. Although initially considered as a temporary fix for a year, the tank is still perfectly leak tight today and the procedure could be repeated if required.

Other than this the stochastic cooling system posed no worries with only very little downtime throughout the years leading up to 2018, start of the long shutdown 2 (LS2).

Following this long operational period with minimum downtime consolidation is becoming important to maintain the high availability. With respect to slow performance degradations observed since 2000, an optimization of the cooling, the bunch rotation before cooling and the debunching and re-capture process is advised to restore fast cooling rates and minimize losses. After LS2 the main RF cavity system will have been replaced by a finemet based cavity, and new means of observation will be available from the low-level RF system and the Schottky monitoring. Moreover, full RF voltage for the two bunch rotation systems will again be available with refurbished tubes following the completed consolidation of this system. The automatic transfer function monitoring system being planned for the stochastic cooling and described further below will help to diagnose issues and optimise the cooling performance.

Noteworthy are small faults on the transmission line connections that were repaired during LS2 when the entire power system was dismantled to gain access to the machine for the magnet consolidation program and a modification of the shielding walls.

The jaws of the pick-up are moving during cooling with all the electronics to drive the system having been consolidated in long shutdown 1 (LS1) in 2013. For the kickers the electronics was renovated as well, however, as the movement was no longer used, the mechanism is now blocked in the

Table 2: Parameters for Cooling at 2.0 GeV/c [4, 5]

Parameter	Design	Achieved
Intensity at 2.0 GeV/c	5×10^7	$\simeq 4 \times 10^7$
Cooling time	15 s	15 s
Hor. emittance (95%)	5π mm mrad	2.9π mm mrad
Ver. emittance (95%)	5π mm mrad	3.3π mm mrad
Momentum width	$\pm 0.15 \times 10^{-3}$	$\pm 0.08 \times 10^{-3}$

ISBN: 978-3-95450-218-9 ISSN: 2226-0374 doi:10.18429/JACoW-COOL2019-MOY01

open position. With a total of 2.4 kW RF power per kicker tank sufficient power is available in order not to need the kicker movement to increase kick strength during cooling.

Plans and Progress with Consolidation

A new cryogenic current comparator [6] is providing precise beam intensity measurements during the cooling plateaus. This has greatly improved observation of beam losses during cooling. Comparison with the consolidated Schottky measurement system [7] will be made from 2021 onward when the machine restarts. Both systems will be needed, as the cryogenic pick-up has not yet reached maturity in terms of availability and the Schottky system is complementary as it also provides information on the momentum spread of the unbunched beam. Improvement of the precision of the Schottky system for current measurement, currently at ±20%, is desirable and may be possible with the new digital system.

A new scraper system similar to the one installed in ELENA was commissioned in 2018 due to obsolete hardware and for standardization. Measured transverse emittances do not correspond to measurements done with the previous system which needs to be kept in mind when evaluating the stochastic cooling system performance.

More machine development (MD) time is desirable for the start-up in 2021 to recommission all systems and optimize performance. With respect to the stochastic cooling system and the RF system the optimization is rather for a smooth handover with minimum losses between the systems and for maintaining fast cooling rates than for minimum final emittances. Lowest emittances are achieved by the final electron cooling before extraction of the beam to ELENA.

A challenge is that currently the machine cannot be kept at 3.57 GeV/c for a prolonged time to optimize the cooling. This is due to insufficient cooling of magnets and too high interlock levels. It needs to be addressed by restoring a higher cooling capacity, adaptation of interlock levels if possible, and by automating the beam transfer function measurements in order to carry out the optimization in the short available time span at flat-top.

One of the upgrades identified with high priority is the replacement of the notch filters in the longitudinal path of the stochastic cooling. Once this upgrade is completed, it will be clear how much delay margin in the system is left to consolidate other parts of the system including the final power amplifiers where an improved mechanical layout may be desirable. Commissioning of the notch filter at 3.57 GeV/c is described in the next section.

COMMISSIONING OF THE NEW NOTCH FILTER AT 3.57 GeV/c

A particular challenge of the commissioning of the new notch filter with optical delay line has been the need to follow this through in parallel with delivering beams to the experiments with minimal dedicated beam time and without being able to measure beam transfer functions (BTFs) for the setting-up due to the magnet cooling issues previously mentioned. Success relied upon carefully comparing the hardware transfer functions (HTFs) in delay, phase and attenuation between old and new system and adjusting the notches to the correct frequency. Figure 2 shows a comparison of the transfer functions. The notch filter depth of the new optical path system is more than 30 dB over the frequency range of interest due to very good matching of phase and attenuation of the direct and delayed path. The variation of phase with frequency is similar for the new and the old system and amounts to 30°. The measurement includes the notch filter, signal transmission and pre-amplification, but neither the first stages of processing after the pick-ups nor

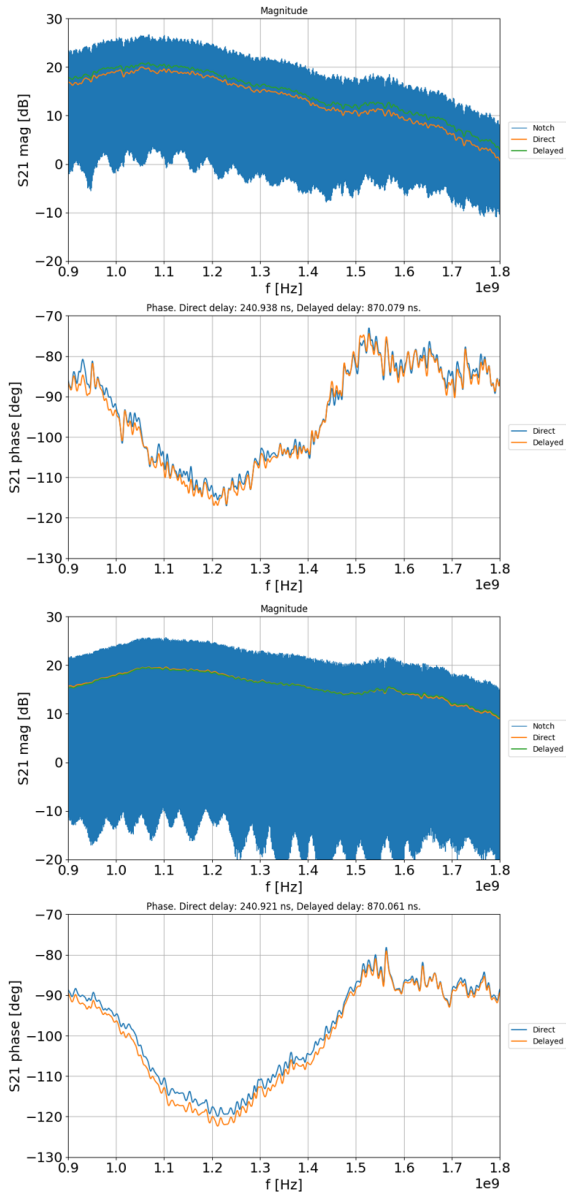

Figure 2: Hardware transfer function (HTF) of coaxial cable notch filter (top) and optical fiber notch filter (bottom); shown are attenuation and phase of the short and long branch and the transfer function with notches.

ISBN: 978-3-95450-218-9 ISSN: 2226-0374 doi:10.18429/JACoW-COOL2019-MOY01

the final 100 W power amplifiers (Fig. 1). A separate transmission path was used for the new system. It can also be seen that the new system provides an overall flatter response with frequency in amplitude. With gains adjusted accordingly the new system provides more gain at higher frequencies and less gain at low frequencies (Fig. 2).

RESULTS WITH BEAM

After closing the loop cooling was optimised by adjusting the gain for best transmission and lowest momentum spread after cooling. Fig. 3 shows the final result as viewed on the down converted FFT spectrum from the online application in the control room. This signal from the longitudinal magnetic pick-up is measured at $2 \times f_{\mathrm{rev}}$, using an analog down conversion to a fixed frequency of 50 kHz and subsequent FFT with a signal analyser. The cooling is also visible in Fig. 4 where two consecutive cycles are shown with green dots representing the momentum spread and 3×10^7 antiprotons after the first cooling plateau (red).

Following these successful tests the plans for LS2 include a second instance of the optical delay notch filter for cooling at 2 GeV/c. Full integration into the control system is foreseen including an automated measurement of transfer function as described in the following, to monitor and pilot adjustments during operation.

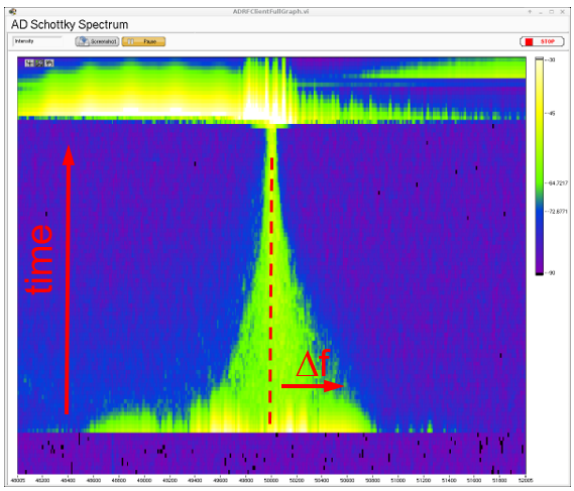

Figure 3: Results with Beam: FFT spectrum during cooling (200 Hz/div); down converted to an IF of 50 kHz from h=2.

ONLINE MONITORING OF HARDWARE TRANSFER FUNCTION

The newly developed optical delay line has been shown to experience drifts. While the majority of this is suspected to be due to an adjustable optical delay line with insufficient stability, a system to periodically monitor the hardware transfer function as basis for automatic or manual corrections is highly desirable. The proposed system which is now being implemented consists of a compact network analyzer that can be remotely controlled and triggered to do a measurement. From the change in transfer function, settings can be deduced for manual correction or for automatic feedback. The measurement can be performed at any time during the AD cycle where stochastic cooling is not used.

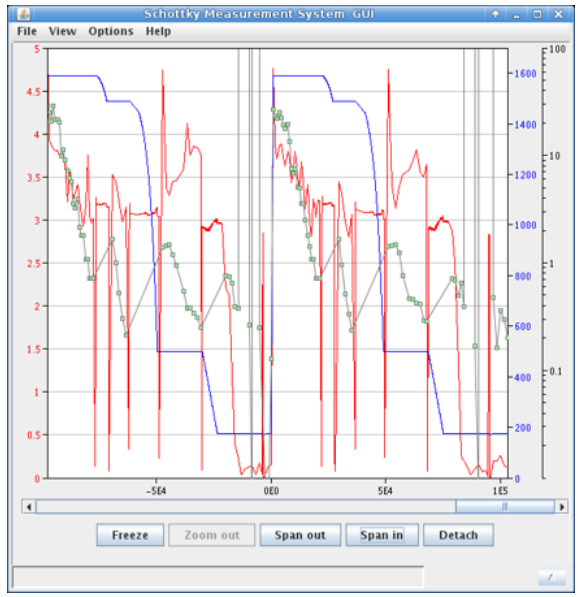

Figure 4: Cooling during the AD cycle; blue: revolution frequency in kHz, green: momentum spread (a.u.); red: beam intensity in 10^7 antiprotons.

Description of Hardware

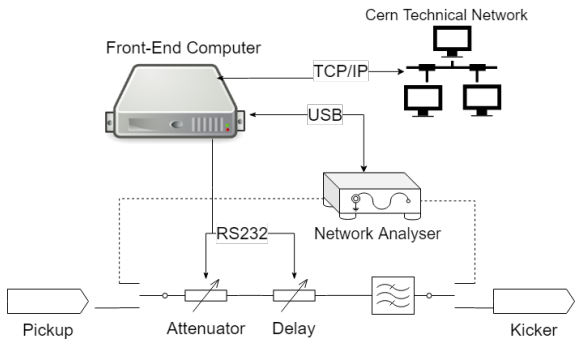

Figure 5: Hardware transfer function monitoring system.

The selected 2-port network analyser (VNA) from Copper Mountain Technologies (model S5085) will be permanently installed in a rack in the AD control room. Remote control functionality is provided by an USB-interface. An external 10 MHz reference ensures synchronisation in frequency with the accelerator for precise determination of notch frequencies that have to match the beam revolution frequency and the RF re-capture frequency. A measurement can be manually initiated from the software or configured to be started by machine timing at a particular moment during the AD cycle (Fig. 5).

In order to send a test signal through the notch filter two relays are used to switch the input and output of the filter to the instrument. As shown in Fig. 1, the signal path to

ISBN: 978-3-95450-218-9 ISSN: 2226-0374 doi:10.18429/JACoW-COOL2019-MOY01

the filter input can come from either the pick-up, or the control room. Likewise, the output can be directed to either the kicker-tank, or back to the control room. In order to make the VNA accessible to the CERN technical network and to handle the USB communication, a controller unit is required. The same unit can also be used to run the control software if automated correction is desired, and to command the motorised delay lines and attenuators. A VME rack mount Men-A25 front-end computer running the CERN CentOS7 operating system complying with current CERN accelerator operations standards is used for this purpose. It is a disk-less and headless computer for high reliability and maintainability. The software will receive timing signals from the technical network to synchronize the measurement with the AD-cycle. The same hardware can also be used to measure beam transfer function triggered by machine timing in a more automated way for periodic checks.

Development of Software Tools

Feedback control software to correct settings of the notch filter is being developed as a FESA-class [8] to also run on a front-end computer on the technical network. This way the control of the feedback system is easily integrated with the CERN-wide standard for accessing devices on the internal network. The software solution consists of three layers: The lower layer is an existing driver that handles the USB-link to the instrument, and enables communication with the instrument by setting up a TCP/IP connection. This is already developed by the VNA manufacturer, but needs to be modified to function correctly on CERN CentOS 7 (CC7). The second layer is a general FESA-class that abstracts the communication with the instrument. It is a general purpose layer that can be used by specialists to set individual parameters in the instrument. The third layer is the control loop itself, utilizing the second layer to command the VNA. The software can be configured for automatic control in regular intervals or for interaction with the operator to request a confirmation to changes proposed by the system.

Demonstration of feedback from HTF

The bulk part of the one-turn delay branch of the notch filter is a long optical fiber inside a temperature-controlled box. The overall delay can be fine tuned by a motorised delay line. Location and depth of the notch is a result both of delay and attenuation. For a first demonstration, only the delay was acted upon using a simple P-controller and measuring the S21 amplitude response and setting the delay line accordingly to place the 1000th notch to 1.589477 GHz. The correction loop was executed in the test every 10 minutes and the actuator is driven only if the error deviates from the set-point more than a programmed limit. This is done to limit the number of times the motorised delay line is driven. The method can be extended to also monitor the notch depth and accordingly adjust the attenuation in one of the branches to keep the notch depth better than a specified limit.

CONCLUSION

The stochastic cooling system in the CERN antiproton decelerator has reliably run for almost two decades, with a minimum of interventions. Investments to consolidate the system are now required and the presented optical delay line notch filter is a key part of the ongoing program. Monitoring and adjustment tools are being developed for setting up the system and for performance control and optimization.

ACKNOWLEDGEMENT

The authors would like to thank W. Maier, C. Peschke and C. Dimopoulou from GSI, Germany for developing the initial notch filter with optical delay and making available their expertise. Support from P. Freyermuth, the team of D. Landre and K. Marecaux, as well as D. Glenat, C. Oliveira and B. P. Bielawski for providing remote control, help with the integration with the control system and careful maintenance of the equipment. Discussions and support by L. Thorndahl are much appreciated.

REFERENCES

[1] B. Autin et al., "Performance of the CERN Antiproton Accumulator Complex", Proc. EPAC'88, Rome, Italy, June 1988; CERN/PS/88-43 (AR), CERN, Geneva, Switzerland, 1988.

[2] G. Carron et al., "The CERN Antiproton Accumulator Complex (AAC): Current Status and Operation for the Nineties", Proc. of XVth International Conference on High Energy Accelerators, Hamburg, Germany, July 1992; CERN/PS 92-41 (AR), CERN, Geneva, Switzerland, 1992.

[3] P. Belochitskii et al., "Commissioning and First Operation of the Antiproton Decelerator AD", Proc. PAC'01, Chicago, Ill., USA, June 2001, pp. 580–584.

[4] F. Caspers and C. Carli, "Stochastic Cooling at the CERN Antiproton Decelerator", Proc. EPAC2000, Vienna, Austria, 2000, pp. 2014–2016.

[5] T. Eriksson, M.-E. Angoletta, L. Arnaudon, P. Belochitskii, L. Bojtar, M. Calviani, F. Caspers, S. Federmann, L. Jørgensen, R. Louwerse, C. Oliveira, G. Tranquille, "AD Status and Consolidation Plans", Proc. of Cool'2013, Mürren, Switzerland, 2013, pp. 36–39.

[6] M. Fernandes et al., "Operation of a cryogenic current comparator with nanoampere resoluation for continuous beam intensity measurements in the anti-proton decelerator", Proc. of IPAC'18, Vancouver, BC, Canada, 2018, pp. 4741–4744.

[7] M. E. Angoletta et al., "A New Digital Low-Level RF and Longitudinal Diagnostic System for CERN's AD", Proc. of IPAC'19, Melbourne, Australia, 2019, pp. 3966–3969.

[8] M. Arruat et al., "Front-End Software Architecture", Proc. of ICALEPCS'07, Knoxville, TN, USA, Oct. 2017, pp. 310-312.

ISBN: 978-3-95450-218-9 ISSN: 2226-0374 doi:10.18429/JACoW-COOL2019-MOY02

STATUS OF THE TURBINE-DRIVEN HV-GENERATOR FOR A RELATIVISTIC ELECTRON COOLER

K. Aulenbacher[†,1], J. Dietrich, W. Klag, Helmholtz Institut Mainz, Germany
[1]also at GSI Helmholtzzentrum für Schwerionenforschung, Darmstadt, Germany

Abstract

Power generation by gas turbines at high potentials can become an alternative to insulating transformers or rotating shafts in electron coolers operating in the range of several MeV. Our main objective is to explore this technique for an application in a high energy cooling device at HESR. The status of the project, its potential advantages and the perspectives are discussed.

INTRODUCTION

Since electron cooling requires fulfilling the condition of equal ion and electron velocity it is mandatory to provide powerful electron beams in the MeV range for the upcoming HESR storage ring at the FAIR facility. The 2 MeV cooler from COSY [1] could be used but will only cover the lower energy range whereas antiproton cooling at the highest HESR-energies would require almost V=8 MV acceleration potential. One should keep in mind that cooling times can be significantly reduced if the beam is magnetized which will be necessary to counteract the heating effect of the internal target at the PANDA-experiment in HESR.

The longitudinal magnetization field is provided by a chain of solenoids which also has to cover the acceleration stage. The solenoids then sit at different potentials and need floating power supplies. Another supply is needed for the electron source/collector system at the HV-terminal. Therefore, several acceleration modules with an individual power supply are needed. If the number of modules is N, the potential difference between the stages is V/N. In a recent design study by Budker Institute for Nuclear Physics (BINP) it was suggested to choose V/N=0.6 MV, which allows using established HV-generators to maintain the voltage between the modules while keeping a pair of solenoids (for accelerated and decelerated beam respectively) at the potential of the module-deck. This arrangement of solenoids would still provide a reasonable field quality.

A number of N = 14 modules is needed to have some margin for an 8 MV device. The power consumption of a stage will be less than 3.5 kW. Including the terminal, a power ~ 50 kW on different HV potentials may be needed. The main purpose of the ongoing work is to demonstrate the reliability of the power generation approach and the scalability of the stages. Therefore, "HESR-prototype" HV-modules of 1:1 scale are being tested. An important question is the method of potential- free ("floating") power generation for which we use a special set-up at Helmholtz Institut Mainz (HIM). We address power generation in the next section and describe the status of HV-module experiments afterwards. Finally, the long-range plans will be explained in the "outlook"-section.

TURBINE APPROACH

There are several potential advantages of turbines as floating power generators compared to existing technologies like insulating transformers or generators driven by insulating rotating shafts which have powered devices at the ~5 MV level already [2,3].

We have demonstrated [4] that commercially available turbine-generators can provide the required power level for extended periods of time (>1000 h) without the need for maintenance. The turbo-generators are sold under the trade name "Green Energy Turbine" (GET) by the company DEPRAG [5] and deliver 5 kW per unit, so a single turbine can drive a HV-module. Investment costs are ~10 €/Watt (including the cost of the compressor) on the terminal and energy efficiency from wall plug to terminal is about 15% for our application. This can be considered as affordable as far as HESR operation is concerned.

The relatively low efficiency is to some extent caused by the pre-cooling of the compressed gas in our commercial compressor system (Fig. 1). The heat of the compressed gas is taken away by cooling water and is therefore lost. This happens *outside* the HV-device. Then the gas is sent to the HV-tank inlet at approximately room temperature. The expanding gas from the turbine *inside the HV-tank* is cooled since energy in form of electrical power is extracted from it. The electrical power is finally transformed again into heat by the loads. It is evident that the exhaust gas can be used to absorb this heat again. In our present set-up this is done by an air/liquid heat exchanger on the HV-deck. Stable thermal conditions at moderate temperature levels of the individual devices can be realized. A thermal management becomes thus possible, keeping temperatures inside the HV-tank at appropriate values. This feature is an advantage for the turbine, since other methods of power generation need additional cooling circuits with connection to heat exchangers at ground potential.

SET-UP AT HIM

Figure 1 shows the compressor with buffer tanks for the compressed gas. Copper tubes lead to the HV-module-inlet from where the gas is guided by a plastic tube towards the turbine. The compressor can drive three such turbines. In September 2018 BINP delivered the first HV-module to HIM, which carries a turbine on the HV-deck. The functionality was successfully tested albeit only at a voltage level of 60 kV due to the absence of a pressure vessel.

ISBN: 978-3-95450-218-9 ISSN: 2226-0374 doi:10.18429/JACoW-COOL2019-MOY02

Figure 1: Compressor system for driving up to three turbines at HIM. Size of compressor (grey box, upper right) is about 2,5*2*1m.

The HV-module (Fig. 2) is 3 meter in diameter in order to leave enough space for all components, in particular the turbines, heat exchangers, remote control, power supplies etc., as well as for the two acceleration channels with a sufficiently large insulation gap between the solenoids and the acceleration tubes. The solenoids consist of four sub-coils with suitable iron cores to achieve field flatness. The power consumption of each solenoid is 1300 Watts. Figure 3 a/b illustrates the dimensions of the solenoids. Due to the potential gradient along the acceleration tube and along the outer main construction frame of the module, the electrical field peaks at the inner as well as on the radial outer surface of the end of the solenoid, see indication in Fig. 3a. Under nominal operation conditions the maximum electrical field strength on the solenoid surface is about 4.2 MV/m [6,7]. This condition is the same for all solenoids in the different modules.

A pressure tank which can hold two modules plus the gun/collector stage has been ordered. Due to space limitations in the HIM experimental hall the inner diameter is restricted to 3.9 meter. The E-field strength on the inner cylinder in a configuration of concentric cylinders of inner and outer radii R_i, and R_o respectively is: $E=V/(R_i \ln(R_o/R_i))$. This function has a minimum at $R_o/R_i=e=2.71\ldots$ which means that for the present ratio $R_o/R_i \sim 1.3$ there is an enhancement of the field at the cylindrical surface by a factor 2 over the minimum achievable E for the present tank diameter. Note that this overshoot would only be 1.1 for a tank diameter of 6 m.

An additional field enhancement factor of < 1.59 [8] for the transition region between the cylindrical and the more or less spherical part in the terminal region should also be taken into account, In our intended operation with two modules at 1.2 MV we therefore estimate the maximum field strength to be <5MV/m. With pure N_2 as insulation gas, a pressure of about 6bar will be sufficient, though the insulating capabilities are lower compared to SF_6 by a factor ~2.5 – see the results by Hellborg [9] which were obtained at comparable voltages. This pressure is within the specifications of our tank. Using N_2 will avoid the administrative and technical complications associated with the use of SF_6.

The tank will be delivered in summer 2020 which will then allow testing the already existing module at the design voltage of 600 kV.

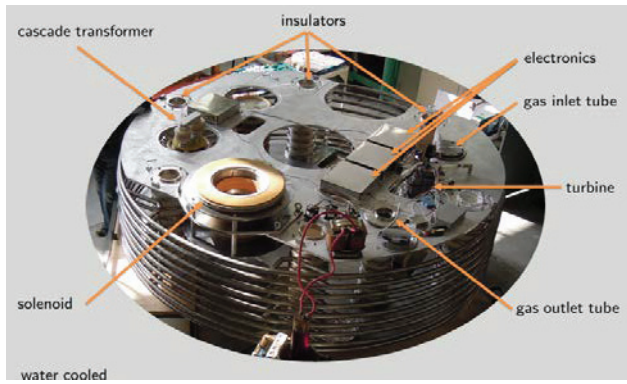

Figure 2: HV-module. Diameter of disc is 2.96 m, height of module is 0.7m. Only one solenoid is installed.

Negotiations for delivery of a second module between BINP and HIM are almost finalized. The operation of two stacked modules at 1.2 MV is intended which would give important information on the scalability of the approach towards higher voltages. This will also include the acceleration tubes with vacuum pumps operating at the module decks (Fig. 3b) which will establish improved vacuum conditions in the acceleration channel.

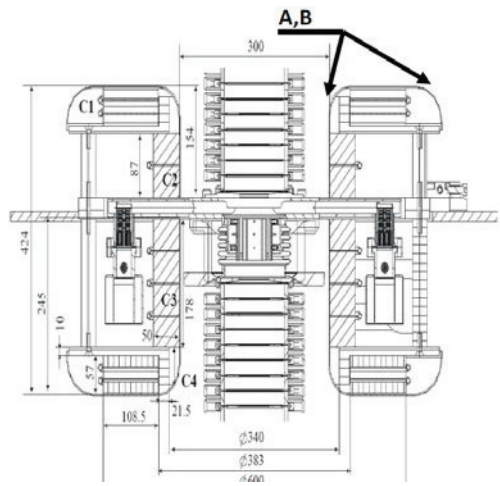

Figure 3a: Mounting of a solenoid on the module baseplate around the acceleration tube [6]. Dimensions in mm. Points A and B are regions of high field strength.

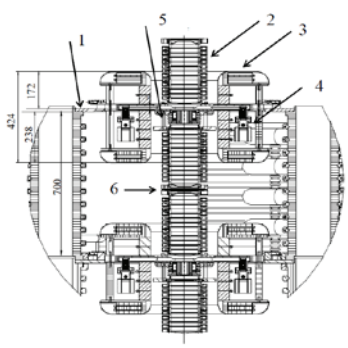

Figure 3b: Arrangement of two solenoids on different decks with 600kV acceleration in between [6]. 1: main construction frame, 2: acceleration tube 3: solenoids 4: vacuum pumps, 5 bellows and beam position monitor, 6: flange connection.

ISBN: 978-3-95450-218-9 ISSN: 2226-0374 doi:10.18429/JACoW-COOL2019-MOY02

OUTLOOK

Our next steps will be directed towards testing several turbines in parallel and to establish a regulation scheme to keep the system in a stable and safe operational state. Practical experience with the gas-distribution system and the heat exchangers inside the HV-tank has to be gained. Demonstration of the HV-capabilities of the turbine driven approach is the most important point, including the hitherto more or less untested gas-flow: gas has to be returned under a pressure of 1 bar to ground potential.

We believe that these experiments will extend over a timespan of several years, the end of which could coincide with the installation of the HESR at the FAIR site. The outcome of the demonstration experiments will allow a decision if the new technology is a suitable approach for high energy cooling at HESR.

In the long run it is also desirable to install a gun/collector system and a return path to be able to operate with electron beam as depicted in Fig. 4. Such an apparatus would come close to an operational electron-cooler. The realization of this device depends on the one hand on the availability of additional resources and on the hand it is not clear as of today if the additional effort will yield enough new insights to justify it.

However, we presently investigate if a similar extension of the apparatus could be used, e.g., to provide beam for experiments in the regime of Ultra-fast Electron Diffraction (UED). Due to the availability of ample electrical power on the terminal one can consider operation of power-demanding technologies such as radiofrequency bunchers which can provide very short bunches at the experimental site after acceleration with rather low energy spread. Moreover, the large size of the HV-modules allows installing also space consuming devices on the terminal, for which spin polarized electron sources are an example. Such sources usually require meters of space in in one direction due to the need for vacuum manipulators. This can be incorporated on the deck of the HV-module. By combination of both advantages one could do completely new experiments on fast processes in magnetic nanostructures by Spin-polarized ultra-fast electron diffraction (SUED).

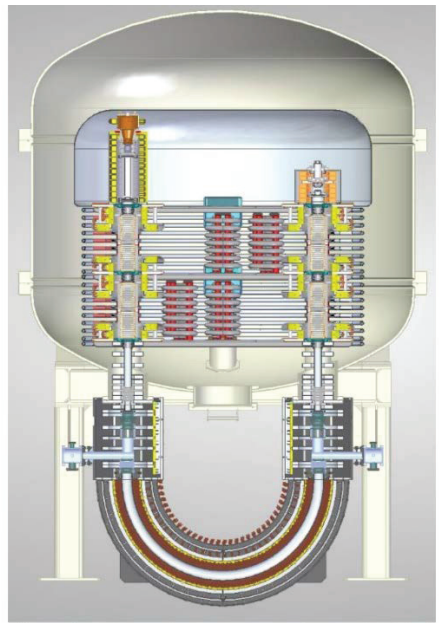

Figure 4: Possible configuration: Two modules at 1.2 MV with source, collector and return loop [7].

ACKNOWLEDGEMENTS

We thank V. V. Parkhomchuk and his team from BINP for important advice and for the fabrication of the hardware.

REFERENCES

[1] V.B. Reva *et al.*, “Experimental Observation of Longitudinal Electron Cooling of DC and Bunched Proton Beam at 2425 Mev/c at COSY”, *in Proc.* of COOL’2015, Newport News, VA, USA, paper MOXAUD02, 2015.

[2] A. Shemyakin and L. R. Prost, “Ultimate Performance of Relativistic Electron Cooling at Fermilab”, *in Proc.* of COOL’11, Alushta, Crime, paper THIOA01, 2011.

[3] M. Letournel, “Industrial Electron Accelerators” R. Hellborg (ed.) *Electrostatic accelerators*, Springer 2005.

[4] A. Hofmann *et al.*, “The Green Energy Turbine as Turbo Generator for Powering the HV-Solenoids at a Relativistic Electron Cooler”, *in Proc.* of COOL’2015, Newport News, VA, USA paper MOPF02, 2015.

[5] https://deprag.com/green-energy/green-energy-turbine/

[6] Budker Institute for Nuclear Physics: Design Report on the Development of a Prototype of a Power Supply Module for 4 – 8 MeV Electron Cooler, 2016.

[7] Budker Institute for Nuclear Physics: Design Study for the High Voltage test bench of 1.2 MeV, 2018.

[8] H.R.McK Hyder, “Electrostatics”, R. Hellborg (ed.) *Electrostatic accelerators*, Springer 2005.

[9] R. Hellborg, “High Voltage Tests of an Electrostatic Accelerator for Different Mixtures of Gases at Various Pressures”, NIM A **379** pp. 185-191, 1996.

ISBN: 978-3-95450-218-9 ISSN: 2226-0374 doi:10.18429/JACoW-COOL2019-MOZ01

THE ELECTRON COOLING SYSTEM FOR HIAF PROJECT IN CHINA*

L.J. Mao†, J. Li, H.J. Lu, X.M. Ma, M.T. Tang, X.D. Yang, L.X. Zhao, Y.B. Zhou,
Insittute of Modern Physics, Lanzhou, China

Abstract

A classical 450 keV magnetized DC electron cooling system is proposed to boost the luminosity of high-density internal targets experiment in the spectrometer ring (SRing) at HIAF. Electron cooling will provide highest phase space density of the stored highly charged heavy ion beams and compensate beam heating during internal target experiments. In addition, it will be used to suppress the beam loss in the deceleration mode. In this paper, the technical design of the electron cooling system is reported. The manufacturing of the key components such as the electron gun and collector is described.

INTRODUCTION

High Intensity heavy-ion Accelerator Facility (HIAF) is a new accelerator complex being constructed at the IMP site in China [1]. SRing is a versatile storage ring employed in nuclear and atomic experiments with stored stable or radioactive ion beams. Especially, the highly-charged stable ions can be used either at the injection energies or at lower energies after deceleration. A powerful electron cooling system is needed for the stable ion beams in the energy range of 800 to 30 MeV/u. It also allows few intermediate energies cooling in the deceleration operation mode, to obtain a high efficiency and low losses during the deceleration of ion beams. The electron beam should be turned off during the ramping of the high voltage deceleration. In addition, the electron cooling involves isotopes beam cooling together with the stochastic cooling system. Figure 1 shows the layout of the HIAF accelerator complex. The electron cooler will be installed in the 16 meter-straight section of SRing. The length of the cooler in ion beam direction is 11.2 m. the height is limited by the tunnel up to 6 m. Therefore, the high voltage tank is equipped on the side of the cooler.

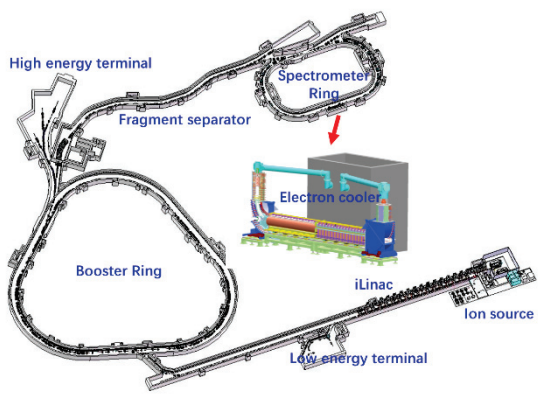

Figure 1: Layout of the HIAF accelerator and its cooler.

* Work supported by National Development and Reform Commission (NDRC), National Natural Science Foundation of China (No.11475235)
† maolijun@impcas.ac.cn

CHOICE OF PARAMETERS

The ion beam $^{238}U^{92+}$ is taken as a reference in the simulation and design work of SRing. The ion energy ranges from 800 MeV/u to 30 MeV/u (deceleration) that corresponds to the electron energy range of 15 keV and 450 keV. The initial beam parameters are defined by the fast extraction system of the booster ring (BRing), as listed in Table 1. The calculations in this paper were performed a multi-particle tracking code, in which the cooling rate was derived from Parkhomchuk cooling force formula:

$$G = \frac{1}{\gamma^2}\frac{4cr_e r_i n_e \eta_c}{\left(\beta^2\gamma^2\frac{\varepsilon_\perp}{\beta_\perp}+\beta^2\left(\frac{\Delta p}{p}\right)^2+\left(\frac{v_{eff}}{c}\right)^2\right)^{\frac{3}{2}}}\frac{Z^2}{A}\ln\left(1+\frac{\rho_{max}}{\rho_{min}+\rho_l}\right). \quad (1)$$

the definition of the parameters can be found in [2]. All parameters should be written in the laboratory reference system.

Table 1: Initial Beam Parameters of SRing

Parameters	Value
Ion	$^{238}U^{92+}$
Energy	800 MeV/u
Emittance (hort./vert.)	4.0/2.0 π.mm.mrad
Momentum spread	8.0×10^{-4}
Stored particle number	10^9

The circumference of SRing is 277.3 m and the longest straight section is 16.0 m. The cooling rate grows linearly with the cooler length. Thus, a long cooler has a high cooling rate. Especially it is essential at the injection (top energy) stage when the emittance and the momentum spread are large. Based on the CSR cooler design, a U-shape electron cooler was proposed with the bending radius of 1.0 m. Further, a space for the compensation solenoids and correctors was considered at upstream and downstream of the cooler. Finally, an 8 m cooling solenoid was chosen for the SRing cooler. The designed β function at the centre of the cooler is 10.0 m, we estimated the maximum β function is not larger than 13.0 m according to the formula $\beta + s^2/\beta$.

The electron intensity also determines the cooling rate. Generally, the cooling rate is proportional to the electron beam current. But on the other hand, the effective velocity induced by a space charge electron drift in the longitudinal magnetic field could reduce the cooling rate. Thus, a very high electron current becomes useless. Figure 2 shows the cooling rate versus the electron current at different values of the magnetic field. The other parameters used in the calculation are listed in Table 2. Based on the operation experience of CSRe 300 kV cooler, and in consideration of the power consumption on the high voltage terminal, the maximum electron currents up to 2.0 A was designed for the

ISBN: 978-3-95450-218-9 ISSN: 2226-0374 doi:10.18429/JACoW-COOL2019-MOZ01

SRing cooler. A thermionic electron gun with an oxide cathode is proposed to use in the cooler. The Ni sponge cathode radius is 15 mm, the emission current density is 0.25 A/cm^2 at the temperature of 700 ºC and 0.50 A/cm^2 at the temperature of 750 ºC, respectively. A prototype of the cathode was already developed [3].

Table 2: Simulation Parameters of SRing Electron Cooling

Parameters	Value
Electron energy	438.8 keV
Lorentz factor	β=0.842, γ=1.853
Electron beam radius	3.0 cm
Electron beam current	2.0 A
Electron beam density (PRF)	9.3×10^6/cm^3
Longitudinal magnetic field	8.0×10^{-4}
Electron beam temperature (horizontal / longitudinal)	0.5 / 3×10^{-5} eV
Magnetic field homogeneity	1×10^{-4}
Beta-function	9.9 m / 9.7 m
Cooling length/circumference	2.6%

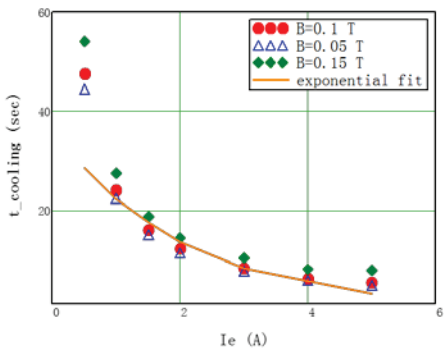

Figure 2: cooling time versus electron current at different values of magnetic field.

It is also observed that the longitudinal magnetic field changes the cooling time. As the magnetized cooling theory, the radius of electron Larmor gyration should be much less than the maximum impact parameter, and more importantly, the electron drift velocity in the space charge fields of the electron beam and the longitudinal magnetic field should be much smaller than the effective velocity induced by the magnetic field homogeneity. Finally, a longitudinal magnetic field up to 1.5 kGs was used for the SRing cooler.

Magnetic field homogeneity in the cooling section is an important parameter in Parkhomchuk formula. It makes a largest contribution to the effective velocity. Figure 3 shows the cooling time versus the field homogeneity. It shows a good magnetic field homogeneity starts at 10^{-4}, further decrease of the homogeneity does not lead to the variation of the cooling time. A pan-cake structure of the cooling section solenoid, which was already used in coolers for CSR successfully [4], obtained a high precise magnetic field with the homogeneity better than 3×10^{-5}. Based on the simulation results and the CSR cooler commissioning experience, a longitudinal magnetic field homogeneity better than 10^{-4} is required at the cooling section solenoid.

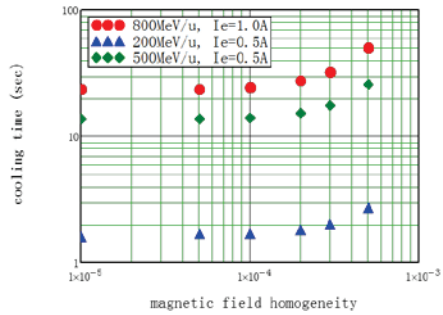

Figure 3: cooling time versus longitudinal magnetic field homogeneity at different energies of cooling.

COOLING PROCESS SIMULATION

The main task of the SRing electron cooler is to reduce the beam phase volume at the injection energies, and provide continually cooling effect at experimental energies for the internal target operation mode. A typical operation scheme is shown in Fig. 4. At the injection energies, the electron cooling is turned on for a few seconds to reduce the emittance several times. It is not necessary to cool down the ion beam to the equilibrium status. Then the electron beam is turned off for the decreasing of the high voltage. After the deceleration, the electron beam is turned on again, to supress the heating effects and compensate the energy loss of the internal target experiments. Optionally, an intermediate cooling is also available to optimize the beam quality in the deceleration mode.

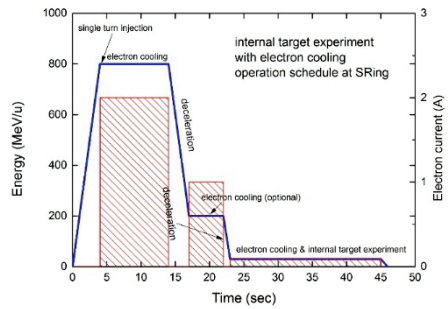

Figure 4: SRing operation scheme with electron cooling.

A cooling process of 800 MeV/u $^{238}U^{92+}$ beam is simulated, as shown in Fig. 5. The input parameters are listed in Tables 1 and 2. It is seen that the emittances and momentum spread are effectively decreased during 10 seconds.

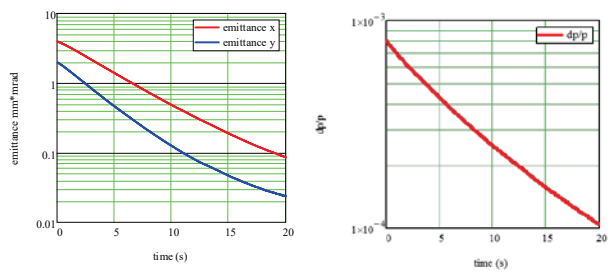

Figure 5: Beam emittances and momentum spread versus time at electron cooling of 800 MeV/u $^{238}U92+$ beam.

ISBN: 978-3-95450-218-9 ISSN: 2226-0374 doi:10.18429/JACoW-COOL2019-MOZ01

SRING ELECTRON COOLER

The general layout of the SRing electron cooler is shown in Fig. 6. Basically, a strong longitudinal magnetic field is used to guide the electron beam and to magnetize the electrons. The electron beam extracted from the gun is accelerated to an energy up to 450 keV and bent into the cooling section. After the interaction, the electron beam is guided to the collector and absorbed in it. The cooler consists mainly of electron gun, collector, acceleration tube, guiding magnets and high voltage tank. The main technical parameters of the SRing electron cooler are listed in Table 3.

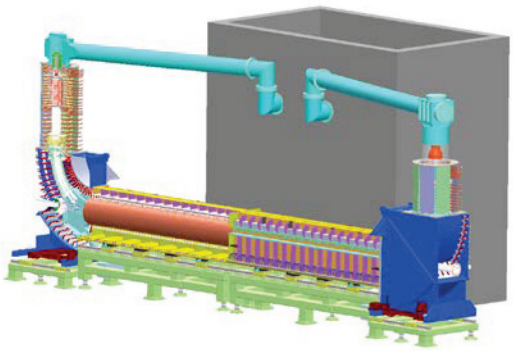

Figure 6: Layout of the SRing electron cooler.

Table 3: Technical Parameters of SRing Cooler

Parameters	Value
Maximum acceleration voltage	450 kV
Voltage ripple	$<5.0\times10^{-5}$
Cathode radius	1.5 cm
Maximum electron current	2.0 A
Gun solenoid field	4.0 kGs
Cooling solenoid field	1.5 kGs
Collector solenoid field	2.0 kGs
Effective cooling length	7.4 m
Vacuum chamber diameter	200 mm
Vacuum	2.0×10^{-11}
Total power consumption	700 kW

Gun and Acceleration

In order to control the electron beam temperature out of the acceleration, the thermionic electron gun together with the acceleration tube immerse in the same longitudinal magnetic field up to 4.0 kGs, as shown in Fig. 7. We use a similar gun geometry of CSRe cooler for the calculation. A 502 mm tube with 23 electrodes and an electrical gradient of 10 kV/cm was used for the acceleration of the electron beam up to 450 keV. Generally, the transverse electric field at the exit of the acceleration tube significant leads to an increasing of the electron beam temperature due to the $E\times B$ drift velocity. An increasing of the longitudinal magnetic field reduces the electron Larmor radius and the drift velocity, thereby obtaining an adiabatically motion. An additional transverse temperature less than 0.1 eV was obtained while the longitudinal magnetic field was 4.0 kGs.

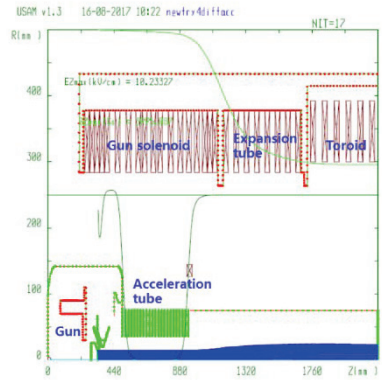

Figure 7: electron trajectory in gun and acceleration tube.

As the same as the CSR coolers' gun, the grid electrode placed between the cathode and the anode is used to produce a variation of the transverse electron beam density distribution [5]. A "hollow" electron beam will be obtained by increasing of the ratio of grid-to-anode voltages V_g/V_a. The calculation by UltraSAM also shows a linear increase of perveance with the increasing of V_g/V_a:

$$P(\mu P) = 15.9\frac{V_g}{V_a} - 1.3. \quad (2)$$

Collector

The SRing cooler collector consists of an oil-cooled oxide-free cupper cup, a suppress electrode and an anode. The magnetic field is optimized in order to minimize secondary electrons emission. The maximum magnetic field in the collector is around 2.0 kGs. The supress electrode is used to form an electrostatic potential barrier to supress electrons escape from the collector. The supress electrode voltage is 400 V. The electrostatic potential and the magnetic field in the collector are shown in Fig. 8. In the ejected electrons trajectory simulation, 200 secondary electrons are generated randomly in the energy range between 0 and 3 keV, the azimuthal angle range between 0 and 2π. The trajectories show that most electrons go back to the collector cup but only few electrons can escape successfully. The simulation results show a collect efficiency better than 10^{-3} is available.

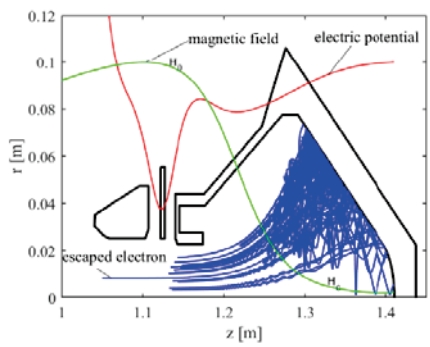

Figure 8: Secondary electrons trajectory in collector.

ISBN: 978-3-95450-218-9 ISSN: 2226-0374 doi:10.18429/JACoW-COOL2019-MOZ01

Magnetic Field

A high-quality magnetic field is required for the SRing cooler, the allowable magnetic field homogeneity is estimated to be less than 10^{-4} in the cooling section and 10^{-3} in other sections, respectively. A 3-D Opera module was used for the analysis, as shown in Fig. 9. The field calculation was done in ion beam direction, especially the toroid section.

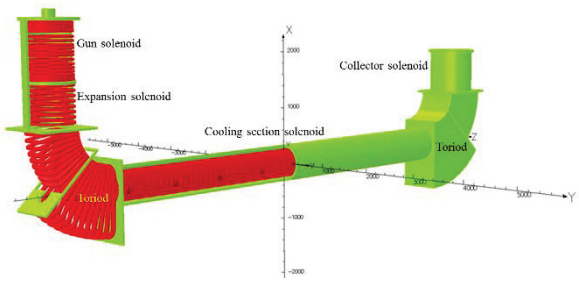

Figure 9: 3-D Opera module of SRing electron cooler.

As expected, a vertical field component with a maximum value of about 700 Gs on the collector-side toroid is shown in Fig. 10. The field direction is upwards since the guiding magnetic field is from the gun to the collector. It causes a severe horizontal ion beam deflection which has to be corrected by a set of steerers around the cooler. A weaker but not negligible orbit distortion in the vertical plane is caused by the horizontal field component.

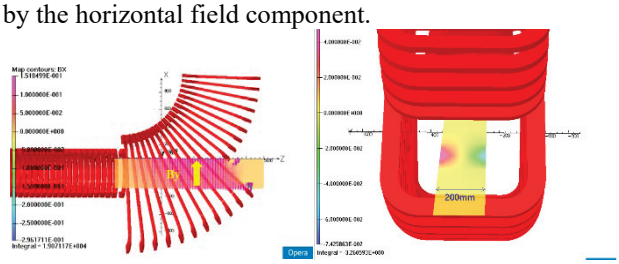

Figure 10: Vertical and horizontal field components on the collector-side toroid.

The magnetic field along the electron beam trajectory was also calculated from the gun side to the collector side. The magnetic field is decreased gradually from 4.0 kGs at the gun section to 1.5 kGs at the cooling section. The transverse electron temperature is expected to be decrease by adiabatic expansion:

$$\zeta = \frac{\lambda}{B_S}\frac{dB}{ds}. \tag{3}$$

where $\lambda = \frac{2\pi\gamma m_e \beta c}{eB_S}$. The total magnetic field and calculated adiabaticity at different electron energies are shown in Fig. 11. It is seen that the adiabaticity parameter is less than 0.15 at the top electron energy of 450 keV, and the parameter decreases with decreasing of the electron energy. The adiabaticity parameter stays always well below 1.0. A good adiabatic condition for electron motion can be achieved.

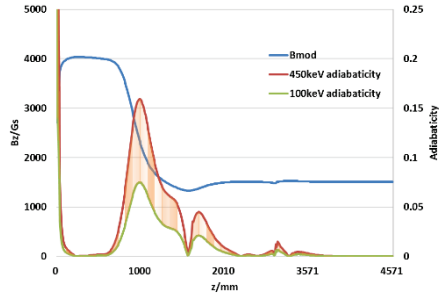

Figure 11: Magnetic field along the electron trajectory and adiabaticity parameters at different energies.

CONCLUSION

The SRing electron cooler has been designed. The effective cooling length is 7.4 m or 2.6% of the ring circumference. The adiabatic parameter along the electron beam trajectory is kept bellow 0.15. This magnetized electron cooler can provide a powerful cooling effects on the highly-charged stable ions or long-lived radioactive isotopes. The main components such as the electron gun, the collector, the magnetic field system have been designed. The technical design of the high voltage system is still under investigation.

ACKNOWLEDGEMENT

The authors would like to thank members of the HIAF design group. We also like to thank Dr. Parkhomchuk, Dr. Reva and Dr. Katayama for the permanent support of this work and helpful discussions.

REFERENCES

[1] J.C.Yang *et al.*, *Nucl. Instr. and Meth. B* vol. 317, pp. 263-265, 2013.

[2] V.V.Parkhomchuk, *Nucl. Instr. and Meth. A* vol. 441, pp. 9-7, 2000.

[3] X. H. Liao, Y. Li, M. F. Meng, X. X. Wang, and Q. L. Zhao, "Study on the Oxide Cathode for HIRFL-CSR Electron Cooler", in *Proc. 7th Workshop on Beam Cooling and Related Topics (COOL'09)*, Lanzhou, China, Aug.-Sep. 2009, paper THPMCP012, pp. 160-163.

[4] L.J.Mao *et al.*, *High Power Laser and Particle Beams*, Vol.17, No.7 pp. 1106-1110, 2005.

[5] A. V. Ivanov *et al.*, "The Electron Gun with Variable Beam Profile for Optimization of Electron Cooling", in *Proc. 8th European Particle Accelerator Conf. (EPAC'02)*, Paris, France, Jun. 2002, paper WEPRI049, p. 1356.

ISBN: 978-3-95450-218-9 ISSN: 2226-0374 doi:10.18429/JACoW-COOL2019-MOA02

DESIGN OF A COMPACT ELECTRON GUN FOR THE HIGH-VOLTAGE ELECTRON COOLING SYSTEM OF THE NICA COLLIDER

A. P. Denisov, M. I. Bryzgunov, A. V. Bubley, A. V. Ivanov, V. V. Parkhomchuk, A. A. Putmakov, V. B. Reva, Budker Institute of Nuclear Physics, Novosibirsk, Russia

Abstract

The low temperature of the electron beam is the key for the high efficiency of the electron cooling, and the strong guiding magnetic field is the means for it. However, high-voltage electron cooling systems come with the challenge of providing the low-temperature beams, as the guiding magnetic field is limited. The electron gun design for the NICA collider cooling systems combines the utilizing the magnetic field and the electrical field constructing, by using the electrodes of special shapes.

INTRODUCTION

The NICA collider is designed to operate ion beams with energies up to 4.5 GeV/u [1]. In order to increase the ions accumulation efficiency and ions lifetime in the collider the electron cooling system must provide 2.5 MeV electron beams [2]. During the electron cooling process, the ions lose excess energy due to electrical interactions with electrons. The more electrons, the more energy it can take from ions. Therefore, the efficiency of the cooling depends on the electron beam current density and the momentum spread in the electron beam [3].

Budker Institute of Nuclear physics has a lot of experience in creating electron cooling systems for different beam energies, starting from the first electron cooling system where the very principle of the electron cooling were demonstrated [4], ending with the high-voltage cooler for COSY [5] and low-energy cooling system for NICA [6] Booster. All those systems exploit the similar design of an electron gun, sometimes with small modifications. The main part of the used gun designs is a control electrode, which allows controlling the emission from different parts of a cathode. Later, for electron coolers for COSY and NICA Booster the design of the control electrode was improved by splitting it into four sectors with independent high-voltage power supplies.

The previous design of electron guns used in electron cooling systems produced in BINP exploit a 3 cm diameter cathode. The radius of ion beams in NICA collider is just 0.3 cm (rms). The high-voltage electron cooling system for the NICA collider will use a new electron gun able to produce a 1 cm diameter continuous electron beam with current up to 1 A.

REQUIREMENTS FOR THE ELECTRON GUN

Electron Beam Current Density

The electron beam current density and momentum spread are two major factors that affect the cooling efficiency. According to Parkhomchuk's empirical formula (1), the cooling time is inversely proportional to the electrons density, and for the NICA collider we want it to be at least one order of magnitude lower than the IBS growth time.

$$\frac{d\vec{p_i'}}{dt'} = \frac{4Z^2e^4n_e'\Lambda}{m_e}\cdot\frac{-\vec{v_i'}}{\left[v_i'^2+v_{eff}^2\right]^{3/2}} \quad (1)$$

Here n_e', v_i', p_i' are the electron density, ions velocity and momentum in the beams frame of reference. v_{eff} is the parameter describing the magnitude of electrons motion, and Λ is a Coulomb logarithm.

Taking into account the NICA collider design parameters, shown in Table 1, and using the cooling time estimation (2) resulting from Parkhomchuk's formula, the necessary electron current density amounts to 0.8 A/cm^2. The final design electron current is 1 A, corresponding to 1.5 A/cm^2.

Table 1: NICA Collider Parameters for Cooling Time Estimations

Parameter	Value		
Z/A	79 / 197		
Ion energy, GeV/u	1.0	3.0	4.5
Hor/ver rms emittance, π·mm·mrad	1.1 / 0.95	1.1 / 0.85	1.1 / 0.75
IBS growth time, s,	160	460	1800
Beta function at the cooling section, m	10		
Collider circumference (L_P), m	503		
Cooling section length (L_C), m	6		
Cooling time (t_{Cool}), s	16	46	180
j_e, A/cm^2	0.05	0.6	0.8

$$\tau_{Cool}\sim\frac{x'^3}{j_e}\cdot\frac{A}{Z^2}\cdot\frac{\gamma^5 m_e m_p v_0^4}{4e^3\Lambda}\cdot\frac{L_P}{L_C} \quad (2)$$

Here v_0 is the mean ion beam velocity, x' is the r.m.s. angle in the ion beam in the cooling section, L_P/L_C is used to take into account that the cooling takes place only in a small part of the ion collider. Λ is approximately equal to 5.

ISBN: 978-3-95450-218-9 ISSN: 2226-0374 doi:10.18429/JACoW-COOL2019-MOA02

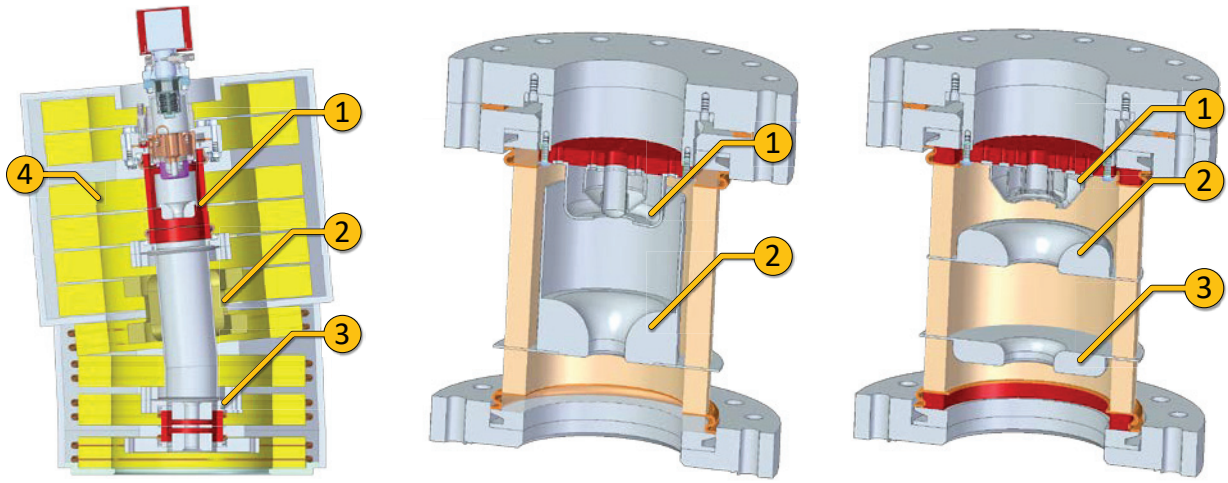

a b c

Figure 1: The design of the electron gun for the NICA collider electron cooling system. (a) is the electron gun with magnetic bending site: (a-1) a cathode assembly, (a-2) magnetic correctors, (a-3) the electrostatic lens, (a-4) solenoid coils for creating guiding magnetic field. (b) is the design of the convex cathode assembly: (b-1) the four-sector control electrode, (b-2) the anode. (c) is the design of the flat cathode assembly: (c-1) the four-sector control electrode, (c-2) the anode, (c-3) the auxiliary electrode for setting the electron beam output energy.

Electron Beam Momentum Spread

The acceptable momentum spread that electron beam can have is defined by the accuracy of available methods to measure it. The new high-voltage electron cooling system [2] is based on the magnetized motion of electrons along the entire electron beam transport channel, and magnetic coils and correctors for creating the guiding magnetic field take most of the space. The only available tools for electron beam diagnostics are beam position monitors (BPM).

In the high-voltage column where the electrical and magnetic fields have axial symmetry, the motion of electrons has axial symmetry as well. Thus, the non-zero electron beam momentum spread results in beam size oscillation in the longitudinal magnetic field. The amplitude of such oscillations can be measured using BPMs [7]. The typical sensitivity of a BPM is about 10-30 μm that corresponds to 1 eV oscillations of electrons in 1.5 kG magnetic field.

THE ELECTRON GUN DESIGN

The new electron gun designed for the high-voltage cooling system of the NICA collider consists of five main parts (Fig. 1a): a cathode assembly, a solenoid for creating the guiding magnetic field, a magnetic bending site, magnetic correctors for compensating drift of electrons in the bending site and the electrostatic lens.

The magnetic bending of the electron beam is necessary to shift the cathode from the acceleration tube axis to protect it from the incident ions of the residual gas occasionally travelled into the acceleration tube.

The cathode assembly for the electron gun has two variants. The first one is based on the convex cathode to achieve larger beam current while preserving the controllability of the beam current density (Fig. 1b). The second one (Fig. 1c) uses a flat cathode and a shielding electrode placed at the Pierce angle to the cathode surface that helps reducing the radial electrical fields near the cathode and the resulting amplitude of electrons Larmor oscillations.

The electrostatic lens (Fig. 2) consists of shielding electrodes at the gun's output potential for localizing the electrical field from the lens, and an electrode, electrical potential of which varies from -7.5 kV to +7.5 kV with respect to the potential of the shielding electrodes. The gap between the lens electrode and shielding electrodes is 7.5 mm, which defines the maximum voltage safe for the lens operation (10 kV/cm). The lens electrode thickness is 5 mm and its aperture is 22 mm. As the radius of the electron beam is 5 mm, the dependency of the radial electrical field of the lens on the radial coordinate is close to linear in the beam area (Fig. 3)

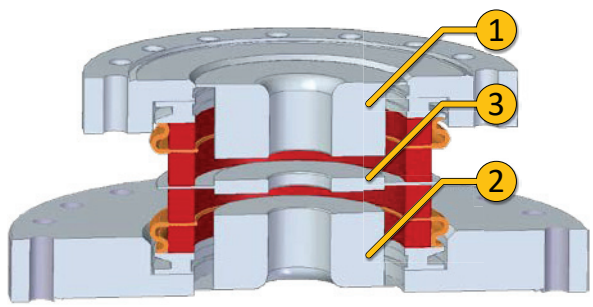

Figure 2: The electrostatic lens design: (1, 2) electrodes at the beam potential, (3) the electrode for creating a focusing electrical field.

CALCULATIONS OF THE CATHODE ASSEMBLY

Both variants of the cathode assembly were optimized to achieve lower electron beam momentum spread values and sufficient controllability. The calculations of electrical

ISBN: 978-3-95450-218-9 ISSN: 2226-0374 doi:10.18429/JACoW-COOL2019-MOA02

fields and electron beam parameters were made using SAM software developed in BINP [8].

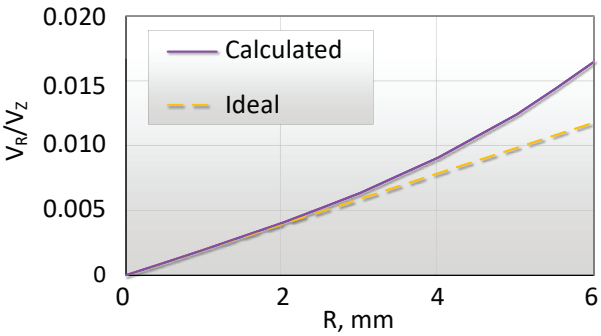

Figure 3: The focusing strength of the electrostatic lens. The lens voltage is 1 kV and energy of electrons is 10 keV.

Naturally, the perveance of the convex cathode is higher as the emissive surface is larger and electrical field is concentrated due to the cathode curvature (Fig. 4a). However, the velocities profile of the electron beam produced by the convex cathode is non-linear (Fig. 4b). By the velocities profile we mean the dependency of the electrons radial velocity on the radial coordinate in the beam cross-section. As electrons oscillate in the magnetic field, the profile changes with the longitudinal coordinate. The profiles shown in Fig. 4b correspond to the moment when the electrons on the beam edge have the radial velocity only. In case of the flat cathode, the electrostatic lens kick can decrease the amplitude of Larmor oscillations. As for the convex cathode, reducing the oscillations amplitude of the electrons near the beam edge using a simple electrostatic lens will lead the electrons near the beam center to gain momentum and vice versa.

The momentum spread of the electron beam at the output of the gun depends on the configuration of the electrical and magnetic fields. The beam energy in the cathode assembly is about 10-20 keV. Given the magnetic field 1000 G, the step of Larmor helix is about 3 cm that is close to the distance between the electrodes. Because of that, there is resonant behaviour in the electrons motion, which can be easily seen in calculations made for the flat cathode assembly, where the additional electrode is introduced. The additional electrode defines the output beam energy 10 kV, while anode has higher voltage to extract more current from the flat cathode (15 kV). The electrons passing through these electrodes gain transverse momenta due to the radial electrical field. However, at a certain value of the guiding magnetic field (1000 G), the direction of the electrical force and the electrons transverse velocity can be out of phase most of the time due to Larmor oscillations, causing the amplitude of oscillations to decrease (Fig. 4c).

According to [9], the controllability of a current density profile is essential to prevent instability development in ion beams caused by overcooling. By increasing electron emission from the cathode edges using the control electrode, the emission from the center of the cathode can be suppressed by the space charge electrical field. In this case, the electron beam becomes “hollow”. The cooling rate for ions with small amplitudes of betatron oscillations is lower than for those with large amplitudes; therefore, the ion beam cools more evenly. The designed gun with a convex cathode allows increasing the emission from the edges about two times, while keeping the current density at the cathode center at 2 A/cm^2 (Fig. 5). The electron gun with a flat cathode is less flexible (Fig. 6). Changing the voltage on the control electrode brings the cathode assembly out of the Pierce optics and causes the radial electrical fields near the cathode to grow. As a result, the increase of the emission from the cathode edge is accompanied by the growth of the electron beam momentum spread. Another disadvantage, caused by the Pierce optics approach used in the gun with the flat cathode, is that changing the voltage on control electrode affects the electrical field near the cathode surface almost evenly, and it is difficult to get current density near the beam edges much larger than near the beam center (Fig. 6).

CONCLUSION

The electron gun for the high-voltage electron cooling system for the NICA collider has the design different from other electron guns produced in BINP for electron coolers.

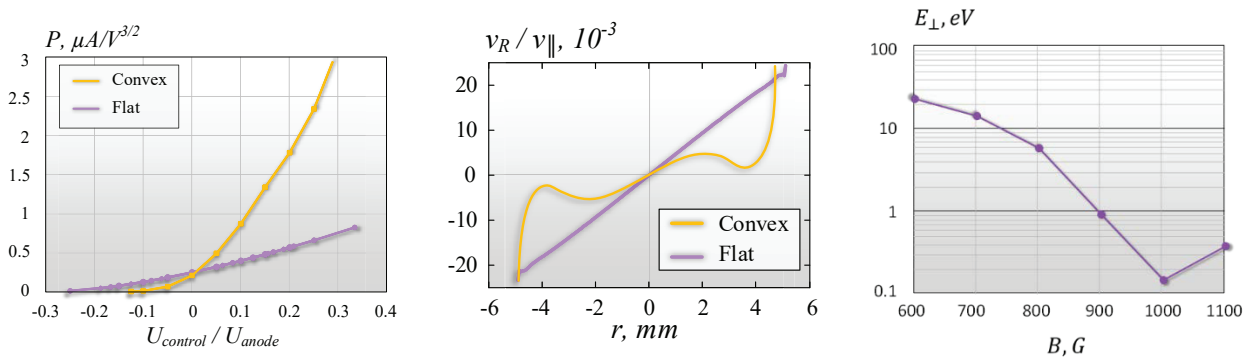

a b c

Figure 4: (a) Computed perveance for two variants of the cathode assembly. (b) Comparison of transverse velocities profiles of electron beams produced by two variants of the cathode assembly. (c) The dependency of the energy of electrons Larmor oscillations at the output of the flat cathode assembly on the magnitude of the guiding magnetic field.

ISBN: 978-3-95450-218-9 ISSN: 2226-0374 doi:10.18429/JACoW-COOL2019-MOA02

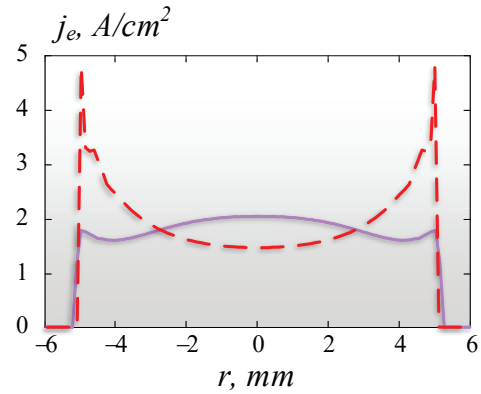

Figure 5: The electron current density distribution of the beam produced by the convex cathode assembly. Normal regime (purple line): U_{anode} = 15 kV, $U_{control}$ = 1.3 kV. Hollow beam (red dashed line): U_{anode} = 10 kV, $U_{control}$ = 2 kV. Guiding magnetic field is 1000 G.

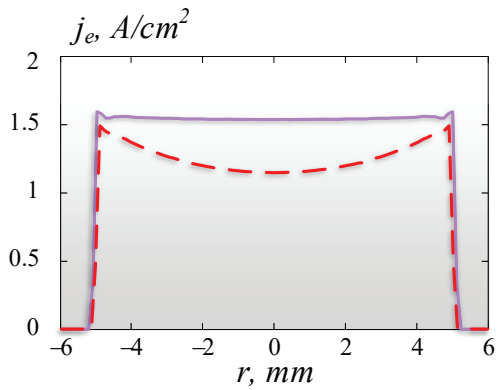

Figure 6: The electron current density distribution of the beam produced by the flat cathode assembly. Normal regime (purple line): U_{anode} = 20 kV, $U_{control}$ = 2.5 kV. Hollow beam (red dashed line): U_{anode} = 10 kV, $U_{control}$ = 4 kV. Guiding magnetic field is 900 G.

It is designed to produce a 1 cm diameter continuous electron beam with current up to 1 A and transverse momentum spread corresponding to the energy about 1 eV.

The new gun design with magnetic bend of the electron beam provides protection of the cathode from the high-energy ions of the residual gas that can occasionally get into the acceleration tube. In order to reduce the amplitude of electrons Larmor oscillations with energies exceeding the defined limit of 1 eV, the supplementary electrostatic lens is placed at the end of the gun site.

The test bench for measuring the parameters of the gun prototype is under construction.

REFERENCES

[1] A. Kovalenko *et al.*, “Status of the NICA project at JINR”, *EPJ Web Conf*, vol. 191, p. 01003, Oct. 2018.

[2] V. B. Reva *et al.*, “High voltage cooler NICA status and ideas”, in *Proc. 11th International Workshop on Beam Cooling and Related Topics (COOL17)*, Bonn, Germany, January 2018, paper TUM21, pp. 25-27.

[3] V. V. Parkhomchuk, A. N. Skrinsky, “Electron cooling: 35 years of development”, *UFN*, vol. 170, no 5, pp. 473–493, 2000, http://mi.mathnet.ru/eng/ufn1754

[4] V. V. Parkhomchuk *et al.*, “Investigation of fast electron cooling”, http://www.inp.nsk.su/images/preprint/1979_056.pdf

[5] V. B. Reva *et al.*, “Recent experiments with high energy electron cooler in COSY”, in *Proc. of RuPAC2016 (RuPAC2016),* St. Petersburg, Russia, October 2016, paper WECAMH04, pp. 67-69.

[6] A. V. Smirnov *et al.*, “Commissioning of electron cooling system of NICA Booster”, in *Proc. of 26th Russian Particle Accelerator Conference (RUPAC2018),* Protvino, Russia, September 2018, paper TUPSA22, pp. 188-190.

[7] V. B. Reva *et al.*, “COSY 2 MeV cooler: design, diagnostics and comissioning”, in *Proc. of IPAC2014,* Dresden, Germany, 2014, paper MOPR1075, pp. 777-779.

[8] A. Ivanov, M. Tiunov, “UltraSAM – 2D code for simulation of electron guns with ultra high precision”, in *Proc. of EPAC 2002,* Paris, France, 2002, pp. 1634-1636.

[9] V. V. Parkhomchuk, “Development of a new generation of coolers with a hollow electron beam end electrostatic bending”, in *Proc. of International Workshop on Beam Cooling and Related Topics (COOL05)*, Galena, Illinois, U.S.A., September 2005, paper CP821, pp. 249-258.

ISBN: 978-3-95450-218-9 ISSN: 2226-0374 doi:10.18429/JACoW-COOL2019-TUX01

STATUS OF THE ELECTRON COOLER FOR NICA BOOSTER AND RESULTS OF ITS COMMISSIONING

M.Bryzgunov, V.Parkhomchuk, V.Reva, A.Bubley, A.Denisov, V.Panasyuk, A.Goncharov, A.Putmakov, N.Kremnev, V.Polukhin, V.Chekavinskiy, I.Gusev, D.Senkov, G.Karpov, E.Bekhtenev, M.Kondaurov, A.Zharikov, Budker Institute of Nuclear Physics SB RAS, Novosibirsk, Russia
A.Kobets, I. Meshkov, S.Melnikov, O.Orlov, A. Sergeev, S.Semionov, A.A.Sidorin, A. Smirnov, Joint Institute for Nuclear Research, Dubna, Russia

Abstract

The electron cooling system of the NICA booster is intended for accumulation of the ion beam at the injection energy and for cooling at some intermediate energy value before acceleration to the extraction energy. The system was produced in BINP (Novosibirsk, Russia) and commissioned in the JINR (Dubna, Russia) in 2019. The current status of the electron cooler and the results of its tests are presented in the article.

INTRODUCTION

In order to achieve needed parameters of the ion beam in the NICA booster the ring will be equipped with low energy electron cooling system, which provides accumulation of ions on injection energy (3.2 MeV/u) and on some intermediate energy (60-100 MeV/u) to prepare the beam for acceleration to the extraction energy.

The electron cooling system was developed and commissioned in the BINP in 2016. In 2017 it was assembled and commissioned in the JINR. Its main parameters are shown in the Table 1.

Table 1: Main Parameters of the Cooler

Parameter	Value
Ion type	$^{197}Au^{31+}$
Electron energy, E	1.5÷60 keV
Electron beam current, I	0.2÷1.0 A
Energy stability, ΔE/E	$<10^{-5}$
Electron current stability, ΔI/I	$<10^{-4}$
Longitudinal magnetic field, B	0.1÷0.2 T
Electron current loses, I_{leak}/I	$<3\cdot10^{-5}$
Vacuum pressure, Pa	$\approx10^{-11}$ mbar

Important feature of the system is possibility of work on different energies in one cycle of booster ring (ramp regime). Since length of booster cycle is several seconds, regime of the cooler have to be changed from injection to intermediate energy in period of about 0.5-1 sec.

CONSTRUCTION

The cooler is produced with the classical scheme (Fig. 1). The DC electron beam is formed in the gun and then it is accelerated to work energy. After acceleration it moves through the toroid magnet to the cooling section, where it interacts with ion beam. After that the electrons move though another toroid to the electron collector where them are decelerated and absorbed on collector surface. Deceleration before collector is made to recuperate electron energy.

On whole way from gun to collector the beam moves in longitudinal magnetic field. There are two reasons for it: the field provides transverse focusing of the beam; in the cooling section the field allows to make, so called, fast electron cooling [1]. In order to reach high homogeneity of longitudinal magnetic field in the cooling section, the solenoid is made of separate coils with possibility to rotate each coil around two transverse axes [2].

To compensate centrifugal force in toroid magnets special electrostatic plates, which produce transverse electric field, are used. Use of electric filed instead of magnetic to compensate centrifugal force allows to increase recuperation efficiency without improving of collector efficiency [3,4].

The gun and the collector are based on constructions used in previous coolers produced in BINP. The collector consists of two parts: main massive, oil cooled, electrode and ceramic insertion before it, which contains suppressor and pre-collector electrodes. The suppressor allows to produce potential barrier on the collector entrance in order to lock secondary electron in the collector, to increase its efficiency. The pre-collector electrode has the same voltage as the collector and provides symmetry of the potential in suppressor region. The electrostatic barrier in the collector is supplemented by magnetic plug, which is produced by special shape of the magnetic filed.

The main gun feature is four sector control electrode that provides measure not only beam position (with the help of beam position monitors, by modulation of voltage on all four sectors simultaneously) but also beam size (by modulation of voltage on every sector separately) [5].

Solenoids of the magnetic system are powered with 4 independent high current power supplies (PS, IST type). Nominal value of the longitudinal field in the system is 1-2 kG.

Besides high current supplies the system contains set of low current power supplies (5 and 20 A), which power magnetic correctors of the cooler.

In order to work in ramp regime, correctors and HV system must have capability to change output parameters for a period of 0.5-1 sec. It was decided, that high current PS (IST) will not change output current during ramp, because

ISBN: 978-3-95450-218-9 ISSN: 2226-0374 doi:10.18429/JACoW-COOL2019-TUX01

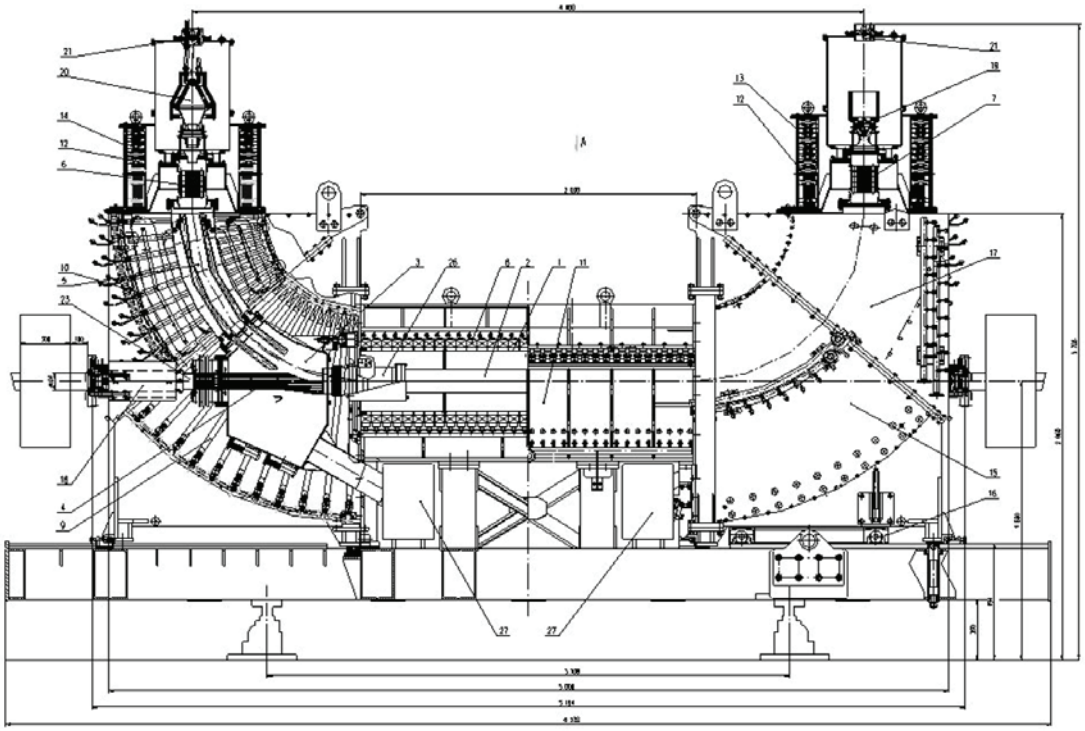

Figure 1: Drawing of the electron cooling system for the NICA booster.

such type of PS are too slow, and there is possibility to make ramp regime without them.

Since synchronous change of electron beam energy with currents in magnetic correctors is difficult task (because it needs fast online measurements) and there is no necessity to cool beam during acceleration, it was decided to turn off the beam before change of its energy and turn it on after energy reaches another value. To turn off the beam anode voltage will be set to 0 and control electrode voltage will be set to -2÷-3 kV. Synchronization of all systems is done with the help of special electronic block (CGTI).

TEST RESULTS

After the cooler was commissioned some additional works with electronics and experiments with electron beam were carried out. Results of some experiments are presented below.

High Voltage Tests

Results of high voltage tests are shown in Fig. 2. Here one can see dependence of leakage current on voltage of the main power supply.

In Fig. 3 dependence of voltage and vacuum pressure on time for the same measurements are shown. Abrupt increase of pressure on high voltage (higher then 40 kV) means that some discharge processes occurs in vacuum chamber of the cooler.

Beam Tests

During tests with electron beam in JINR current up to 500 mA was achieved. Figure 4 shows dependences of main beam current and leakage current on time. Electron energy here is 10 keV.

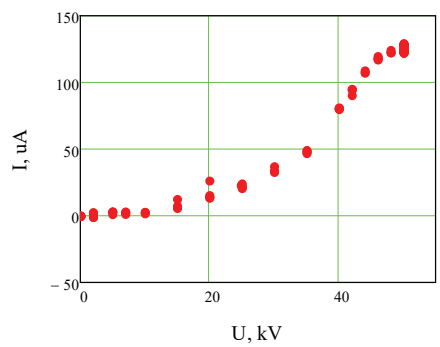

Figure 2: Dependence of leakage current on voltage of main PS

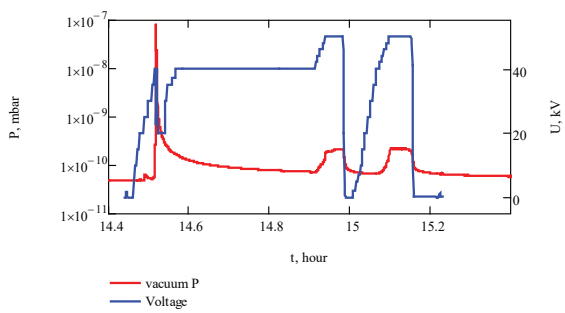

Figure 3: Dependence of voltage of main PS and vacuum pressure on time during high voltage test.

ISBN: 978-3-95450-218-9 ISSN: 2226-0374 doi:10.18429/JACoW-COOL2019-TUX01

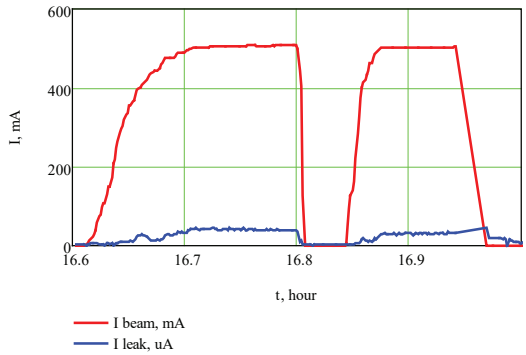

Figure 4: Results of tests with beam.

An interesting effect, which was observed during commissioning in JINR is vacuum pumping by the electron beam (during commissioning in BINP it was observer too). In Fig. 5 dependences of beam current, leakage current and vacuum pressure on time are shown. One can see, that when the beam is turned off vacuum pressure increases.

Design of the electron collector of the cooler supposes, that space charge of electron beam forms additional potential barrier in the collector entrance, improving collector efficiency. It means that on high values of current of main beam increase of beam current can lead to decrease of leakage current [6]. Since absorption of leaked electrons by walls of vacuum chamber, can cause desorption of neutral molecules and increase vacuum pressure, decrease of leakage current (while increase beam current) will decrease vacuum pressure. But in Fig. 5 one can see, that the leakage current decreases almost to zero value during turn off of the beam, that means the effect doesn't related with leakage current.

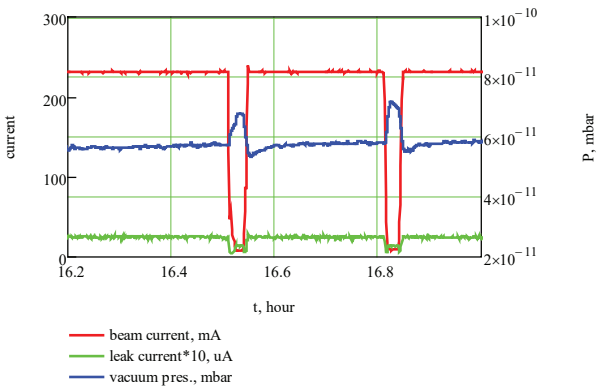

Figure 5: Dependence of the main beam current, leakage current and vacuum pressure on time.

Such dependence of vacuum pressure on beam current can be explained by ionization of rest gas by main electron beam. Produced positive ions of gas can move along the beam to gun or collector, where they are absorbed on walls of vacuum chamber. This effect was observed on previous electron coolers [7].

If electron trajectory length from gun to collector is L and ionization cross-section is σ, then one electron moving from gun to collector ionizes all atoms in volume v_1:

$$v_1 = \sigma L . \quad (1)$$

Assuming that all ions later die on walls of the vacuum chamber, the volume v_1 is equal to volume, evacuated by one electron. Number of electrons per second can be calculated from electron current:

$$\frac{dN}{dt} = \frac{I}{e} . \quad (2)$$

Resulting pump speed (evacuated volume per second) is equal to volume evacuated by one electron multiplied by number of electrons per second

$$\frac{dv}{dt} = v_1 \frac{dN}{dt} = \frac{\sigma L I}{e} . \quad (3)$$

For good vacuum conditions rest gas mainly consists of hydrogen molecules. Estimations of pump speed for electron current 230 mA give pumping speed about 5 l/s, that is close to observed results.

Space Charge Effect

As it was said before, the electron gun has four sector control electrode, which allows to measure not only beam position, but also beam size. On Fig. 6 four pictures, showing results of the beam size measurements on different BPMs with different current values are shown.

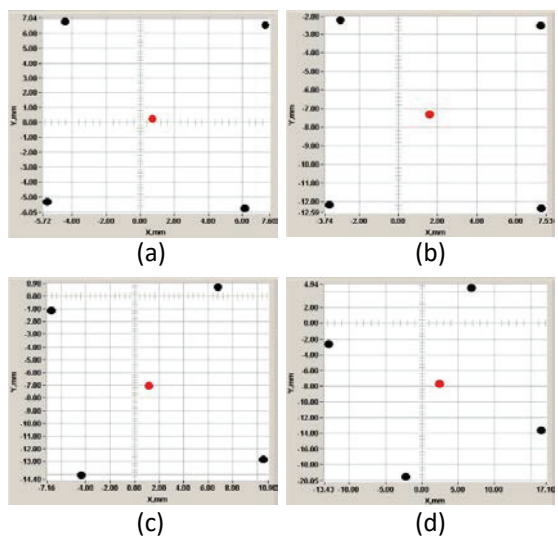

Figure 6: Electron beam size on different BPMs for different current of the beam: a) 1-st BPM with 30 mA beam, b) 3-rd BPM with 30 mA, c) 3-rd BPM with 115 mA, d) 3-rd BPM with 200 mA.

The first picture shows 30 mA beam on the 1-st BPM. The BPM is installed right after the electron gun and only beam size can be changed here. This picture can be considered as a reference for other pictures. Other pictures show

ISBN: 978-3-95450-218-9 ISSN: 2226-0374 doi:10.18429/JACoW-COOL2019-TUX01

measurements from 3-rd BPM, which is installed in the end of the cooling section (about 4 m farther). One can see, that the picture depends on beam current value. Beam rotation can be observed here, which depends on beam current value. For small current (30 mA) there is almost no rotation, but for higher current the rotation (counterclock-wise) is stronger. This is result of the transverse drift of electrons in field of beam's space charge and longitudinal magnetic field.

In axial symmetric system the electric field E_r from the electron beam in radius R can be calculated with formula:

$$E_r = \frac{4\pi}{RV_0}\int_0^R rj(r)dr\,, \qquad (4)$$

where V_0 – electron velocity, $j(r)$ – beam current density.

Assuming, that transverse beam size is constant, one can estimate angle of beam rotation along system

$$\Delta\varphi = \omega_{DR}\tau = c\frac{E_r}{B_\square R}\frac{L}{V} = \frac{4\pi cL}{B_\square R^2 V_0^2}\int_0^R rj(r)dr\,, \qquad (5)$$

here L – distance, which beam passes, τ – time of flight, R – radius of electron, c – speed of light, $B_\parallel$ – longitudinal magnetic field.

For 10 kV beam with current 200 mA the equation (5) gives angle 15-20º, that is close to measured value.

CONCLUSSION

The electron cooling system was commissioned in the JINR in 2017 and tested during last years. Electron beam current up to 500 mA and voltage up to 50 kV were obtained.

Results of measurements obtained in JINR (such as vacuum pressure and vacuum pumping by electron beam) show that quality of beam and vacuum conditions are good enough for system work in the booster.

Despite some additional work with electronics of the cooler is needed, the system is ready for work with ion beam.

REFERENCES

[1] N.S. Dikansky, V.I. Kudelainwn, *et al.,* "Ultimate possibilities of electron cooling", Novosibirsk, Budker INP Preprint, 88-61, 1988.

[2] V.N. Bocharov A.V. Bublei, S.G. Konstantinov, V.M. Panasyuk, V. V. Parkhomchuk, "Precision Measurements and Compensation for the Transverse Components of the Solenoids Magnetic Field", *Instruments and Experimental Technique*, Vol.48, No. 6, p. 772—779, 2005.

[3] T. Ellison, D. Friesel, R. Brown, "Status and performance of the IUCF 270 electron cooling system", *in Proceedings of PAC 1989*, Chicago, IL, 1989, P. 633-635.

[4] M. Bryzgunov, V. Panasyuk, V. Parkhomchuk, V. Reva, M. Vedenev, "Recuperation of Electron Beam in the Coolers with Electrostatic Bending", *in Proceedings of COOL 2005*, Galena, USA, 2005, p. 341-345.

[5] M. Bryzgunov, A. Bubley, A. Ivanov, V. Parkhomchuk, V. Reva, A. Kruchkov, Electron Gun with Variable Beam Profile for COSY Cooler // Proceedings of COOL'11, Alushta, Ukraine, P. 99-102.

[6] A.N. Sharapa, A.V.Shemyakin, Secondary electron current loss in electron cooling devices // Nuclear Instruments and Methods in Physics Research: Section A, 1994. Vol. 351, P. 295-299.

[7] V.V. Parkhomchuk, V.B. Reva, V.D. Shil'tsev, Interaction between an Intense Proton Bunch and Electron Beam in a Tevatron // Technical Physics, Vol. 48, Iss. 8, 2003, P. 1042-1046

ISBN: 978-3-95450-218-9 ISSN: 2226-0374 doi:10.18429/JACoW-COOL2019-TUY01

RF ACCELERATOR FOR ELECTRON COOLING OF ULTRARELATIVISTIC HADRONS

N. A. Vinokurov†[1], V. V. Parkhomchuk[1], A. N. Skrinsky, Budker Institute of Nuclear Physics, Novosibirsk, Russia
[1]also at Novosibirsk State University, Novosibirsk, Russia

Abstract

New projects of high-energy hadron colliders could be improved by far by using the electron cooling technique. However, a source of high-current relativistic electron beam appears to be a technical challenge. Indeed, the intrinsic energy limitations of high-voltage DC accelerators lead to necessity to perform acceleration using not static but vortex electrical fields. Induction and radiofrequency (RF) accelerators employ such fields. Moreover, to keep the damping times small enough at high energies, it is necessary to increase the electron peak current to tens of amperes. The feasibility of RF energy recovery linac (ERL) application to electron cooling is discussed. The ERL of the Novosibirsk free electron laser facility is used as a reliable prototype.

INTRODUCTION

New projects of high-energy hadron colliders could be improved by far by using the electron cooling technique [1-7]. However, a source of high-current relativistic electron beam appears to be a technical challenge. Indeed, the intrinsic energy limitations of high-voltage DC accelerators lead to necessity to perform acceleration using not static but vortex electrical fields. Induction and radiofrequency (RF) accelerators employ such fields. Moreover, to keep the damping times small enough at high energies, it is necessary to increase the electron peak current to tens of amperes. As the duty factor of the cooler shall also be high, the desirable average beam current of the cooling electron beam is about 1 A or more.

Skipping at this point the betatron option, we will discuss the feasibility of RF energy recovery linac (ERL) application to electron cooling.

The necessity of high current and relatively low (less than 100 MeV) electron energy leads to the choice of an ERL with a low-frequency non-superconducting accelerating RF system. Indeed, the characteristic parameters for longitudinal stability of the average electron beam current I_{beam} and charge per bunch q are the ratio of the beam power to the power consumption in the RF cavities

$$\frac{P_{beam}}{P_{RF}} \approx \frac{I_{beam}U}{U^2/(2R)} = \frac{2I_{beam}R}{U} = \frac{QI_{beam}2(R/Q)}{U} \sim \frac{QI_{beam}}{10\,\mathrm{kA}} \quad (1)$$

and the energy deposition per bunch to the stored energy of RF cavity

$$\frac{qU}{CU^2/2} = \frac{q\omega 2(R/Q)}{U} \sim \frac{q\omega}{10kA}, \quad (2)$$

where R/Q, ω, $C = (\omega R/Q)^{-1}$, and U are the characteristic impedance, fundamental eigenfrequency, effective capacity, and voltage amplitude of single cavity, respectively. For the typical values U = 1 MV and $2R/Q$ = 100 Ohm, $U/(2R/Q)$ = 10 kA. Then Eqs. (1) and (2) give the following limitations for the average current and the bunch charge:

$$I_{beam} < \frac{10\,\mathrm{kA}}{Q} \quad (3)$$

and

$$q < \frac{10\,\mathrm{kA}}{\omega}. \quad (4)$$

For the non-superconducting cavities of the Novosibirsk free electron laser (FEL) facility [8, 9], ERL Q = 20000 and $\omega = 2\pi\cdot 180$ MHz, and Eqs. (3) and (4) give reasonable limiting values of 0.5 A and 10 μC, but for the superconducting cavities they are several orders of magnitude lower. For low-frequency non-superconducting RF systems, the transverse stability conditions are also much easier.

INJECTOR

To provide high charge per bunch, one can use a low-frequency RF gun. A 90 MHz CW RF gun with an average current of more than 0.1 A was built and tested at Budker INP [10]. In fact, in more than twenty years, Budker INP has manufactured tens of RF guns with electron energy of up to 1 MeV as industrial accelerators, referred to as ILU-8 [11]. The ILU-8 accelerators operate in a high duty cycle pulse mode and provide a peak current of up to 5 A.

For further gain in the bunch charge, it is necessary to increase the cathode diameter and decrease the RF and bunch repetition frequencies. A frequency of 30 MHz seems to be as a reasonable compromise between increasing the RF cavity size and obtaining more than 10 nC in each bunch. With a peak cathode current of 4 A and an initial bunch duration of about 4 ns, one can obtain a bunch charge of 16 nC. To have a significant accelerating gradient in an RF structure, it is necessary to use a higher RF frequency. Then, for further RF acceleration it is necessary to compress the bunch. In the consideration below, we will

† vinokurov@inp.nsk.su

ISBN: 978-3-95450-218-9 ISSN: 2226-0374 doi:10.18429/JACoW-COOL2019-TUY01

use the parameters of the RF system of the Novosibirsk ERL, which has been operated successfully at the Novosibirsk FEL facility [8, 9] for last 16 years. Its operating frequency is 180 MHz. To suppress the space-charge phenomena, we plan to accelerate electrons to a kinetic energy of 2 MeV in three similar 30 MHz RF cavities. The first one is the RF gun cavity and the two others are the accelerating ones.

The proposed compression system compresses the 2 MeV, 16 nC bunch from 4 ns to 0.5 ns duration. It uses the energy chirp of 2 MeV bunches, additional energy modulation in an auxiliary RF cavity, operating at a subharmonic of the main accelerating structure frequency of 180 MHz, and a magnetic buncher. For the required energy modulation to have an acceptable value (less than ±10%), the buncher shall have a high value of the longitudinal dispersion R_{56}. A second-order achromat is desirable for operation with large energy spread. The general scheme of the proposed magnetic buncher is presented in Fig. 1.

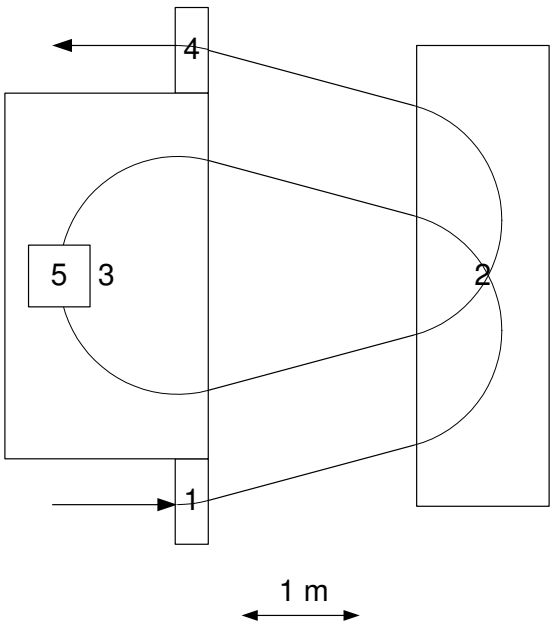

Figure 1: Magnetic buncher. 1 and 4 – parallel-edge magnets, 2 and 3 – magnetic mirrors, 5 – sextupole corrector.

It contains two magnetic mirrors with a homogeneous field and auxiliary magnets.

ERL

The above 2 MeV electron beam is to be accelerated further in an ERL. In the simplest case, the above-mentioned Novosibirsk ERL may be used to this end. In fact, this option is interesting in the context of improving the parameters of Novosibirsk FEL facility and will be considered in more details elsewhere. Below we describe a more advanced and expensive scheme of ERL with two accelerating structures [12]. It is more flexible and allows better control of the beam parameters.

The scheme of cooling ERL is shown in Fig. 2. Electrons pass each of the 30 accelerating cavities twice, obtaining energy of 50 MeV, are used in cooling section, are decelerated to 2 MeV in the same RF cavities, and are directed to the beam dump.

The estimated parameters of electron bunch are listed in Table 1. The bunch repetition frequency is limited by the average current of the electron gun and may exceed 10 MHz.

Table 1: Electron Bunch Parameters

Energy E, MeV	50
Charge q per bunch, nC	16
Number N_e of electrons	10^{11}
Longitudinal emittance ε_s, keV·ns	10
Normalized transverse emittances ε_t, mm·mrad	10

ELECTRON COOLING

The first successful demonstration [7] of the electron cooling of ion bunches using the RF electron linac at the RHIC shows clearly its high prospects. Let us estimate the cooling rate in the case of a long superconductive solenoid with a magnetic field B = 1 T.

Let the electron bunch length l_b be 60 cm. The longitudinal emittance ε_s = 10 keV·ns will define the energy spread of bunch $\sigma_E = c\varepsilon_s / l_b$ =5 keV, where c is the velocity of light. Then the longitutinal electron velocity spread in the beam rest frame is $V_{se} = c\sigma_E / E = 3\cdot10^6$ cm/s. For an ion beta function $\beta_i = 3\cdot10^4$ cm and an ion normalized transverse emittance $\varepsilon_i = 10^{-4}$ cm, the transverse velocity spread in the beam rest frame is $V_{xi} = c\sqrt{\gamma\varepsilon_i / \beta_i} = 1.7\cdot10^7$ cm/s, and the transverse beam size is $a_i = \sqrt{\varepsilon_i \beta_i / \gamma} = 0.17$ cm (γ is the Lorentz factor). Let the flat electron beam enter the flat solenoid edge. For a vertical beta function β_y = 100 cm, the vertical beamsize is $a_y = \sqrt{\varepsilon_t \beta_y / \gamma} = 0.032$ cm, and the vertical angular spread is $\theta_y = \sqrt{\varepsilon_t / (\gamma\beta_y)} = 3.2\cdot10^{-4}$. For a horizontal beta function β_x = 40000 cm, the horizontal beamsize is $a_x = \sqrt{\varepsilon_t \beta_x / \gamma} = 0.64$ cm and the horizontal angular spread is $\theta_x = \sqrt{\varepsilon_t / (\gamma\beta_x)} = 1.6\cdot10^{-5}$, which is much less than the r. m. s. horizontal kick $a_y/R = 2\cdot10^{-3}$ ($R = \gamma mc^2/(eB)$ = 17 cm) at the flat edge of the solenoid. Then the r.m.s. Larmor radius is equal to a_y. After transformation in solenoid we obtain a round beam with an r. m. s. sizes a_e of 0.15 cm, which exceeds the r.m.s. Larmor radius 5 times. The peak electron current is $qc/(\sqrt{2\pi} l_b) =$ 3.2 A, and the electron rest-frame density is $n_e = N_e / (2^{3/2}\pi^{3/2} l_b a_e^2 \gamma)$ = $5\cdot10^7$. The cooling rate in the lab frame can be estimated as [1–3]

ISBN: 978-3-95450-218-9 ISSN: 2226-0374 doi:10.18429/JACoW-COOL2019-TUY01

$$\delta_{cool} = \frac{2\pi n_e r_e r_i c^4}{\left(V_{xi}^2 + V_{se}^2\right)^{3/2}} \frac{\eta}{\gamma} \ln \frac{a_e}{R}, \quad (5)$$

where r_e is the classical radius of electron, r_i is the classical radius of ion, and η is the fraction of the collider perimeter occupied by the cooling section. For ions with the charge Z = 92, atomic weight A = 200, and η = 0.01, $\tau_{cool} = 1/\delta_{cool}$ = 100 s. This result shows good prospects for using this cooling system with a low-frequency ERL.

CONCLUSION

High energy electron cooling (>10 MeV) should use an RF linac for generation of electron beam. A low-frequency linac can produce an intensive electron beam for cooling ion bunches in the collider.

ACKNOWLEDGEMENTS

Authors thanks colleagues from Budker INP for discussions on the subject.

REFERENCES

[1] V. V. Parkhomchuk, A. N. Skrinskii, "Electron cooling: 35 years of development", *Phys. Usp.*, vol. 43, no. 5, p. 433–452, 2000. doi: 10.1070/PU2000v043n05ABEH000741

[2] V. V. Parkhomchuk, "New insights in the theory of electron cooling", *Nucl. Instr. and Meth. A*, vol. 441, Iss. 1-2, p. 9-17, Febr. 2000. doi: 10.1016/S0168-9002(99)01100-6

[3] A. Skrinsky, "Continuous Electron Cooling for High Luminosity Colliders", *Nucl. Instr. and Meth. A*, vol. 441, Iss. 1-2, p. 286-293, Febr. 2000. doi: 10.1016/S0168-9002(99)01147-X

[4] Ya. S. Derbenev, "Prospects of High Energy Electron Cooling", in *Proc. 7th European Particle Accelerator Conference (EPAC 2000)*, Vienna, Austria, June 2000, paper MOZE03, pp. 8-12, accelconf.web.cern.ch/AccelConf/e00/PAPERS/MOZE03.pdf

[5] A. Skrinsky, "Electron cooling and electron nuclei colliders", in *Proc. APS / DPF / DPB Summer Study on the Future of Particle Physics (Snowmass 2001)*, Snowmass, Colorado, June 2001, paper T903, eConf C010630 (2001) T903

[6] N. S. Dikanskii *et al.*, "Development of techniques for the cooling of ions", *Phys. Usp.*, vol. 61, p. 424–434, 2018. doi: 10.3367/UFNe.2018.01.038297

[7] BNL TEAM, "Electron Bunches Keep Ions Cool at RHIC" https://www.bnl.gov/newsroom/news.php?a=215585

[8] N. A. Vinokurov, O. A. Shevchenko, "Free electron lasers and their development at the Budker Institute of Nuclear Physics, SB RAS", *Phys. Usp.*, vol. 61, p. 435–448, 2018. doi: 10.3367/UFNe.2018.02.038311

[9] B. A. Knyazev *et al.*, "Recent experiments at NovoFEL user stations", *EPJ Web of Conferences*, vol. 195, p. 00002, 2018. doi: 10.1051/epjconf/201819500002

[10] V. N. Volkov *et al.*, "Test Stand Results of CW 100 mA Electron Gun for Novosibirsk ERL based FEL", in *Proc. 26th Russian Part. Accel. Conf. (RUPAC 2018)*, Protvino, Russia, Oct. 2018, paper THPSC53, pp. 507-509, doi:10.18429/JACoW-RUPAC2018-THPSC53

[11] V. L. Auslender *et al.*, "An ILU-8 pulsed high-frequency electron linear accelerator", *Instruments and Experimental Techniques*, vol. 52, no. 3, p. 400–405, 2009. doi: 10.1134/S0020441209030178

[12] D. Douglas, "A Generic Energy-Recovering Bisected Asymmetric Linac (GERBAL)", *ICFA BD-Nl*, vol. 26, p. 40–45, 2001.

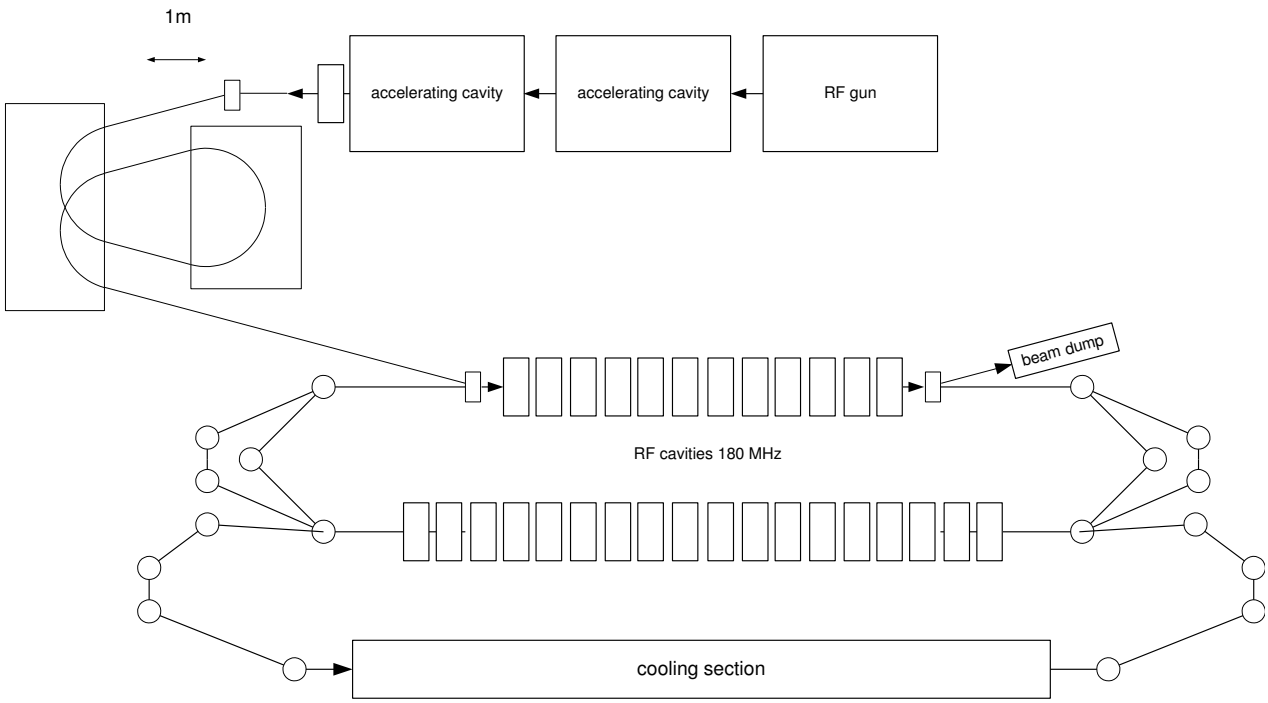

Figure 2: Scheme of cooling ERL.

ISBN: 978-3-95450-218-9 ISSN: 2226-0374 doi:10.18429/JACoW-COOL2019-TUY02

PROGRESS IN MUON IONIZATION COOLING DEMONSTRATION WITH MICE*

D. M. Kaplan†, Illinois Institute of Technology, Chicago, IL 60616 USA
K. Long, Imperial College London, London SW7 2AZ, UK

on behalf of the MICE collaboration

Abstract

The Muon Ionization Cooling Experiment (MICE) at RAL has collected extensive data to study the ionization cooling of muons. Several million individual particle tracks have been recorded passing through a series of focusing magnets in a number of different configurations and a liquid-hydrogen, lithium-hydride, or polyethylene-wedge absorber. Via measurement of the tracks upstream and downstream of the absorber, we have observed ionization cooling. Our measurement is in good agreement with our simulation of the effect. Further studies are now providing more and deeper insight.

INTRODUCTION

High-energy lepton colliders have been proposed as potential future facilities to follow up on discoveries made and to be made at the LHC. The design of such machines is strongly influenced by radiative effects (synchrotron radiation and beamstrahlung). Since these scale with the fourth power of lepton mass, the use of the muon rather than the electron would substantially suppress them. Muon colliders can thus employ rings of small circumference for acceleration and collisions, reducing facility footprints and construction and operating costs. Muons likewise give more-monochromatic collisions and allow much higher energies (10 TeV or more) [1,2] than do electrons. Moreover, the coupling of the Higgs field to leptons being proportional to the square of lepton mass, the muon collider has the unique ability to produce the Higgs boson exclusively, in the *s* channel. This, along with the highly precise muon beam energy spread and calibration ($\Delta E/E \lesssim 10^{-5}$), enables a direct measurement of the Higgs mass and width [3]. While it complicates beam handling, muon decay (mean lifetime = 2.2 μs) enables stored-muon-beam neutrino factories—the most capable technique yet devised for precision measurements of neutrino oscillation and searches for new physics in the neutrino sector [4-10].

Figure 1 compares muon collider and neutrino factory schematic layouts. Two muon-production approaches are under consideration: via pion production and decay, or via $e^+e^- \rightarrow \mu^+\mu^-$ just above threshold (in a positron storage ring with internal target)—the Low EMittance Muon Accelerator, or LEMMA [11]. While potentially bypassing the need for muon cooling, the LEMMA approach itself has significant technical challenges to overcome if the desired high $\mu^+\mu^-$ luminosity ($\geq 10^{34}$ cm^{-2} s^{-1}) is to be achieved; it also produces insufficient muons for use as a neutrino factory.

* Work supported by STFC
† kaplan@iit.edu

If the pion-production approach is chosen, the facility performance and cost depend on the degree to which a muon beam can be cooled. The desired emittance reduction factor for a neutrino factory is $\mathcal{O}$(10–100), with 4D transverse cooling sufficing, while that for a muon collider is $\mathcal{O}(10^6)$, and 6D cooling is required [12,13].

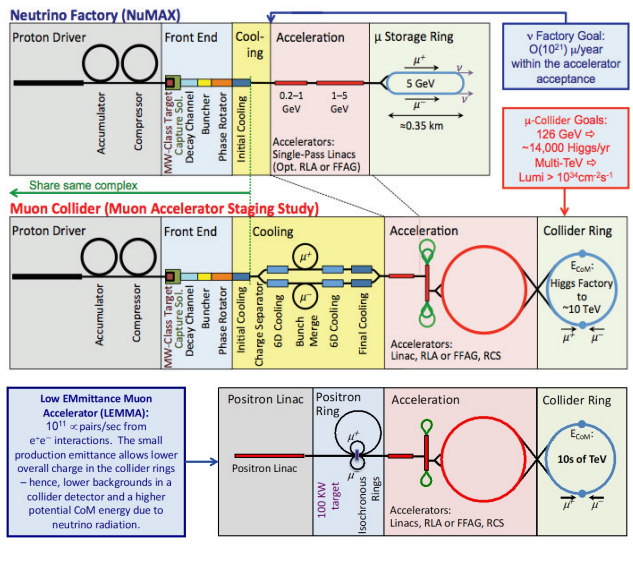

Figure 1: Schematic layouts of possible muon accelerator facilities: (top) neutrino factory; (center) muon collider, employing pion production and decay; and (bottom) employing $\mu^+\mu^-$ pair production in fixed-target e^+e^- collisions (LEMMA).

IONIZATION COOLING

Established methods of particle-beam cooling (electron, laser, stochastic, and synchrotron-radiation cooling) are ineffective for the muon due to its short lifetime, large mass, and lack of internal substructure, thus non-traditional approaches are required. Only one cooling mechanism —ionization cooling[1] [14-19] — works on muons in microseconds, allowing small enough emittances to be reached with $\mathcal{O}(10^{-2\pm1})$ muon survival. Moreover, like electron cooling, ionization cooling was first proposed at the Budker Institute of Nuclear Physics (BINP). Thus it is fitting that we report here at BINP at the COOL'19 Workshop on the progress of its experimental demonstration.

[1] Essentially a form of electron cooling, but with an electron density many orders of magnitude larger than is possible in an electron beam.

ISBN: 978-3-95450-218-9 ISSN: 2226-0374 doi:10.18429/JACoW-COOL2019-TUY02

In ionization cooling, muons traverse a series of energy absorbers, of low atomic number, in a focusing magnetic lattice, with normalized transverse emittance evolving according to [16-19]

$$\frac{d\varepsilon_n}{ds} \approx \frac{-1}{\beta^2}\left\langle \frac{dE_\mu}{dx}\right\rangle \frac{\varepsilon_n}{E_\mu} + \frac{\beta_\perp (13.6\,\mathrm{MeV})^2}{2\beta^3 E_\mu m_\mu c^2 X_0}. \quad (1)$$

Here βc is the muon velocity, $\beta_\perp$ the lattice betatron function at the absorber, $\langle dE_\mu/ds\rangle$ the mean energy loss per unit length, m_μ the muon mass, and X_0 the absorber radiation length. ($\beta_\perp$ takes the place of the more usual β_x or β_y when cylindrically symmetric solenoidal focusing is used; thus we have here $\beta_x = \beta_y \equiv \beta_\perp$, with cooling equal in the x-x' and y-y' phase planes.) To allow repeated cooling, absorbers are interspersed with accelerating cavities.

In Eq. 1, the first term describes cooling, and the second, heating due to multiple Coulomb scattering.[2] To minimize the heating term, small $\beta_\perp$ (strong focusing) and large X_0 (low-Z absorber material) are employed. For a given cooling-channel design, cooling proceeds towards an equilibrium emittance value at which the heating and cooling terms balance. Once equilibrium is reached, continued cooling requires a revised design with lower $\beta_\perp$. Ionization cooling works optimally near ≈ 200 MeV/c momentum [16-19], at which the dE/dx energy loss rate in matter is (counterintuitively) near its minimum [20] (see Fig. 2). This reflects the trade-off between heating effects of "straggling" at higher momenta and the negative slope of the dE/dx curve at momenta below the minimum (leading to problematic, positive feedback for energy-loss fluctuations).

Emittance Exchange

Ionization cooling as just described is a purely transverse effect. In the longitudinal phase plane it tends to heat the beam due to the negative dE/dx slope. While longitudinal cooling might appear to be feasible by operating at somewhat higher momentum, where the dE/dx slope becomes positive, in practice it is rendered ineffective due to straggling. Cooling of all six phase-space dimensions is nevertheless required for a muon collider of useful luminosity. It is accomplished by the use of longitudinal–transverse emittance exchange, illustrated schematically in Fig. 3. A dipole field is employed to create dispersion. A wedge absorber can then be used to compensate for the beam momentum spread, reducing the longitudinal emittance at the expense of a wider spread in transverse position. It should be noted that the process can be exploited in either direction. In current muon collider designs, (forward) emittance exchange enables 6D cooling, and *reverse* emittance exchange is employed after 6D cooling, in order to reduce transverse emittance at the expense of longitudinal and further boost the luminosity (Fig. 4). (This is found to work better than attempting to tune the degree of 6D-channel emittance exchange to approach the desired final emittance directly.)

[2] Analogous to beam cooling by synchrotron radiation, in which energy loss provides cooling, while heating is caused by quantum fluctuations.

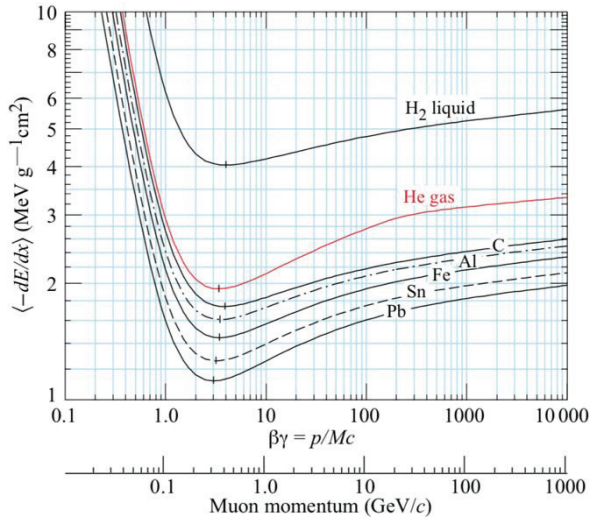

Figure 2: Ionization energy-loss rate vs. momentum (from [9]).

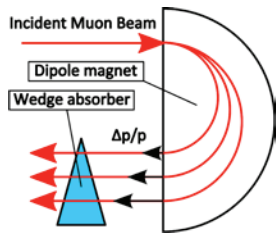

Figure 3: Principle of emittance exchange.

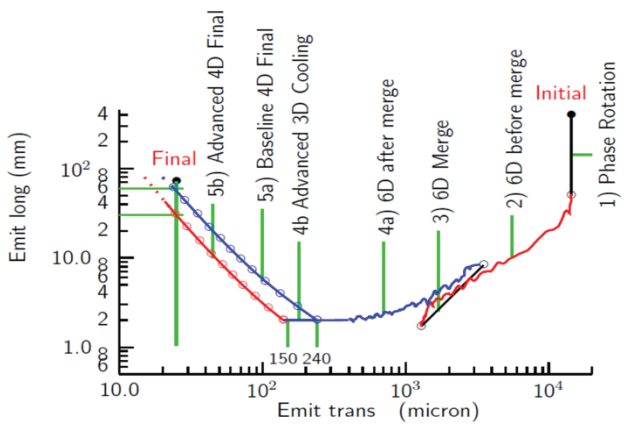

Figure 4: Emittance trajectory followed in a representative muon collider cooling design [21].

MICE

While the physics of Eq. 1 is well established, poorly modeled tails of distributions, as well as engineering limitations, could have important impact on ionization cooling-channel cost and performance. An initiative was therefore undertaken to build and test a realistic section of cooling channel: the international Muon Ionization Cooling Experiment (MICE) [22]; one component of the MICE program was to precisely measure the absorber material properties (dE/dx and multiple scattering distributions) that determine the performance of ionization cooling. Ionization cooling channels are tightly packed assemblies with

ISBN: 978-3-95450-218-9 ISSN: 2226-0374 doi:10.18429/JACoW-COOL2019-TUY02

liquid hydrogen, superconducting magnets, and high-gradient normal-conducting RF cavities in close proximity and concomitant safety issues with which little previous experience was available. Moreover, the cooling effect of the $\mathcal{O}(10^3)$ ionization cooling cells required to reach collider luminosities of interest might be degraded by poorly measured tails of the energy-loss and multiple-scattering distributions. An experimental demonstration was thus deemed essential to further progress.

MICE was proposed as a test of one lattice cell of the Feasibility Study II [23] transverse cooling channel (Fig. 5a). Being limited for cost reasons to an $\mathcal{O}(10\%)$ emittance reduction, it was conceived as a high-precision measure-

(a)

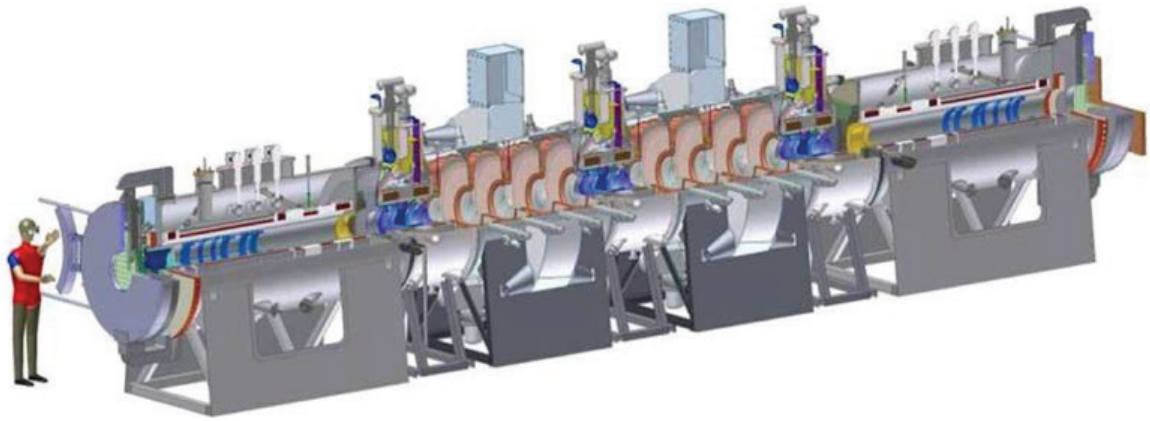

(b)

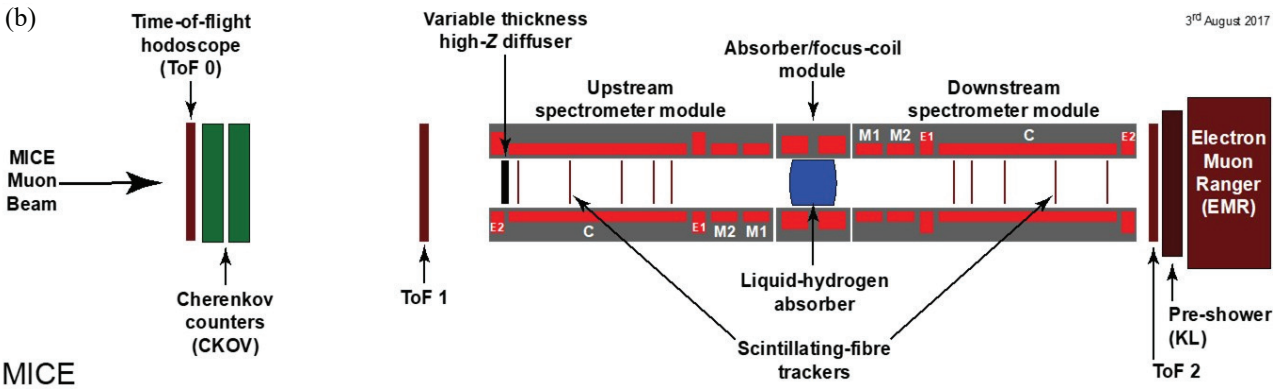

(c)

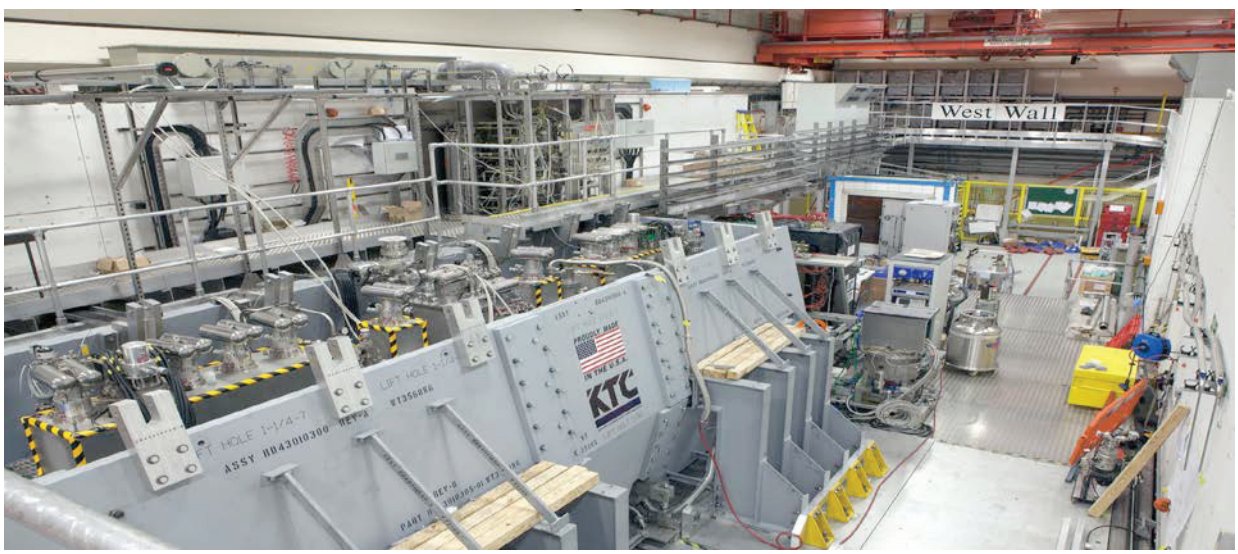

Figure 5: (a) MICE apparatus as originally proposed, with 3 absorbers and 8 RF cavities; (b) schematic of MICE apparatus as built; (c) installed in its hall off the RAL ISIS 800 MeV synchrotron, with solenoids surrounded by magnetic shielding.

ISBN: 978-3-95450-218-9 ISSN: 2226-0374 doi:10.18429/JACoW-COOL2019-TUY02

Figure 6: Photo of ½ of polyethylene-wedge absorber.

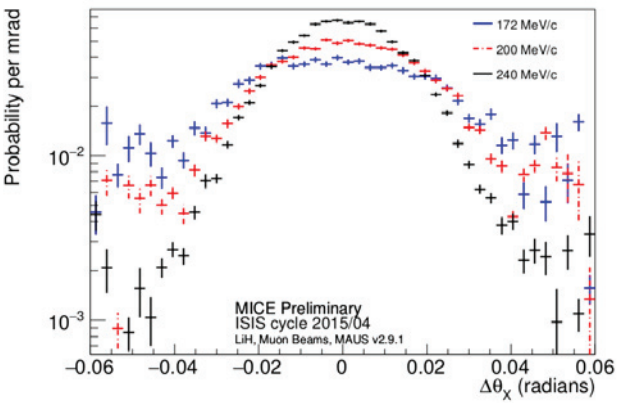

Figure 7: Deconvolution of observed scattering-angle distributions in x in three muon momentum settings.

ment of a low-intensity beam, via particle tracking carried out one muon at a time, with the unprecedented emittance resolution of 1‰. It was proposed by an international collaboration [22] and approved in 2003 at Rutherford Appleton Laboratory in the UK. After an extended design, construction, installation, and commissioning process, MICE recorded a substantial dataset (3.5×10^8 events) in 2016–17 with one absorber and no RF cavities. Various absorber materials (Table 1) were studied, including liquid hydrogen (LH_2) and lithium hydride (LiH), with a range of beam momenta and lattice focusing strength. Data were also taken with a 45° polyethylene wedge absorber (Fig. 6), in order to demonstrate emittance exchange.

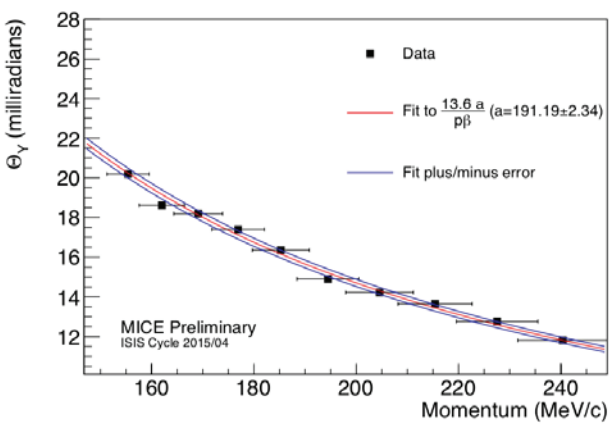

Figure 8: RMS of Gaussian fit to central ±40 mrad of deconvoluted scattering-angle distribution in y vs. muon momentum.

Table 1: Absorber Specifications

Absorber	Diameter (cm)	Thickness (cm)
LH_2	30	35
LiH	30	6.5
Polyethylene wedge	39	0 to 21 (5.2 on axis)

Study of Material Properties

Two approaches were taken to measuring multiple scattering: with solenoid fields off, and with them on. The field-off approach, with the advantages of analysis simplicity and straightforward systematics, is further along at present, and is the one presented here; the field-on measurement (once complete) should cover a wider range of scattering angle. Requirements on events included a reconstructed upstream track within the time of flight (TOF) and fiducial limits: that the measured time of flight between the TOF0 and TOF1 detector planes be consistent with that of a muon, and that the projection of the upstream track to the end of the downstream tracker lie within a 140 mm radius of the tracker center. The excellent resolution of the MICE TOF counters (≈55 ps) [24] allows reconstruction of the momentum of each muon, thus the analysis is carried out within 200 ps TOF bins. The TOF momentum is corrected to second order for the trajectory length of each muon and for energy loss in material (the TOF counters, tracker planes, helium, air, and windows). Data were taken with the (LiH) absorber removed or (LH_2) empty as well as with absorbers installed and full, allowing deconvolution of measurement resolution effects. Figure 7 shows the deconvolution results in x from three beam-momentum settings. Gaussian fits to the central ±40 mrad were performed independently in x and in y in each 200 ps TOF bin; results of the y fit are shown in Fig. 8 and are consistent with the results in x and with the expected $1/p\beta$ dependence. Study of systematic uncertainties is currently in progress. Results on the dE/dx distributions in LH_2 and LiH are also anticipated. A more detailed account appears in [25].

Cooling Results

Figure 9 illustrates how muons are selected, and pions and decay electrons rejected, by imposing two-dimensional cuts in the TOF–momentum plane. The first meas-

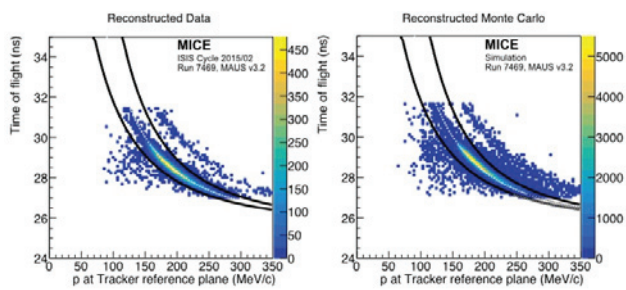

Figure 9: Observed (left) and simulated (right) time of flight vs. reconstructed momentum, showing bands of muons and (further up and to the right) pions. Curves show requirements used to select muons.

ISBN: 978-3-95450-218-9 ISSN: 2226-0374 doi:10.18429/JACoW-COOL2019-TUY02

urement of emittance using tracker information [26] is shown in Fig. 10, for data obtained in the nominal "3 mm·rad" emittance setting. While fair agreement with simulation is observed, the comparison is sensitive to poorly modelled features of pion production in 800 MeV proton-titanium interactions, thus precise agreement is not expected. Our cooling analysis, based on how the observed input emittance is modified by passage through absorbers, is insensitive to such modeling discrepancies.

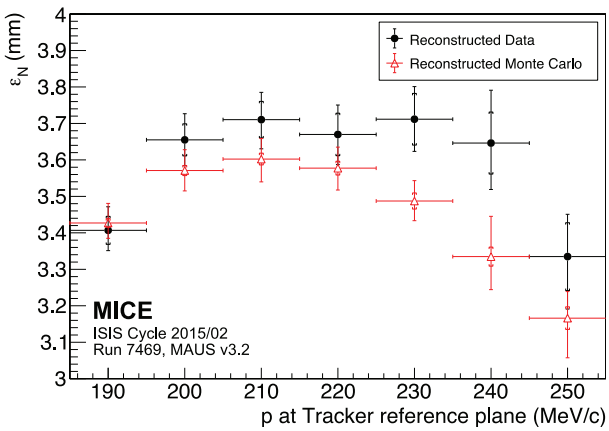

Figure 10: Measured input emittance vs. momentum [26].

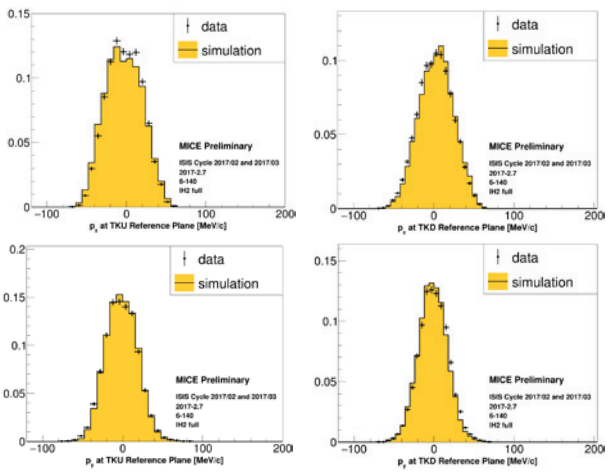

Figure 11: Comparison of observed and simulated (top) p_x and (bottom) p_y distributions, (left) upstream and (right) downstream of LH_2 absorber in 6 mm, 140 MeV/c sample.

In Fig. 11 the horizontal and vertical momentum-component distributions upstream and downstream of the LH_2 absorber are compared for the "6-140" data sample (i.e., nominal input emittance 6 mm·rad, nominal momentum 140 MeV/c). Cooling (narrowing of the transverse-momentum distributions) by a small amount is qualitatively apparent. To make the point more quantitative, Fig. 12 compares the observed distributions of single-particle amplitude (transverse distance from the beam centroid, measured in emittance units) upstream and downstream of the absorber for both the 6-140 and 10-140 datasets. Due to cost-saving compromises made during MICE construction, the beam transmission through the cooling cell was limited at large amplitude by apertures; furthermore, as is not uncommon, the beam at large amplitude was not well described by a Gaussian. For these reasons, the usual beam-quality figure of merit—total bunch RMS emittance—is not so useful. Thanks to the MICE single-particle measurement capability, the crucial behavior at and near the core of the beam is nevertheless clearly observable: with no absorber the phase-space density near the core is seen to decrease from upstream to downstream, while with either absorber in, it increases; this is the hallmark of cooling.

Figure 13 shows the cumulative ratio vs. amplitude of the number of muons downstream to that upstream of the absorber, again indicative of the change in phase-space density in the core of the beam. With no absorber, the density at the beam core slightly decreases. For both the LH_2 and LiH absorbers, a clear increase in core density is seen for both input-beam emittances.

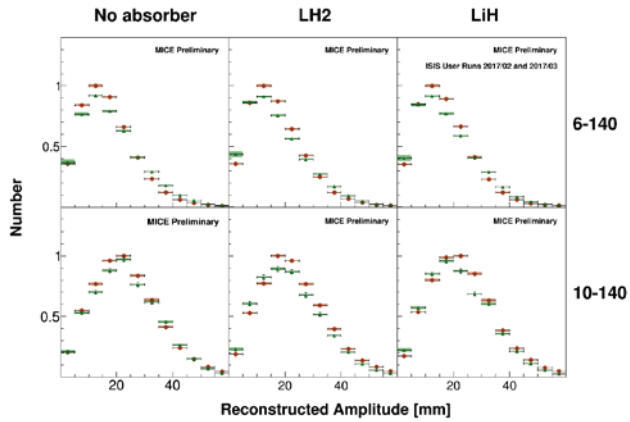

Figure 12: Comparison of upstream (red) and downstream (green) amplitude distributions without and with LH_2 and LiH absorbers for 6-140 and 10-140 datasets.

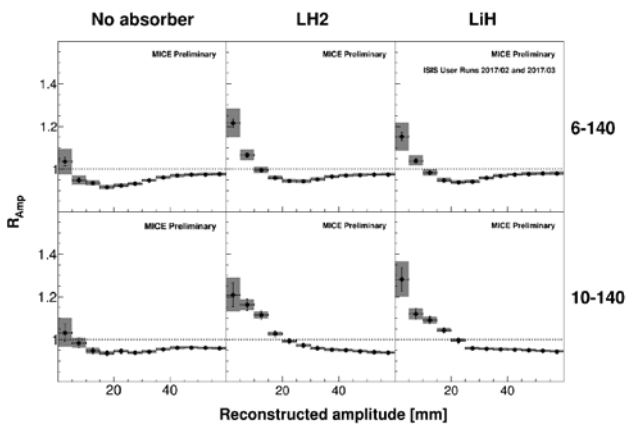

Figure 13: Cumulative ratios of downstream to upstream amplitude distributions without and with LH_2 and LiH absorbers for 6-140 and 10-140 datasets.

ISBN: 978-3-95450-218-9 ISSN: 2226-0374 doi:10.18429/JACoW-COOL2019-TUY02

CONCLUSION

The MICE Collaboration has recorded a substantial dataset with which to demonstrate muon ionization cooling and is well on its way to accomplishing its goals. Clear evidence of transverse ionization cooling has been presented. A more conclusive analysis including extensive discussion of systematics will appear in a future paper [27].

ACKNOWLEDGEMENTS

One of us (D.M.K.) gratefully acknowledges the kind hospitality experienced at the Budker Institute of Nuclear Physics.

REFERENCES

[1] R. Palmer, "Muon Colliders," *Rev. Accel. Sci. Tech*. 7 (2014) 137.

[2] D. Neuffer and V. Shiltsev, "On the feasibility of a pulsed 14 TeV c.m.e. muon collider in the LHC tunnel," *JINST* 13 (2018) T10003.

[3] D. Neuffer, M. Palmer, Y. Alexahin, C. Ankenbrandt, J. P. Delahaye, "A muon collider as a Higgs factory," in *Proc. of IPAC2013*, Shanghai, China, May 2013, paper TUPFI056.

[4] S. Geer, "Neutrino beams from muon storage rings: Characteristics and physics potential," *Phys. Rev. D* 57, 6989 (1998); ibid. 59, 039903E (1999).

[5] C. Albright *et al*., "Physics at a Neutrino Factory," FERMILAB-FN-0692, May 2000, hep-ex/0008064.

[6] M. Apollonio *et al*., "Oscillation Physics with a Neutrino Factory," CERN-TH-2002-208 Oct. 2002.

[7] A. Bandyopadhyay *et al*., "Physics at a future Neutrino Factory and super-beam facility," *Rep. Prog. Phys.* 72, 106201 (2009), arXiv:0802.4023 [physics.acc-ph].

[8] M. Lindner, "The physics potential of future long baseline neutrino oscillation experiments," in *Neutrino Mass*, G. Altarelli, K. Winter, Eds., *Springer Tracts in Modern Physics* 190, 209, 2003.

[9] The ISS Accelerator Working Group, "Accelerator design concept for future neutrino facilities," *JINST* 4, P07001 2009.

[10] S. Choubey *et al*. (IDS-NF Collaboration), "International Design Study for the Neutrino Factory, Interim Design Report," arXiv:1112.2853 [hep-ex] Mar. 2011.

[11] J. P. Delahaye *et al*., "Muon Colliders" (Input to the European Particle Physics Strategy Update), arXiv:1901.06150 [physics.acc-ph] 2019.

[12] D. M. Kaplan, "Muon cooling, muon colliders, and the mice experiment," in *Proc. COOL2013*, paper MOAM2HA01.

[13] D. M. Kaplan, "Muon Colliders, Neutrino Factories, and Results from the MICE Experiment," in *Proc. CAARI 2018*, *AIP Conf. Proc.* 2160, 040011 (2019).

[14] Y. M. Ado, V. I. Balbekov, "Use of ionization friction in the storage of heavy particles," *Soviet At. Energ*. 31(1) 40 (1971), English translation in *Atomic Energy* (Springer) 31(1) 731, http://www.springerlink.com/content/v766810126338571/.

[15] D. Neuffer, in *Advanced Accelerator Concepts, AIP Conf. Proc.* 156, 201 (1987).

[16] D. V. Neuffer, R. B. Palmer, "A high-energy high-luminosity μ+-μ− collider," in *Proc. 1994 Eur. Part. Accel. Conf. (EPAC94)*, p. 52.

[17] R. C. Fernow, J. C. Gallardo, *Phys. Rev. E* 52, 1039 (1995).

[18] C. M. Ankenbrandt *et al*., "Status of Muon Collider Research and Development and Future Plans," *Phys. Rev. ST Accel. Beams* 2, 081001 (1999).

[19] D. Neuffer, "μ+ μ− Colliders," Yellow Report CERN-99-12 (1999).

[20] "Passage of Particles Through Matter," in M. Tanabashi *et al*. [Particle Data Group], *Phys. Rev. D* 98, 030001 (2018).

[21] D. Neuffer, H. Sayed, J. Acosta, T. Hart and D. Summers, "Final cooling for a high-energy high-luminosity lepton collider," *JINST* 12 (20187) T07003.

[22] G. Gregoire *et al*., "An International Muon Ionization Cooling Experiment (MICE)," Proposal to Rutherford Appleton Laboratory, http://mice.iit.edu/micenotes/public/pdf/MICE0021/MICE0021.pdf

[23] S. Ozaki *et al*., "Feasibility Study-II of a Muon-Based Neutrino Source," https://www.cap.bnl.gov/mumu/studyii/FS2-report.html, BNL-52623 (2001).

[24] R. Bertoni *et al*., "The Design and Commissioning of the MICE Upstream Time-of-Flight System," *Nucl. Instrum. Meth. A* 615 (2010) 14.

[25] D. M. Kaplan, J. C. Nugent, and P. Soler, "Recent Results from MICE on Multiple Coulomb Scattering and Energy Loss," in *Proc. COOL'19* (this workshop), paper TUB01.

[26] D. Adams *et al*. [MICE Collaboration], "First particle-by-particle measurement of emittance in the Muon Ionization Cooling Experiment," *Eur. Phys. J. C* 79 (2019) 257.

[27] M. Bogomilov *et al*. [MICE Collaboration], submitted for publication (2019).

ISBN: 978-3-95450-218-9 ISSN: 2226-0374 doi:10.18429/JACoW-COOL2019-TUZ01

COHERENT ELECTRON COOLING EXPERIMENT AT RHIC: STATUS AND PLANS *

Vladimir N. Litvinenko[1,2†], Zeynep Altinbas[2], Jean Clifford Brutus[2], Anthony Di Lieto[2], David Gassner[2], Thomas Hayes[2], Patrick Inacker[2], James Jamilkowski[2], Yichao Jing[1,2], Robert Kellermann[2], Jun Ma[2], George Mahler[2], Michael Mapes[2], Robert Michnoff[2], Kentaro Mihara[1], Michiko Minty[2], Toby Allen Miller[2], Geetha Narayan[2], Matthew Paniccia[2], Irina Petrushina[1], David Phillips[2], Igor Pinayev[2], Thomas Roser[2], Scott Keith Seberg[2], Freddy Severino[2], Kai Shih[1], John Skaritka[2], Loralie Smart[2], Kevin S. Smith[2], Zachary Sorrell[2], Roberto Than[2], Joseph Tuozzolo[2], Erdong Wang[2], Gang Wang[1,2], Yuan Hui Wu[1], Binping Xiao[2], Tianmu Xin[2], Alex Zaltsman[2]
[1] Department of Physics and Astronomy, Stony Brook University, Stony Brook, USA
[2] Collider-Accelerator Department, Brookhaven National Laboratory, Upton, USA

Abstract

We present currents status of the CeC experiment at RHIC and plans for future. Special focus will be given to unexpected experimental results obtained during RHIC Run 18 and discovery of a previously unknown type of microwave instability. We called this new phenomenon micro-bunching Plasma Cascade Instability (PCI). During this year we demonstration control of this instability in our SRF CW accelerator. We present plan for future experiments using this instability as a broad-band amplifier in the CeC system – so called PCA-based CeC.

INTRODUCTION

An effective cooling of ion and hadron beams at energy of collision is of critical importance for the productivity of present and future colliders. Coherent electron cooling (CeC) [1] promises to be a revolutionary cooling technique which would outperform competing techniques by orders of magnitude. It is possibly the only technique, which is capable of cooling intense proton beams at energy of 100 GeV and above.

The CeC concept is built upon already explored technology (such as high-gain FELs) and well-understood processes in plasma physics. Since 2007 we have developed a significant arsenal of analytical and numerical tools to predict performance of a CeC. Nevertheless, being a novel concept, the CeC should be first demonstrated experimentally before it can be relied upon in the up-grades of present and in the designs of future colliders.

A dedicated experimental set-up with FEL amplifier, shown in Fig. 1, has been under design, manufacturing, installation and finally commissioning during last few years [2-4]. The CeC system is comprised of the SRF accelerator and the CeC section followed by a beam-dump system. It is designed to cool a single bunch circulating in RHIC's yellow ring (indicated by yellow arrow in Fig. 1). A 1.25 MeV electron beam for the CeC accelerator is generated in an 113 MHz SRF quarter-wave photo-electron gun and first focused by a gun solenoid. Its energy is chirped by two 500 MHz room-temperature RF cavities and ballistically compressed in 9-meter long low energy beamline compromising five focusing solenoids. A 5-cell 704 MHz SRF linac accelerates the compressed beam to 14.5 MeV. Accelerated beam is transported through an achromatic dogleg to merge with ion bunch circulating in RHIC's yellow ring. In CeC interaction between ions and electron beam occurs in the common section, e.g. a proper coherent electron cooler. The CeC works as follows: In the modulator, each hadron induces density modulation in electron beam that is amplified in the CeC amplifier; in the kicker, the hadrons interact with the self-induced electric field of the electron beam and receive energy kicks toward their central energy. The process reduces the hadron's energy spread, i.e. cools the hadron beam.

Finally, the used electron beam is bent towards an aluminum high-power beam dump equipped with two quadrupoles to over-focus the beam.

STATUS

The CeC accelerator SRF system uses liquid helium from RHIC refrigerator system, which operates only during RHIC runs. The commissioning of the CeC accelerator was accomplished during RHIC 15-18 runs. Electron beam parameters at the design level or above, except the beam energy, had been successfully demonstrated – see Table 1 [5-16]. Accordingly, we had adjusted the ion beam energy to 26.5 GeV/u to match relativistic factors with that of electron beam.

Our attempt to demonstrate cooling during RHIC run 18 was not successful. While the attempt was hindered by a number of technical problems beyond control of the CeC group, the main reason for our inability to demonstrate cooling was excessive noise in the electron beam at frequencies ~ 10 THz (wavelength ~ 30 μm).

As soon as we achieved all necessary electron beam parameters, we demonstrated high gain operation of our FEL by observing very strong amplification of the IR radiation from the FEL with increase of the beam peak current. The power of generated radiation was measured by broad-band IR diagnostics [17] (including a spectrometer), which was upgraded to be sensitive in far-IR range before the 2018 run. After that we verifiably aligned electron and an ion bunches both transversely and temporarily well within the

* Work is supported by Brookhaven Science Associates, LLC under Contract No. DEAC0298CH10886 with the U.S. Department of Energy, DOE NP office grant DE-FOA-0000632, and NSF grant PHY-1415252.
† vladimir.litvinenko@stonybrook.edu

ISBN: 978-3-95450-218-9 ISSN: 2226-0374 doi:10.18429/JACoW-COOL2019-TUZ01

beam's sizes and duration. Next important steps in our plan was to match relativistic factors of electron and ion beam by observing increase in the spontaneous radiation of electron beam caused by the ion's imprint (induced density modulation). Specifically, each ion interacting with electron beam in the CeC modulator [1,16] creates a localized density modulation whose intensity depends on the mismatch between relativistic factors of the beams – Fig. 2.

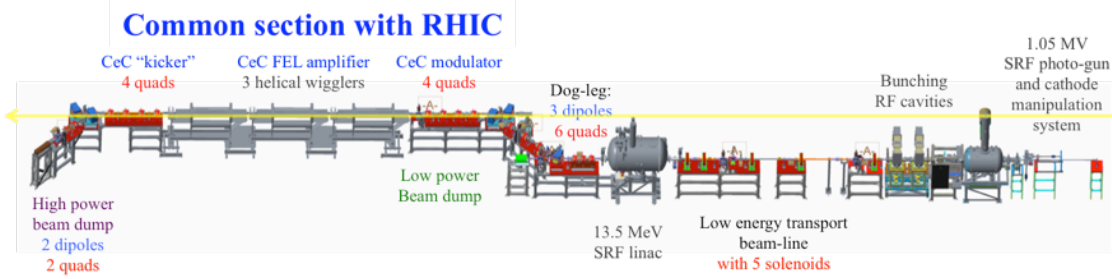

Figure 1: Layout of the CeC proof-of-principle system at IP2 of RHIC. Out CW SRF accelerator uses LiHe delivered by RHIC cryogenic system – it can operated only when RHIC is running.

Table 1: Main Parameters of the CeC System

Parameter	Design	Achieved	Comment
Species in RHIC	Au^{+79}, 40 GeV/u	Au^{+79} 26.5 GeV/u	To match e-beam
Particles/bucket	10^8 - 10^9	10^8 - 10^9	✓
Electron energy	21.95 MeV	14.5 MeV	SRF linac quench
Charge per e-bunch	0.5-5 nC	0.1- 10.7 nC	✓
Peak current	100 A	50-100 A	Sufficient for this energy
Pulse duration, psec	10-50	10-20	✓
Beam emittance, norm	<5 mm mrad	3 - 5 mm mrad	✓
FEL wavelength	13 μm	30 μm	New IR diagnostics

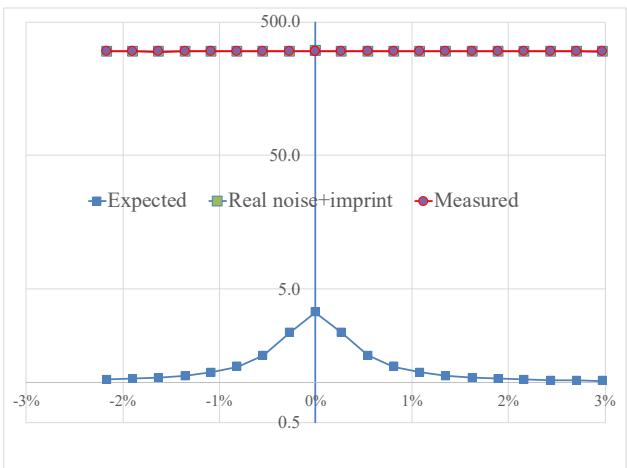

Figure 2: Predicted and measured dependence of radiation power from the electron beam resulting from ion beam imprint. Vertical scale is logarithmic and shows radiated power normalized to the natural synchrotron radiation (e.g. by shot noise with Poisson statistics) as a function of relative difference of relativistic factors in two beams.

Observing tripling of the radiation power predicted by the theory and simulation would not be a problem, but our attempts to observed it by scanning energy of the electron beam were unsuccessful. Surprized by experimental measurements showing no indication of the measurable "imprint" from the ion beams, we verified that beam indeed overlap, and that beam's relativistic factors were equal within ±1%. We also observed interactions between overlapping electron and ion bunches. By design of the CeC experiment, electron beam interacts only with one of ion bunches circulating in RHIC yellow ring. Hence, we compared bunch-lengthening rate of interacting ion bunch (effected only by IBS) with witness bunches and found growth rate is doubled, when the CeC FEL gain was high – see Fig. 3. Turning the FEL gain off (observed by the FEL power level) eliminated the heating of the interacting bunch.

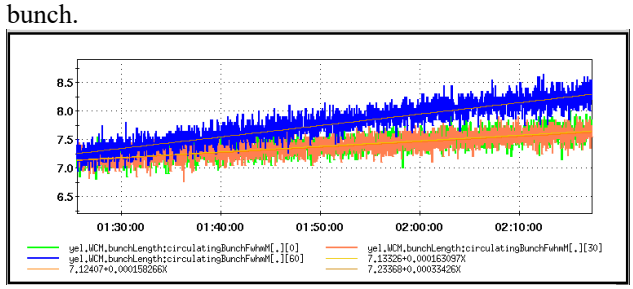

Figure 3: Evolution of the bunch lengths for interacting (blue trace, RF bucket #30) and witness bunches (orange and green traces, RF buckets #0 and #60) shows doubling of the growth rate.

We continued improving our measurement technique and clearly demonstrated (see Fig. 2) absence of measurable imprint within a statistical error of 2% Attempts to resolve the "imprint absence" puzzle did not allow us to investigate the cooling in FEL-based CeC.

ISBN: 978-3-95450-218-9 ISSN: 2226-0374 doi:10.18429/JACoW-COOL2019-TUZ01

This was definitely unexpected result: all in-depth simulation using standard accelerator physics codes (PARMELA, ASTRA, GPT, Elegant, etc.) predicted that there will be no instabilities in the electron beam transport from the gun to the FEL amplifier. Our experiment proved this assumption to be wrong when we were unable to observe expected strong "imprint" from ion beam in the radiation power of the electron beam. This puzzle was not resolved till the end of regular RHIC run with ion beam in mid-June 2018. We took advantage of availability of LiHe during the summer for commissioning of Low Energy RHIC electron Cooler (LEReC) and found a new instability occurring in beams propagating in straight section, which we called Plasma-Cascade Instability [14-16].

Post-Run Studies. We completed CeC run 18 by investigating electron beam quality and resolving the "imprint" measurement puzzle, for which we considered a number of possible explanations (such as 3% error in beam energies, FEL saturation, poor beam overlap, etc.), all of which were eliminated (or proved highly unlikely), except excessive noise in the election beam at frequencies ~ 10 THz.

While there were a number of other indications, the most convincing measurement was when we fully opened FEL wiggler (e.g. effectively turned them off) and found that measured radiation power of electron beam from a bending magnet exceeded natural (spontaneous or Poison statistical random noise) level by ~300-fold. E.g. in the lattice used for the "imprint" studies the amplitude of the beam density modulation at frequency ~ 10 THz was ~17-fold above the shot-noise level. While this was sufficient to explain the results shown in Fig. 2, we wanted to find the origin of this broad-band noise. The possibility of instabilities caused by CSR and wakefield were eliminated in our simulations. We also eliminated possibility that this modulation originates at the laser pulse structure by measuring its spectrum. Finally, we discovered the real culprit of this noise – a Plasma-Cascade Instability (PCI) in the low energy beam transport used for ballistic bunch compression. We demonstrated both experimentally and later in simulations that PCI is driven by strong modulation of the beam radius [16]. We gain sufficient experience and understanding of PCI both to predict it and, when needed, to suppress it.

CONTROL OF NOISE IN ELECTRON BEAM

We learned how to use one of the most universal codes, Impact T, to simulate PCI in the CeC SRF accelerator. Two samples of successful simulations, using NERSC supercomputer, are shown in Fig. 4. It took us awhile to learn how to the code for simulating PCI at 10s of THz correctly: specifically, we adjusted the mesh size, the time steps and number of macroparticles to avoid massive superficial spikes in the spectrum. Some of the remaining spikes can be seen in red line near 15 THz and 20 THz. While Impact T allowed us to simulate PCI, it worth noting that the noise floor in these simulations exceeds that of the baseline (e.g. of shot noise with Poisson statistics) by about an order of magnitude.

The simulations for graphs showing in Fig. 4. were performed for 1.25 MV SRF gun voltage, standard bunching cavity voltages for 20-fold compression of electron bunches. They were done for a regular (strong focusing) lattice and a relaxed lattice in the low-energy beam transport of the CeC accelerator. We were able to show in these simulations that (1) indeed we had strong PCI with the lattice we used for the ion impact studies; (2) that we can reduce noise level in the electron beam using relaxed lattice with a smooth beam envelope.

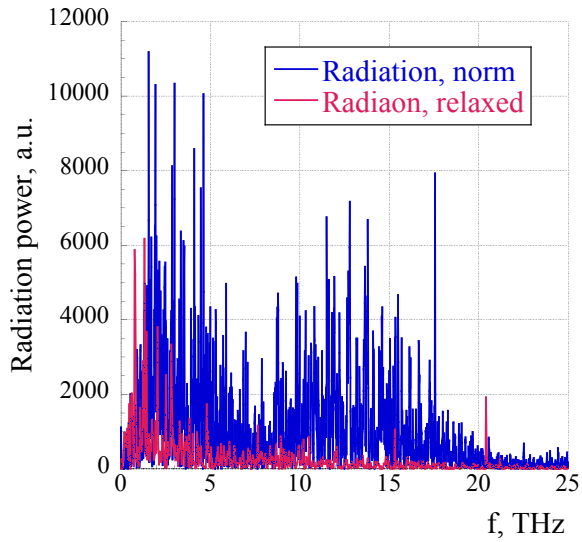

Figure 4: Radiation spectrum of the compressed 0.7 nC electron bunch profile at the exit of the SRF linac simulated by Impact-T. Blue colour line is for strong focusing lattice (used during RHIC Run 18) and Red colour lines are for a relaxed lattice of the CeC accelerator. Horizontal axis is the frequency measured in THz.

These simulations were indications of possibility to control noise level in electron beam and making it useful for CeC experiments. We just needed to demonstrate it using a real "quantum computer" – the beam itself.

During RHIC run 19, we had a short three-week-long experiment with CeC accelerator with main goal of reducing noise in electron beam to acceptable level. We installed new broad-band mid-IR diagnostic system down-stream of the first bending magnet located just downstream of our SRF linac. During this run, access to the RHIC vacuum system was terminated and the beam was dumped into the wall of the dipole magnet vacuum chamber. In this mode, the beam current was limited to 2.5 μA.

The layout of IR diagnostic system is shown in Fig. 5. Electron beam is bent by 45-degree dipole magnet and IR radiation is reflected by 45-degree Cu mirror though CVD diamond window in atmosphere. The window is covered by metal 1.4 mm x 1.4 mm mesh to prevent sub-THz radiation from reaching the IR detector. 2" off-axis parabola focuses radiation onto the entrance window of GentecTHZ5I-BL-BNC pyroelectric detector. This detector is sensitive to all sources of energy including X-ray, vibrations and audio noise, and has only a slow AC msec scale

ISBN: 978-3-95450-218-9 ISSN: 2226-0374 doi:10.18429/JACoW-COOL2019-TUZ01

response time. We operated electron beam with 10 Hz trains of 78 kHz bunches and used lock-in amplifier to achieve necessary sensitivity.

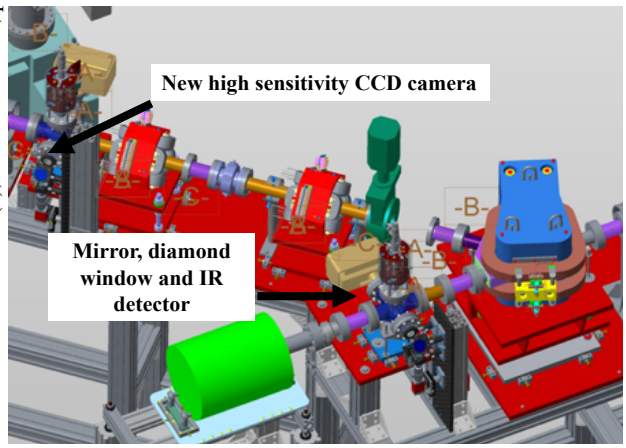

Figure 5: IR diagnostics set-up for the noise-control experiment. The reflecting mirror is located 0.73 meters downstream of the front edge of the bending magnet.

We used Igor-Pro code and measured map of magnetic field to calculate distribution of radiation power at the 1" reflecting mirror and the energy spectrum of the radiation reflected to the IR detector – see Fig. 6.

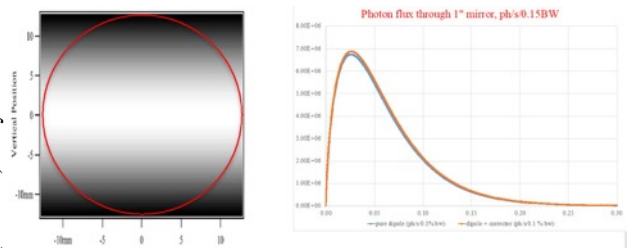

Figure 6: Left is the distribution of IR radiation power at 1" reflecting mirror (red circle) and right is simulated spectrum for normal and tilted by 2.5 mrad entrance into the bending magnet. Simulations done with Igor-Pro code.

The most important part of the experiment was to establish the baseline, e.g. the power originating from Poisson statistics shot noise. With typical beam current of 1.5 μA and ~50% transport efficiency (most of the losses originated from the metal mesh) total baseline radiation power reaching the IR detector was ~ 50 pW. The corresponding signal from lock-in amplifier would be ~ 20 μV*, e.g. the expected baseline ratio between measured voltage and beam current is ~15 V/A.

We measured the baseline level using a weakly compressed (only by 4-fold) electron beam and relaxed lattice of the accelerator. To demonstrate that shot noise in our beam was not amplified by instabilities, we measurements radiation power with the bunch charge varied by a factor of 5, e.g. with 0.3 nC and 1.5 nC bunches. Measured powers normalized to the average current agreed well within measurement errors.

The baseline measurements were non-trivial and required use of modulation-demodulation (MDM) technique in addition to the lock-in amplifier. Specifically, we were inserting and removing reflecting mirror and measured difference between two states. Measurements were performed for few (from 2 to 12) hours to achieve necessary accuracy. While all our measurements were performed by a dedicated MDM code, which was taking into account the state of the accelerator as well as pausing during transition between states, here we present in Fig. 7, a graph from RHIC control system illustrating the need for the MDM measurements. The base line was measured in 4 long MDM scans to be 14.5±1.5 V/A

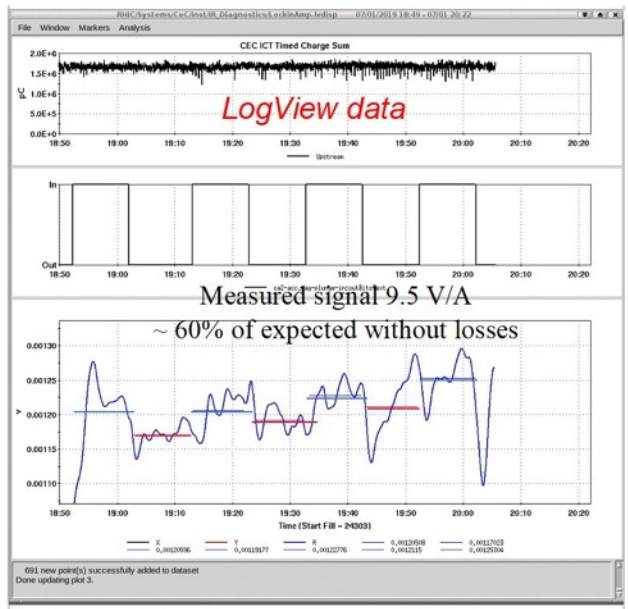

Figure 7: Illustration of the evolution of signal from lock-in amplifier and the need for the MDM method. Top graph shows the charge per bunch train. The middle graph shows location of the reflecting mirror (IN/OUT). The bottom graph shows evolution of the lock-in signal with time constant of 30 seconds. Significant drifts illustrate the need for averaging and the MDM method for accurate measuring the radiation power at this level.

The applied methods allowed us to achieve the required sensitivity and to reliably measure the baseline of radiation power and to compare it with that for the compressed beam. First, we confirmed that the noise level in the electron beam used for the Run 18 imprint studies (600 pC per bunch, 20X compression, strong focusing lattice) has noise power level ~ 250 above the baseline.

After that we investigated dependence of the noise level in electron beam with 1.5 nC per bunch compressed to 75 A beam current as function of solenoid focusing of the low energy transport line. We found that there is a rather large

* Main uncertainty comes from approximation in the transparency of the metal mesh.

ISBN: 978-3-95450-218-9 ISSN: 2226-0374 doi:10.18429/JACoW-COOL2019-TUZ01

valley of setting with noise level at or below 10-fold the baseline. Figure 8 shows one of best results obtained during these studies when the noise level was reduced to about 6-times of the baseline.

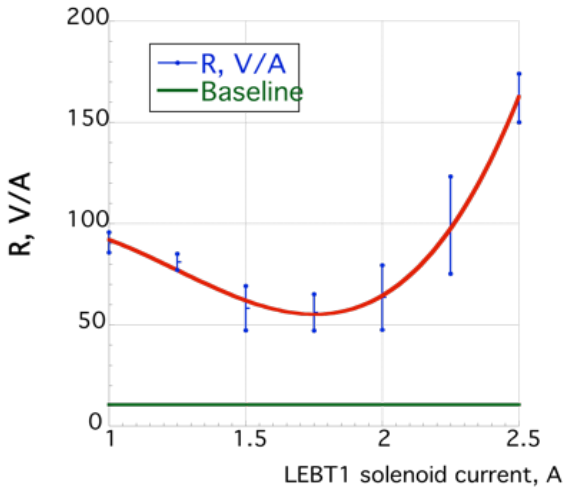

Figure 8: Redline is the measured ratio of the lock-in amplifier voltage to the average beam current, R, as function of the current in LEBT1 solenoid Green line shows the baseline for R value corresponding to the shot noise.

PLANS

Starting from Run 19 RHIC switched to low energy operation. This mode requires avery large aperture, which is incompatible with that of the CeC FEL wiggler. Hence, the FEL wigglers system had been removed and the system was replaced with large aperture chamber. We designed new CeC system compatible with this new requirement. Our next step in the CeC demonstration experiment with microbunching Plasma-Cascade Amplifier (PCA) is shown in Fig. 9.

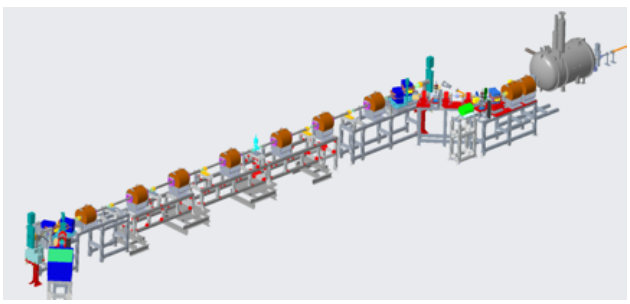

Figure 9: Layout of the CeC experiment with micro-bunching Plasma-Cascade Amplifier at IP2. It has seven solenoids: the modulator section IS between THE first and THE second solenoids, strong-focusing 4-cess PCA formed by 5 central solenoids, and the kicker section is upstream of the last solenoid.

Our broadband (~20 THz) PCA is the only micro-bunching amplifier which does not require separation and delay system for ion beam. In other words, this is the unique possibility to demonstrate CeC with micro-bunching amplifier without a millions-dollars investment in significant lattice modification of RHIC. The vacuum system for PCA_based CeC experiment is already installed. All solenoids had been produced, underwent magnetic measurements and are in the process of installation.

During last year we developed reliable self-consistent full-3D simulations of PCI and PCA capable of predicting CeC performance– see Fig. 5.

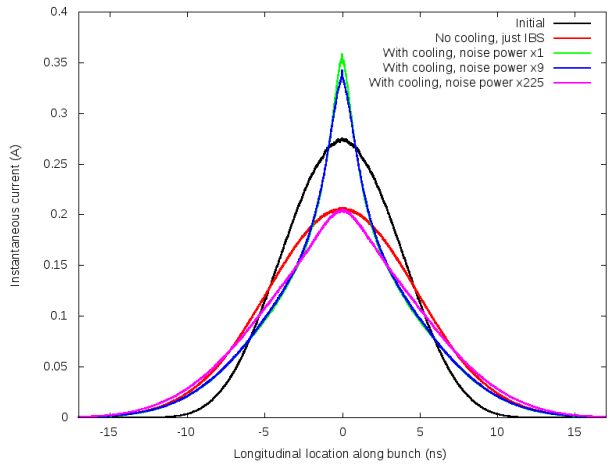

Figure 10: Evolution of the 26.5 GeV/u ion bunch profile in RHIC. Black - initial profiles at t=0. All other profiles are shown at t=40 minutes. Red– evolution of witness bunch without cooling; green – cooled with e-beam having natural shot noise; blue- cooled with e-beam with 9 time increase in the noise power; crimson - e-beam with 255 time increase in noise power.

Successful demonstration of electron beam with low noise gives us confidence that we should be able to demonstrate cooling of 26.5 GeV/u ion beam in RHIC – e.g. something resembling blue line in Fig. 10. Our three-year plan includes demonstration of ion imprint and PCA during RHIC run 20, followed by demonstration of longitudinal (energy) cooling during RHIC run 21, and simultaneous transverse and longitudinal cooling during RHIC run 22.

CONCLUSION

We successfully commissioned SRF-based CeC electron accelerator and achieved all design beam parameter, except the energy. Unfortunately, we stumble into a previously unknown microwave instability - occurring in beam propagating along straight line – which prevented demonstration of FEL-based CeC last year. We developed a new – more advanced - CeC system, which is fully compatible with RHIC low energy operation requirements, to continue our experimental program. The hardware necessary for the next step of our experiment is in the process of installation. Successful commissioning of this system will allow us to demonstrate CeC experimentally in near future.

REFERENCES

[1] V.N. Litvinenko, Y.S. Derbenev, *Physical Review Letters* **102**, 114801, 2009.

ISBN: 978-3-95450-218-9 ISSN: 2226-0374 doi:10.18429/JACoW-COOL2019-TUZ01

[2] V. Litvinenko *et al*., "Proof-of-principle Experiment for FEL-based Coherent Electron Cooling", in *Proc. 33rd Int. Free Electron Laser Conf.* (FEL'11), Shanghai, China, Aug. 2011, paper WEOA3, pp. 322-325.

[3] I. Pinayev *et al*., "Present Status of Coherent Electron Cooling Proof-of-principle Experiment", in *Proc. 9th Workshop on Beam Cooling and Related Topics* (COOL'13), Mürren, Switzerland, Jun. 2013, paper WEPPO14, pp. 127-129.

[4] I. Pinayev *et al*., "First Results of the SRF Gun Test for CeC PoP Experiment", in *Proc. 37th Int. Free Electron Laser Conf.* (FEL'15), Daejeon, Korea, Aug. 2015, paper TUD03, pp. 564-566.

[5] I. Pinayev *et al*., "Helical Undulators for Coherent Electron Cooling System", in *Proc. 38th Int. Free Electron Laser Conf.* (FEL'17), Santa Fe, NM, USA, Aug. 2017, pp. 519-521. doi:10.18429/JACoW-FEL2017-WEP051

[6] I. Petrushina *et al*., "Novel Aspects of Beam Dynamics in CeC SRF Gun and SRF Accelerator", in *Proc. 38th Int. Free Electron Laser Conf.* (FEL'17), Santa Fe, NM, USA, Aug. 2017, pp. 313-316. doi:10.18429/JACoW-FEL2017-TUP034

[7] I. Petrushina *et al*., "Mitigation of multipacting in 113 MHz superconducting RF photo-injector", *Phys. Rev. Accel. Beams* 21, 082001, 2018.

[8] K. Mihara, Y. C. Jing, V. Litvinenko, I. Petrushina, I. Pinayev, and G. Wang, "Emittance Measurements from SRF Gun in CeC Accelerator", in *Proc. 38th Int. Free Electron Laser Conf.* (FEL'17), Santa Fe, NM, USA, Aug. 2017, pp. 470-474. doi:10.18429/JACoW-FEL2017-WEP025

[9] G. Wang, Y. C. Jing, V. Litvinenko, and J. Ma, "Electron Beam Requirements for Coherent Electron Cooling FEL System", in *Proc. 38th Int. Free Electron Laser Conf.* (FEL'17), Santa Fe, NM, USA, Aug. 2017, pp. 323-325. doi:10.18429/JACoW-FEL2017-TUP039

[10] Y. C. Jing, V. Litvinenko, and I. Pinayev, "Simulation of Phase Shifters Between FEL Amplifiers in Coherent Electron Cooling", in *Proc. 38th Int. Free Electron Laser Conf.* (FEL'17), Santa Fe, NM, USA, Aug. 2017, pp. 386-388. doi:10.18429/JACoW-FEL2017-TUP072

[11] T. Xin, J. C. Brutus, S.A. Belomestnykh, I. Ben-Zvi, C. H. Boulware, T. L. Grimm, *et al*., *Review of Scientific Instruments,* 87, 093303, 2016.

[12] I. Pinayev, V.N. Litvinenko, *et al*., "High-gradient High-charge CW Superconducting RF gun with CsK2Sb photocathode", arXiv:1511.05595, 17 Nov 2015.

[13] V. Litvinenko *et al*., "Commissioning of FEL-Based Coherent Electron Cooling System", in *Proc. 38th Int. Free Electron Laser Conf.* (FEL'17), Santa Fe, NM, USA, Aug. 2017, pp. 132-135. doi:10.18429/JACoW-FEL2017-MOP041

[14] V.N. Litvinenko, G. Wang, D. Kayran, Y. Jing, J. Ma, I. Pinayev, "Plasma-Cascade micro-bunching Amplifier and Coherent electron Cooling of a Hadron Beams", arXiv preprint arXiv:1802.08677.

[15] Vladimir N. Litvinenko, Gang Wang, Yichao Jing, Dmitry Kayran, Jun Ma, Irina Petrushina, Igor Pinayev and Kai Shih, "Plasma-Cascade Instability- theory, simulations and experiment", arXiv:1902.10846, 2019

[16] J. Ma, V. Litvinenko, and G. Wang, "Simulations of Modulator for Coherent Electron Cooling", in *Proc. 9th Int. Particle Accelerator Conf.* (IPAC'18), Vancouver, Canada, Apr.-May 2018, pp. 2953-2956. doi:10.18429/JACoW-IPAC2018-THPAF005

[17] T. A. Miller, D. M. Gassner, V. Litvinenko, M. G. Minty, I. Pinayev, and B. Sheehy, "Infrared Diagnostics Instrumentation Design for the Coherent Electron Cooling Proof of Principle Experiment", in *Proc. 36th Int. Free Electron Laser Conf.* (FEL'14), Basel, Switzerland, Aug. 2014, paper THP074, pp. 905-908.

ISBN: 978-3-95450-218-9 ISSN: 2226-0374 doi:10.18429/JACoW-COOL2019-TUB01

RECENT RESULTS FROM MICE ON MULTIPLE COULOMB SCATTERING AND ENERGY LOSS

D. M. Kaplan, Illinois Institute of Technology, Chicago, Il 60616 USA
J. C. Nugent*, P. Soler, University of Glasgow, Glasgow, United Kingdom
On behalf of the MICE Collaboration

Abstract

Multiple coulomb scattering and energy loss are well known phenomena experienced by charged particles as they traverse a material. However, from recent measurements by the MuScat collaboration, it is known that the available simulation codes (Geant4, for example) overestimate the scattering of muons in low Z materials. This is of particular interest to the Muon Ionization Cooling Experiment (MICE) collaboration which has the goal of measuring the reduction of the emittance of a muon beam induced by energy loss in low Z absorbers. MICE took data without magnetic field suitable for multiple scattering measurements in the spring of 2016 using a lithium hydride absorber. The scattering data are compared with the predictions of various models, including the default Geant4 model.

INTRODUCTION

Results from atmospheric neutrinos at Super-Kamiokande [1] and from solar neutrinos at the Sudbury Neutrino Observatory [2] conclusively demonstrated that neutrinos have a non-zero mass and oscillate between different flavours. A facility promising precision measurement of neutrino oscillations parameters is the Neutrino Factory [3], where neutrinos would be produced via muon decay rings. Before the muons are injected into the storage ring the phase-space volume of the beam must be reduced. The only cooling technique which can act within the lifetime of the muon is ionization cooling and has shown in simulation to reduce the phase-space volume of the beam by a factor of 100,000. MICE Step IV is current taking data to provide the first measurement of ionization cooling. This demonstration is an essential part of the worldwide research effort towards building a Neutrino Factory. A Neutrino Factory is the only proposed facility with the capability to measure the CP violation phase, δ_{CP}, with 5° accuracy.

MICE BEAM LINE AND EXPERIMENT

The MICE experiment is located at the Rutherford Appleton Laboratory (RAL) in the UK and operates parasitically on the ISIS proton accelerator [4], producing beam for the newly built MICE Muon Beam (MMB) by the insertion of an internal pion-production target. MICE is a novel single particle experiment designed to perform high precision measurements of normalized emittance both upstream and downstream of the ionization cooling equipment. The MMB

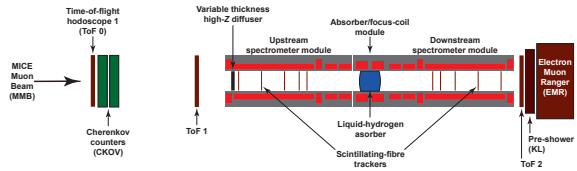

Figure 1: Schematic of Step IV of the MICE experiment, with the Absorber Focus Coil module between the two Spectrometer Solenoids.

is composed of three quadrupole triplets, two dipole magnets, which select the momentum, and a decay solenoid (DS), which increases the number of muons in the beam. The MICE Step IV setup is shown in Fig. 1. It consists of an Absorber Focus Coil (AFC) module located between two measurement stations. These stations are composed of particle identification suites including a total of three time-of-flight detectors (TOFs) [5], two Cherenkov detectors (Ckova and Ckovb) [6], the KLOE-light sampling calorimeter (KL) [7] and the Electron Muon Ranger (EMR) [8]. Each station has a Tracker [9] with five planes of scintillating fibres inside a 4 T Spectrometer Solenoid (SS) to measure track and momentum information (x, y, p_x and p_y), so as to reconstruct the emittance before and after cooling. The AFC module, which houses the liquid hydrogen or lithium hydride absorber within a pair of focusing coils, is located between the two measurement stations.

OVERVIEW OF MULTIPLE COULOMB SCATTERING

The PDG recommends an approximate multiple scattering formula [10], [11], which is found to be accurate to approximately 11%:

$$\theta_0 \approx \frac{13.6\,\mathrm{MeV}}{p_\mu \beta_\perp}\sqrt{\frac{\Delta z}{X_0}}\left[1 + 0.0038\ln\left(\frac{\Delta z}{X_0}\right)\right], \qquad (1)$$

where θ_0 is the rms width of the projected scattering angle distribution, X_0 is the radiation length of the material and Δz is the thickness of the absorber, p_μ is the momentum of the muon and the muon velocity is $\beta_\perp\, p_\mu c/E_\mu$, with E_μ its energy. From this an approximate cooling formula can be derived (ignoring the logarithmic term of equation 1),

$$\frac{d\varepsilon_n}{dz} \approx -\frac{\varepsilon_n}{E_\mu \beta_{\mathrm{rel}}^2}\left\langle\frac{dE_\mu}{dz}\right\rangle + \frac{\beta}{2m_\mu \beta_{\mathrm{rel}}^3}\frac{(13.6\,\mathrm{MeV})^2}{E_\mu X_0}, \qquad (2)$$

where ε_n is the normalised transverse (two-dimensional) emittance of the beam, β is the betatron function, and m_μ

* john.nugent@glasgow.ac.uk

ISBN: 978-3-95450-218-9 ISSN: 2226-0374 doi:10.18429/JACoW-COOL2019-TUB01

the energy and mass of the muons [12]. Given that the goal of MICE is to measure the reduction in normalised emittance with 1% precision, which requires an absolute emittance measurement precision of 0.1%, this approximate formula is not sufficient for the needs of MICE. This demands an accurate measurement of MCS for relevant low-Z materials, such as liquid hydrogen and lithium hydride, where simulations are not in good agreement with data. The MUSCAT experiment carried out a measurement of muon scattering in low-Z materials [13] and found significant differences between a number of models and the measured distributions.

The theory of Multiple Coulomb Scattering, developed by Rossi and Greisen [14] and Molière [15], considered Rutherford scattering with a low angle cut-off

$$\frac{\theta_0^2}{z} = 16\pi N_A \frac{Z^2}{A} r_e^2 \left(\frac{mc}{p_\mu \beta}\right) \ln\left(196 Z^{-1/3}\left(\frac{Z}{A}^{1/6}\right)\right) \approx \frac{(21.2\text{MeV})^2}{p_\mu^2 \beta^2} \frac{1}{X_0} \quad (3)$$

where only interactions with the atomic nucleus are included, with a distribution proportional to Z^2, where Z is the atomic number of the scattering material. Bethe [16] adapted the Molière theory to include atomic electron scattering, which implied a proportionality of $Z(Z+1)$; however this theory still assumed equal weight was given to both nuclear and atomic electron scattering. Early theories of MCS were reviewed by Scott [17]. Further modifications were made to the original theory by Lynch and Dahl to incorporate a path length dependance which resulted in the PDG formula quoted in equation 1. Both the Molière and Bethe theories were compared to MCS data for a variety of absorbers in MUSCAT, and it was found that these theories did not describe low-Z materials adequately.

Most particle physics simulations use Geant4 [18] to evaluate particle interactions with matter. Geant4 makes a parameterisation of the scattering distribution for finite thickness of the material then proceeds stepwise through the simulated material, calculating the contribution for each step. Multiple scattering in Geant4 does not use a small angle approximation and relies on a Legendre polynomial expansion, where the default physics list evaluates the Urban cross-section [19], [20] for most particles and the Wentzel single-scattering cross-section for muons. This model works well for high-Z materials but overestimates scattering for low-Z materials. Alternative models which can overcome these shortcomings have been proposed, namely the Cobb-Carlisle model [21], [22] which samples directly from the Wentzel single-scattering cross-section and simulates all collisions with nuclei and electrons. This includes a cut-off for the nuclear cross-section and separate contributions from

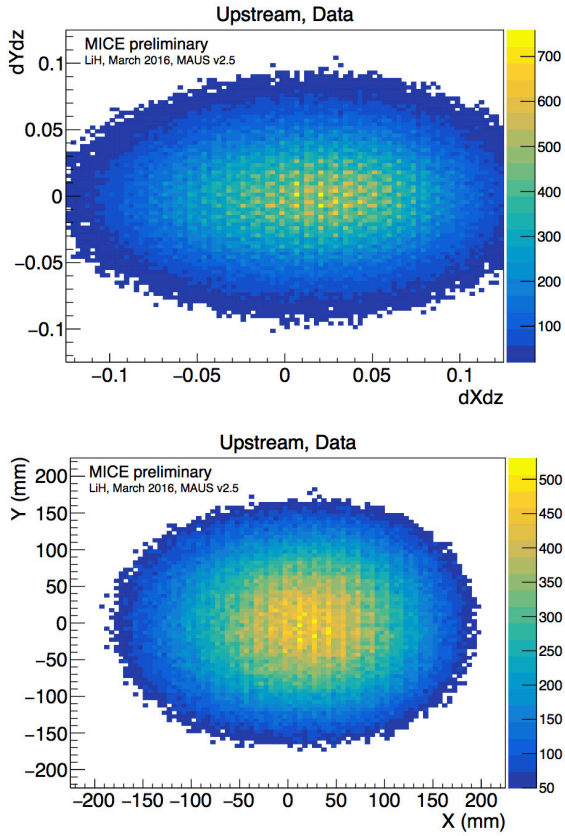

Figure 2: Upstream position distributions for a 200 MeV/c muon beam in the LiH data after particle selection.

the nuclear and atomic electron scattering:

$$\frac{\theta_0^2}{z} = 8\pi N_A \frac{Z^2}{A} r_e^2 \left(\frac{mc}{p_\mu \beta}\left[\ln\left(\frac{\theta_2}{\theta_1}^2 + 1\right) - 1\right] + \frac{1}{Z}\left[\ln\left(\frac{\theta_2^e}{\theta_1^e}^2 + 1\right) - 1\right]\right) \quad (4)$$

Therefore, MICE will need to measure MCS for low-Z materials, such as liquid hydrogen and lithium hydride, to perform an accurate measurement of ionisation cooling. The lithium hydride absorber has a thickness of 65 mm (6.7%X_0) where the lithium hydride composition is: 81% ^{6}Li, 4% 7Li, 14% ^{1}H with traces of C, O, and Ca.

SCATTERING DATA

The MICE Muon Beam has been fully characterised [23] and has a pion contamination of less than 1.4% at 90% C.L. [24]. For the lithium hydride data the beam was operated in "muon mode" giving an almost pure muon beam at a variety of momenta. For this measurement a beam with a 3π mm·rad emittance beam was selected. The lithium hydride MCS data taking period was during the 2015/04 ISIS user cycle from the 23rd of February until the 24th of March 2016. The volume between the absorber and the two trackers was filled with helium to minimise multiple

ISBN: 978-3-95450-218-9 ISSN: 2226-0374 doi:10.18429/JACoW-COOL2019-TUB01

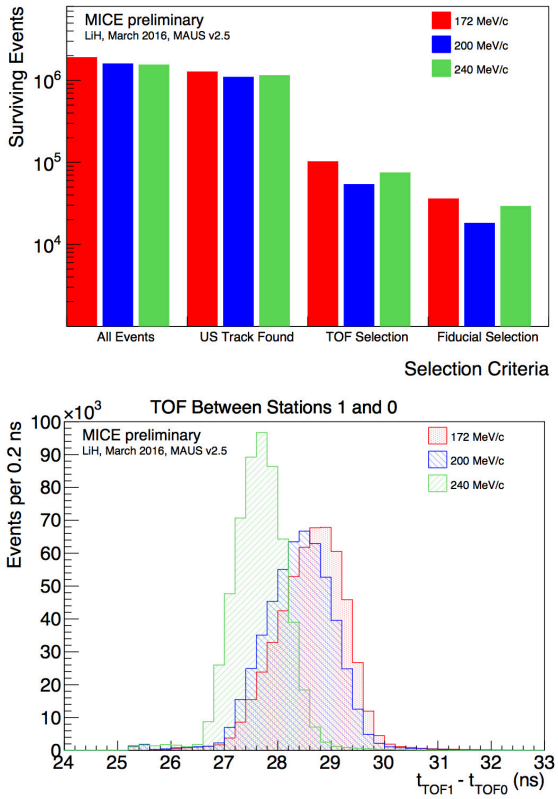

Figure 3: Top: The survival of muons after each stage of the selection. Bottom: The time of flight for muons between TOF0 and TOF1 for each of the nominal momentum points at which MICE will measure scattering at.

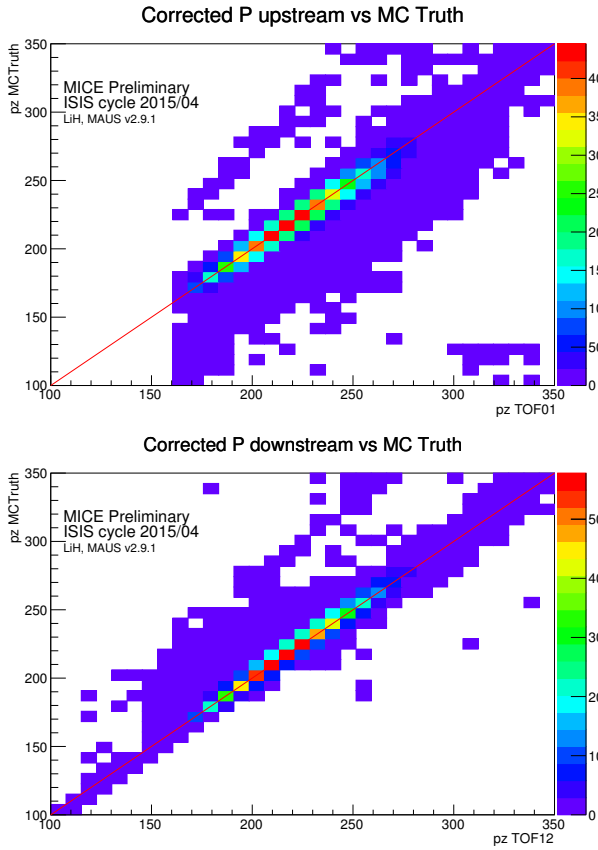

Figure 4: Figures showing the agreement between the momentum calculated by the correction up- (left) and downstream (right) and the momentum determined from MC truth.

scattering not due to the absorber. The measurements were carried out without a magnetic field either in the tracker volume or surrounding the absorber. During the 2015/04 data taking period, the channel was entirely empty when the lithium hydride was removed. Momentum measurements were carried out using the time-of-flight difference between TOF1 and TOF2. Only tracks that have hits in TOF1 in both planes, with one muon reconstructed in each event and within the time of flight window, are selected for the analysis. Tracks are projected downstream from the upstream tracker volume to the reference plane of the downstream tracker and must be within a 140 mm radius from the centre of the reference plane to be selected. The beam spot in the trackers after selection is shown in Fig. 2 and the population of muons after each selection is shown in Fig. 3.

MOMENTUM CORRECTION

The two MICE trackers can measure the momentum of muons up- and downstream of the absorber when both spectrometer solenoids are energised. When the solenoidal magnetic fields are present in the channel muons follow a helical trajectory from which a momentum measurement can be made. In the case where there are no magnetic fields in the cooling channel no measurement of momentum can be made with the trackers. In this scenario a momentum measurement is made with the MICE time of flight system using the expression

$$p = \frac{m}{\sqrt{\frac{t_{12}^2 c^2}{L^2} - 1}} \quad (5)$$

However this expression is based on several assumptions, namely that the muons are on axis and undergo no energy loss between the TOF stations. To account for these effects a correction is applied to the momentum as reconstructed by the TOF system to reconstruct the exact momentum at the centre of the absorber. The calculation is an analytic expression which is the second order expansion of the Taylor series in p/mc for the exact path of the muon between TOF stations. One caveat of this method is that constant energy loss is assumed. However even with this approximation good agreement between reconstructed momentum and that obtained from MC truth is shown in Fig. 4 with the residuals shown in Fig. 5.

TRACKER ACCEPTANCE

The geometric acceptance of the scattering angles that can be measured by MICE are determined by the apertures of the cooling channel. The effect of this acceptance on the

ISBN: 978-3-95450-218-9 ISSN: 2226-0374 doi:10.18429/JACoW-COOL2019-TUB01

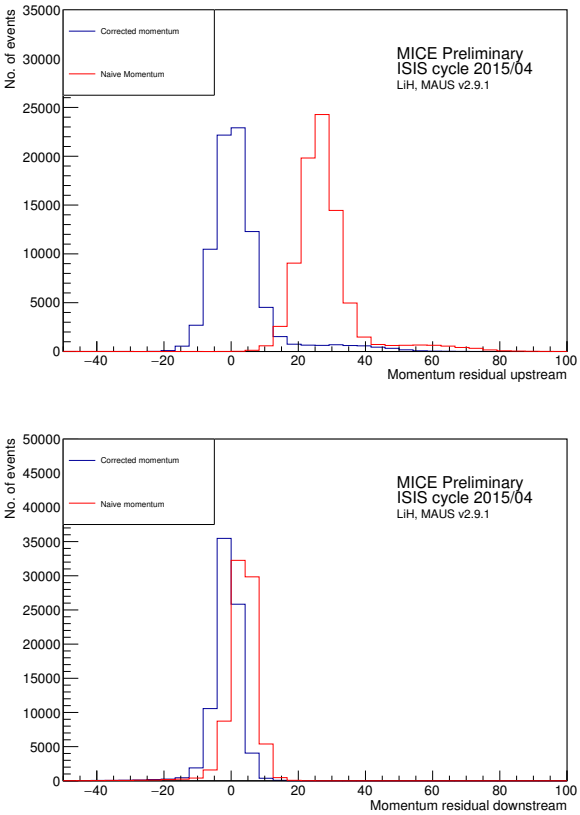

Figure 5: Shows the residual between the momenta before and after correction up- (top) and downstream (bottom) and the momentum determined from MC truth.

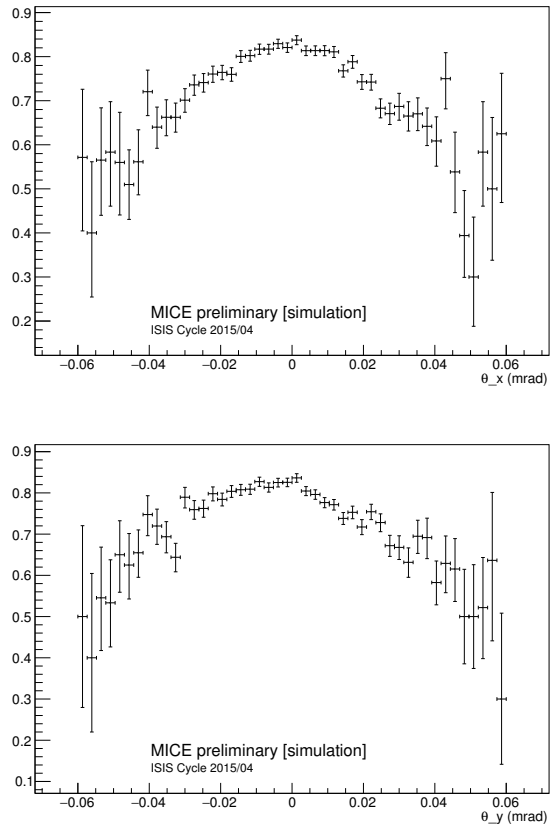

Figure 6: Shows the downstream tracker acceptance in θ_x (top) and θ_y (bottom).

scattering distributions must be accounted for and is determined by considering Monte Carlo (MC) simulations of the MICE beam. In simulation both the number of tracks which are expected (i.e., seen in MC truth) and number of tracks reconstructed (i.e., seen in the reconstructed data) are known. The full analysis chain is then run, tracks are matched upstream and downstream, the selection is performed and the scattering angle is calculated. The downstream acceptance is then defined as

$$\frac{\text{No. of tracks in } \theta \text{ bin MC Truth that are reconstructed}}{\text{No. of tracks in } \theta \text{ bin MC Truth}}. \quad (6)$$

It is assumed that the upstream efficiency is 100%, as by construction if a track is never seen upstream then no scattering angle is ever measured. The calculated acceptance is shown in Fig. 6

DECONVOLUTION OF RAW SCATTERING DATA

The scattering in the absorber material is the physical quantity of interest. To extract this information the effects of scattering in non absorber materials and detector resolution that will appear in the overall scattering measurement must be deconvolved from the required scattering distribution.

A deconvolution algorithm using Bayesian statistics [25] has been used based on the implementation contained in the RooUnfold package [26]. This method uses the simulation to provide a probability of observing a given scattering angle from the trackers for a given true scattering angle in the absorber, $P(\Delta\theta_j^{\text{tracker}}|\Delta\theta_i^{\text{abs}})$. This conditional probability is then used to estimate the number of particles that experience an absorber scattering angle,

$$n(\theta_i^{abs}) = \sum_{j=1}^{n_E} n(\theta_j^{tracker}) P(\theta_i^{abs}|\theta_j^{tracker}), \quad (7)$$

which requires the calculation of the conditional probability

$$P(\theta_i^{abs}|\theta_j^{tracker}) = \frac{P(\theta_j^{tracker}|\theta_i^{abs}) P_0(\theta_i^{abs})}{\sum_{l=1}^{n_c} P(\theta_j^{tracker}|\theta_l^{abs}) P_0(\theta_l^{abs})} \quad (8)$$

The estimate is refined through multiple applications of the algorithm by updating the prior probability by letting $P_0(\theta_i^{abs}) = n(\theta_i^{abs})/\sum_{i=1}^{n_c} n(\theta_i^{abs})$ in iterations subsequent to the initial calculation in which a flat prior is used. The conditional probability $P(\theta_j^{tracker}|\theta_i^{abs})$ is derived from the convolution where $\theta^{tracker}$ is drawn from the sum of the reconstructed scattering angle in the empty absorber data and the scattering angle in the absorber from the convolution model, and θ_i^{abs} is the scattering angle in the absorber

ISBN: 978-3-95450-218-9 ISSN: 2226-0374 doi:10.18429/JACoW-COOL2019-TUB01

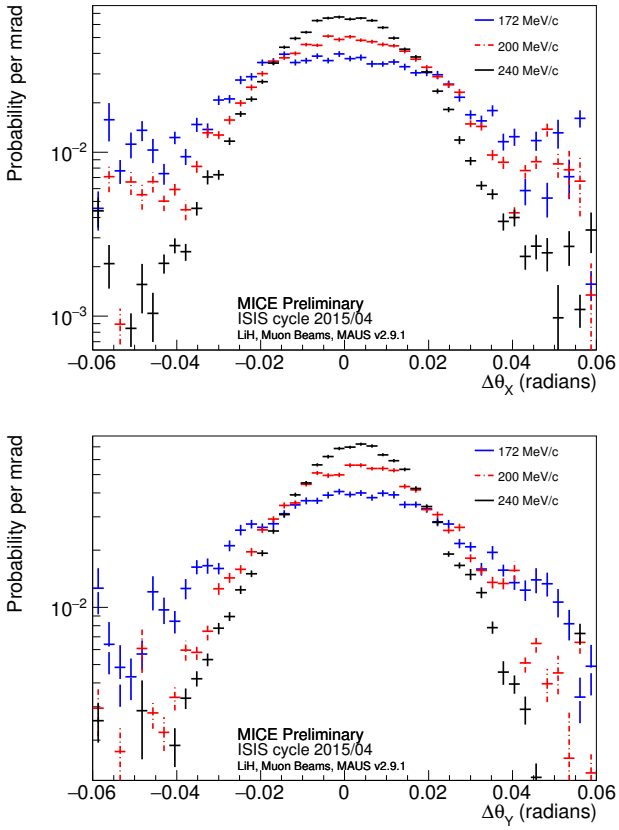

Figure 7: The results of the scattering analysis using data from all three nominal beam settings. Scattering widths are reported after application of deconvolution.

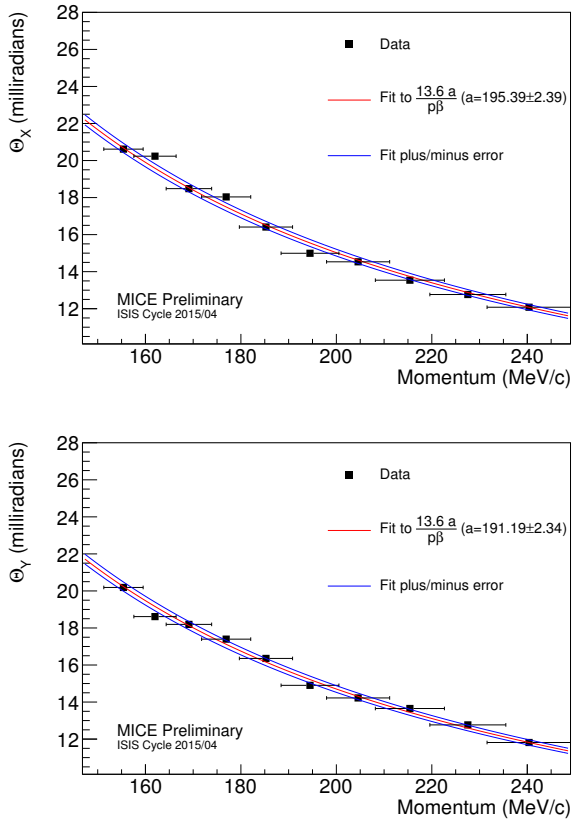

Figure 8: The results of the scattering analysis using data from all three nominal beam settings after application of deconvolution.

alone. The final scattering distributions at each of the nominal momentum points are shown in Fig. 7 and over the full momentum range in 8.

CONCLUSION

MICE has measured multiple Coulomb scattering in a lithium hydride target for muons with momentum between 140 and 240 MeV/c. A study of the systematics is in progress with a MICE publication currently being prepared. Future work will including a measurement of multiple Coulomb scattering in liquid hydrogen, a measurement of scattering with magnetic field in the cooling channel and an energy loss measurement.

REFERENCES

[1] Y. Fukuda et al. "Evidence for oscillation of atmospheric neutrinos". In: *Phys.Rev.Lett.* 81 (1998), pp. 1562–1567. DOI: 10.1103/PhysRevLett.81.1562. arXiv: hep-ex/9807003 [hep-ex].

[2] J. Farine. "Measurement of the rate of $\nu_e + d \rightarrow p + p + e^-$ interactions produced by B-8 solar neutrinos at the Sudbury Neutrino Observatory". In: *Phys. Atom. Nucl.* 65 (2002), pp. 2147–2155. DOI: 10.1134/1.1530292.

[3] S. Geer. "Neutrino beams from muon storage rings: Characteristics and physics potential". In: *Phys. Rev.* D57 (1998), pp. 6989–6997. DOI: 10.1103/PhysRevD.57.6989,10.1103/PhysRevD.59.039903. arXiv: hep-ph/9712290 [hep-ph].

[4] M. Bogomilov et al. "The MICE Muon Beam on ISIS and the beam-line instrumentation of the Muon Ionization Cooling Experiment". In: *JINST* 7 (2012), P05009. DOI: 10.1088/1748-0221/7/05/P05009. arXiv: 1203.4089 [physics.acc-ph].

[5] R. Bertoni et al. "The design and commissioning of the MICE upstream time-of-flight system". In: *Nucl. Instrum. Meth.* A615 (2010), pp. 14–26. DOI: 10.1016/j.nima.2009.12.065. arXiv: 1001.4426 [physics.ins-det].

[6] Lucien Cremaldi, David A. Sanders, Peter Sonnek, et al. "A Cherenkov Radiation Detector with High Density Aerogels". In: *IEEE Trans. Nucl. Sci.* 56 (2009), pp. 1475–1478. DOI: 10.1109/TNS.2009.2021266. arXiv: 0905.3411 [physics.ins-det].

[7] M. Adinolfi, A. Aloisio, F. Ambrosino, et al. "Calibration and reconstruction performances of the KLOE electromagnetic calorimeter". In: *Nucl.Instrum.Meth.* A461 (2001), pp. 344–347. DOI: 10.1016/S0168-9002(00)01240-7.

[8] D. Adams et al. "Electron-Muon Ranger: performance in the MICE Muon Beam". In: *JINST* 10.12 (2015), P12012.

ISBN: 978-3-95450-218-9 ISSN: 2226-0374 doi:10.18429/JACoW-COOL2019-TUB01

DOI: 10.1088/1748-0221/10/12/P12012. arXiv: 1510.08306 [physics.ins-det].

[9] M. Ellis et al. "The Design, construction and performance of the MICE scintillating fibre trackers". In: *Nucl. Instrum. Meth.* A659 (2011), pp. 136–153. DOI: 10.1016/j.nima.2011.04.041. arXiv: 1005.3491 [physics.ins-det].

[10] K. A. Olive et al. "Review of Particle Physics". In: *Chin. Phys.* C38 (2014), p. 090001. DOI: 10.1088/1674-1137/38/9/090001.

[11] Gerald R. Lynch and Orin I. Dahl. "Approximations to multiple Coulomb scattering". In: *Nucl. Instrum. Meth.* B58 (1991), pp. 6–10. DOI: 10.1016/0168-583X(91)95671-Y.

[12] David Neuffer. "Principles and Applications of Muon Cooling". In: *Proceedings, 12th International Conference on High-Energy Accelerators, HEACC 1983* C830811 (1983), p. 481.

[13] D. Attwood et al. "The scattering of muons in low Z materials". In: *Nucl. Instrum. Meth.* B251 (2006), pp. 41–55. DOI: 10.1016/j.nimb.2006.05.006. arXiv: hep-ex/0512005 [hep-ex].

[14] Bruno Rossi and Kenneth Greisen. "Cosmic-ray theory". In: *Rev. Mod. Phys.* 13 (1941), pp. 240–309. DOI: 10.1103/RevModPhys.13.240.

[15] G. Moliere. "Theory of the scattering of fast charged particles. 2. Repeated and multiple scattering". In: *Z. Naturforsch.* A3 (1948), pp. 78–97.

[16] H. A. Bethe. "Moliere's theory of multiple scattering". In: *Phys. Rev.* 89 (1953), pp. 1256–1266. DOI: 10.1103/PhysRev.89.1256.

[17] William T. Scott. "The theory of small-angle multiple scattering of fast charged particles". In: *Rev. Mod. Phys.* 35 (1963), pp. 231–313. DOI: 10.1103/RevModPhys.35.231.

[18] S. Agostinelli et al. "GEANT4: A Simulation toolkit". In: *Nucl. Instrum. Meth.* A506 (2003), pp. 250–303. DOI: 10.1016/S0168-9002(03)01368-8.

[19] Laszlo Urban. "A model for multiple scattering in Geant4". In: (2006). CERN-OPEN-2006-077.

[20] V. N. Ivanchenko, O. Kadri, M. Maire, et al. "Geant4 models for simulation of multiple scattering". In: *J. Phys. Conf. Ser.* 219 (2010), p. 032045. DOI: 10.1088/1742-6596/219/3/032045.

[21] Thimothy Carlisle. "Step IV of the Muon Ionization Cooling Experiment (MICE) and the multiple scattering of muons". In: *DPhil thesis, University of Oxford* (2013).

[22] T. Carlisle, J. Cobb, and D. Neuffer. "Multiple Scattering Measurements in the MICE Experiment". In: *Conf. Proc.* C1205201 (2012), pp. 1419–1421.

[23] D. Adams et al. "Characterisation of the muon beams for the Muon Ionisation Cooling Experiment". In: *Eur. Phys. J.* C73 (2013), p. 2582. DOI: 10.1140/epjc/s10052-013-2582-8. arXiv: 1306.1509 [physics.acc-ph].

[24] M. Bogomilov et al. "Pion Contamination in the MICE Muon Beam". In: *JINST* 11.03 (2016), P03001. DOI: 10.1088/1748-0221/11/03/P03001. arXiv: 1511.00556 [physics.ins-det].

[25] G. D'Agostini. "A Multidimensional unfolding method based on Bayes' theorem". In: *Nucl. Instrum. Meth.* A362 (1995), pp. 487–498. DOI: 10.1016/0168-9002(95)00274-X.

[26] Tim Adye. "Unfolding algorithms and tests using RooUnfold". In: *Proceedings of the PHYSTAT 2011 Workshop, CERN, Geneva, Switzerland, January 2011, CERN-2011-006, pp 313-318*. 2011, pp. 313–318. arXiv: 1105.1160 [physics.data-an]. URL: http://inspirehep.net/record/898599/files/arXiv:1105.1160.pdf.

ISBN: 978-3-95450-218-9 ISSN: 2226-0374 doi:10.18429/JACoW-COOL2019-TUB02

PLASMA-CASCADE INSTABILITY

Vladimir N. Litvinenko [1,2 †], Gang Wang[2,1], Yichao Jing[2,1], Dmitry Kayran[2,1], Jun Ma[2], Irina Petrushina[1], Igor Pinayev[2] and Kai Shih[1]
[1] Department of Physics and Astronomy, Stony Brook University, Stony Brook, USA
[2] Collider-Accelerator Department, Brookhaven National Laboratory, Upton, USA

Abstract

In this paper we describe a new micro-bunching instability occurring in charged particle beams propagating along a straight trajectory. Based on the dynamics of this parametric instability we named it a Plasma-Cascade Instability. Such instability can strongly intensify longitudinal micro-bunching originating from the beam's shot noise, and even saturate it. On the other hand, such instability can drive novel high-power sources of broadband radiation. We discovered this phenomenon in a search of a broadband amplifier for Coherent electron Cooling [1,2], which does not require separating electron and hadron beams.

INTRODUCTION

High brightness intense charged particle beams play critical role in the exploration of modern science frontiers Such beams are central for high luminosity hadron colliders as well as for X-ray free-electron-lasers (FEL) with ultra-fast time structures reaching the femtosecond level. Dynamics of intense charged particle beams is driven by both external factors – such as focusing and accelerating fields - and self-induced (collective) effects.

While external factors are typically designed to preserve beam quality, the collective effects can result in an instability. Such instabilities can severely degrade beam quality by spoiling its emittance(s) – increasing beam's momentum spread or creating density modulation or even filamentation in the beam. On the other hand, such instabilities can be deliberately built-in to attain specific results [1-6]. The Plasma-Cascade micro-bunching Instability (PCI) occurs in a beam propagating along a straight line. By its nature, the PCI is a parametric instability driven by variation of the electron beam density and corresponding change of the plasma oscillation frequency [5]. Conventional micro-bunching instability in beams travelling along a curved trajectory (for example, in a magnetic chicane or in an arc of an accelerator) is a well-known. But none of them includes PCI –a micro-bunching longitudinal instability driven by modulations of the transverse beam size.

PLASMA-CASCADE INSTABILITY

We start from a qualitative description of the PCI, which will be followed by rigorous theory, 3D simulations and experimental observation of this phenomena. Figure 1 depicts periodic focusing structure where the charged particle beam undergoes periodic variations of its transverse size. It is known small electron density perturbations $\tilde{n}(\vec{r}), |\tilde{n}| << n_o$ in a cold, infinite and homogeneous plasma will result in oscillations with plasma frequency, ω_p [7]:

$$\frac{d^2\tilde{n}}{dt^2} + \omega_p^2 \tilde{n} = 0;\ \omega_p = c\sqrt{4\pi n_o r_c}, \qquad (1)$$

where n_o is the particles density (in our case, in the beam's co-moving frame), c is the speed of the light and $r_c = e^2/mc^2$ is classical radius of the particles.

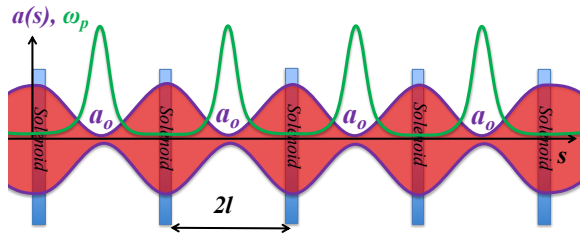

Figure 1: A sketch of four focusing solenoids cells with periodic modulations of beam envelope, *a(s),* and the plasma frequency, ω_p. Beam envelope has waists, a_o, in the middle of each cell where plasma frequency peaks. Both vertical and horizontal scale are optimized for illustration of the process.

For the beam propagating with velocity v_o in the periodic lattice with period *2l*, shown in Fig. 1, it would lead to a periodic modulation of the density $n_o \sim 1/a^2$ and the plasma frequency $\omega_p \sim 1/a$ with a period of $T = 2l/\gamma_o v_o$, where we took into account the relativistic time dilation in the co-moving frame by the beam's relativistic factor $\gamma_o = \left(1-\beta_o^2\right)^{-1/2}, \beta_o = v_o/c$. It is well known in classical oscillator theory [8] that rigidity modulation close to a half of oscillation period would result in exponential growth of oscillation amplitude: the phenomena known as parametric resonance. The extreme case of δ-function-like modulation is also well known: periodic focusing lenses with focal length is shorter than a quarter of the separating distances a ray instability in system. Hence the modulation of the transverse size could, in principle, results in unstable, e.g. growing longitudinal oscillation density. Such instability can also be a result of aperiodic frequency modulation: it is well known in accelerator physics that a solution of *s*-dependent Hill's equation, *x"+K(s)x=0*,can lead to unstable oscillations in focusing system with *K(s)>0.*

Analytical Studies

To switch from qualitative to qualitative description of PCI we need to identify a problem which is analytically tractable. In mathematical terms, we need to separate transverse and longitudinal degrees of freedom. As shown in [5,6] desirable separation is possible for long bunch, σ_s

† vladimir.litvinenko@stonybrook.edu

ISBN: 978-3-95450-218-9 ISSN: 2226-0374 doi:10.18429/JACoW-COOL2019-TUB02

$(\gamma_o\sigma_s >> a)$ with transverse Kapchinsky- Vladimirsky (KV) distribution [9]:

$$f_\perp(x,x',y,y') = N\cdot\delta\left(\frac{x^2+y^2}{a^2}+\frac{(ax'-a'x)^2+(ay'-a'y)^2}{\varepsilon^2}-2\right); \quad (2)$$

where ε is the envelope emittance. The KV beam has uniform density is uniform within the beam radius, defined by the envelope $r \le a(s)$, and zero density outsize it. Uniform particle's density results in linear defocusing electric field, which in combination with linear transverse focusing, preserves the KV distribution (2) with self-consistent beam envelope defined by a nonlinear equation [10]:

$$\frac{d^2a}{ds^2}+K(s)a-\frac{2}{\beta_o^{\,3}\gamma_o^{\,3}}\frac{I_o}{I_A}\frac{1}{a}-\frac{\varepsilon^2}{a^3}=0;\ K(s)=\left(\frac{eB_{sol}(s)}{2p_oc}\right)^2 \quad (3)$$

where I_o is the beam current, $p_o=\gamma_o\beta_o mc$ is particles momentum, and K is external focusing provided by solenoids and $I_A = mc^3/e \approx 17\ kA$ is Alfven current. With few exceptions [5,6] this has to be solved numerically to define the density (in the co-moving frame):

$$f_\perp = n_o(t) = \frac{I_o}{e\beta_o\gamma_o c}\frac{1}{\pi a^2(\gamma_o\beta_o ct)}. \quad (4)$$

Let's consider the distribution function in the co-moving frame as a weak perturbation $\tilde{f}$, $|\tilde{f}| << f_o$:

$$f = f_\perp\cdot f_\parallel(z,\mathrm{v},t);\ f_\parallel(z,\mathrm{v},t) = f_o(\mathrm{v})+\tilde{f}(z,\mathrm{v},t), \quad (5)$$

where v is z-component of velocity. Evolution of $\tilde{f}$ described by a linearized set of Vlasov- Poisson equations [11], $\tilde{n}(z,t) = n_o(t)\cdot\int_{-\infty}^{\infty}\tilde{f}\,d\mathrm{v}$:

$$\frac{\partial}{\partial t}\tilde{f}+\mathrm{v}\frac{\partial\tilde{f}}{\partial t}+\frac{eE_z}{m}\cdot\frac{\partial f_o}{\partial \mathrm{v}}=0;\ \frac{\partial E_z}{\partial z}=4\pi e\tilde{n}. \quad (6)$$

To exclude transverse components of the electric field in (6), e.g. for complete separation of longitudinal and transverse degrees of freedom, we added additional requirements for the longitudinal modulation: it has to at wavelength much shorter than the beam radius $\lambda_m << a$ [5]. Following technique developed in [12]: assuming κ-1 longitudinal velocity distribution $f_o(\mathrm{v}) = \sigma_\mathrm{v}/\pi(\sigma_\mathrm{v}^{\,2}+\mathrm{v}^2)$ and applying Fourier transformation $f_k = \int f\exp(-ikz)dz$ reduces eq. (7) to an oscillator equation:

$$\frac{d^2\tilde{n}_k}{dt^2}+\omega_p^2(t)\tilde{n}_k=0;\ \tilde{n}_k = \exp(|k\sigma_\mathrm{v}t|)\int_{-\infty}^{\infty}\tilde{f}_k(\mathrm{v})d\mathrm{v}; \quad (7)$$

for density perturbation corrected by Landau damping $\exp(|k\sigma_\mathrm{v}t|)$ term. Solution of eq. (7) can be expressed using symplectic ($det\,\mathbf{M}$=1) matrix: $X(t) = \mathbf{M}(0|t)\cdot X_o$:

$$\mathbf{M}(0|t) = \exp\left(\int_0^t\mathbf{D}(\tau)\,d\tau\right);\ \mathbf{D}(t)=\begin{bmatrix}0 & 1\\ -\omega_p^2(t) & 0\end{bmatrix}, \quad (8)$$

with either stable or growing solutions determined by the matrix's eigen values $\lambda_{1,2}:\det[\mathbf{M}-\lambda_{1,2}\cdot\mathbf{1}]=0;\ \lambda_1\lambda_2=\det\mathbf{M}=1\cdot$

Periodic system comprised of n bilaterally-symmetric cells, such as shown in Fig. 1, allows a well-defined parametric study of the PCI growth rates:

$$\mathbf{M}(0|nT)=\mathbf{M}_c^{\,n};\ \mathbf{M}_c\equiv\mathbf{M}(0|T)=\begin{bmatrix}m_{11} & m_{12}\\ m_{21} & m_{11}\end{bmatrix}; \quad (9)$$

$$\lambda_1 = m_{11}-\sqrt{m_{11}^{\,2}-1};\ \lambda_2=\lambda_1^{-1};$$

$|m_{11}|>1$ and signal evolution as:

$$X(mT)=\begin{bmatrix}\tilde{n}(mT)\\ \dot{\tilde{n}}(mT)\end{bmatrix}_o=\begin{bmatrix}g_+ & \mathrm{b}\cdot g_-\\ g_-/b & g_+\end{bmatrix}\tilde{n}_o+\begin{bmatrix}\mathrm{b}\cdot g_-\\ g_+\end{bmatrix}\dot{\tilde{n}}_o; \quad (10)$$

$$g_+=\frac{\lambda_1^{\,n}+\lambda_1^{-n}}{2};\ g_-\frac{\lambda_1^{\,n}-\lambda_1^{-n}}{2};\ \mathrm{b}=\frac{-m_{12}}{\sqrt{m_{11}^{\,2}-1}}.$$

Additional utility of periodic (cell) structure is dimensionless form of equations (3) and (7):

$$\frac{d^2\hat{a}}{d\hat{s}^2}-k_{sc}^{\,2}\hat{a}^{-1}-k_\beta^{\,2}\hat{a}^{-3}=0;$$
$$\frac{d^2}{d\hat{s}^2}\tilde{n}_k+2\frac{k_{sc}^2}{\hat{a}(\hat{s})^2}\cdot\tilde{n}_k=0;\ \hat{a}=\frac{a}{a_o};\ \hat{s}=\frac{s}{l}, \quad (11)$$

with well-defined dimensionless variables $\hat{a}\ge 1;\ \hat{s}\in\{-1,1\}$ and the system dynamics fully defined by two dimensionless parameters

$$k_{sc}=\sqrt{\frac{2}{\beta_o^{\,3}\gamma_o^{\,3}}\frac{I_o}{I_A}\frac{l^2}{a_o^{\,2}}};\ k_\beta=\frac{\varepsilon l}{a_o^{\,2}},$$

representing space charge and emittance effects. Figure 2 shows the growth rate per cell in such system evaluated by a semi-analytical code in Mathematica using 4-th order symplectic integrators [12] with canonical Hamiltonians:

$$\hat{h}=\frac{\hat{a'}^2}{2}-k_{sc}^2\ln\hat{a}+\frac{k_\beta^2}{2\hat{a}^2}=\frac{k_\beta^2}{2}=inv;\ \hat{h}(s)=\frac{\tilde{n}_k'^2}{2}+\frac{k_\beta^2}{\hat{a}^2(s)}\tilde{n}_k^{\,2}.$$

Growth rate with λ=4 can be reached with modest parameters of k_{sc}=3 and $k_\beta=10$. A "ridge" with maximum growth rates approximately following the line $k_\beta = 3\cdot(k_{sc}-1.2)$ with growth rate approximated by $\lambda\propto 1.25k_{sc}\approx 1.5+0.413\,k_\beta$. While λ does not contain any dependence on the wavelength of modulation ($k=2\pi/\lambda_m$), or corresponding frequency of modulation in the lab-frame ($\omega_m=\gamma_o\mathrm{v}_o k$), the PCI growth is inhibited both at high and low frequencies. At high frequencies the growth is limited by Landau damping (7) to

$$k_{\max}=\frac{\ln\lambda}{T\sigma_\mathrm{v}};\ \omega_{\max}=\frac{\mathrm{v}_o}{2l}\cdot\frac{\gamma_o^{\,3}}{\sigma_\gamma}\ln\lambda,$$

ISBN: 978-3-95450-218-9 ISSN: 2226-0374 doi:10.18429/JACoW-COOL2019-TUB02

where is σ_γ / γ_o is the relative energy spread in the beam, related to the velocity spread in the co-moving frame as: $\sigma_\gamma / \gamma_o = \sigma_v / c$. Analytical studies of modulation at low frequencies are rather elaborate (see [5,6]) and here we provide an approximate scaling at low frequencies of space charge coefficient $k_{sc} \to k_{sc} \cdot \left(k\langle a(s)\rangle\right), k\langle a(s)\rangle < 1$.

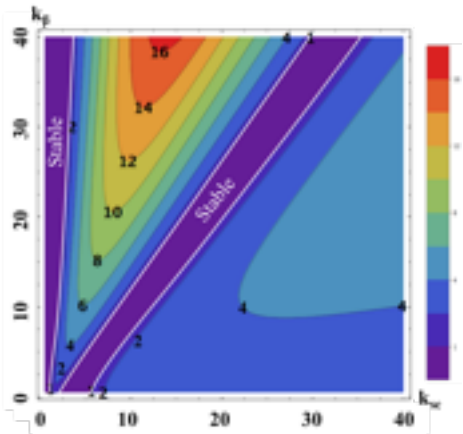

Figure 2: Contour plots of $\lambda = \max\left(\left|\mathrm{Re}\,\lambda_1\right|, \left|\mathrm{Re}\,\lambda_2\right|\right)$, the absolute value of maximum growth rate per cell. Purple area highlighted by white lines indicates areas of stable oscillation $\left|\lambda_{1,2}\right| = 1$. Oscillations, e.g. density modulations, grow exponentially outside these areas. Instability vanished at low cut-off frequency, when the "working point" k^*_{sc}, k_β reaches stable region.

Table 1: Parameters for PCI Simulations and Tests

Name	Experiment	Case 1	Case 2
PCA	LEBT	4 sec.	4 sec.
γ	3.443	28.5	275
E, MeV	1.76	14.56	140.5
l, m	Var, 1.5 - 3	1	10
a_0, *mm*	Min 0.3	0.2	0.1
I_0, A	1.75	100	250
ε_{norm}, *m*	$1\ 10^{-6}$	$8\ 10^{-6}$	$4\ 10^{-4}$
k_{sc}	Varies	3.56	3.76
k_β	Varies	7.02	14.55
λ_1, per cell	N/A	-4.06	-5.10
Energy spread	$1\ 10^{-4}$	$1\ 10^{-4}$	$1\ 10^{-4}$
f, THz	0.4	25	1,000

Numerical Studies

While both qualitative and semi-analytical studies reveal the nature of the PCI, modern particle-in-cell codes allow 3D investigations of PCI without any predetermined assumption. We used code SPACE [13-15] for accurate simulation of PCI in electron beam with constant beam energy propagating along the straight section with focusing solenoids. Two samples of such simulations. with parameters listed in Table 1, are shown in Fig. 3. In both cases density modulation grew by about 100-fold in a 4-cell system. Solenoid strengths were selected to provide the designed value of the beam envelope, a_o, at the waists located in the middle of the cells. Amplitude of density modulation, $\tilde{n}_k$, was then tracked as a function of the propagation distance. Figure 3 clearly demonstrate the nature of this instability: in a quarter of a plasma oscillation, the density modulation is transferred into the velocity modulation (at locations of the density minima). In return, in the next quarter of plasma oscillation, the velocity generates larger density modulation (but with an opposite sign). This cascade-type process of plasma oscillation is the origin of the name for this instability—PCI. Our 3D simulations also confirmed analytical expectation that PCI is a broad-band instability. They also clearly indicate, that as predicted by analytical studies, the PCI is diminishing both at low and high frequencies. In contrast to 1D analytical description, the 3D SPACE provides information about spatial distribution of the evolving density modulation. Figure 4 illustrates these additional features, including bending of the modulation wave-fronts.

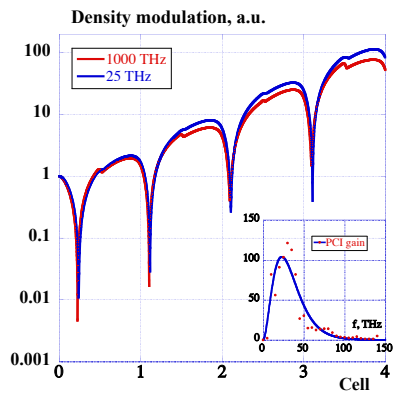

Figure 3: Evolution of density modulation amplitude in 4-cell PCI periodic lattice with parameters shown in Table 1: Blue line, *Case 1*, gain = 114 (b) Red line, *Case 2*, gain=75. The PCI gain spectrum for Case 1 in shown in a clip in the bottom-right corner: All simulations were performed by 3D code SPACE.

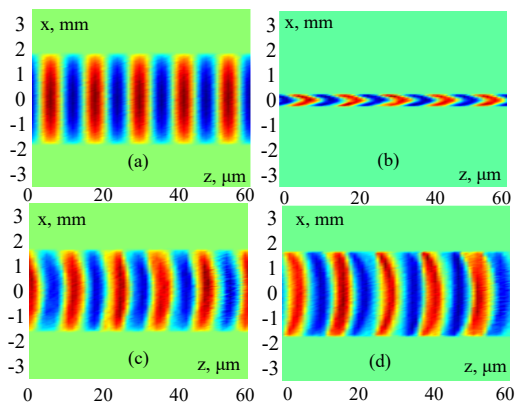

Figure 4: Evolution of the 3D profile of the e-beam density modulation at 25 THz (Case 1). Only normalised AC portion of the density is shown: red color corresponds to

ISBN: 978-3-95450-218-9 ISSN: 2226-0374 doi:10.18429/JACoW-COOL2019-TUB02

increased density and blue to reduced beam density. (a) – at the system entrance; (b) in the middle of the 2nd cell (beam waist); after the 3rd cell and (d) after 4-cell system.

Experimental Demonstration

Two room temperature RF 500 MHz cavities were used to correct the RF curvature and reducing energy spread in the bunch to 0.01% level. Six solenoids in the low energy beam transport (LEBT) were used for strong-focusing aperiodic lattice providing beam envelope shown in Fig. 5. To observed density modulation expected from very strong PCI we transformed our SRF linac and dipole beamline system in time-resolving system with sub-psec time resolution. We operated the linac at zero crossing with low accelerating voltage, V ~100-200 kV, to correlate particle's energy with the arriving time $E = E_o + eV\sin\omega_L t$. The 45º dipole and the profile monitor 4 served energy spectrometer: the measured energy distribution was a carbon copy for time profile of the bunch. We found that the best data quality was obtained at 100 kV setting and Fig. 6 shows few selected density profiles measured by our system as well as their spectra. We observed very large, up to ±50%, density modulation that can be seen both captured images or density profiles in Fig.6 (a) and (c). Fig. 6 (b) shows measured bunch spectra, which compare very well with simulation: a broadband PCI gain breaking at ~ 0.4 THz. We also calculated correlation length of the density modulation to be ~ 1-2psec, which is in good agreement with the spectral bandwidth $\Delta f/f \sim 1$.

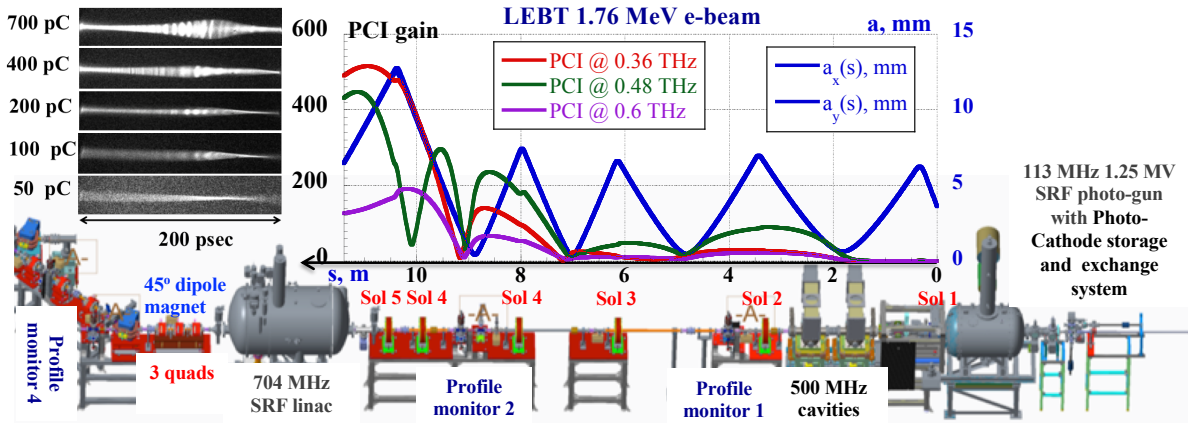

Figure 5: Layout of the CeC accelerator with the SRF electron gun, two bunching RF cavities, the LEBT line equipped with six solenoids and two profile monitors, the 13.1 MeV SRF linac and a 45º bending magnet beam line with beam profile monitor. The top graph shows simulated evolutions in the LEBT of the beam envelope (*a(s)*, blue line) and PCI gains at frequencies of 0.36 THz (red line), 0.48 THz (violet), and 0.6 THz (green). Simulations were done with for 1.75 MeV (γ=3.443), 0.7 nC, 0.4 nsec electron bunch with 1 μm slice normalized emittance and 0.01% slice RMS energy spread. Clip in the left-top corner shows time-resolve bunch profiles measured by the system for various charge in 400 psec electron bunches.

Because of the random nature of amplified shot noise, each bunch had its individual time structure and it was critical to measure structure of individual bunches in a single shot.

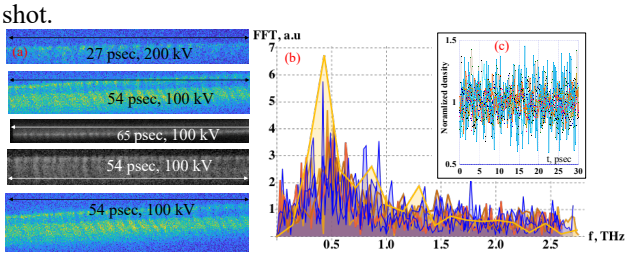

Figure 6: Measured (a) time profiles of the 1.75 MeV electron bunched bunch emerging from LEBT (charge per bunch from 0.45 nC to 0.7 nC). (b) Shows seven overlapping spectra of the bunch density modulation and PCI spectrum simulated by SPACE (slightly elevated yellow line). (c) Clip show 30-psec cut-off of seven measured density modulation.

In conclusion, we would like to announce discovery of novel microbunching instability occurring in charged particle beams propagating along a straight trajectory—Plasma-Cascade Instability. PCI can be both a menace and a blessing—it can strongly intensify longitudinal microbunching originating from the beam's shot noise, and even saturate it. For example, PCI can serve as a broadband amplifier in the CeC scheme [5,6] or used for boosting power of THz and PHz radiation.

Authors would like to thank all our colleagues from BNL contributed to the CeC project: Toby Miller high precision beam profile monitor diagnostics, Thomas. Hayes, Geetha Narayan and Freddy Severino for their help with using CeC SRF linac for time resolved studies, Dr. Peter Thieberger for pointing on important 3D aspects of the problem, and Dr. Thomas Roser for unrelenting support of this research. First author also would like to thank Prof. Pietro Musumeci (UCLA), who mentioned during our discussion about energy conservation in longitudinal plasma oscillations, that modulation of the transverse beam size

ISBN: 978-3-95450-218-9 ISSN: 2226-0374 doi:10.18429/JACoW-COOL2019-TUB02

can violate this perception. His notion was one of the initial signals that modulation of the transverse beam size can cause an instability. This research was supported by and NSF grant PHY-1415252, DOE NP office grant DE- FOA-0000632, and by Brookhaven Science Associates, LLC under Contract No. DEAC0298CH10886 with the U.S. Department of Energy.

REFERENCES

[1] V.N. Litvinenko, Y.S. Derbenev, "Coherent Electron Cooling", *Phys. Rev. Lett.* **102**, 15801, 2009.
[2] D. Ratner, "Microbunched Electron Cooling for High-Energy Hadron Beams", *Phys . Rev. Lett*. **111** 084802, 2013.
[3] V.N. Litvinenko, Y.S. Derbenev, in *Proc. of 29th International Free Electron Laser Conference* (FEL'07), Novosibirsk, Russia, 2007, p. 268.
[4] V.N. Litvinenko, "Advances in Coherent Electron Cooling", In *Proc. of COOL 2013 workshop*, June 2013, Mürren, Switzerland, p. 175, ISBN 978-3-95450-140-3.
[5] V.N. Litvinenko, G. Wang, D. Kayran, Y. Jing, J. Ma, I. Pinayev, "Plasma-Cascade micro-bunching Amplifier and Coherent electron Cooling of a Hadron Beams", arXiv:1802.08677, February 2018.
[6] V.N. Litvinenko, G. Wang, Y. Jing, D. Kayran, J. Ma, I. Petrushina, I. Pinayev, K. Shih, Plasma-Cascade Instability- theory, simulations and experiment, 2019, arXiv:1902.10846.
[7] D.R. Nicholson, Introduction in Plasma Theory, John Wiley & Sons, 1983.
[8] L.D. Landau, E.M. Lifshitz, Classical Mechanics, Elsevier Science, 1976, ISBN-10 050628960.
[9] I.M. Kapchinsky and V.V. Vladimirsky, in *Proc. of Int. Conf. on High-Energy Accelerators and Instrumentation,* CERN, 1959, p. 274.
[10] M. Reiser, Theory and design of charged particle beams, John Wiley & Sons, 2008.
[11] A. A. Vlasov, "On Vibration Properties of Electron Gas", *J. Exp. Theor. Phys.* (in Russian). 8 (3) 1938, 291.
[12] G.Wang, M.Blaskiewicz, *Phys Rev E*, volume 78, 026413, 2008.
[12] E. Forest, "Forth-order symplectic integrator", SLAG-PUB-5071, LBL-27662, August 1989.
[13] X. Wang, R. Samulyak, J. Jiao, K. Yu, "Adaptive Particle-in-Cloud method for optimal solutions to Vlasov-Poisson equation", *J. Comput. Phys.,* 316, pp. 682-699, 2016.
[14] K. Yu and V. Samulyak, "SPACE Code for Beam-Plasma Interaction", in *Proc. 6th Int. Particle Accelerator Conf. (IPAC'15)*, Richmond, VA, USA, May 2015, pp. 728-730. doi:10.18429/JACoW-IPAC2015-MOPMN012
[15] V.N. Litvinenko, Z. Altinbas, R. Anderson, S. Belomestnykh, C. Boulware *et al*., "Commissioning of FEL-based Coherent electron Cooling system", In *Proc. of 38th Int. Free Electron Laser Conf.* (FEL'17), Santa Fe, NM, USA, August 20-25, 2017, p. 132.

ISBN: 978-3-95450-218-9 ISSN: 2226-0374 doi:10.18429/JACoW-COOL2019-WEX03

ELENA COMMISSIONING

D. Gamba*
CERN, Espl. des Particules 1, 1211 Meyrin, Switzerland

Abstract

The Extra Low Energy Antiproton storage ring (ELENA) is an upgrade project at the CERN Antiproton Decelerator (AD). ELENA will further decelerate the 5.3 MeV antiprotons coming from the AD down to 100 keV and allow the experiments typically operating traps to increase the capture efficiency. ELENA features electron cooling for emittance control during the deceleration and therefore preserve the beam intensity and to generate bright bunches extracted towards the experiments. The ring has been completed with the installation of the electron cooler at the beginning of 2018. The electron cooler is meant to operate at an electron energy of 355 eV and 54 eV, corresponding to a pbar momentum of 35 MeV/c and 13.7 MeV/c. First observations of cooling have been observed at both energies, and decelerated ion beams with characteristics close to the design values have been obtained before the start of CERN Long Shutdown 2 (LS2). The latest results of ELENA commissioning will be presented, together with an overview of the project and status and plans.

INTRODUCTION

The antimatter experiments at CERN presently take 5.3 MeV kinetic energy antiprotons beams from the AD decelerator. The recent installation of ELENA and its ability to further decelerate the antiprotons down to 100 keV will be a major breakthrough for the antimatter physics research, as it will allow to trap and study at least one order of magnitude more antiprotons per shot than what has typically been achieved before. A more detailed report on the ELENA Commissioning have been recently presented and described in [1]. In the following, only a short summary of [1] is reported.

ELENA OVERVIEW

The ELENA ring has a hexagonal shape and its circumference is about 30 m. Figure 1 shows a picture of the ring after its complete installation in 2018, with its main components highlighted.

For machine commissioning purposes, a standalone ion source able to provide 100 keV H^- or proton beams is installed next to the ELENA ring, between the ELENA injection and extraction beamlines shown in Fig. 2. An electrostatic ion switch installed at the intersection between injection and extraction lines allows for injecting H^- and proton beams in either directions in the ring. Unfortunately, the insulation transformer of the ion source High Voltage (HV) cabinet had several problems, and it eventually failed completely during the 2018 run, preventing further use of ion beams. Moreover, observed shot-to-shot H^- intensity variation limited the amount of studies that could be done while the source was operational. Despite several attempt to solve those problems, most of the ELENA commissioning had to be performed with limited pbar beam-time dedicated by AD to ELENA.

The typical pbar decelerating cycle is depicted in Fig. 3. The beam is injected as a single bunch from the AD at 100 MeV/c in a waiting RF bucket in ELENA. A first deceleration step brings the beam down to 35 MeV/c where the beam is debunched and the electron cooler is used to reduce the beam emittances to compensate for the adiabatic emittance blow-up (about a factor 3) induced by the deceleration. After being re-bunched, the beam is further decelerate down to 13.7 MeV/c where it is again debunched and cooled.

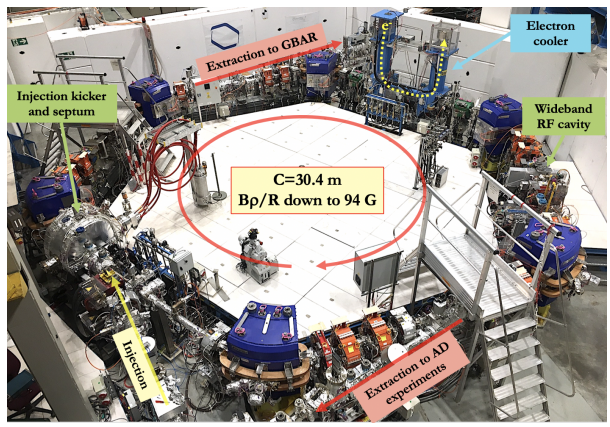

Figure 1: Picture of the ELENA Ring after installation. The main components, including the electron cooler, are highlighted.

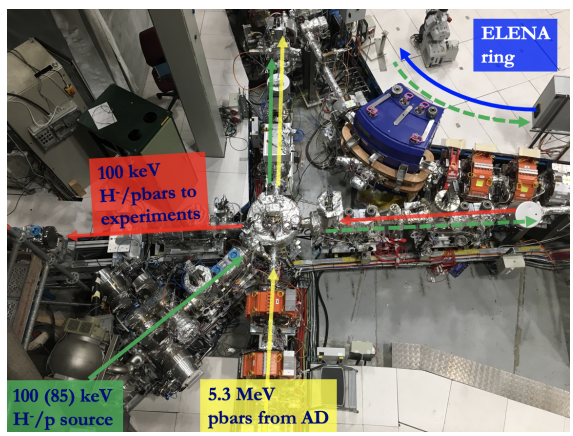

Figure 2: Injection and extraction lines toward main experiments. The ion source is partially visible in the bottom left corner. The possible beam paths are highlighted.

* davide.gamba@cern.ch

ISBN: 978-3-95450-218-9 ISSN: 2226-0374 doi:10.18429/JACoW-COOL2019-WEX03

The beam is finally re-bunched and extracted toward the experiments. By design, the final re-bunching is performed at harmonic four and the electron cooler is kept ON for "bunched beam cooling" in order to obtain short bunches with sufficiently low momentum spread.

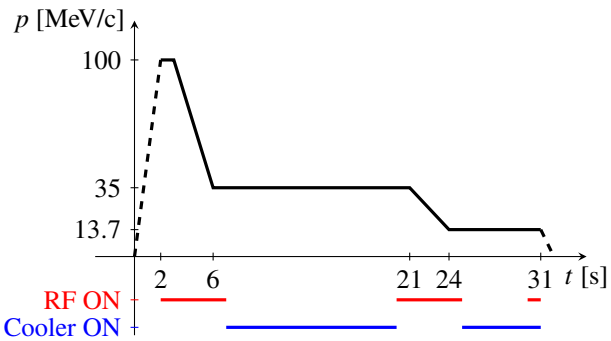

Figure 3: Typical ELENA pbar cycle. A solid black line indicates the period with circulating beam. RF and electron cooler are ON during the periods highlighted in red and blue, respectively. The time scale is an approximation of what was being used by the end of 2018.

ELECTRON COOLER SETUP

The electron cooler was installed in the ELENA ring at the beginning of 2018, and it was made fully operational by July 2018. Due to the limited beam time availability, only the minimum necessary studies on cooling efficiency were performed with the main purpose to commission a full decelerating cycle. The electron beam velocity was adjusted for each plateau to match the circulating beam velocity by looking at longitudinal Schottky signal, which was taken from a single Beam Position Monitor (BPM) sum signal. Alignment and overlap of the electron and ion beams were empirically adjusted with orbit bumps on the circulating beam while minimising the final emittance measured with the scraper. After all adjustments, the effect of cooling was clearly visible in both the transverse (e. g. Fig. 4) and longitudinal (e. g. Fig. 5) planes. The measured longitudinal cooling time of the order of a second, as well as the obtained beam size reduction are compatible with expectations, despite more studies are needed to verify the actual cooling dynamics.

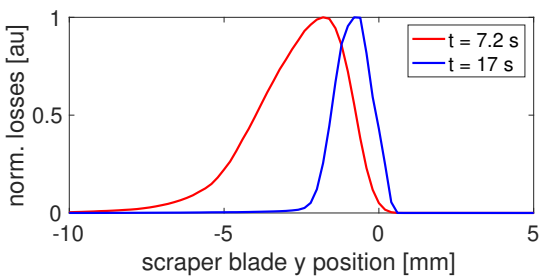

Figure 4: Normalised beam losses as a function of the vertical scraper position before (red) and after (blue) cooling. The width of the signal corresponds to half the beam size.

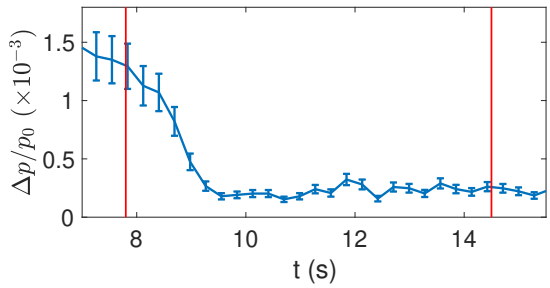

Figure 5: RMS momentum spread obtained from the longitudinal Schottky signal during the intermediate plateau with e-cooling. The start times of the scraper measurements in Fig. 4 are indicated in red.

Table 1: Design [4] and Obtained [5] Beam Parameters Before LS2 for the pbar Cycle

Parameter	Design	Obtained
Q_x/Q_y	≈ 2.3/≈ 1.3	2.46/1.41
Cycle duration [s]	20	30
Injected intensity [pbars]	3e7	3.7e7
Efficiency [%]	60	50
Extracted bunches [#]	4	4
Bunch population [pbars]	0.45e7	0.43e7
$\Delta p/p_0$	5e-4	7e-4
Bunch length [ns]	75	85
ϵ_{phys} x/y [μm]	1.2/0.75	4.1/1.5

Due to several failure and instability issues of the H^- source, very limited attempts of cooling H^- has been performed. However, during the limited experience, no evident degradation of the H^- lifetime due to the possible interaction with cooler electrons have been observed.

More details on the ELENA electron cooler commissioning can be found in [3].

OBTAINED BEAM PERFORMANCES

Despite the little beam time availability and the issues with the ion source, and thanks to several empirical optimisations, by the end of 2018 it was possible to achieve beam parameters for the bunches before extraction which are reasonably close to the design values. Both achieved and design values are summarised in Table 1. Note that most measured values have a rather high uncertainty as very little statistics could be accumulated and not all diagnostics could be fully calibrated.

Figure 6 shows the typical beam transmission obtained along the deceleration cycle toward the end of the 2018 run. Note that the blue trace is affected by the bunch intensity but also by bunch length and number of bunches. The small signal during the second ramp is due to the use of the fourth RF harmonic ($h = 4$) instead of $h = 1$ as for the first ramp.

ISBN: 978-3-95450-218-9 ISSN: 2226-0374 doi:10.18429/JACoW-COOL2019-WEX03

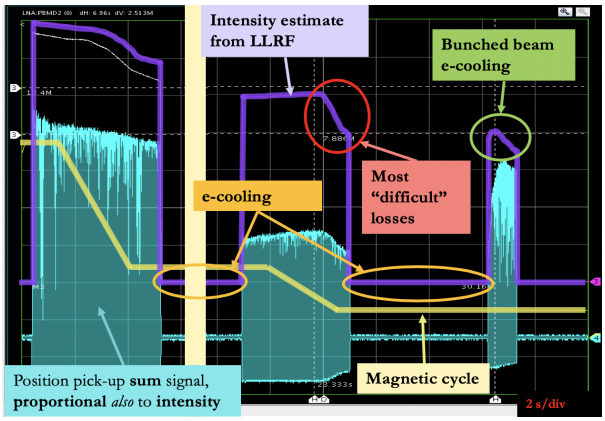

Figure 6: Beam intensity (purple) and magnetic cycle (yellow) as a function of time. The blue trace is the peak line density of the beam seen by one BPM.

Also during the final bunched beam cooling the RF was set to $h = 4$ and one can see the increase of the line density corresponding to the shortening of the bunches due to bunched beam cooling. The use of $h = 4$ during the second ramp was not the baseline option, but it seemed to have a beneficial impact on transmission, even though considerable losses are still present toward the end of this ramp. Those losses were the most difficult to reduce for reasons which are still unclear, and will require further measurements and studies during the next run.

CONCLUSIONS

2018 was a very fruitful year for ELENA commissioning. The finally obtained beam parameters at extraction were close to the design values, despite the limited available beam time. Transverse emittance reduction up to about 80 % was achieved even at the lowest plateau at 100 keV [2]. The final machine settings were obtained after several steps of systematic and empirical tuning of the available machine knobs, which surely left room for improvements.

During the present CERN Long Shutdown 2 (LS2) the main activity is the installation and commissioning with H^- of all electrostatic transfer lines toward the "old" AD experimental zone. Figure 7 shows a layout of the experimental areas next to the ELENA ring with all transfer lines being installed. Moreover, several consolidation works are also ongoing to ensure a restart of operation with H^- in mid 2020 and with pbars in mid 2021.

More details on ELENA and its electron cooler commissioning can be found in [1, 3].

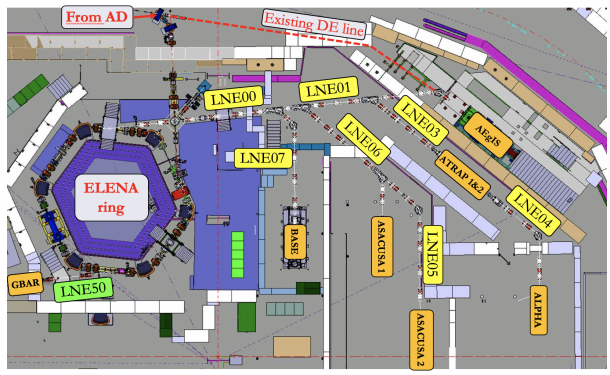

Figure 7: Layout of ELENA extraction lines. The lines being built during LS2 are highlighted in yellow.

REFERENCES

[1] D. Gamba *et al.*, "ELENACommissioning", in *Proc. NA-PAC'18*, Lansing (MI), USA, Sep 2019, paper WEYBB1.

[2] J.R. Hunt *et al.*, "Emittance Evolution of Low Energy Antiproton Beams in the Presence of Deceleration and Cooling", in *Proc. IPAC'19*, Melbourne, Australia, May 2019, paper WEPGW090.

[3] L. V. Joergensen *et al.*, "Commissioning the ELENA Electron Cooler", in *Proc. COOL'19*, Novosibirsk, Russia, Sep 2019, paper TUPS12, this proceedings.

[4] V. Chohan (ed.) *et al.*, "Extra Low ENergy Antiproton (ELENA) ring and its Transfer Lines: Design Report", CERN, Geneva, Switzerland, Rep. CERN-2014-002, Jan. 2014.

[5] *Extended ECC meeting*, 7 March 2019, `https://indico.cern.ch/event/803767/`.

ISBN: 978-3-95450-218-9 ISSN: 2226-0374 doi:10.18429/JACoW-COOL2019-THX01

THE STATUS OF THE ELECTRON COOLING SYSTEM FOR THE NICA COLLIDER *

M.B. Bryzgunov, A.V. Bubley, A.D. Goncharov, A.P. Denisov, N.C. Kremnev, V.V. Parkhomchuk, V.M. Panasuk, A.A. Putmakov, V.B. Reva, S.V. Shiyankov, Budker INP, Novosibirsk, Russia

Abstract

The new electron cooling system is being designed to cool two heavy ion beams propagating in opposite directions at a distance of about 30 cm from each other. Engineering solutions for its basic elements are presented. The measurements of the magnetic system of the electron cooler and the influence of the adjacent solenoids in the cooling section on the resulting magnetic field are described. The potential opportunities to improve parameters of experiments with ion beams using the electron cooling system are discussed

INTRODUCTION

The history of the development of electron cooling began at the Institute of Nuclear Physics (Novosibirsk) just after the first successful experiments conducted there with electron-electron and electron-positron colliding beams. Radiation cooling plays a decisive role in achieving high luminosity in electron and electron-positron colliders. Cooling based on ionization losses in the matter was suggested earlier, but the interaction with the target nuclei hampered application of this method because it makes the beam lifetime too short.

The idea of using electron cooling, proposed by G.I. Budker in 1965 [1], consisted in switching from cooling with a stationary target to using a pure beam of electrons (without nuclei). The electron cooling progress began in 1967 with theoretical studies [2] and the development of an electron beam facility [3] (Fig. 1). That project was to verify the electron cooling concept. The electrons travel with the same average velocity as the proton beam does. Of course, the electron beam density is much smaller than the electron density in condensed matter, but in this case electrons are traveling together with the proton beam and the interaction efficiency between the two beams depends only on the spread of relative velocities of the protons and the electrons. The drift motion of the electron beam because of space charge repulsion is suppressed using a high magnetic field B along the electron trajectory. A strong longitudinal magnet field in the cooling section is used for suppression of ion-electron recombination. The main feature of cooling by magnetized electron beams is the possibility of suppression of the ion electron recombination due to high transverse temperature of electrons without losses in the cooling efficiency [4].

Since 1991 BINP have produced a lot of coolers for different laboratories: GSI SIS-18, IMP CSRm, CSRe, and CERN LEIR. The cooler with a highest voltage of 2 MV was designed for Forschungszentrum Julich (KFA) GmbH. The experience of designing the COSY cooler was used as a base for the 2.5 MV cooler for the NICA ion*ion collider at JINR (DUBNA). Figure 2 shows the origination of the NICA cooler.

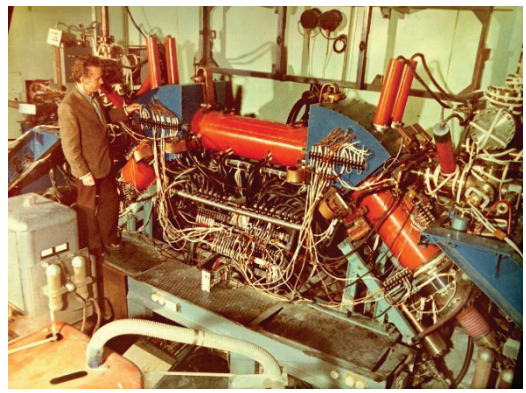

Figure 1: First electron cooling installation in NAP-M storage ring (1974).

The cooler will be placed in a special building near the beam straight section of the NICA ring. The vertical distance between the ion beams is only 32 cm, and the design of two solenoids with such a small gap is a very complicated task. For testing the design, a prototype 1 m long of the cooling section was created (Fig. 3).

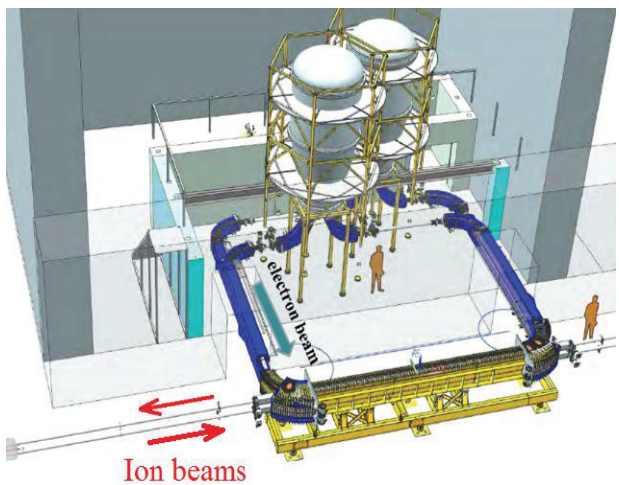

Figure 2: 3D design view of 2.5 MV NICA cooler.

The maximum magnetic field in the cooling section is 0.2 T. The solenoids consist of adjustable coils for straightening the lines of magnet field by rotating coils. This procedure will involve a specially designed compass with a laser beam reflecting from the compass mirror for precise angle measurement.

The penetration of the transverse magnetic field from the upper solenoid to the lower solenoid does not exceed 0.01, and thus the procedure of magnetic field measure-

ISBN: 978-3-95450-218-9 ISSN: 2226-0374 doi:10.18429/JACoW-COOL2019-THX01

ment should ensure suppress ion of the mutual influence of the two solenoids.

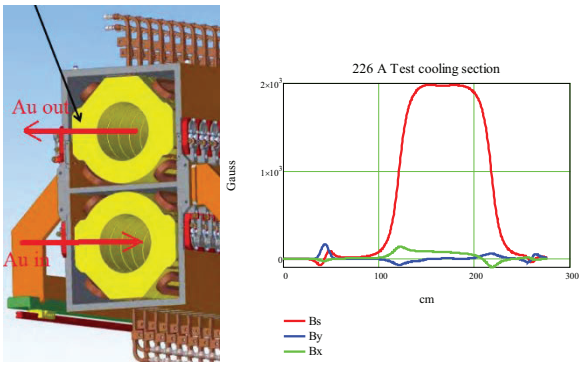

Figure 3: Design of solenoids for cooling section and results of magnetic field measurement along center line of solenoid.

The maximum magnetic field in the cooling section is 0.2 T. The direction of the lines of the magnetic field of solenoid will be corrected by gentle inclination or rotation of coils in the vertical axis. Figure 4 shows the change in the magnetic fields when one coil is tilted by 4 mm.

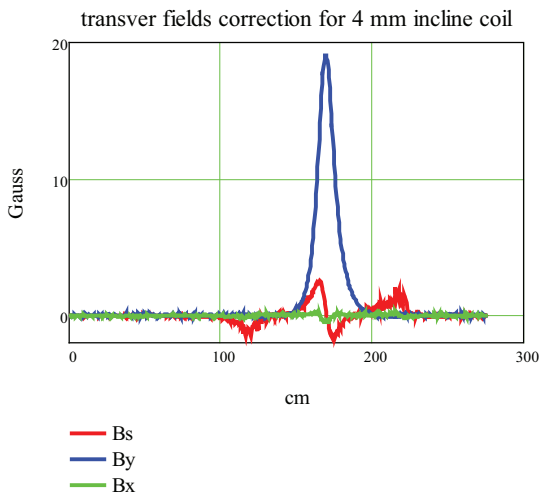

Figure 4: Change in vertical component of solenoid after tilting single coils of solenoid by 4 mm.

From Fig. 4 it is clear that inclination of individual coils by 4 mm corrects the angle of line by $\Delta B\perp/B\ 10^{-3}$. For the accuracy of the magnetic line angle to be better than 10^{-5}, the shifting accuracy should better than 0.04 mm.

DESIGN OF NICA COOLER

The main task for the NICA cooler will be to obtain high luminosity in the ion*ion collision mode. Table 1 shows the main parameters of the NICA cooler. The most serious limitation was from the restriction to the total power consumption. It means that the maximum amount of copper is limited by distance of 32 cm between the ions of orbit.

Table 1: Main Parameters of NICA Cooler

Parameter	Value
Energy range	0.2 – 2.5 MeV
Number of the cooling sections	2 for both beams
Stability of energy (ΔU/U)	$\leq 10^{-4}$
Electron current	0.1 – 1 A
Diameter of electron beam in the cooling section	5 – 20 mm
Length of cooling section	6 m
Bending radius in the transport channel	1 m
Magnetiv fiels in the cooling section	0.5 – 2 kG
Vacuum pressure in the cooling section	10^{-11} mbar
Height of the beam lines	1500/1820 mm
Total power consumption	500 – 700 kW

Figure 5 shows the plane of the cooling section more than 6 m long.

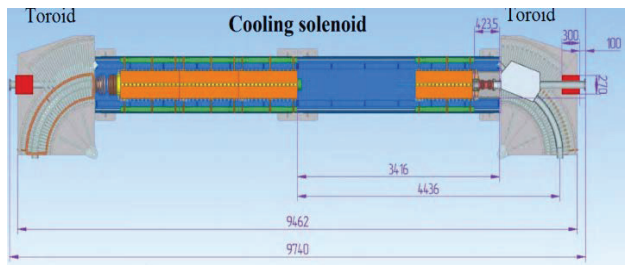

Figure 5: Cooling section sketch.

The toroid part is for separation of the ion beam orbits and turning the electron beam through 90 degrees for sending the electron beam by the transport beamline to the acceleration tube in the vertical vessel. The toroid is the most complicated place, where two beamlines (for electrons and ions) meet together. In addition, the ion corrector should be located in this place, as well as vacuum pumps. The coils for the bending field are placed on the toroid side. In addition to all other problems, the distance between the two electron beams should be 32 cm (Fig. 6).

Most of the problems can be solved via decreasing the magnetic field in the toroid. However, there is no such thing as a free lunch. The cooling section (6 m) is shorter than the straight section along the ion orbit (6.84 m). The distance of 0.84 m is used for the matching section.

ISBN: 978-3-95450-218-9 ISSN: 2226-0374 doi:10.18429/JACoW-COOL2019-THX01

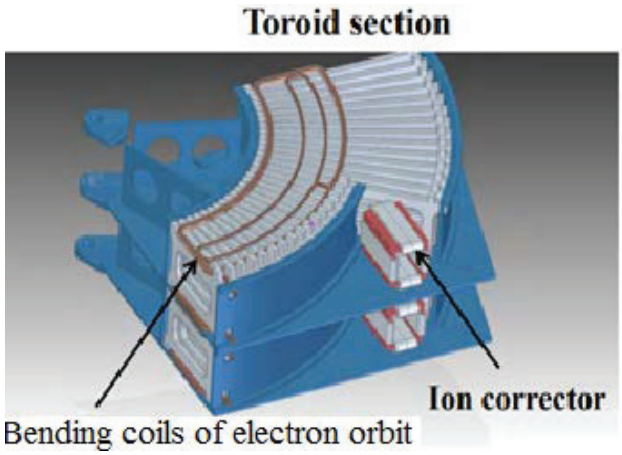

Figure 6: Toroid for bending electron beams.

ELECTRON COOLING

The experience of cooling of high-charge ions at the existing coolers shows very high brightness of ion beam after electron cooling. From the very beginning, there was a problem of ion losses from the ion beam because of recombination. The experiment at the NAP and ESR [4,5] demonstrated that at a strong magnetic field and high "Larmor" temperature, the recombination rate is less than the cooling rate. In the NICA case, the cooling time can be estimated as follows:

$$\tau_{cool} = \frac{\gamma(\frac{V_i}{c})^3}{4r_e r_i n_e \eta c ln(\frac{\rho_{max}+\rho L}{\rho L})}, \quad (1)$$

where $\rho_{max} = \Theta_i dl_c$, $\Theta_i = \sqrt{\varepsilon/\beta_x}V_i$ is the velocity of ion in the beam system, $\rho L = (m*c*VL)/e*Bs$ is the radius of the Larmor rotation, γ is the relativistic factor, βx is the beta function in the cooler, ne is the electron beam density in the beam system (moving), and η is the ion orbit fraction occupied by the cooler. For calculation of the recombination we used the well known equation [6]

$$\alpha_{REC} = 1.92\times10^{-13}\ \mathrm{cm^3\ s^{-1}} \times \frac{q^2}{\sqrt{kT_{e\perp}}} \times \left\{\ln\left(\frac{5.66q}{\sqrt{kT_{e\perp}}}\right) + 0.196\left(\frac{kT_{e\perp}}{q^2}\right)^{1/3}\right\} \quad (2)$$

,

Where $T_{e\perp} = me*VL^2/2$ is the temperature of the Larmor rotation in eV. The recombination lifetime is

$$\tau_{rec} = \gamma/(\alpha_{rec}*ne*\eta) \quad (3)$$

For the 4 GeV/u NICA cooling, results for gold ions (+79Au197) are shown in Table 2.

Table 2: Results for Gold Ions

Te, eV	τcool, sec	τrec, sec	τrec/τcool
0.1	16	76	4.7
1	19	182	14
10	25	1000	42
100	35	4200	120
100	55	17000	320

It is easy to see from this calculation that with increasing energy of the Larmor rotation, the recombination decreases very fast as compared with the cooling rate. It is one of main advantages of "magnetized cooling".

HIGH VOLTAGE ACCELERATION

The electron beam is generated inside the vessel filled with SF6 (elgas) under a pressure of up to 10 bar, Fig. 7a.

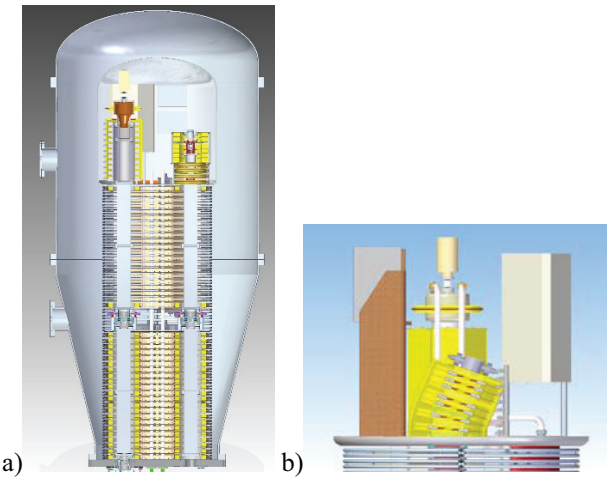
a) b)
Figure 7: a) Vessel for acceleration section and acceleration tube. B) electron gun with bending of electron beams for saving cathode.

The bending part near the electron gun protected the cathode from bombardment by the secondary ions from ionization of the residual gas in the acceleration tube (Fig. 7b). A few prototype acceleration sections were tested with air at a voltage of up to 20 kV. The corona current was measured from 10 kV, but training with air increased the voltage for sparking. The sections along the columns are powered by a cascade transformer consisting of 42 rings coupled by insulated coils, Fig. 8. The operation frequency is 20 kHz and the power exceeds 30 kW.


Figure 8: Cascade transformer on test bench for solenoid component after tilting individual coils of solenoid by 4 mm.

ISBN: 978-3-95450-218-9 ISSN: 2226-0374 doi:10.18429/JACoW-COOL2019-THX01

Figure 9: Vessel for high voltage equipment produced in Novosibirsk

Figure 9 show vessel after production at Novosibirsk factory.

THE ELECTRON COOLING AT NICA

The interaction between the cooler and NICA is subject of many articles and discussion. This article gives no space for discussion, but it will be interesting to see any results on these questions. The dynamics of emittance at NICA were calculated in a simple model including IBS and electron cooling. For calculation of the influence of the space charge, the IBS was intensified when the Laslet tune got closer to a value of 0.1. It is clear that this model is too simple, but a more skilful model has not yielded calculation results so far. Any way, it would be interesting to look at the results of the very simple model, shown in Fig. 10.

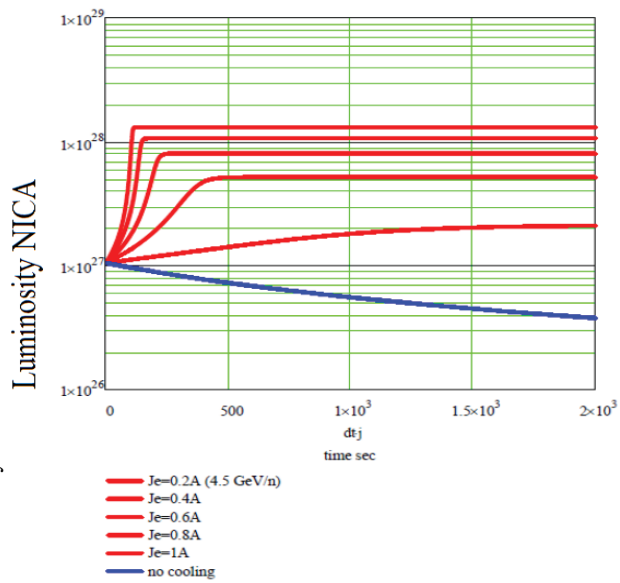

Figure 10: Time variation of luminosity for electron current varying from 0 to 1 A.

As shown in Fig. 10, an electron current of just over 0.2 A will increase the luminosity. The development of the simulation code will continue at BINP and JINR, but we will be able to verify the results after commissioning of NICA with the cooler.

CONCLUSION

The high-voltage cooler with the magnetized electron beam will help to obtain high luminosity of the NICA collider. This collider is one of a few Mega-science projects in Russia, and its commissioning is very important for future acceleration science.

ACKNOWLEDGMENT

The authors are only a small part of the large collective of BINP working on problems of the design and construction of coolers. The authors are thankful to A. Batrakov, O. Belikov, E. Bekhtenev, I. Gusev, V. Chekavinsky, S. Fadeev, M. Fedotov D. Senkov and many other colleges who help to create the high voltage cooler for NICA.

REFERENCES

[1] G.I Budker, “Efficient method for damping of particle oscillations in proton and antiproton storage ring”, *Atomnaya Energiya* 22 p.346-348, 1967.

[2] V.V. Parkhomchuk, A. N. Skrinskii, “Electron cooling: 35 years of development”, *Phys. Usp.*, vol. 43, no. 5, p. 433–452, 2000. doi: 10.1070/PU2000v043n05ABEH000741

[3] V. V. Parkhomchuk, “New insights in the theory of electron cooling”, *Nucl. Instr. and Meth. A*, vol. 441, Iss. 1-2, p. 9-17, Febr. 2000. doi: 10.1016/S0168-9002(99)01100-6

[4] N. S. Dikanskii *et al.*, “Development of techniques for the cooling of ions”, *Phys. Usp.*, vol. 61, p. 424–434, 2018. doi: 10.3367/UFNe.2018.01.038297

[5] P. Beller, K. Becket, *et al.,* “Observation of a reduction of recombination between ions and electrons”, *Nuclear Instruments and Methods in Physics Research* Section A, Volume 532, 2004, p. 427-432.

[6] H. Beyer, *et al. Part. Accel.* 24 (1989)1989.

ISBN: 978-3-95450-218-9 ISSN: 2226-0374 doi:10.18429/JACoW-COOL2019-THX02

ELECTRON COOLING IN THE NICA PROJECT: STATUS AND PROBLEMS

I. N. Meshkov†,[1], A. V. Philippov, E. M. Syresin, Joint Institute for Nuclear Research, Dubna, Russia
N. V. Mityanina[2], Budker Institute of Nuclear Physics, Novosibirsk, Russia
[1]also at Saint Petersburg State University, Saint Petersburg, Russia
[2]also at Novosibirsk State University, Novosibirsk, Russia

Abstract

The Nuclotron-based Ion Collider fAcility (NICA) project at the Joint Institute for Nuclear Research (JINR, Dubna, Russia), reached the phase of mounting and commissioning of the accelerator complex elements. The first stage of the project is "The Baryonic Matter at Nuclotron" (BM@N), fixed target experiment. It requires operation of the heavy ion synchrotron Booster, where electron cooler is used for formation of ion beam of a high intensity. One of limitation of intensity of partially ionized heavy ion beams is recombination with cooling electrons. This process is planned to be studied on the Booster, which is under mounting presently. The experiments at NICA collider with the heavy ion beams is the second stage of the project. High energy electron cooler that is under fabrication at BINP is a key tool for NICA collider allowing to reach the project luminosity in all ion energy range of $\sqrt{s_{NN}} = 4 \div 11$ GeV/u. Recombination of bare nuclei of heavy ions in the electron cooler leads to significant beam losses that shorten ion life time and may generate considerable background in NICA detector (MultiPurpose Detector — MPD). The third stage is spin physics studies in collisions of polarized protons ($\sqrt{s_{NN}} = 27$ GeV) and deuterons. This stage expect the use of the Spin Physics Detector — SPD. The report presents status of the NICA project development and discusses the problems described above.

INTRODUCTION: THE NICA PROJECT AT JINR

The NICA project aims to design, construction and commissioning at JINR a modern accelerator complex based on existing synchrotron Nuclotron equipped with two detectors: MPD and SPD. Experimental studies planned at NICA will be dedicated to search of the mixed phase of baryonic matter and the nature of nucleon/particle spin. Briefly speaking, we intend to study the Universe as it was 13.799 ± 0.021 billion years ago [1] and of the order of $10 \div 100$ μs after Big Bang, the first goal. The second goal is to understand the nature of particle spin, so called "spin puzzle".

The project development has three stages as described in the Abstract and in the [2]. The scheme below (Fig. 1) demonstrates all main elements of the NICA.

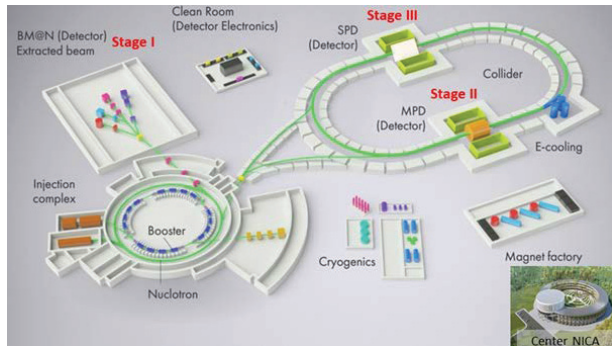

Figure 1: Scheme of the NICA facility.

NICA STAGE I: EXPERIMENT "THE BARYONIC MATTER AT NUCLOTRON"

For the full configuration of the Stage I we need [2] the following elements and accelerators.

1. Injector: Cryogenic ion source KRION + Heavy ion Linear Accelerator (HILAC) + Beam transfer line (BTL) from HILAC to the Booster;
2. KRION is in the stage of "working prototype" that will be used for generation of heavy ion beam. The main goal is generation of $^{197}Au^{31+}$. The HILAC was commissioned in 2016. Construction of the BTL is close to completion and will be tested with the ion beam this year;
3. Booster — superconducting (SC) synchrotron is under mounting (Fig. 2, 3). Its electron cooler was constructed by BINP and is under commissioning in the working position on the Booster. First test of the SC focusing system of the Booster is planned at the end of this year, ion beam injection into Booster is expected in May 2020;
4. BTL Booster-Nuclotron (under manufacturing at BINP, to be finally delivered to JINR in July 2020, commissioning — October 2020);
5. Upgrade of BTL Nuclotron-BM@N for transportation of ions accelerated in Nuclotron and extracted by slow extraction system. The upgrade includes improvement of vacuum condition in the channel and development of power supplies for the channel magnets.

The first run of BM@N experiment with heavy ions at maximum energy of Nuclotron is scheduled for November 2020.

† meshkov@jinr.ru.

ISBN: 978-3-95450-218-9 ISSN: 2226-0374 doi:10.18429/JACoW-COOL2019-THX02

Figure 2: SC magnets of the Booster in the yoke of the dismounted Synchrophasotron.

Figure 3: Power supplies of the Booster magnets mounted on the top the yoke.

ELECTRON COOLING APPLICATION TO THE NICA BOOSTER

Injection of ions into Booster will be fulfilled by one of three schemes: single turn or multiturn injection and multicycle injection at the ion energy of 3.2 MeV/u. All the schemes will use electron cooling (electron energy of 1.765 keV) The electron cooler of the Booster is mounted already in working position and commissioned with electron beam [3].

The basic type of ions to be injected into Booster is $^{197}Au^{31+}$. The ion charge state is chosen by criterion of minimum recombination rate: this state has 48 electrons, which completely fill the subshells up to $[Kr]5s^2 4d^{10}$ [4]. As result, the recombination coefficient for this ion is equal to $\alpha = 10^{-7}$ cm^3·s^{-1}. At Booster electron cooler parameters and electron beam current of 0.2 A it gives the ion lifetime of 13.3 s, when vacuum lifetime at injection energy and vacuum of 10^{-11} Torr is 4.4 s.

Such a choice provides also the minimum recombination rate at the ion energy of 50 MeV/u (electron energy of 27.233 keV) during acceleration in the Booster when the plateau of 1 s duration is made for electron cooling of ions. The recombination lifetime on the plateau differs from it on the injection energy by the value of Lorenz factor squared and at electron beam current of 1 A is 11.1 s.

Note the application of $^{197}Au^{30+}$ would reduce recombination time by 5 ÷ 10 times [4].

STAGE II: SEARCH FOR THE MIXED PHASE AND NEW PHYSICS IN HEAVY ION COLLISIONS AT NICA COLLIDER

At this stage the most promising part of the NICA project program will be implemented. Three new elements of the NICA will have to be constructed — two rings SC collider, BTL from Nuclotron to Collider (BTL NC) and MPD.

BTL NC was designed in cooperation with the company SigmaPhi and is under manufacturing presently. Beginning of delivery of the BTL elements is planned for the end of the year. Mounting and commissioning of the BTL of 340.5 m length will be fulfilled in 2020.

The Collider mounting will be started September 2021 and first beam injection is planned for February 2022. Presently its SC focusing system is under fabrication: 18 of 88 SC “twin” dipoles and 1 SC “twin” quadrupole lens have been fabricated (Fig. 4) and passed magnetic measurements at liquid helium temperature (the term “twin” means here the magnets have design where two identical magnets of two Collider rings are placed one above other).

Figure 4: SC “twin” dipoles of Collider.

Main elements of the Collider are under fabrication as well. Essential part of them was designed and being fabricated at BINP. First of all, it relates to RF stations (Fig. 5) and High Voltage Electron Cooler (HVEC) [5].

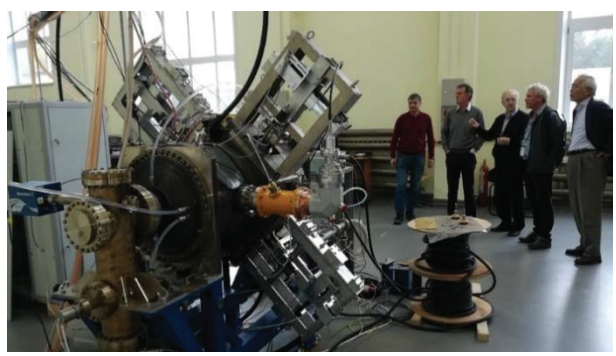

Figure 5: Members of NICA Machine Advisory Committee are introduced to RF-2 first station at test.

Application of the HVEC at NICA Collider has several specific features never met before:

1. Energy range 1 ÷ 4.5 GeV/u for $^{197}Au^{79+}$ ions (0.55 ÷ 2.45 MeV electrons);

ISBN: 978-3-95450-218-9 ISSN: 2226-0374 doi:10.18429/JACoW-COOL2019-THX02

2. Electron beam current 0.1 ÷ 1.0 A at such high energy;
3. Solenoid magnetic field up to 0.2 T;
4. Two cooling electron beams operated simultaneously;

All these features make the project of HVEC rather challenging. Besides the "old" and well known problems (that does not make them easy) remain:

5. Suppression of ion beam space charge and intrabeam scattering (IBS);
6. Suppression of ion recombination with cooling electrons.

NICA COLLIDER: PROBLEMS AND SOLUTIONS

The HVEC is designed to solve several problems. The first of them is ion storage in the Collider rings.

Ion stacking. In NICA ions generated in the ion source KRION come through BTL to the Booster, are accelerated in it, stripped at extraction to bare nuclei state, transferred to Nuclotron and, after acceleration up to storage energy, transferred in one of two Collider rings. Injection of the ions into Collider rings is produced by turns with periodicity of $T_{inj} = 8.04$ s. Ion accumulation in Collider rings is carried out using "barrier" RF voltage [6]. During the time T_{inj} between two injection pulses the new injected ions are cooled by electron beam or/and stochastic cooling system and merge with previously stored ions ("stack"). The time dependence of the maximum ion betatron amplitude in the stack after n-th injection $x_{max}(t)$ can be described by the recurrent formula

$$x_{max}^{(n)}(t) = x_{inj}\left(\sum_{m=1}^{n} e^{-(m-1)\alpha}(1+r)^{m-1}\right)\cdot e^{-\alpha(t-n)}, \quad (n-1) \le t \le n \qquad (1)$$

Here n is number of injection pulse, $\alpha = T_{inj}/\tau_{cool}$ is cooling decrement, τ_{cool} is cooling time, t is time in T_{inj} units, parameter $r = \Delta x/x_{max}$ is increase of the stack x-size under action of aftereffect ripples of the kicker pulse. We note that in stacking scheme with barrier RF the aftereffect ripples of the kicker pulse affect the stack, and not the injected bunch.

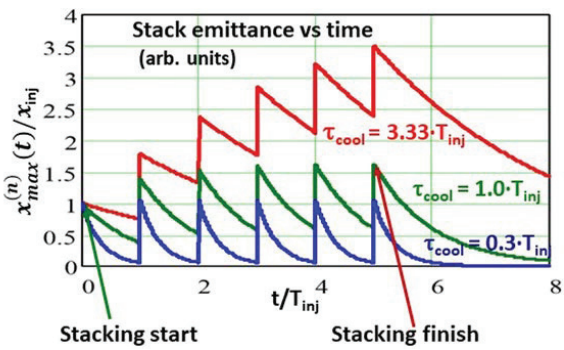

Figure 6: Dynamics of the maximum ion betatron amplitude in the stack size for τ_{cool}/T_{inj}: 0.3, 1.0 and 3.33.

Depending of cooling time (parameter α) the maximum ion betatron amplitude in the stack size (Fig. 6) comes to saturation (blue and green curves), either can grow up unlimitedly (red curve).

The cooling time requirement follows from the saturation condition:

$$x_{eq} = x_{max}^{(n+1)} = x_{max}^{(n)}. \qquad (2)$$

Here x_{eq} is saturation ("equilibrium") size of the stack just after $(n+1)$-st injection. Its value we find from Formula (2) and the equality:

$$x_{max}^{(n+1)} = x_{max}^{(n)} e^{-\alpha}(1+r) + x_{inj},$$

According (2) we can insert in here x_{eq} instead $x_{max}^{(n+1)}$ and $x_{max}^{(n)}$ and find

$$x_{eq} = \frac{x_{inj}}{1-(1+r)e^{-\alpha}}. \qquad (3)$$

This Formula allows us to find x_{eq} if ignoring other effects, e.g. described below. We note this consideration assumes independence of cool of beam transverse size (betatron amplitude).

Space charge and IBS. The estimates of space charge and IBS effects were made for ion beam linear density dN_i/ds of coasting beam depending of ion momentum spread (Fig. 7). The black dot curves describe equilibrium between IBS and electron cooling at given cooling time τ_{cool} values. Herewith the beam emittance is defined from the equilibrium condition, IBS increments were calculated following [7]. Longitudinal effect of the beam space charge was calculated by well-known Keil-Schnell Criterion a $(Z/n)_{max}$ Ohm (blue solid curve with dots). Red dot-dashed curve shows limitation caused by barrier RF voltage. As result, we obtain some area of the parameters dN_i/ds and $\Delta p/p$ where accumulated coasting beam is stable (shown in grey). Red dot horizontal line shows project value of linear density and red dot vertical one indicates the $\Delta p/p$ value corresponding 1/3 of separatrix $\Delta p/p$.

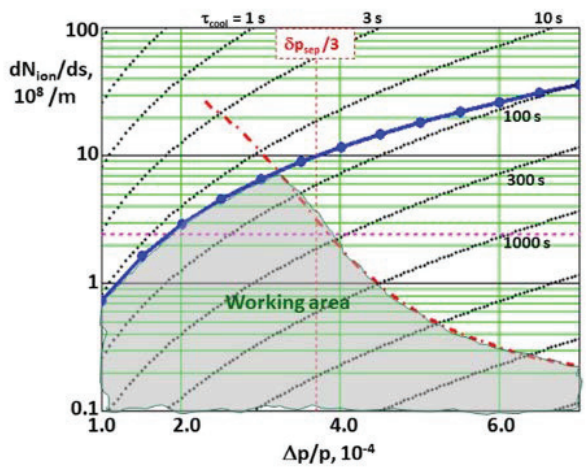

Figure 7: Estimates of critical parameters of the ion beam in NICA Collider at ion stacking.

This consideration allows us to conclude the area of stable coasting beam parameters is sufficiently large for the

ISBN: 978-3-95450-218-9 ISSN: 2226-0374 doi:10.18429/JACoW-COOL2019-THX02

beam before bunching. Formation of the bunched ion beam is presented in [8].

Recombination in HVEC and its suppression. The recombined ions flux from the electron cooler is harmful for several reasons. First of all, it shortens ion beam lifetime. Then, these ions may generate parasitic signals (background) in the MPD. This can be prevented by collimation. And finally, this flux increases radiation level in vicinity of the NICA facility.

One can estimate the flux magnitude using experimental data on the recombination of bare nuclei in electron coolers [4]. Dependence of experimental value of recombination rate coefficient τ_{rec} on electron energy shift (electron temperature T_e in the ion rest frame) can be approximated as follows:

$$\alpha_{rec}(T_e) = 10^{-13} \cdot Z^2 T_e^k \ \mathrm{cm}^3/\mathrm{s}, k = -0.3849673, \quad (4)$$

Then one can calculate ion lifetime the NICA Collider using the formula

$$\tau_{rec} = \eta_{cool} \frac{\gamma^2}{\alpha_{rec} n_e} \quad (4)$$

where η_{cool} is ratio of the cooling section length to the Collider ring circumference, ne is cooling electron density in the Lab. frame, γ is the Lorenz factor. The results of τ_{cool} and τ_{rec1} for the NICA Collider at ion energy of 4 GeV/u and electron beam current of 1 A are given in table 1. The calculations of τ_{cool} (column 2) and τ_{rec1} (column 3) have been performed by V. Parkhomchuk [5][1] using BETACOOL code [11] and the Bell formula [12]. The results of τ_{rec2} (column 4) were calculated by formulas (4), (5).

Table 1: Cooling and Recombination Time Values for NICA Collider

1	2	3	4
T_e, eV	τ_{cool}, s	τ_{rec1}, s	τ_{rec2}, s
0.1	18.45	87.6	295
1.0	21.91	209.9	717
10	28.8	1153	1740
100	40.35	4843	2800

Luminosity Optimization. Luminosity of the NICA Collider was calculated using optimization method proposed in [13]. The method is based on two effects limitations: so called Laslett betatron tune shift ΔQ and beam-beam betatron tune shift ξ. Their sum has not to exceed certain value $\Delta Q_{\max}$. As is known for experiment, the beam is stable if $\Delta Q_{\max} = 0.05$. For NICA Collider in ion mode the dominant Laslett tune shift (Fig. 8a). Method of choice of optimal values of other parameters is described in [13], the results are demonstrated in Fig. 8b. However, luminosity of NICA Collider can be limited by intensity of the injection chain and MPD capability.

[1] The calculations in [5] have been done for enlarged ring circumference that is corrected in present article.

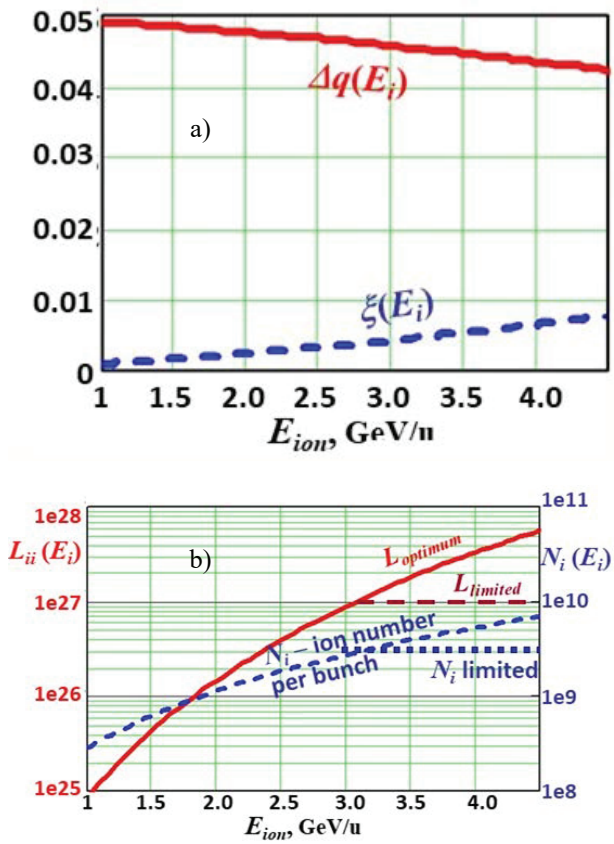

Figure 8: Tune shifts of betatron frequencies caused by beam space charge action (a) and number ion per bunch and luminosity (b) vs ion energy.

STOCHASTIC COOLING

Both electron and stochastic cooling methods are complimentary and will be applied to ion beams of the NICA Collider. This version of the stochastic cooling method is under active development [9], [10]. Implementation of the proton mode is much more complicated problem. We lose stochastic signal value by the factor $Z = 79$ and get increasing of cooling time by factor N_{proton}/N_{ion}. This problem is under investigation as well by NICA group.

CONCLUSION

The presented report describes the current status of the NICA project with focusing on the problems related to application of electron cooling at the steps of ion injection and acceleration in the NICA Booster and ion storage in the NICA Collider. Bunched beam formation in the Collider is described in [8]. Both talks demonstrate that electron cooling is a key issue of the NICA project and its implementation is realistic.

REFERENCES

[1] Planck Mission data, https://www.cosmos.esa.int/web/planck/publications

ISBN: 978-3-95450-218-9 ISSN: 2226-0374 doi:10.18429/JACoW-COOL2019-THX02

[2] I. N. Meshkov, G. V. Trubnikov, "NICA Project: Three Stages and Three Coolers", in *Proc. 11th Workshop on Beam Cooling and Related Topics (COOL'17)*, Bonn, Germany, Sep. 2017, paper THM21, pp. 84-88, ISBN: 978-3-95450-198-4, https://doi.org/10.18429/JACoW-COOL2017-THM21, 2018.

[3] M. Bryzgunov *et al.,* "Status of the Electron Cooler for NICA Booster and Results of Its Commissioning", presented at COOL'19, Novosibirsk, Russia, September 2019, paper TUX01, this conference.

[4] A. B. Kuznetsov, I. N. Meshkov, A. V. Philippov, *Phys. Part. Nucl. Letters*, 2012, Vol. 9, No. 4-5, pp. 346-351.

[5] V. Parkhomchuk *et al.,* "The status of the electron cooling system for the NICA Collider", presented at COOL'19, Novosibirsk, Russia, September 2019, paper THX01, this conference.

[6] I. N. Meshkov, *Phys. Part. Nucl.*, 2014, V. 45, pp. 452-471.

[7] S. S. Nagaitsev, *Phys. Rev. ST – Accelerators And Beams*, 2005, V. 8, p. 064403.

[8] N. Mityanina *et al.,* "Longitudinal Particle Dynamics and Cooling in NICA Collider", presented at COOL'19, Novosibirsk, Russia, September 2019, paper THA01, this conference.

[9] K. Osipov *et al.,* "Parameter Optimization of Ring Slot Coupler Pickup and Kicker for the NICA Stochastic Cooling System", presented at COOL'19, Novosibirsk, Russia, September 2019, paper TUPS17, this conference.

[10] I. V. Gorelyshev *et al.,* "Phase Step Method for Friction Force Measurement in Stochastic Cooling", presented at COOL'19, Novosibirsk, Russia, September 2019, paper TUPS18, this conference.

[11] http://betacool.jinr.ru

[12] M. Bell and J. S. Bell. Particle Accelerators. 1982. V. 12. P. 49-52.

[13] I. N. Meshkov, *Phys. Part. Nucl.,* 2019, V. 6 (to be published); Preprint D1-2019-40, JINR, 2019.

ISBN: 978-3-95450-218-9 ISSN: 2226-0374 doi:10.18429/JACoW-COOL2019-THA01

LONGITUDINAL PARTICLE DYNAMICS AND COOLING IN NICA COLLIDER

N. Mityanina, V.Petrov, E.Rotov, A.Tribendis,
Budker Institute of Nuclear Physics, Siberian Branch, Russian Academy of Sciences, Novosibirsk, Russia
I. Meshkov, A.Sidorin, E. Syresin,
Joint Institute for Nuclear Research, Dubna, Moscow Region, Russia

Abstract

A feature of the NICA acceleration complex is high luminosity of colliding beams. Three types of RF stations will be used in the NICA Collider to reach the necessary beam parameters. The first type is for accumulation of particles in the longitudinal phase space with the moving barrier buckets under action of stochastic and/or electron cooling systems. The second and the third RF stations are for formation of the final bunch size in the colliding regime. This report presents brief description of three types of RF stations constructed in BINP and numerical simulations of longitudinal beam dynamics which take into consideration account the longitudinal space charge effect, cooling and IBS during the accumulation and bunching procedures.

INTRODUCTION

The goal of the NICA facility [1] in the heavy ion collision mode is to reach the luminosity level of 10^{27} $cm^{-2}s^{-1}$ in the energy range from 1 GeV/n to 4.5 GeV/n.

The RF systems of the Collider [1] have to provide accumulation of required numbers of ions in the energy range 1-3.9 GeV/n, accumulation at some optimum energy and acceleration to the energy of the experiment in the range of 1-4.5 GeV/n, formation of 22 ion bunches, and achievement of the required bunch parameters.

This can be done with the help of three RF systems [1], one of the broad-band type and two narrow-bands ones. The first one accumulates particles in longitudinal phase space with application of RF barrier bucket technique. The maximal voltage of the barrier is 5 kV, it has rectangular shape with phase length π/12. By applying additional voltage of 300 V, one can also use the meander between the barriers for inductive acceleration. The second RF system works on the 22nd harmonic of the revolution frequency and is used for formation of the proper number of bunches. The maximal RF2 voltage is 100 kV. The RF2 can also be used for beam acceleration or deceleration. The third RF system works on the 66th harmonic and is used for the final bunch formation and maintenance of the bunch parameters during the collision mode. The maximal RF3 voltage is 1 MV. The RF3 system is also used for ion beam acceleration or deceleration. All stages of the bunch formation as well as the collision mode are accompanied by a cooling process, either stochastic or electron.

Previous calculations modelling longitudinal beam dynamics were fulfilled in approach neglecting change of transverse emittance and cooling time during accumulation or bunching [2]. Now we take into account dependence of IBS and electron cooling force on transverse emittance which also changes in accordance with these effects in RMS model.

ACCUMULATION OF IONS

Moving Barrier Buckets

Accumulation is fulfilled with separated regions of injection and storage. Two pairs of voltage impulses form 2 separatrices, the 1st one for injection, the 2nd - for storage of ions (stack). After injection the impulses of injection separatrix move close to the stack, then impulses separating injected bunch from stack decrease, and separatrices join (Fig.1). If the length of combined separatrix exceeds half of the ring perimeter, it will be compressed.

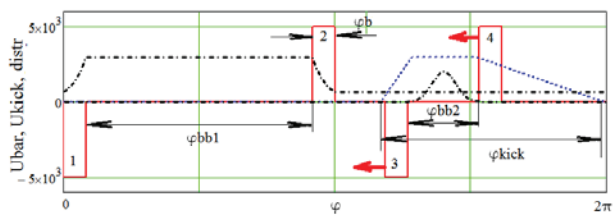

Figure 1: Barrier voltage (red line), density of stored and newly injected beam (black dash-dot line), impulse of kicker(blue dashes). φ_b, $\varphi_{bb1,2}$, φ_{kick} - phase lengths of voltage impulse, 2 separatrices and kicker impulse.

Calculation Model

At the calculation all the effects are separated (movement of barrier buckets, cooling, IBS, loss of ions at injection). All movements are slow, with conserved longitudinal emittance.

Electron cooling force is taken into account in a form of V.Parkhomchuk [3], with parameters of the electron beam (current, radius, transverse and longitudinal temperatures) $I_e = 1A$, $r_e = 1\,cm$, $T_{et} = 5\,V$, $T_{el} = 5\,mV$. We use in calculacion the longitudinal component of cooling force averaged over transverse velocities and averaged over all 3 velocities distributions values of longitudinal and transverse decrements.

IBS is taken into account in a form of a diffusion coefficients calculated with a model of S.Nagaitsev [4], for NICA magnetic structure of 2018.

ISBN: 978-3-95450-218-9 ISSN: 2226-0374 doi:10.18429/JACoW-COOL2019-THA01

After merging 2 separatrices till a new injection the RMS beam parameters change with account of averaged cooling decrements down till their stationary values, at which the times of cooling and IBS growth equal.

During injection the kicker injecting new portion of ions into stationary orbit simultaneously removes all ions of previously stored beam placed in the region of kicker impulse. The main goal of present calculations was an attempt to take into account nonlinearity of the cooling force and it's influence on the distribution function and hence on the losses at injection. For that we have used two models: gaussian distribution with current value of impulse spread σ_p (for linear cooling force) and the obtained as the first approach $f_1(\delta_p)$ ($\delta_p = \Delta p / p$) to the solution of the one-dimentional Fokker-Plank equation with account of diffusion coefficient and nonlinear averaged longitudinal cooling force (nonlinear distribution).

Outside of voltage barrier buckets the distribution is one-dimensional. We use obtained distribution $f_1(\delta_p)$ as a distribution inside the stack. But the losses at injection are difined by the one-dimensional distribution outside the stack $f_2(\delta_p)$, which is coupled with the distribution inside the stack $f_1(\delta_p)$ with the equation of motion along the phase trajectory and equation of continuity, resulting in $f_2(\delta_p) = f_1(\sqrt{\delta_p^2 + \delta_{psep}^2})$, which is used for calculation of losses at injection.

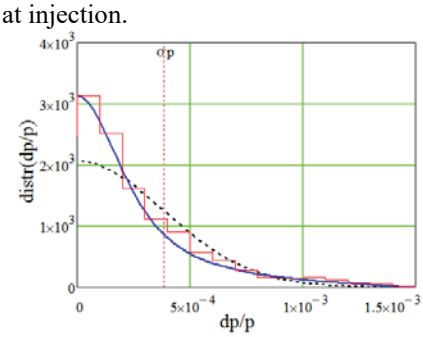

Figure 2: Stationary distributions. obtained with Betacool program (red steps), proposed nonlinear distribution (blue line) and gaussian distribution for the same impulse spread σ_p (black dashes).

Figure 2 presents stationary distributions obtained with Betacool [5] program (red steps), proposed nonlinear distribution (blue line) and gaussian distribution for the same impulse spread σ_p (black dashes). Stationary solutions for impulse spread and transverse emittance in dependence on number of ions also are in good accordance with Betacool RMS results. According to them the necessary number of ions $N_0 = 55 \cdot 10^9$ (at the energy $E_k = 3\ GeV/n$) can be accumulated in stationary regime (when the time between injections Δt_{inj} is much more than the averaged cooling time) at the electron beam currents $I_e > 0.65\ A$, with cooling time at stationary parameters being several tens of seconds. But for projected $\Delta t_{inj} = 8$ sec the process of accumulation cannot be treated as stationary and one should take into account the dependence of RMS parameters on time.

Thus, the process of accumulation was modelled with account of next effects at each injection: averaging of RMS parameters at uniting separatrices; cooling and IBS; compression of the stack $\sigma_{p2} = \sigma_{p1} L_1 / L_2$ at conserved longitudinal emittance; losses of ions at injection.

Calculation of Ion Accumulation

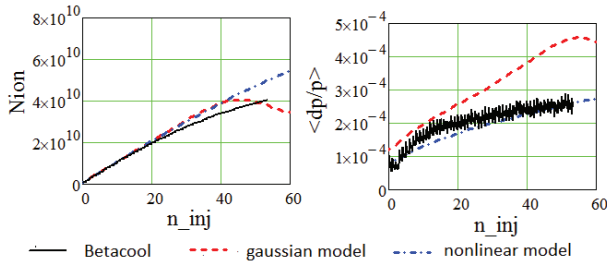

Figure 3: Number of accumulated ions, RMS impulse spread versus number of injections.

Calculations were done for the ions' energy E_k=3 *GeV/n*, the cooling electron current I_e= 1 *A*, parameters of injected bunch $\sigma_{si} = 10\ m$, $\sigma_{pi} = 1.2 \cdot 10^{-4}$, $N_i = 10^9$, $\Delta t_{inj} = 8$ sec, length of injection separatrix $\varphi_{bb2} = 6\sigma_{si}$.

In a result of calculations for 50 injections (Fig.3) we have $4 \cdot 10^{10}$ ions (Betacool); $4 \cdot 10^{10}$ ions (gaussian model) / $5 \cdot 10^{10}$ ions (nonlinear model). Necessary number of ions $5.5 \cdot 10^{10}$ can be obtained in ~80 injection (extrapolation of Betacool results); in 55 injections (nonlinear model); can not be reached (gaussian model). For gaussian model this number of ions can be accumulated at higher electron current I_e=*1.25A*, in 60 injections.

Impulse spread for gaussian model is significantly larger than for nonlinear model and for Betacool. Thus, the nonlinear model of one-dimensional code seems to be more close to Betacool solution than the gaussian model, but with some overestimated cooling (~30%) .

ADIABATIC CAPTURE AND BUNCHUNG OF ION BEAM

Preparation of beams for ion-ion collision is performed in two stages. Firstly 22 bunches are produced using adiabatic capture technique at slowly increasing RF voltage.

Starting voltages of RF2, RF3 were chosen with the account of conditions of minimal required power of generator at the maximal voltage and of absence of static instability at the start of increase of the voltage of RF3: $U_{2\min} \approx 1.5kV$, $U_{3\min} \approx 22.5kV$.

When RF2 voltage reaches the maximum of 100 kV, the electron cooling is switched on for some time (Fig.4, [t1,t2]). When the bunch length becomes short enough due to cooling and RF2 maximal voltage, the voltage of the

ISBN: 978-3-95450-218-9 ISSN: 2226-0374 doi:10.18429/JACoW-COOL2019-THA01

RF3 system working on the 66th harmonic (after a time of cooling) starts adiabatically increasing from 22 kV.

The maximal RF2 voltage together with cooling should provide conditions when the final longitudinal bunch length at interception into RF3 system voltage must be equal to the length completely fitting into the bucket of the RF3 system. However, a small number of ions at interception can be captured in the parasitic side separatrix of 66th harmonic. This leads to parasitic collisions in the Collider. The ratio of the number of captured ions in the side parasitic separatrix to the total number of bunch ions strongly depends on the RMS bunch length after the RF2 bunching and cooling. Further adiabatic increase in the RF3 voltage together with following cooling time (Fig.4, t>t4) provides formation of an ion bunch with the length of 60 cm and momentum spread of 10^{-3} required for colliding experiments.

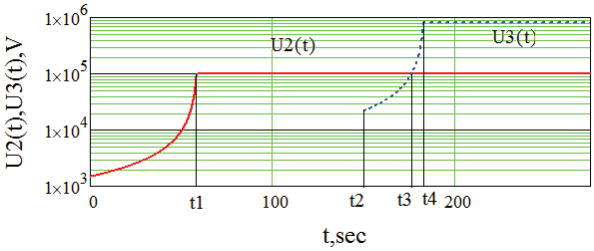

Figure 4: Amplitudes of voltages RF2, RF3 versus time.

One-dimensional Longitudinal Tracking

For estimation of capture and bunching a one-dimensional tracking code was developed. It implies a model of macroparticles for modelling the beam in the limits of one separatrix of 22-nd harmonic; numerical integration of equations of motion (4-th order Runge-Kutta method); variable time step proportional to the period of small synchrotron oscillations. At each time step we use arbitrary kicks $\sqrt{D(\sigma_p,\sigma_s)\Delta t}\cdot rnd_i$ (for σ_p,σ_s calculated over current distribution of macroparticles) to each macroparticle to modell IBS. The averaged longitudinal component of cooling force is taken into account in the same way as at accumulation. Change of transverse emittance is taken into account in RMS approach (1). While the generators of RF3 are still switched off, the induced by the ion beam voltage on the cavities of RF3 is taken into account. To speed up the calculation we use compression of the process time by the factor 0.1-0.001, together with times of cooling and IBS growth time, while synchrotron frequencies being unchanged. It means decrease of the number of fast oscillations by this factor, keeping them still fast in comparison with slow processes of cooling, IBS growth and adiabatic increase of voltage amplitudes.

Figure 5 shows stationary bunch RMS length at 3 significant moments of bunching,in dependence of electron beam current. Red line corresponds to $U_2 = U_{2\max}, U_3 = 0$. It defines minimal bunch length before increasing U_3; at $I_e = 1A$ $\sigma_{s1st} = 1.425\,m$. Blue dash-dots correspond to $U_2 = U_{2\max}, U_3 = U_{2\max}$ (arising the side separatrices). Comparing this bunch length with $\lambda_{66}/6 = 1.27\,m$, 1/6 of the wavelength of 66-th harmonic defines the number of ions in side separatrices. ($\sigma_{s2st} < \lambda_{66}/6$ at $I_e > 0.3A$). Black dashes correspond to $U_{2\max}, U_{3\max}$. These stationary parameters define final parameters after cooling and should be $\sigma_{s3st} < 0.6\,m$ - necessary for experiment. It can be achieved at $I_e > 0.5A$.

Stationary Parameters

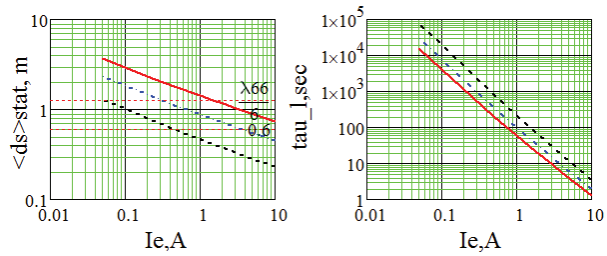

Figure 5: Stationary RMS length versus electron beam current; averaged longitudinal cooling times at stationary parameters.

Beam Capture with RF2

Below there are the results of calculation of capture and bunching of ion beam with described above 1-dimentional tracking code . Initial parameters $\sigma_{p0} = \left(\delta_{p\,sep}\right)_{RF1}/3$, $\varepsilon_{x0} = 0.1\pi\cdot mm\cdot mrad$ correspond to these values after accumulation of ions, $I_e = 1A$.

The calculations are fulfilled for the rate of detuning change $da/dt = 3\,\mathrm{sec}^{-1}$ time of tuning for RF2 ~60 sec and for RF3 - ~30 sec (Fig.4). After reaching maximal voltages of RF2 and RF3 cooling is switched on to reach necessary stationary parameters (Fig.5, left), for the time estimated by cooling times at Fig.5 (right) .

Figure 6 shows the results of the ion beam capture by RF2. Induced by the ion beam current voltage on the cavities of RF3 while switched off appears to be small in comparison with voltage of RF2, so it practically does not influence the dynamics of the ions.

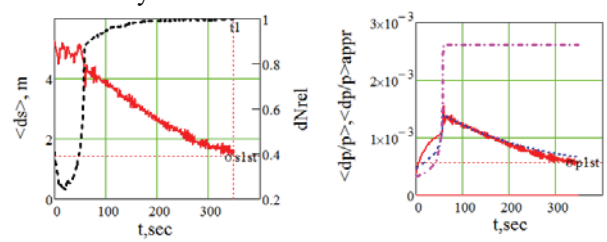

Figure 6: Left: RMS bunch length versus time (red line) and relative number of ions captured into separatrix. (black dashes). Right: RMS impulse spread versus time, tracking (red line) and approximation (blue dashes); separatrix amplitude (pink dash-dotes).

A beam can be cooled to $\sigma_{s\,st} = 1.425\,m$ with the electron beam current $I_e = 1A$.

ISBN: 978-3-95450-218-9 ISSN: 2226-0374 doi:10.18429/JACoW-COOL2019-THA01

Further Bunching with RF2+RF3

Increase of voltage of RF3 leads to formation of 3 separatrixes of 66-th harmonic instead of 1 separatrix of 22-nd harmonic, with further compression of the bunch length, ideally to $\sigma_s < \lambda_{66}/6$, so that the bunch as a whole is located in the cenral separatrix, and the side separatrices contain a small share of ions. The goal is to minimize this share.

Figure 7 shows the results of further bunching of ions by RF3 together with RF2. Figure 8 shows relative number of particles outside the central separatrix versus RMS bunch length at the start of increasing voltage of RF3 and minimal electron beam current at which this length could be reached. At $\sigma_{s0} = 1.5m$ 2.5% of ions are outside the central separatrix. In order to decrease this number, one should increase the electron current. At $I_e = 1.5\ A$ $\sigma_{s1st} = 1.2m$, ~1% of ions are outside the central separatrix.

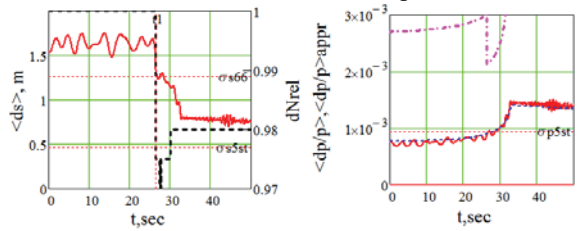

Figure 7: Left: RMS bunch length versus time (red line) and relative number of ions captured into the central separatrix. (black dashes). Right: RMS impulse spread versus time, tracking (red line) and approximation (blue dashes); separatrix amplitude (pink dash-dotes).

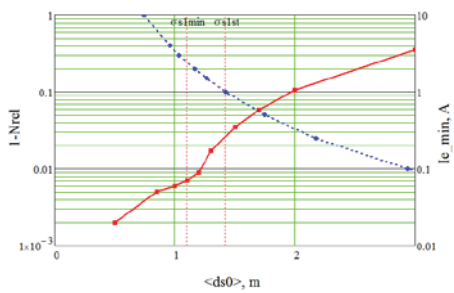

Figure 8: Relative number of particles outside the central separatrix versus RMS bunch length at the start of increasing voltage of RF3 (red line) and minimal electron beam current at which this length could be reached (blue points).

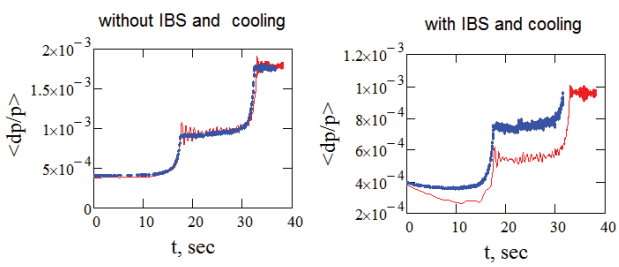

Figure 9: Impulse spread versus time at capture and bunching of ions. Red thin line - 1-dimentional tracking code, blue thick dashes - Betacool.

Comparison with Betacool

Figure 9 shows the results of one-dimensional tracking with Betacool results in comparison (here $da/dt = 10\ \mathrm{sec}^{-1}$). Left figure shows the impulse spread versus time without cooling and IBS, with times of calculation of one order; right figure shows the result with cooling ($I_e = 1A$) and IBS. Betacool calculation here requires ~15 times more time). One can see that the cooling in the one-dimensional tracking is overestimated. The result with $I_e = 0.6A$ coincides with the same Betacool result for $I_e = 1A$.

The Table 1 shows the relative number of ions left in side separatrices in these 3 calculations, which shows the same difference and coincidence of results as impulse spread at the Fig. 9.

Table 1: Number of Ions in Side Separatrices

	no cooling&IBS	with cooling&IBS
1-dim. tracking ($I_e = 1A$)	10.4%	3.2%
1-dim. tracking ($I_e = 0.6A$)		4.8%
Betacool	9.6%	5.1%

CONCLUSION

1. Different considered models show the possibility of accumulation of necessary number of ions at 3 *GeV/n* at the electron cooling current $I_e = 1\ A$ or at increased current $I_e = 1.25\ A$.

2. At $I_e = 1\ A$ 2.5% of ions are outside the central separatrix. In order to decrease this share till 1% the electron current should be increased at least up to $I_e = 1.5\ A$.

3. Final parameters ($\sigma_{sf} = 0.6\ m$) can be reached at electron current $I_e > 0.5\ A$.

4. At comparison with Betacool one can see that stationary solutions have sufficient accordance, but the time-dependent solutions have a certain difference. It looks like cooling in one-dimensional tracking is overestinated ~1.7 times. So, the one-dimentional approach code can be used for estimation of dependences on variating parameters, but final calculation requires more accurate (but rather slower) 3D calculation.

REFERENCES

[1] Technical Project of NICA Acceleration Complex, Dubna, Russia, 2015.

[2] E. Syresin *et al.*, "Longitudinal Particle Dynamics in NICA Collider", in *Proc. 10th Int. Particle Accelerator Conf. (IPAC'19)*, Melbourne, Australia, May 2019, pp. 455-457. doi:10.18429/JACoW-IPAC2019-MOPMP015

[3] V.V. Parchomchuk, "New insights in the theory of electron cooling", *NIM in Physical Research* A 441, 2000.

[4] S. Nagaitsev, "Intrabeam scattering formulas for fast numerical evaluation", *Physical Review Special Topic*, AB, 8, 064403, 2005.

[5] I. Meshkov, A. Sidorin *et al.*, "Physics guide of BETACOOL code", C-A/AP#262, BNL, Upton, NY.

ISBN: 978-3-95450-218-9 ISSN: 2226-0374 doi:10.18429/JACoW-COOL2019-THB02

SIMULATION OF ELECTRON-OPTICAL SYSTEMS OF ELECTRON COOLERS

A.V. Ivanov, M.I. Bryzgunov, V.M. Panasyuk, V.V. Parkhomchuk, V.B. Reva,
The Budker Institute of Nuclear Physics, Novosibirsk, Russia

Abstract

To provide successful operation of electron coolers one need thorough simulation and development of electron-optical system. In this paper simulations of electron gun, accelerating structure and collector are discoursed. Particular attention is paid to obtaining high perveance electron beam with a small transversal temperature and controlled profile, and collector with low flux of secondary electrons. Bends of electron beam are also considered.

Main program for simulations is SAM code. This code is based on boundary integral method, its main advantage is precision and speed of calculations.

INTRUDUCTION

At the development of such large facilities as electron coolers, it is necessary to perform an initial numerical simulation of all the important parts. In this paper, we focus on numerical calculations and optimization of the electron-optical system of electron coolers and the dynamics of electron beams in them. Since the coolers created in BINP use magnetized beams, the following tasks can be distinguished: first, it is necessary to build and optimize the magnetic system in the region of the electron gun and the collector. The second task is the numerical development of the electron gun itself as well as the collector. The third task is the development of a magnetic system for bends and matching system and optimization the beam motion in these regions.

To solve these problems, SAM [1, 2] and MAG3D [3] packages are mainly used in BINP. These programs were developed at the Institute; their main peculiarity is the use of integral methods for calculations, which ensures good accuracy and speed of calculations. The SAM program is intended for simulation of axially symmetric electron optical systems with space charge consideration. These systems can include electrodes, dielectrics, coils, permanent magnets, linear ferromagnetics. Tasks with space charge can also be simulated with help of the SAM program, that allows calculation of electron guns and collectors. MAG3D program is used to solve problems of nonlinear 3D magnetostatics.

SIMULATION OF ELECTRON GUNS

The specificity of electron cooling makes the following requirements for electron guns used in coolers:

- required perveance;
- independent current and energy control;
- low (< 1 eV) transverse temperature of the beam;
- independent adjustment of the current density distribution across the beam.

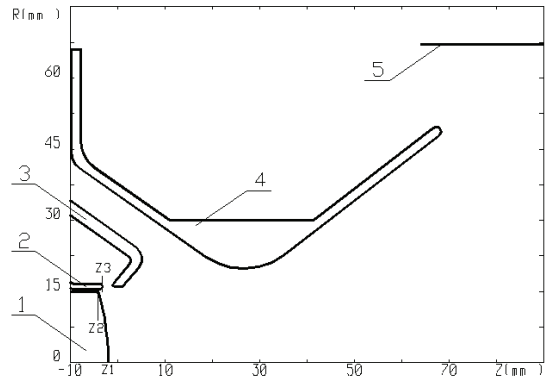

Figure 1: Geometry of electrodes of the electron gun with variable beam profile.

To meet these requirements, an electron gun was developed in the Institute, the drawing of which is shown in Fig. 1. The convex cathode 1 immersed into longitudinal magnetic field is used. To form the electron beam control electrode 3 is used together with anode 4. The control electrode is placed near the cathode edge and influences the emission from this area. By applying different potential on this electrode the beam with radial current density distribution from parabolic to hollow can be obtained.

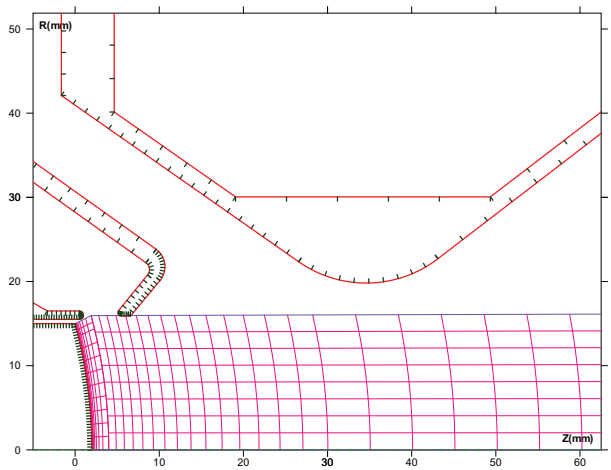

Figure 2: The mesh used for calculation of the electron gun.

The calculation and optimization of this gun was performed using the SAM package, the mesh used for the calculations and the collocation points are shown in Fig. 2. The total number of collocation points is less than 200, total number of cells in mesh – less than 500. With such a number of nodes calculation takes little time – less than 1 minute, even on a relatively low-power personal computer. However, the ability of the SAM complex to

ISBN: 978-3-95450-218-9 ISSN: 2226-0374 doi:10.18429/JACoW-COOL2019-THB02

describe the emission from cathodes of complex shape and the ability to thicken the cells allowed not only to achieve high accuracy of calculations, but also to describe the emission from the very edge of the cathode.

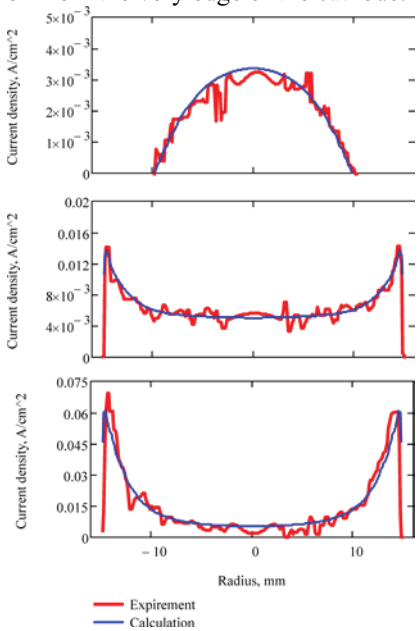

Figure 3: Calculated and experimentally obtained beam profiles at various potential of control electrode.

Experimental studies had confirmed [4] all the main parameters of the gun obtained previously in numerical simulations, including its perveance, the threshold of the virtual cathode, and the dependence of the beam profile on the voltage ratio of the control electrode and anode (see Fig. 3).

SIMULATION OF COLLECTORS

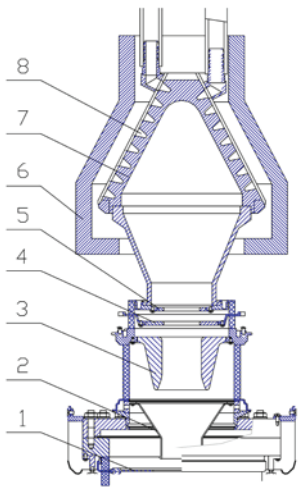

Figure 4: The collector of electron coolers for CSR and LEIR rings.

In electron coolers, when the electron beam moves from the electron gun to the cooling solenoid, it passes one or more bends. In the accompanying magnetic field, this movement is accompanied by centrifugal drift, which must be compensated. In the electron coolers created in the BINP for CSR (IMP, China) and LEIR (CERN) rings, this compensation is carried out by creating a transverse electrostatic field in the bends. Such electrostatic compensation works equally well for both the primary electron beam and the secondary beam moving from the collector in the opposite direction. In such a system, it is not necessary to provide a very small secondary collector emission factor to ensure low total losses. In the coolers for COSY (Jülich, Germany) and NICA (JINR, Russia) rings, the electrostatic compensation is replaced by a magnetic one, with a strong transverse displacement of the secondary beam after cornering. In this case, a very small collector secondary emission factor ($< 10^{-5}$) is required to ensure stable operation of the entire cooler.

The collector of electron coolers for CSR and LEIR rings is shown in Fig. 4. The massive magnetic shield 6 weakens the magnetic field inside the collector, the electron beam expands and comes to the cooled inner surface 7 with an acceptable current density. This reduced field also forms a barrier – a magnetic plug – on the path of secondary electrons that try to leave the collector following the magnetic field lines. The second barrier to the way of this secondary flow is the electrostatic barrier formed by the suppressor electrode 4.

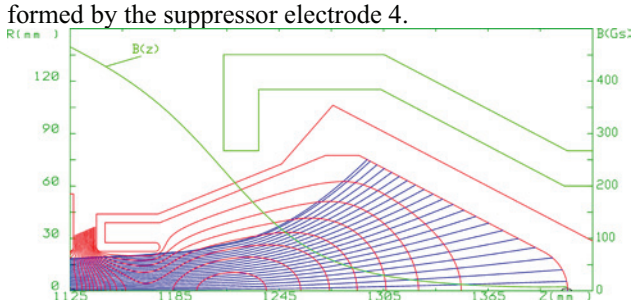

Figure 5: Equipotentials and trajectories of electrons in the collector for CSR ring.

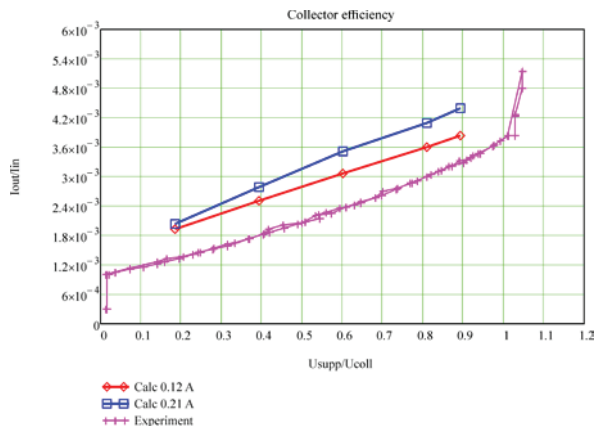

Figure 6: Dependence of collector efficiency from the suppressor potential.

The SAM program was also used to calculate and optimize this collector taking into account the space charge of both primary beam and secondary electrons. The electron beam was calculated from the Neumann boundary located in front of the collector, the calculation time is also insignificant. The results of collector calculation are shown in Fig. 5.

ISBN: 978-3-95450-218-9 ISSN: 2226-0374 doi:10.18429/JACoW-COOL2019-THB02

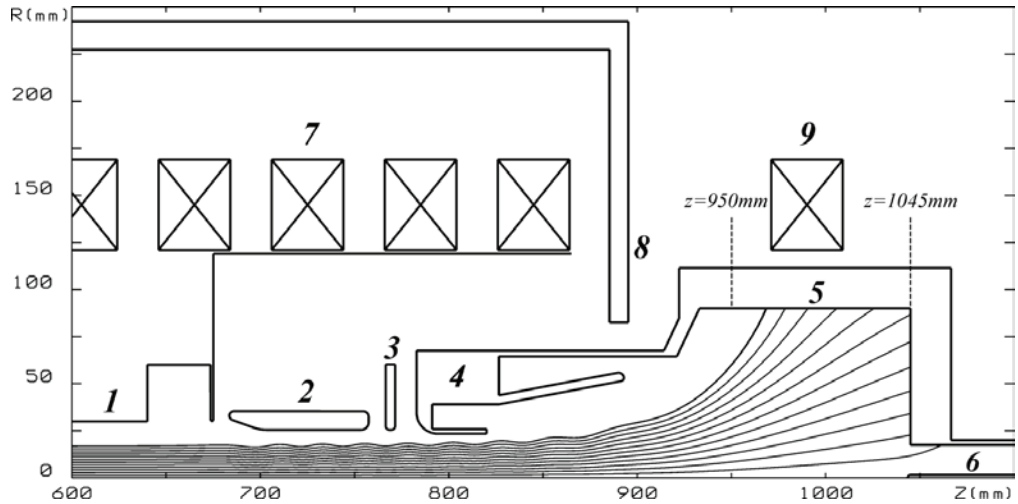

Figure 7: The collector for COSY ring and the electron beam trajectories.

The secondary emission model integrated into the SAM complex was used in the calculations. This model considers all three types of secondary electrons – true secondary electrons, rediffused and backscaterred electrons. Their total coefficients, angle and energy distributions are taken into account. Several generations of secondary electrons are also considered. These calculations allowed us to estimate the output flow of secondary electrons from the collector (see Fig. 6), subsequent measurements confirmed the dependence obtained in numerical simulations [5].

In COSY and NICA coolers to reduce secondary coefficient of collector, a Wine filter is placed between the collector itself and accelerating column. In this filter, additional electrodes create a transverse electric field, and a set of permanent magnets create a transverse magnetic field. These fields for the primary beam compensate each other, and for the secondary beam that goes in the opposite direction, they reinforce each other. As a result, the primary beam passes this filter without noticing these fields, and the secondary beam experiences a strong transverse displacement and goes to the diaphragm. Calculation of the Wine filter was performed with help of MAG3D program. This system showed the efficiency several orders of magnitude better than the efficiency of a single collector [6].

Due to the presence of Wien filter, the collector itself can have a simpler design (see Fig. 7), without the need for a massive magnetic screen. To reduce the magnetic field in the collector region, it was enough to put a magnetic wall 8 that divides the collector from main magnetic system, and for further decrease of magnetic field one standard coil 9 with the opposite direction of current can be used.

SIMULATION OF ELECTRON MOTION IN BENDS

As mentioned above, when the magnetized beam moves in bends, the centrifugal drift of electrons is compensated by either the force from the electrostatic field in CSR and LEIR coolers, or Lorentz force in NICA and COSY coolers. To maintain the beam orbit in the same plane, these forces must compensate for each other on average, but it is impossible to achieve their complete mutual compensation at each point of the beam path. An uncompensated transverse force appears; this force is especially big at the entrance to the bend and at the exit from it, causing a significant transverse motion of electrons. It is necessary to choose the dynamics of the particles in bends in such a way that these two impacts will compensate for each other.

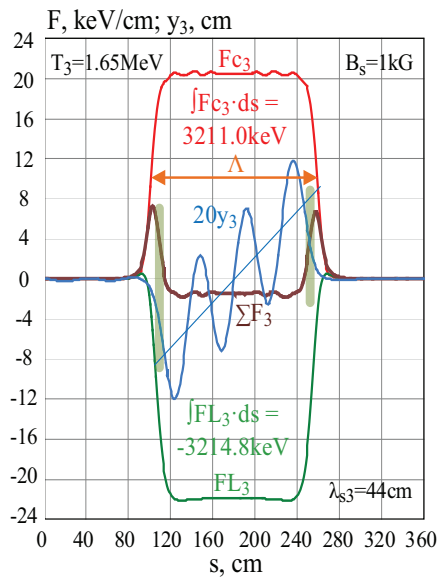

Figure 8: Centrifugal and Lorentz force in bends in COSY cooler and y-coordinate of the central electron.

The results of the calculation of the forces acting on central electrons in the turns and the results of the trajectory analysis of these particles in the optimized system are shown in Fig. 8. These calculations were performed with help of MAG3D program. Less than 3,000 elementary volumes were required to model the magnetic elements of the transport system, and the total calculation time was less than one hour [7].

ISBN: 978-3-95450-218-9 ISSN: 2226-0374 doi:10.18429/JACoW-COOL2019-THB02

CONCLUSION

Software packages SAM and MAG3D, developed at BING, are successfully used in the development of electron coolers at the Institute. With the help of the SAM package, an electron gun with high perveance, low transverse temperature and a controlled beam profile was created, as well as two electron beam collectors with the required perveance and secondary emission coefficient. The MAG3D complex was used to calculate the transport system of our coolers with a longitudinal magnetic field and to optimize the motion of the electron beam in them. Test measurements confirmed the calculated parameters of these systems, which ensured the successful commissioning and operation of coolers.

REFERENCES

[1] B. Fomel, M. Tiunov, V. Yakovlev, "Computer-aided electron gun design", *in proceedings of the XIII International Conference on High Energy Accelerators,* Novosibirsk, 1987, v.1, p.353-355.

[2] A. Ivanov, M. Tiunov, "ULTRASAM - 2D Code for Simulation of Electron Guns with Ultra High Precision", *in proceedings of EPAC'02*, Paris, June 2002, paper WEPRI050, p. 1634, 2002.

[3] MAG3D User's Guide, Novosibirsk, Russia, 2006.

[4] A.V. Bubley *et al.,* "Measuring a hollow electron beam profile", *Nuclear Instruments and Methods in Physics Research* A 532 (2004) 413–417.

[5] V.N. Bocharov, A.V. Bubley, M. Vedenev, *et al*, "Commissioning of electron cooler EC-300", preprint, Budker INP, Novosobirsk, 2004.

[6] M.I. Bryzgunov *et al.,* "Collector for electron cooling systems with suppression of reflected electron flux", *in Proc. Of COOL'13 Workshop*, Lanzhou, China, Sept 2013, p.103-106.

[7] V.M. Panasyuk, *et al.,* "The magnetic system of electron cooler of collider NICA", *in Proc. Of COOL'19 Workshop,* Novosibirsk, Sept 2019, paper TUPS15, this proceedings.

ISBN: 978-3-95450-218-9 ISSN: 2226-0374 doi:10.18429/JACoW-COOL2019-FRX01

RECENT DEVELOPMENTS AND EXPERIMENTAL RESULTS FROM ELECTRON COOLING OF A 2.4 GeV/c PROTON BEAM AT COSY

P. Niedermayer*, A. Halama, V. Kamerdzhiev, N. Shurkhno, R. Stassen,
Institut für Kernphysik, Forschungszentrum Jülich, Germany
V. Reva, Budker INP, Novosibirsk, Russia
T. Katayama, Nihon University, Japan

Abstract

The COSY control system as well as other subsystems are being upgraded. The 2 MeV electron cooler was recently extended with the EPICS control system and thereby integrated into the control and data acquisition system of the Cooler Synchrotron COSY. Taking advantages of the new software capabilities, studies of transverse and longitudinal magnetized electron cooling of a proton beam at 2.4 GeV/c were carried out. Electron and stochastic cooling were combined to reduce the cooling time while achieving lowest possible emittance and momentum spread. Results from experiments are discussed including cooling dynamics during operation of an internal cluster-jet target designed for the PANDA experiment at HESR. We present the results of probing the electron velocity distribution by means of the strongly cooled beam itself. The shape of the measured distibution may be caused by the galloping/scalloping effects within the electron beam. This effect plays a significant role in the strong dependence of the longitudinal and transverse electron cooling process on the proton beam size. Also discussed are the technical developments, achievements and further plans regarding the control system upgrade.

INTRODUCTION

The Cooler Synchrotron (COSY) is a storage ring operated at the Nuclear Physics Institute (IKP) at Forschungszentrum Jülich. Polarized as well as unpolarized proton and deuteron beams in the energy range 45 MeV to 2700 MeV can be delivered.It is equipped with a stochastic cooling system and two electron coolers. Currently a stochastic cooling system for the HESR is tested. While the 100 keV electron cooler operates mostly at injection energy, the 2 MeV electron cooler is designed for proton beam momenta beyond the COSY operating range of up to 4.5 GeV/c. The high energy electron cooler was developed at the Budker Institute of Nuclear Physics [1] and is being operated at COSY since 2013 [2].

TECHNICAL DEVELOPMENTS

EPICS Integration

The control system of the 2 MeV electron cooler was originally designed as a standalone-system. Six servers exist for control and diagnostics of the hardware components: the primary and secondary magnetic guiding system controlling the electron beam orbit, the beam position monitors (BPM) measuring the orbit, the electron gun and collector, the high-voltage accelerating sections as well as an interlock system for safety aspects. These systems are located in a separated environment with a custom control system.

In the course of upgrading the COSY control system to the Experimental Physics and Industrial Control System (EPICS) [3] it was decided to incorporate the 2 MeV electron cooler into the new control system. Having a common standard allows not only to further automate the beam cooling systems but also eases the handling of experimental data across various systems.

In order to integrate the 2 MeV electron cooler's control system into EPICS, an Input-Output-Controller (IOC) was developed. The IOC communicates with the cooler's systems using the EPICS modules *Stream* and *AsynDriver* while leaving the existing systems untouched. It provides the various parameters as process variables (PVs) to the EPICS control system, taking care of binary conversion and physical quantities. In addition, the EPICS alarm system is used to notify operators of critical values outside the normal operation ranges. [4]

Table 1 gives a statistical overview of the PVs made available. Currently the parameters of all systems are provided for readout and additional PVs exist to control the magnetic guiding system and electron gun. It is planned to further expand the control capabilities.

By having incorporated the 2 MeV electron cooler into the COSY control system EPICS, several advantages were achieved. The cooler's data is now centrally archived in a time correlated manner. This provides easier data-analysis after the experiments because all data is now saved continuously and stored in one single place. It is much easier to correlate the electron cooling data with other accelerator systems like beam diagnostics or timing. Furthermore a wide range of established tools designed for EPICS is used, e.g. to analyse data on-the-fly, producing physically meaningful displays which are vital for machine operation. Due to the

Table 1: Implemented Parameters

	Readout	**Control**
Analogue	610	63
DAC	*71*	*63*
ADC	*539*	
Binary status	381	60
Other	38	
Total	1029	123

* p.niedermayer@fz-juelich.de

ISBN: 978-3-95450-218-9 ISSN: 2226-0374 doi:10.18429/JACoW-COOL2019-FRX01

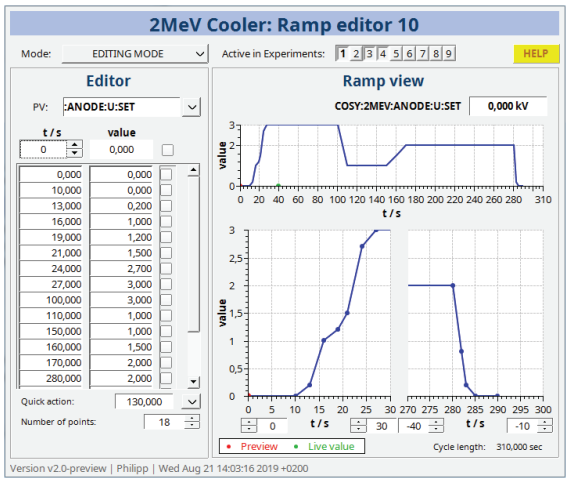

Figure 1: Screenshot of the ramp editor CSS-GUI.

common control system an enhanced interaction between the accelerator and electron cooler is possible, e.g. by means of automation (see also next section).

In addition to the 2 MeV electron cooler's EPICS integration, the most important parameters of the 100 keV cooler were also made available as PVs just recently. We are currently working on integrating the stochastic cooling system as well.

Ramp Editor

In order to automate the operation of the electron cooler a ramp editor was developed. Figure 1 shows a screenshot of the user interface. Based on the EPICS control system the editor allows to define arbitrary waveforms for a given parameter. The values are then interpolated based on the specified waveform and synchronised to the COSY timing system. This allows an automated, synchronous ramping of any desired parameter. For example, the electron current can be ramped up with the lowest possible beam loss by fine-tuning the voltage ramps of the electron gun. Once set up according to the experimental requirements, the system will provide reproducible cooling properties for every machine cycle.

COMBINED ELECTRON AND STOCHASTIC COOLING

Stochastic Pre-Cooling

Taking advantages of the new control system components, studies of transverse and longitudinal magnetized electron cooling with a proton beam at 2.4 GeV/c were carried out [5]. Thereby the electron cooling was combined with the stochastic cooling system at COSY. The stochastic cooling works best at high beam emittance where electron cooling is comparatively slow while the electron cooler performs better at low emittance. Figure 2 shows a typical setup where stochastic pre-cooling is followed by electron cooling. The equilibrium momentum distribution reached for the given setup of the stochastic cooling is shown by the black spectrum. Afterwards fast electron cooling is observed at low beam emittance. The 2 MeV electron cooler is capable of further reducing the momentum uncertainty by a factor of 6.6 (as shown by the blue spectrum) as well as the emittance by a factor of 2 compared to the stochastic cooling system.

Our experiments show that not only the equilibrium momentum spread but also the cooling time can be reduced by using stochastic pre-cooling compared to electron cooling only. Stochastic cooling was only required in the transverse direction, reducing the initial beam emittance of about 0.3 mm mrad to 0.09 mm mrad (horizontal) and 0.8 mm mrad to 0.12 mm mrad (vertical). This leads to a faster electron cooling not only in transverse direction but also longitudinally. The momentum cooling time is reduced from $\tau = 20.2(10)$ s to 7.7(3) s due to the lower emittance. At the same time the equilibrium momentum uncertainty is reduced from $\Delta p/p = 6.1(2) \times 10^{-5}$ to $3.0(2) \times 10^{-5}$ while showing a more symmetric shape.

This shows how cooling can be improved significantly by combining the advantages of both cooling systems.

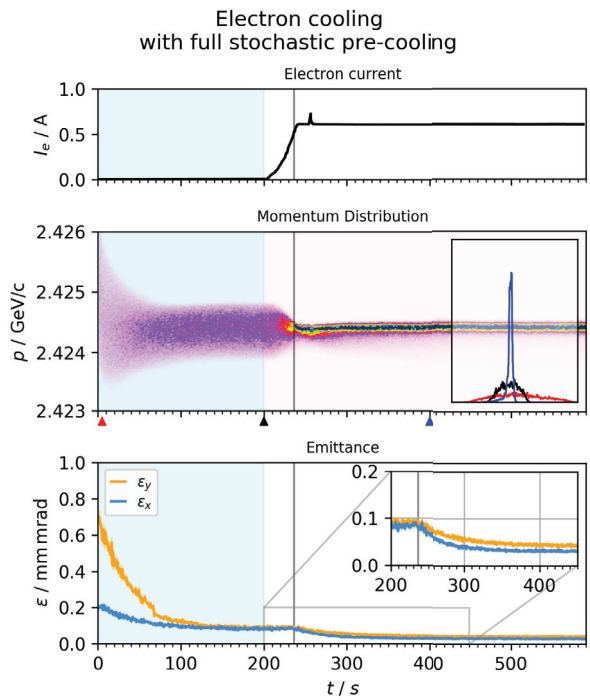

Figure 2: Momentum distribution (middle plot) and emittance (lower plot) of a 2.425 GeV/c proton beam consisting of $3 \cdot 10^8$ particles. The beam is cooled with longitudinal and transversal stochastic cooling for the first 200 s. Afterwards electron cooling is applied. The electron current of 0.73 A at 907.9 keV is shown in the upper plot. The initial momentum spread of $\Delta p/p = 5 \cdot 10^{-4}$ (red marker and spectrum) is reduced to $2 \cdot 10^{-4}$ (black) and finally $0.3 \cdot 10^{-4}$ (blue).

ISBN: 978-3-95450-218-9 ISSN: 2226-0374 doi:10.18429/JACoW-COOL2019-FRX01

Counteracting Adverse Target Effects

Additional experiments with the electron cooler were carried out while a target was installed in the ring. The PANDA Cluster-Jet Target [6] generates hydrogen clusters with an effective density of 1×10^{13} cm^{-2} to 2×10^{15} cm^{-2}. Measurements at a density of 1×10^{15} cm^{-2} showed that the emittance control in the present set-up is not strong enough to compensate the emittance growth due to beam-target-interaction. The mean energy loss can be compensated for by the barrier bucket system.

However, at an average target density of 2×10^{14} cm^{-2} the most emittance growth can also be compensated by electron cooling. It is again useful to combine the electron cooling with transverse stochastic cooling so a low emittance is reached faster. With electron cooling only, the momentum distribution is broader and energy loss due to the target is clearly visible (see Fig. 3). By using transverse stochastic pre-cooling and therefore having a lower emittance we were able to enhance the electron cooling process. This results in narrower and more symmetric momentum distribution and fewer beam losses (see Fig. 4).

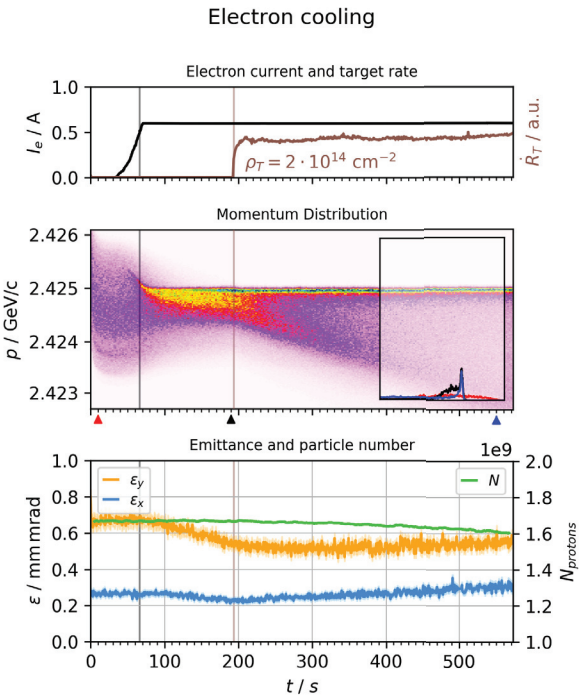

Figure 3: Momentum distribution (middle plot) and emittance (lower plot) of a 2.425 GeV/c proton beam consisting of $1.7 \cdot 10^9$ particles. The beam is cooled with electron cooling only. The electron current of 0.6 A at 908 keV is shown in the upper plot along with the target-beam-interaction event rate. The initial momentum spread of $\Delta p/p = 6 \cdot 10^{-4}$ (red marker and spectrum) is reduced to $2 \cdot 10^{-4}$ (black) before target operation. The target is switched on at 190 s.

During our experiments an artefact appeared in the schottky-spectrum when electron and transverse stochastic cooling were applied at the same time. The artefact is clearly visible in the momentum distribution calculated from the schottky-signal measured at the stochastic cooling pick-up in Fig. 4. The reason for its appearance in the schottky-signal is not yet fully understood. One can also see a disturbance in the horizontal emittance at the same time. However this is purely an effect of calculation when obtaining the emittance from a beam profile measurement (dispersion). The beam profile measured with an Ionisation Profile Monitor (IPM) does not show the disturbance in either plane. Therefore it is possible that the observed artefact is a coherent effect rather than a beam instability. It might possibly be related to the pick-up used, which is part of the stochastic cooling loop.

ELECTRON VELOCITY PROFILE

Method

We describe a method of measuring the electron velocity distribution within the electron beam by probing it with the pencil proton beam. Therefore the beam is well cooled in advance of the measurement. Making use of the new EPICS software components the electron orbit is then shifted in the cooling section by keeping it parallel to the proton beam. Thereby the relative position of the pencil proton

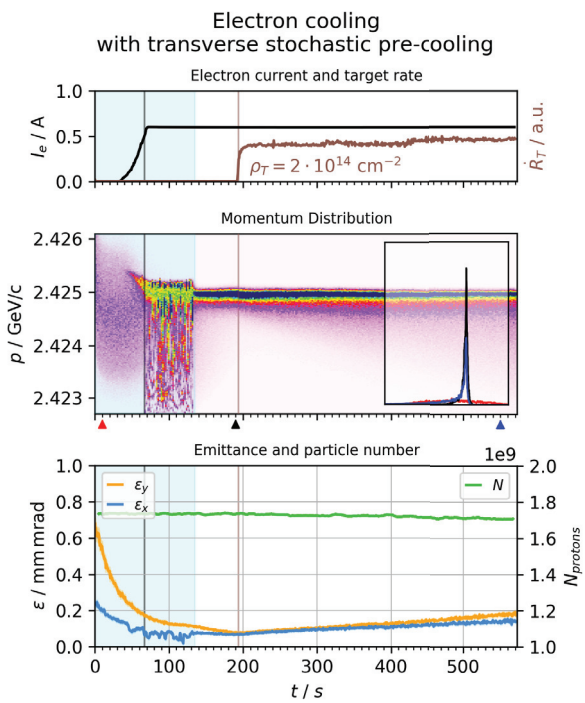

Figure 4: Beam properties as in Fig. 3. Here the beam is cooled with transversal stochastic cooling for the first 135 s and electron cooling starting at 50 s. The initial momentum spread of $\Delta p/p = 6 \cdot 10^{-4}$ (red marker and spectrum) is reduced to and kept at $3 \cdot 10^{-5}$.

ISBN: 978-3-95450-218-9 ISSN: 2226-0374 doi:10.18429/JACoW-COOL2019-FRX01

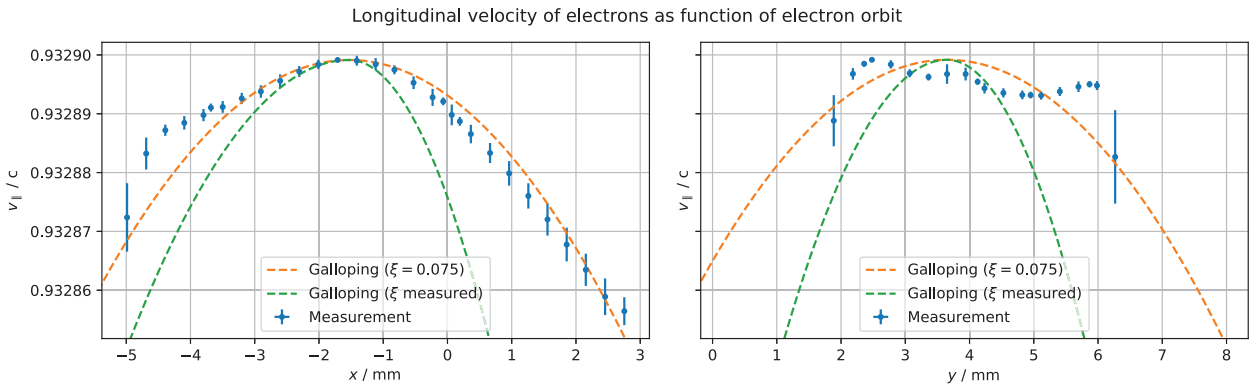

Figure 5: Measurement of the horizontal and vertical distribution of the electron's longitudinal velocity component within the electron beam. The fitted theoretical shape due to galloping effects is indicated for comparison (orange dashed lines). The rate was also obtained by measuring the larmor radius as function of the magnetic field (shape in green dashed lines).

beam within the (larger) electron beam is changed systematically.

Due to the cooing dynamics the protons adjust to the local velocity of the electrons. When moving the electron beam around the fixed pencil proton beam stepwise, the proton velocity changes accordingly. This yields a distribution of the effective electron velocity component parallel to the proton orbit. The velocity change of the protons can be deduced from the frequency change visible in a schottky-spectrum measurement. This way the electron velocity distribution within the electron beam (*velocity profile*) can be obtained.

Measurement Results

Figure 5 shows the measured velocity distribution within the electron beam. It is clearly visible that there is a maximum point from where the longitudinal velocity decreases with distance. The horizontal profile shows a nearly parabolic shape where the velocity at the edge of the electron beam is reduced by a factor of about $5 \cdot 10^{-5}$. However the vertical profile has a complex shape where the velocity component is only reduced by a factor of $1 \cdot 10^{-5}$.

The reduced longitudinal electron velocity suggests an increased velocity component transverse to the particle motion. This can be explained by larmor oscillations due to the strong longitudinal magnetic guiding field in the cooling section (magnetized cooling). The effect is called galloping (or scalloping in some papers) as the transverse motion and therefore larmor-radius increases with distance from a maximum point [7].

The dashed curves in Fig. 5 indicate the theoretical distribution due to galloping with a fitted and measured galloping rate. The distribution seems to be dominantly caused by these effects, but the asymmetry especially in the vertical profile suggest an additional cause. This might be a higher order beam motion which can also explain the asymmetry in the vertical plane compared to the horizontal distribution. Also space charge effects have not been considered in the theoretical deliberations.

The presence of larmor oscillations impairs the transverse cooling. This is particularly critical for large diameter proton beams (high emittance) because interaction with the hot electrons at the outer region can not be prevented. Therefore much better cooling results are obtained for narrow proton beams.

SUMMARY AND OUTLOOK

Based on the EPICS integration of the 2 MeV electron cooler and related systems, measurements of combined stochastic and electron cooling were carried out. These show a significantly faster electron cooling and a lower equilibrium momentum spread for low beam emittance due to stochastic pre-cooling. This way we were able to combine the advantages of both cooling systems.

During simultaneous operation of the stochastic and electron cooling an artefact in the schottky spectrum was observed. We suspect that this might be a measurement-induced effect and intend to study the cause in the next beam time. Therefore it is planned to measure the schottky signal with an independent pick-up and also to check possible dependencies on the stochastic cooling loop and electron energy.

Additionally a measurement of the velocity distribution within the electron beam was performed. This indicates an issue with the transverse electron temperature mainly caused by larmor rotations. In order to improve the cooling process it is of high importance to compensate this transverse motion wherever possible. Space charge effects as well as the influence of the beam density profile were not yet taken into account. It is further planned to also consider asymmetric effects in the bending sections of the electron beam transport channel. These might give a possible explanation for the difference between the horizontal and vertical profile.

The present experiments prove that the combined use of stochastic and electron cooling is useful to obtain a small momentum spread and transverse emittance even while an internal target of high density is inserted in the ring. It is

ISBN: 978-3-95450-218-9 ISSN: 2226-0374 doi:10.18429/JACoW-COOL2019-FRX01

strongly suggested to use this kind of beam cooling method for the PANDA experiment and future HESR operation up to an anti-proton beam energy of about 3 GeV. The electron cooling will also be very effective for cooling of highly charged ion beams and therefore inevitably necessary to reach similar experimental conditions for ions in the HESR.

REFERENCES

[1] M. I. Bryzgunov *et al.*, "Features of cooling dynamics in a high-voltage electron cooling system of the COSY", *Technical Physics* 60.8 (2015), p. 1227-–1233. ISSN: 1063-7842. DOI: 10.1134/S1063784215080046

[2] V. Kamerdzhiev *et al.*, "2MeV electron cooler for COSY and HESR – first results", In *Proc. of the 5th International Particle Accelerator Converence*, IPAC2014, Dresden, Germany, May 2014. DOI:10.18429/JACoW-IPAC2014-MOPRI070

[3] EPICS: Experimental Physics and Industrial Control System. URL: https://epics-controls.org

[4] P. Niedermayer, "Integration of the COSY 2MeV Electron Cooler into EPICS", *Annual report 2018*, Institut für Kernphysik / COSY, 2018, p. 92–93. https://www.fz-juelich.de/ikp/DE/Service/Download/Downloads/jahresbericht_2018.pdf.

[5] P. Niedermayer, "Charakterisierung der Kühldynamik des 2MeV Elektronenkühlers am Beschleuniger COSY", 2019. Bachelor thesis, FH Aachen.

[6] A. Khoukaz *et al.*, "Technical Design Report for the PANDA Internal Targets: The Cluster-Jet Target and Developments for the Pellet Target", 2012. https://panda.gsi.de/publication/re-tdr-2012-002.

[7] M. I. Bryzgunov *et al.*, "Calculations of Electron Beam Motion in Electron Cooling System for COSY", in *Proc. of COOL09*, Lanzhou, China, September 2009, p. 134-–137. https://accelconf.web.cern.ch/accelconf/COOL2009/papers/thpmcp004.pdf.

ISBN: 978-3-95450-218-9 ISSN: 2226-0374 doi:10.18429/JACoW-COOL2019-TUPS01

SIMULATION OF ELECTRON COOLING AND IBS AT EICC*

X. D. Yang†, Institute of Modern Physics, CAS, Lanzhou, China

Abstract

Electron Cooling will be considered in the future project EICC. In this high energy region, electron cooling is very different from the traditional low energy situation. For getting high luminosity, the high intensity and long lifetime of ion beam was required with the help of electron cooling. Electron cooling and IBS were simulated in the cases of high energy and high intensity for typical ion, proton and Uranium. Some initial parameters were obtained from the simulation. It will be helpful for the understanding of high energy electron cooling.

INTRODUCTION

Based on the HIAF (the Heavy Ion High Intensity Accelerator Facility, approved in 2015 in China), a high luminosity polarized Electron Ion Collider facility in China (EicC) was proposed to study of hadron structure and the strong interaction and to carry out the frontier research on both nuclear and particle physics.

EicC will be constructed in two phases, EicC-I and EicC-II. In the first phase, the proton beam with energy between 12~30 GeV will collide with electron beam with energy between 3~5 GeV in the collider. Both electron and ion beam are polarized. The luminosity will expect to achieve 4×10^{33}.

In the second phase, the energy of proton will upgrade to 60~100 GeV, and the energy of electron beam will increase to 5~10 GeV, the luminosity will expect to achieve 1×10^{35}. The primary design and some initial parameters of EicC will be found in the reference [1].

In order to obtain the expected luminosity in collider, the polarized proton beam should be cooled by various cooling methods among the whole energy range. In the case of high intensity high energy ion beam especially, the intra-beam scattering effect should be taken into account in the collider design. Some primary simulation on the electron cooling and intra-beam scattering were presented in this contribution.

SIMULATION OF COOLING

The cooling rate not only depends on the storage ring lattice parameters, the Betatron function, dispersion of the cooling section, initial emittance and momentum spread of ion, energy and charge state of ion beam, but also on the construction of electron cooling device, the strength of magnetic field, the parallelism of magnetic field in the cooling section, the effective cooling length, and the parameters of electron beam, such as radius, density and transverse temperature of electron beam. These parameters are determined by the storage ring and the technology limitation, on the other hand, they are influenced and restricted each other.

With the help of electron cooling code SIMCOOL [2, 3], the cooling time of ion beam were extensive simulated in various parameters of the ion beam in the EicC, such as ion beam energy, initial transverse emittance, and momentum spread. The influence of the machine lattice parameters-Betatron function, and dispersion function on the cooling time was investigated. The parameters of electron beam and cooling devices were taken into account, such as effective cooling length, magnetic field strength and its parallelism in cooling section, electron beam current.

Ion Beam Parameters

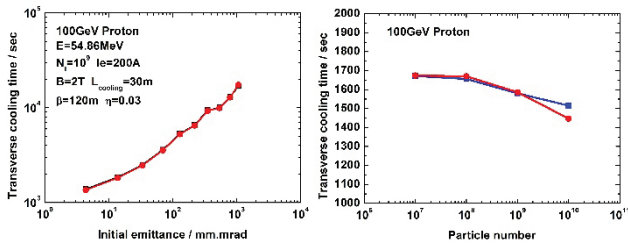

Figure 1: The transverse cooling time as a function of the initial emittance (left) and the particle number in the ion beam (right).

Left diagram of Fig. 1 shows the transverse cooling time as a function of the initial emittance. Right diagram of Fig. 1 gives the dependence of cooling time of the transverse direction on the particle number in the ion beam. In the case of other fixed parameters, the transverse cooling increases with the initial emittance and slightly decreases with the particle number in the ion beam.

Electron Beam Parameters

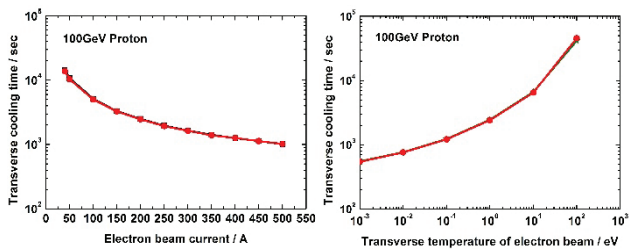

Figure 2: The transverse cooling time as a function of the electron beam current (left) and the transverse temperature of electron beam (right).

In order to decrease the transverse cooling time, the current of electron beam and length of cooling section was set as a bigger value. Left diagram of Fig. 2 presents the transverse cooling time as a function of the electron beam current. Right diagram of Fig. 2 indicates the cooling time depends on the transverse temperature of electron beam. In

* Work supported by NSFC No. 11375245, 11475235, 11575264
† yangxd@impcas.ac.cn

ISBN: 978-3-95450-218-9 ISSN: 2226-0374 doi:10.18429/JACoW-COOL2019-TUPS01

the case of other fixed parameters, the transverse cooling time decreases with the increasing electron beam current and decreasing transverse temperature of electron beam.

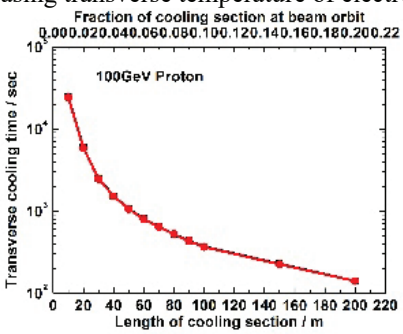

Figure 3: The transverse cooling time as a function of the length of the cooling section.

Figure 3 shows the transverse cooling time varies as a function of the length of the cooling section. In the case of other fixed parameters, the transverse cooling time decreases with the length of the cooling section. The length of cooling section strongly influence the cooling time.

Magnetic Field Parameters

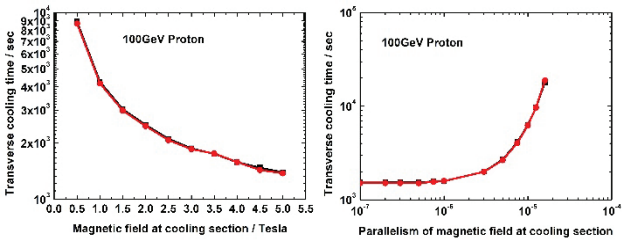

Figure 4: The transverse cooling time as a function of the magnetic field strength in the cooling section (left) and the parallelism of magnetic field in the cooling section (right).

Left one of Fig. 4 shows the transverse cooling time as a function of the magnetic field strength in the cooling section, and right one of Fig. 4 presents the transverse cooling time as a function of the parallelism of magnetic field in the cooling section. In the case of other fixed parameters, the transverse cooling time decreases with the magnetic field strength in the cooling section. The transverse cooling time decreases with the increasing parallelism of magnetic field in the cooling section. From Fig. 4, one can see the magnetic field strength strongly influence on the cooling time. The cooling time becomes shorter when the magnetic field parallelism is higher in the cooling section.

Storage Ring Parameters

Left diagram of Fig. 5 gives the dependence of transverse cooling time on the transverse Betatron function. The transverse cooling time decreases with the Betatron function in the cooling section. Right diagram of Fig. 5 presents the transverse cooling time as a function of dispersion. If the dispersion in the cooler position is positive, the cooling time becomes shorter than zero dispersion.

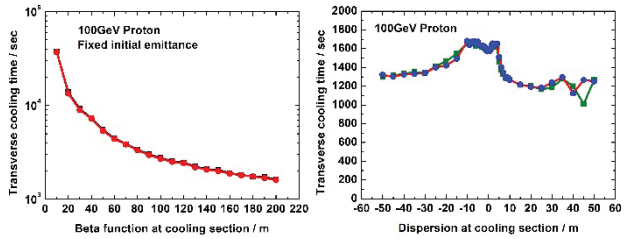

Figure 5: The transverse cooling time as a function of the Betatron function in the cooling section (left) and the dispersion function in the cooling section (right).

SIMULATION OF IBS

The luminosity is determined by the quality of ion beam, and the quality of ion beam was determined by the initial emittance, momentum spread and longitudinal size.

The ability of cooling was determine by the parameters of electron beam, such as electron beam density, temperature and length of cooling section in the storage ring, but also depends on the magnetic parameters in the cooling section.

The effect of intra-beam scattering depends on the particle density and ion species. It is more serious and important in the situation of high intensity, high energy, high charge state of heavy ion beam.

In order to simulate the intra-beam scattering, the electron beam current was set as zero in the simulation code SIMCOOL. There is no cooling effect in this case, and only scattering effect in the simulation. The transverse scattering time was derived from the data fitting of simulation results.

In order to compare the simulated results, only one parameter was changed during the simulation, and the other parameters were kept as fixed.

In the case of fixed initial emittance, for the situation of bigger particle number, the ion beam scattered at the beginning, and then cooled, finally keep the emittance constant. The final emittance were different under the cooling by different electron beam current.

Initial Emittance

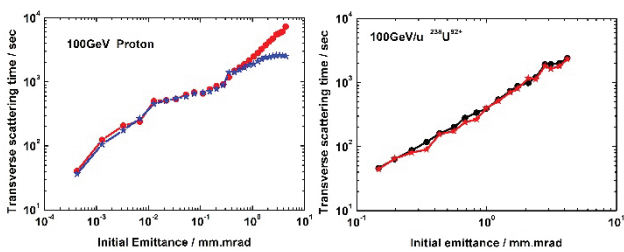

Figure 6: The transverse scattering time as a function of the initial emittance of proton (left) and uranium (right) ion beam.

The transverse scattering time as a function of the initial emittance of proton beam (left) and uranium beam (right) were illustrated in the Fig. 6. In the case of other fixed parameters, the transverse scattering time increases with the increasing initial emittance. The similar behaviour was observed in the two kind of ion beam.

ISBN: 978-3-95450-218-9 ISSN: 2226-0374 doi:10.18429/JACoW-COOL2019-TUPS01

Particle Number

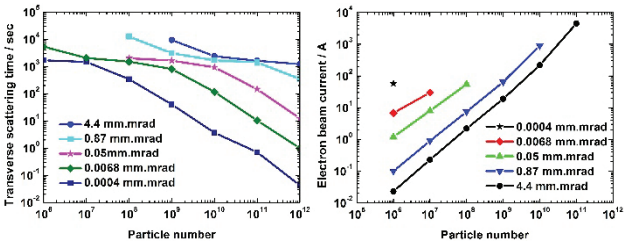

Figure 7: The transverse scattering time as a function of the particle number in the ion beam (left). The necessary electron beam current as a function of the particle number in the ion beam in order to keep the emittance constant in the case of different initial emittance (right).

The transverse scattering time as a function of the particle number in the uranium ion beam was demonstrated in left of Fig. 7. In the case of fixed other parameters, the transverse scattering time decreases with the increasing particle number in the ion beam.

Final Equilibrium Emittance

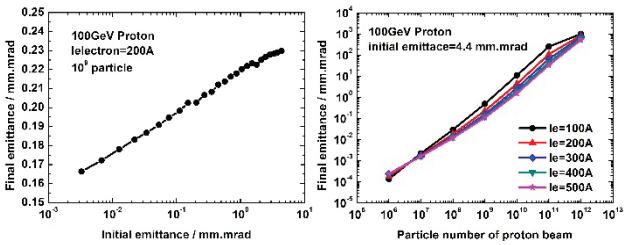

Figure 8: The final equilibrium emittance as a function of the initial emittance in the case of 200 A electron beam cooling (left). The final equilibrium emittance as a function of the particle number in the ion beam in the case of different electron beam cooling (right).

Left one of Fig. 8 shows the final equilibrium emittance as a function of the initial emittance in the case of 200 A electron beam cooling. Left one of Fig. 8 presents the final equilibrium emittance as a function of the particle number in the ion beam in the case of different electron beam cooling. The final equilibrium emittance was mainly dominated by the particle number in the ion beam.

Necessary Electron Beam Current to Keep the Emittance Constant

Right picture of Fig. 7 gives the necessary electron beam current as a function of the particle number in the ion beam in order to keep the emittance constant in the case of different initial emittance. The bigger electron beam current was needed in the case of large particle number.

SUMMARY

From the simulated results, the transverse cooling time of proton beam with 100 GeV is over 1000 seconds. The transverse cooling time can be shorten with the help of proper configuration of the parameters, such as smaller initial emittance and electron transverse temperature, higher magnetic field strength, parallelism of magnetic field in the cooling section, longer length of electron cooling section, stronger electron beam current, and bigger beta function and dispersion function in the cooling section.

With respect to IBS, the transverse scattering time not only depends on initial emittance, but also depends on the particle number. The final equilibrium emittance was dominated by the particle number in the ion beam.

In order to maintain the final emittance as constant value, the minimum electron beam current are different in the case of different emittance and particle number.

The emittance, particle number and longitudinal length of ion beam should be optimized and compromise carefully in order to obtain the required luminosity. By the way, the strategy of cooling are important too, such as multi-stage cooling [4] at different energy or different period. The emittance should be cooled to the required value by the stronger electron beam in the first stage, and then the smaller emittance will be maintained by the weaker electron beam.

For the sake of obtaining and keeping the smaller emittance in the case of proton beam with energy 100 GeV, the cooling should counteract the scattering at the different situation and period, and provide high quality proton beam for the higher luminosity in the storage ring. The detailed and exact simulation will be necessary for the real lattice design of the EicC storage in the future.

In the interest of achieving the required luminosity from physics experiments, the parameters of ion beam, electron cooling device and storage ring should be optimized carefully and compromised each other, and attempt the different configurations from the point of view of realizable technical solutions.

ACKNOWLEDGEMENT

The author would like to thank Prof. V. Parkhomchuk for him to provide the simulation code SIMCOOL and useful guidance in the simulation during this work.

REFERENCES

[1] Xurong Chen, “A Plan for Electron Ion Collider in China”, in *Proceedings of sciences, XXVI International Workshop on Deep-Inelastic Scattering and Related Subjects (DIS2018)*, Kobe, Japan, 16-20 April 2018.

[2] Vasily Parkhomchuk, Ilan Ben-Zvi, “Electron cooling for RHIC”, BNL C-A/AP/47, April 2001.

[3] A.V. Fedotov, I. Ben-Zvi, Yu. Eidelman, *et al*, “Simulation of high-energy electron cooling”, in *Proceedings of 2005 Particle Accelerator Conference*, Knoxville, Tennessee, USA, paper TPAT090, pp. 4251-4263.

[4] H. Zhang, Y. Zhang, Ya. Derbenev, *et al*, “Multi-stage electron cooling scheme for JLEIC”, in *9th International Particle Accelerator Conference IPAC’2018*, Vancouver, BC, Canada, paper MOPML006, pp. 397-399. doi:10.18429/JACoW-IPAC2018-MOPML006

ISBN: 978-3-95450-218-9 ISSN: 2226-0374 doi:10.18429/JACoW-COOL2019-TUPS03

VACUUM SYSTEMS FOR THE COOLERS OF THE NICA PROJECT

A. Bainazarova, M. Bryzgunov, A. Bubley*, N. Kremnev,
V. Parkhomchuk, A.Putmakov, V. Reva,
Budker INP SB RAS, Novosibirsk, Russia

Abstract

The NICA accelerator complex contains two electron coolers, one sits at booster and another at NICA collider. They have requirements for the vacuum of 10^{-11} mbar. Despite the coolers have different design the problems of getting vacuum are similar, lack of space along vacuum chambers, presence of the electron beam and oxide cathode usage. The solutions for achieving such a strict requirements are discussed in the article.

INTRODUCTION

The main part of the NICA accelerator complex is the collider for heavy ions up to $^{197}Au^{31+}$, which contains the 2.5MeV cooler. The injection chain of the NICA complex have the gold ions booster. Low energy cooler is one of the elements of the booster that provides sufficient improvement of the ion beam quality. The requirement for vacuum condition is usual for heavy ion accelerators of about 1×10^{-11} mbar [1,2].

VACUUM SYSTEMS

Vacuum system of the high energy cooler consist of two similar parts as shown on Fig. 1. They have identical structure and a little bit different size. Every system may be separated on to three parts by means of gate valves. Main part contains cooling section, which is installed at straight line of the collider so the chamber belongs to the cooler and collider, simultaneously. Other two parts are similar and include part of the transport channel and accelerating (or decelerating) column as shown on Fig. 2.

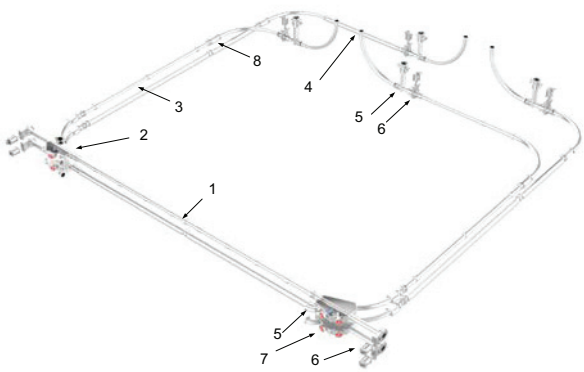

Figure 1: 1 - Cooling section vacuum chamber with BPMs (every one meter), 2 – toroid bend chamber equipped with two 2000 l/s NEG cartridges each, 3 – straight transport channel chamber with BPM, 4 – transition to the electrostatic accelerator, 5 – pumping ports, 6 – gate valves, 7 - NEG cartridges, 8 – special insertion with 1400 l/s NEG cartridge.

VACUUM GENERATION

The vacuum system of the cooler of the NICA booster has similar structure as the main part of vacuum system for the collider despite of the fact that they have completely different size and the shape. As the low energy cooler was successfully commissioned [3] and vacuum condition of 2×10^{-11} mbar was achieved, we rely on all solutions applied for this. Vacuum equipment is similar for both coolers (see Table 1).

Table 1: Vacuum Equipment for One Vacuum System of the High Energy Cooler

Cooling section	Agilent VacIon Plus 300 Noble Diode with TSP Cartridge	2
	CAPACITORR CF 100 MK5 NEG cartridge	4
	Pfeiffer IMR 430, Extractor-system, DN 40 CF-F	1
	VAT All-metal angle valve DN160CF	2
	Turbomolecular pump 700 l/s	1
Transport channels	UHV1400 WAFER MODULE NEG cartridge	1
	VAT All-metal angle valve DN100CF	1
Accelerating column with bending chamber	Agilent VacIon Plus 300 Noble Diode with TSP Cartridge	1
	CAPACITORR D 100 NEG cartridge	4
	Pfeiffer IMR 430, Extractor-system, DN 40 CF-F	1
	Turbomolecular pump 300 l/s	1

Both coolers have oxide cathode as an electron emitter for the electron gun. The oxide cathode, as required, has to be activated during the vacuum system bake-out with back pumping. The activation process is very sensitive to the vacuum condition when the cathode surface is overheated to provide necessary temperature.

Use of the NEG pumps for the distributed pumping was chosen for all vacuum systems belonged to high or low energy coolers. All of those pumps have to be activated at first time of use and reactivated in a definite period according to manual. In a process of reactivation the sufficient amount of hydrogen is released from the pumps surface that have to be pumped with the turbomolecular

ISBN: 978-3-95450-218-9 ISSN: 2226-0374 doi:10.18429/JACoW-COOL2019-TUPS03

pump. The influence of the hydrogen to the oxide cathode was studied during low energy cooler commissioning [4].

All components of the vacuum system of the low energy cooler were baked out up to 300ºC for about two days with back pumping that provided us required vacuum condition. On the other hand, for the high energy cooler the situation is rather different. According to design, vacuum components of the electrostatic accelerator cannot be backed out. Other parts i.e. cooling section and transport channels are going to be backed up to 250 ºC [5].

ELECTROSTATIC COLUMS

Every electrostatic accelerator of the cooler for collider contains accelerating and decelerating columns equipped with the electron gun and collector correspondently. Schematic view of the columns is shown on Fig.2. One can see that they are very similar to those installed at COSY 2MeV cooler [4]. Main different is the intermediate part as shown on Fig.2. Both columns have four 700 mm long tubes, those provide accelerating or decelerating of the electron beam up to 2.5MeV and down.

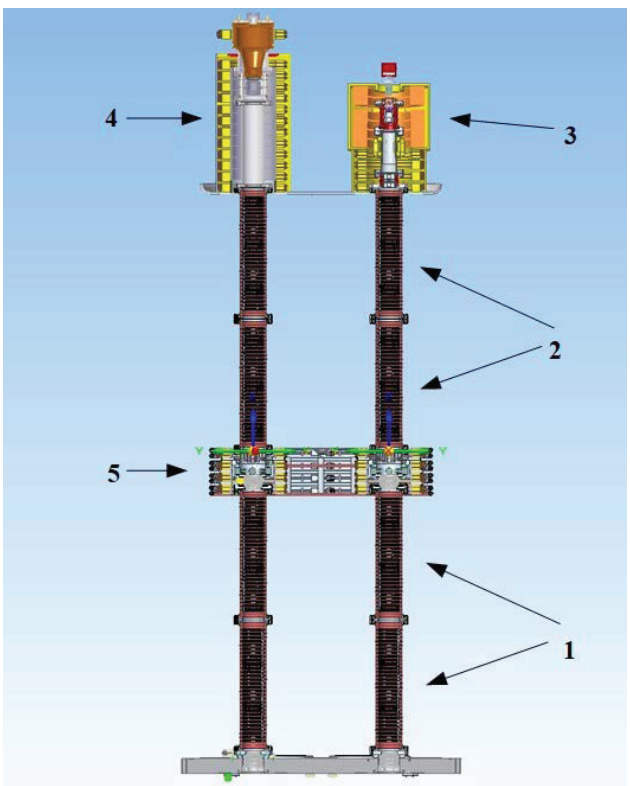

Figure 2: 1 -lower parts of the acceleration tube, 2 - upper parts of the acceleration tube, 3 –gun, 4 – collector, 5 – intermediate plate with mechanical support and NEG pumping chamber including bellows and BPM-s.

Scheme of the intermediate unit of the accelerating column is shown in Fig.3. This part has mechanical support to the column of the high voltage sections so that upper tube has fixed position. Lower tube has a bellows on the top to eliminate possible small misalignment. BPMs are included in to intermediate unit for both accelerating and decelerating columns to measure whether centre of the electron beam is on the right position. Four NEG pumps are installed on the middle of the module to provide distributed pumping.

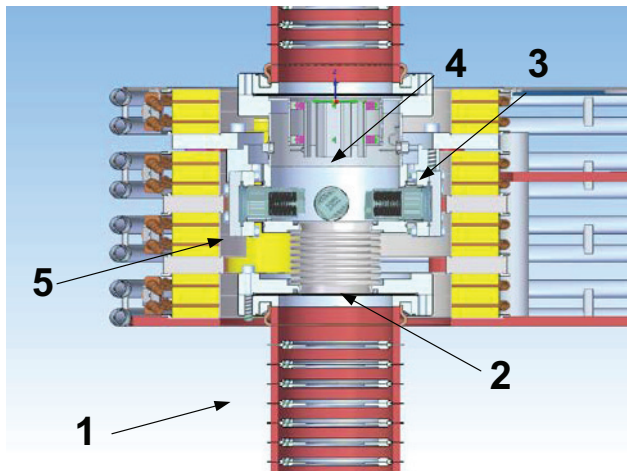

Figure 3: 1 – accelerating tube, 2 – bellows, 3 - mechanical support, 4 - BPMs, 5 - NEG pumps.

ACCELERATING TUBES

Each part of the tube consists of several ceramic and titanium rings brazed togrther as a “sandwich” unless ends where stainless rings are attached (see Fig.2).

Ceramic rings properties:

- outer diameter 135 mm
- wall thickness 7,5 mm
- height 19 mm
- material 94% Al_2O_3, admixture – manganese (pink cesamics)

electrical strength is not less then 10 kV/cm

Accelerating electrodes distributed along the section with the step of 19 mm and have inner diameter of 60 mm. Electrodes on the ends of tube have special shape (see Fig.4) in order to produce more or less homogeneous longitudinal electical field.

Flanges DN160CF are welded on the both sides of the module to connect it to other vacuum parts.

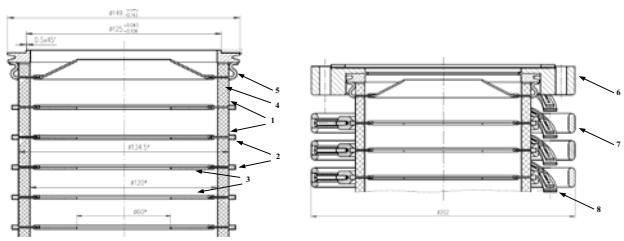

Figure 4: Schematic drawing of the part of the accelerating tube. 1 - ceramics, 2 – titanium rings, 3 – stainless steel electrodes, 4 – ceramic compensator, 5 – stainless steel ending for welding. 6 – flange DN160CF, 8 – divider (chain of HV resistors), 7 – stainless outer rings.

ISBN: 978-3-95450-218-9 ISSN: 2226-0374 doi:10.18429/JACoW-COOL2019-TUPS03

VACUUM CONDITION ESTIMATION

The vacuum condition estimation was made for the chosen geometry of the accelerating column including tube, gun, collector etc. (see above). Every module was taken as regular structure with total length of 700 mm, pumping speed for both sides is 200 l/s,
thermal desorption for the electrodes surface (room temperature) is 10^{-10} mbar×l/(s×cm^2)

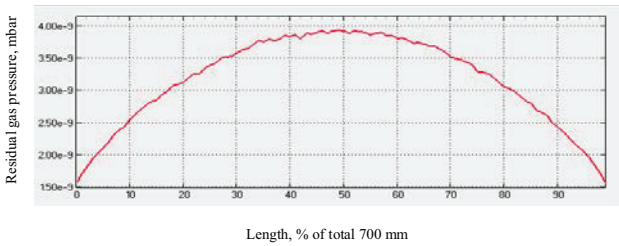

Figure 5: Residual gas pressure depending on accelerating tube length.

Figure 5 shows results of simulations of the residual gas pressure inside accelerating module.
Vacuum conductivity for the accelerating module is calculated as approximately 23 l/s.

The main problems for the required vacuum condition obtaining is the lack of space for the pumping equipment inside high-pressure vessel so it is difficult to increase the pumping speed significantly, besides low conductivity of the tube also limits the ultimate vacuum.

As a result of simulation we should mention that ultimate vacuum inside accelerating tube strongly depends on thermal desorption for the electrodes surface that was taken as 10^{-10} mbar×l/(s×cm^2). This value may vary within 10^{-11} - 10^{-13} mbar×l/(s×cm^2) for the stainless steel annealed in the vacuum oven at 450ºC.

In so far as current design of the electrostatic accelerator doesn't presuppose any backing-out of the vacuum parts inside high pressure vessel in complete assembly the following technique is proposed:

- every vacuum module is backed-out at the special vacuum test bench located as close to the place of assembling as possible.
- after the required vacuum is obtained the module is filled with dry nitrogen (or another appropriate gas)
- module is mounted to the assembly as fast as possible.

SUMMARY

The low energy electron cooler was successfully commissioned at NICA booster. All vacuum techniques were successfully tested during this time.

The high-energy cooler is under construction at BINP. Similar equipment and are applied to it's vacuum system. Nevertheless, the use of other techniques is still possible. So for example, NEG coating of the inner surface of the vacuum chambers is still under consideration.

REFERENCES

[1] I. N. Meshkov and G. V. Trubnikov, "NICA Project: Three Stages and Three Coolers", in *Proc. 11th Workshop on Beam Cooling and Related Topics (COOL'17)*, Bonn, Germany, Sep. 2017, pp. 84-88. doi:10.18429/JACoW-COOL2017-THM21

[2] N.Agapov, A.Butenko, *et al.*, "Booster synchrotron for NICA collider", *Physics of Particles and Nuclei Letters*, 2010, Vol. 7, No. 7, pp. 723–730.

[3] A.Bubley, *et al.*, "Low energy electron cooler for the NICA collider", in *Proc. 11th Workshop on Beam Cooling and Related Topics (COOL'17)*, Bonn, Germany, Sep. 2017, doi:10.18429/JACoW-COOL2017-TUM11

[4] Reva V. B. *et al,* "COSY 2 MeV Cooler: Design, Diagnostic and Commissioning" *in Proc. of IPAC 2014*, Dresden, Germany, May 2014, p. 777-779.

ISBN: 978-3-95450-218-9 ISSN: 2226-0374 doi:10.18429/JACoW-COOL2019-TUPS04

PRELIMINARY STUDIES OF BEAM-INDUCED FLUORESCENCE AND STATUS OF THE BEAM-CURRENT UPGRADE OF THE ELECTRON-COOLER TEST-BENCH AT HIM*

T.Beiser†[1], M. W. Bruker[2,4], K. Aulenbacher[2,3], J. Dietrich[2]
[1]Institut für Kernphysik, Johannes-Gutenberg Universität, Mainz, Germany
[2]Helmholtz-Institut Mainz, Mainz, Germany
[3]GSI Helmholtzzentrum für Schwerionenforschung, Darmstadt, Germany
[4]now at Thomas Jefferson National Accelerator Facility, Newport News, VA, U.S.A.

Abstract

First wavelength-resolved studies of the beam-induced fluorescence (BIF) have been made at the cooler teststand. Its upgrade to 30 kV has been completed, which will allow operation at 1 Ampere beam current. Operation with the upgraded parameters is imminent and options for further experiments will be discussed.

ELECTRON COOLER TEST BENCH AT HIM

A electron cooler test bench including components from TSL (Uppsala) and BINP (Novosibirsk) has been put into operation at Helmholtz-Institut Mainz (HIM) and is currently working at $U_{\mathrm{Source}} = 17\,\mathrm{kV}$, $U_{\mathrm{Collector}} = 3\,\mathrm{kV}$ and $I = 0.55\,\mathrm{A}$ (figure 1). From the source to the collector, the

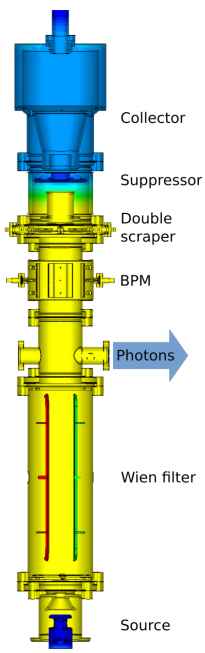

Figure 1: Schematic sketch of the electron cooler at HIM.

beam is immersed in a longitudinal magnetic field. So far, the main investigations were related to the relative number of backstreaming electrons from the collector. The results indicate that the flow of electrons towards ground potential in a fully magnetized high energy cooler is very low. This is mainly due to the implementation of the Wien filter, which was already installed in the COSY cooler developed by BINP [1]. A detailed description of our apparatus and the results achieved can be found in [2]. The present study aims at optical detection as a method of obtaining information about the electron beam intensity distribution.

OPTICAL BEAM DIAGNOSTICS

We have observed that even under UHV conditions (pressure when electron beam is on: $< 2 \cdot 10^{-10}$mbar) photons are emitted from the apparatus. In order to find out if they are related to the beam or to other background sources (e.g. light emitted from the collector), we have performed several test experiments.

At the windowed flange just above the Wien filter (position marked "Photons" in figure 1), photons emitted from the beam pipe can be observed. These were measured by an optical setup consisting of a remotely controllable lens and slit in front of a cooled photomultiplier tube (PMT, $T_{\mathrm{PMT}} = -20\,^{\circ}\mathrm{C}$). The distance of the lens from the beam orbit is varied with the intention to find a distance where a sharp image is obtained. The definition of the image was investigated in one dimension by moving the slit laterally in front of the PMT (figure 2).

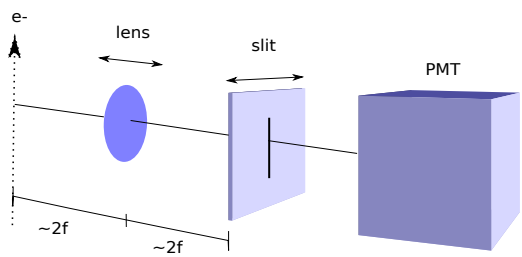

Figure 2: Schematic of the optical setup.

A series of bandpass filters with different center wavelengths (400 nm, 450 nm, 500 nm, 550 nm, 600 nm, 650 nm, 700 nm) and a FWHM bandwidth of $\lambda_{\mathrm{FWHM}} = 50\,\mathrm{nm}$ were added behind slit in order to obtain wavelength-resolved measurements. Transmission of the sapphire viewport (79-84%) and the quantum efficiency of the PMT (15-30%) were taken into consideration. This

* Work supported by BMBF Verbundforschung 05P18UMRB1
† thbeiser@uni-mainz.de

ISBN: 978-3-95450-218-9 ISSN: 2226-0374 doi:10.18429/JACoW-COOL2019-TUPS04

setup allowed us to scan the images width and the depth of field of the signal for a beam current of $I = 0.55$ A, as shown in figure 3. A background signal measured without an electron beam was subtracted. The infrared background caused by the dispenser cathode (BaW) behaves according to planck's law (figure 4) and becomes dominant above $\lambda_{CWL} = 550$ nm (figure 5). We have also determined the number of photons as a function of the beam current, which increases overproportionally (figure 6). A sharp image could not be observed, which is presumably due to reflections from the walls of the observation chamber.

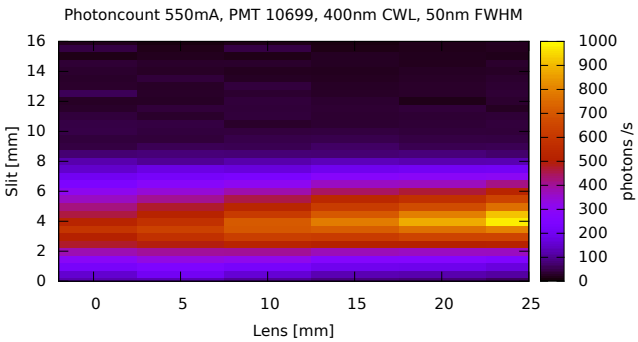

Figure 3: Photons per second for different lens and slit positions at a beam current of $I = 0.55$ A at $\lambda_{CWL} = 400$ nm; a background measurement with no electron beam has been subtracted.

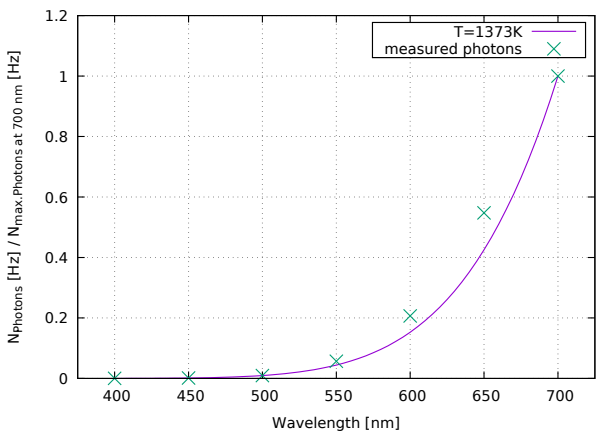

Figure 4: Background measurements compared to the black body radiation of the cathode at $T = 1373$ K.

These measurements do not contradict the preliminary hypothesis of fluorescence caused by ions (e.g. H_2^+) trapped in the electron beam potential [4] and suggest wavelength-resolved measurements at higher resolution with a higher beam current.

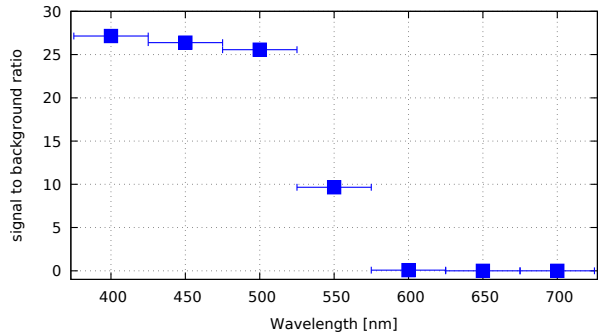

Figure 5: Signal to noise ratio for the measured wavelengths.

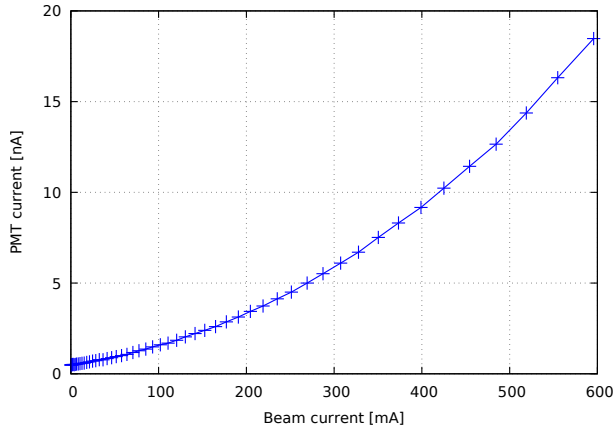

Figure 6: Photon signal for fixed lens and slit positions at different beam currents.

UPGRADE OF THE TEST BENCH

In order to increase the beam current to $I = 1$ A, the acceleration voltage needs to be raised to $U_{Source} = 30$ kV, which is why the test bench was fitted with larger electrical insulators. In first measurements, for solenoid fields at the source of $B_{Solenoid} \geq 60$ mT, it showed a tendency for gas-discharges, likely due to trapping, which requires avoidance of potential minima in regions A and B as shown in figure 7 [3].

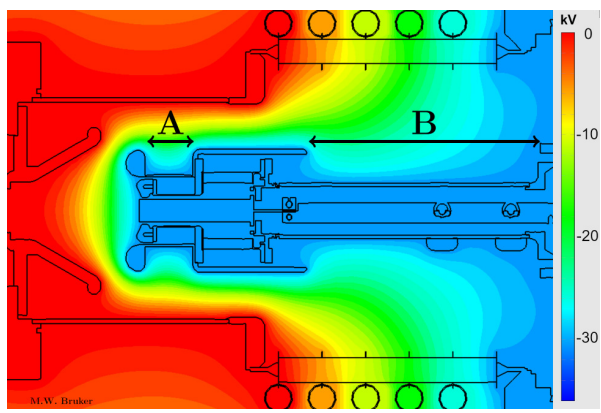

Figure 7: Potential map of the 17 kV source with regions A and B.

ISBN: 978-3-95450-218-9 ISSN: 2226-0374 doi:10.18429/JACoW-COOL2019-TUPS04

The source was altered with parts manufactured in-house (except the ceramics for the HV insulators) to allow an increase in HV and to shrink region B and avoid the narrowing in region A (figure 8).

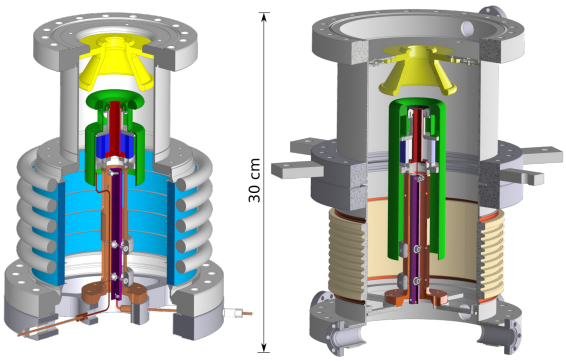

Figure 8: CAD models of the old (left) and new (right) source design.

After assembly in the HIM cleanroom (figure 9) the HV tests were executed successfully and the redesign proved to be robust against gas-discharges up to $B_{\text{Solenoid}} = 90\,\text{mT}$, with additional elongation (through addition of a second, identical coil (figure 10)) of the solenoid field against the beam direction up to the, with the given magnets, highest achievable field $B_{\text{Solenoid}} = 115\,\text{mT}$.

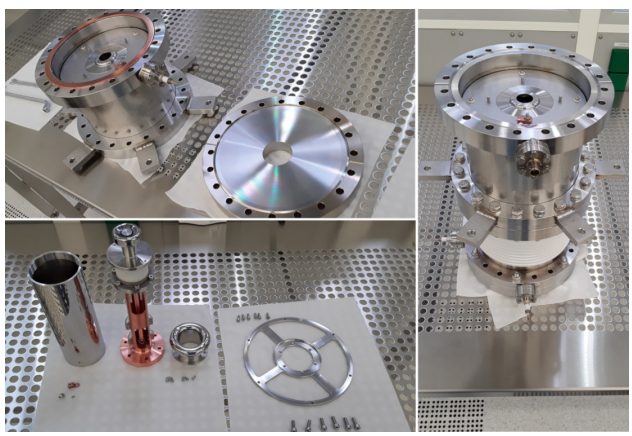

Figure 9: Different stages of assembly of the redesigned source in the HIM cleanroom.

In addition to the endeavor to increase the beam current, the observation chamber has been modified to decrease infrared background, i.e. it has been blackened with a graphite coating and a reflective screen mounting system was removed. After the HV tests of the source, the whole test bench has been assembled, evacuated and baked out. Improved HV- and radiation protection measures are being implemented as of the publication of this paper.

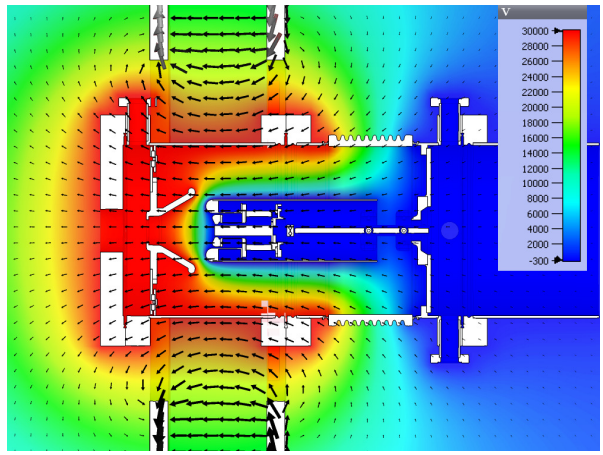

Figure 10: Potential map with magnetic field lines of the 30 kV source with the longer solenoid field.

CONCLUSION

Wavelength-resolved measurements of beam induced fluorescence (BIF) have been made via a cooled photomultiplier tube. These measurements show an overproportional correlation with the beam current and support the preliminary hypothesis of fluorescence caused by ions trapped in the beam potential. Measures to increase the beam current and reduce the infrared background caused by the hot dispenser cathode have been taken. Operation of the upgraded test bench is imminent. A cooled CCD camera for faster and more detailed measurements will be acquired in the near future and a higher resolution spectral analysis of the photon signal is in the planning stages.

REFERENCES

[1] M.Bryzgunov *et al.*, "Efficiency improvement of an electron collector intended for electron cooling systems using a Wien filter", *Technical Physics Vol. 58 No. 6*, 2013, pp.139-146.

[2] M.W. Bruker *et al.*, "Secondary electron measurements at the HIM electron cooler test set-up", *Nuclear Inst. and Methods in Physics Research*, A 872 (2017), pp.169–173.

[3] M.W. Bruker, "Untersuchung der Rückgewinnungseffizienz eines Kühlerelektronenstrahls in longitudinalem Magnetfeld", *PhD thesis (2016)*, pp.79-87.

[4] C. J. Brasefield *et al.*, "The Spectrum of the Hydrogen Molecular Ion", *Proc Natl Acad Sci U S A. 1928 Sep; 14(9)h*, pp.686–689.

ISBN: 978-3-95450-218-9 ISSN: 2226-0374 doi:10.18429/JACoW-COOL2019-TUPS05

THE HIGH VOLTAGE POWER SUPPLY SYSTEM FOR THE ELECTRON COOLER FOR CSRe

D. N. Skorobogatov, M. I. Bryzgunov, M. Kondaurov, A. Putmakov, V. B. Reva, V. V. Repkov
Budker Institute of Nuclear Physics of SB RAS, Novosibirsk, Russia

Abstract

The high-voltage power supply system for upgrade of the electron cooling system of CSRe ring in the IMP, was developed at the BINP in 2014 - 2019. The main features are - maximum voltage is 300 kV, stability - 10ppm, with the ability of quick changing of voltage in range ±10% of nominal voltage for a time not more than 500 μs. The key points of this design are presented in this article.

INTRODUCTION

In 2014 – 2019 upgrade of the electron cooling system of CSRe ring in the IMP (Lanzhou, China) was carried out. The high-voltage power supply system for upgrading was developed at the BINP. The power supply system consists of 10 controlled modules, distributed by the high voltage potential. Each module has a precision controlled voltage source. All the systems are controlled through the wireless network interface. System was installed and tested at CSRe ring in IMP at May – June of 2019.

High voltage system of such a modular structure already was created in BINP earlier for an high voltage electron cooler for heavy ions, which was installed on the COSY accelerator (Jülich, Germany) [1, 2]. New system has essential differences from old one. It does not have current sources for solenoids, but it has additional circuits for detuning mode. This mode allows change the energy of electron beam within 10% range from mean level. The main parameters of the cooler are as follows: the electron energy is from 5 keV to 300 keV and the current is up to 2 A. The energy instability of the new supply system will not exceed 10 ppm. Main limitations for installation is the need to fit into an existing vessel installed on an already-existing electron cooling system.

The main parameters of the accelerator column of the cooler are presented in Table 1.

Table 1: Main Parameters of the Power Supply System

Parameter	Units	Value
Supply voltage	kV	5 - 300
Voltage instability, less than	ppm	10
External power supply	V	400 - 500
Carrier frequency	kHz	20
Power consumption	kW	3-5
Total height of the column	m	1

Designed power supply system along with precision output parameters should have high reliability and resistance to high voltage discharges.

STRUCTURE OF THE POWER SUPPLY SYSTEM

The structure of the power supply system is shown in Fig. 1.

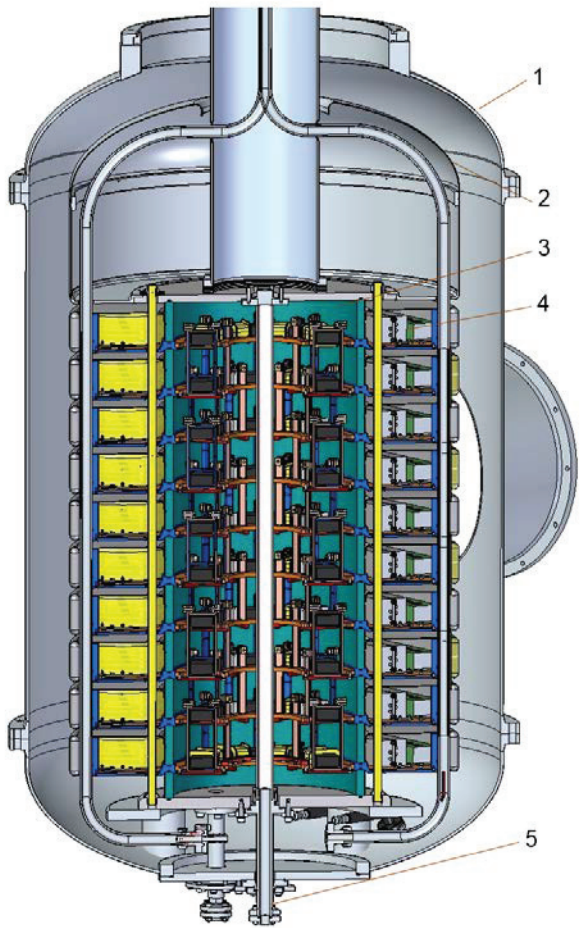

Figure 1: The structure of the high voltage column. 1 – SF_6 tank; 2 – shielding cover; 3 – high voltage cascade transformer; 4 – high voltage section; 5 – isolating and cooling oil tubes.

The high voltage column is placed in the tank, filled with SF_6, and contains high-voltage sections, cascade transformer, oil tubes for high voltage terminal, and communication circuits.

The SF_6 tank already exists in the cooling system, so dimensions of sections are determined by the tank dimensions and high voltage clearances. The cascade transformer provides required power for the high voltage sections and high-voltage terminal. The high voltage

ISBN: 978-3-95450-218-9 ISSN: 2226-0374 doi:10.18429/JACoW-COOL2019-TUPS05

sections provide a voltage required for electron beam acceleration.

Requirements to high voltage in the accelerator column are pretty tough: the ripple and long-term instability shall not exceed 10^{-5}. A full voltage is generated by 10 high-voltage sections with a maximum voltage of 30 kV each. Additional requirement to high voltage section is ability of quick changing of accelerating voltage in range of ±10 % for the time of 500 μs.

The general view of the section is shown in Fig. 2.

Figure 2: The general view of the high voltage section.

The high-voltage section is powered from the power-takeoff winding on the corresponding section of the cascade transformer. Externally, the section looks like a disc 80 mm high of 750 mm in diameter, with a cascade transformer in center, closed with screens from above and below. The bottom screen is also a load-bearing element and supports the entire structure. Along the perimeter, the section is shielded with metal bands. A section comprises two aluminum support plates with electronic installed on them.

KEY POINTS OF DEVELOPING

From a user's point of view, the electronics of the high-voltage section is a high-precision regulated high-voltage power supply (1 mA, 30 kV), integrated into a shielded housing. One section consumes no more than 300 W: about 50 W for generation of high voltage, 20 W for thermal stabilization of precision divider, and the rest for providing fast energy changes. Acceptable supply voltages vary from 100V to 250V.

The essential part of electronics unit is precision high voltage divider. This part is enclosed in isolating box and has thermal stabilization for providing precision measurements of output voltage and feedback in the high-voltage stabilization circuits. A general view of the divider is shown in Fig. 3.

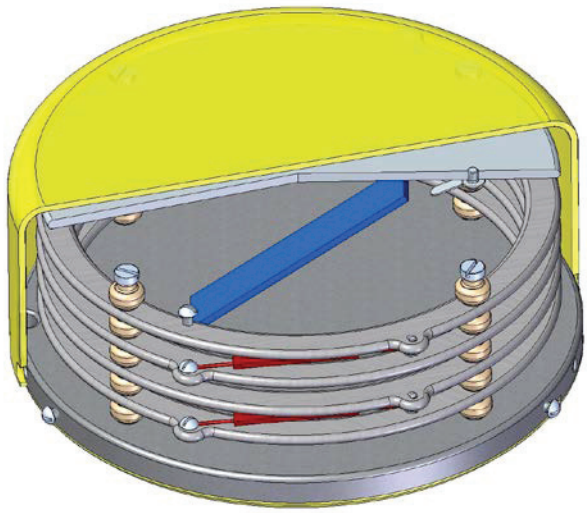

Figure 3: General view of the precision high voltage divider.

Key difference from earlier COSY cooler supply system is detuning operation mode. In this mode energy of electron beam changes in the range of ±10 % from mean value. So as load for the supply system is high voltage terminal, relatively high current needed to charge high voltage terminal capacitance during this energy changes. To have ability to change energy in 500 μs, peak current should be about 300 mA. Taking into account voltage up to 300 kV, peak power during this changes should be up to 100 kW (10 kW per section). Special high voltage amplifier designed to supply this power and provide accuracy.

Section also contains auxiliary power supply for the electronics, filtering elements, controller board, and a transceiver for communication with the controlling server by the radio frequency channel.

The control interface is realized in a ZigBee self-organizing network based on Telegesis transceivers [3]. This network operates in the 2.5 GHz radio frequency band, which allows to communicate without a large number of optical lines and simplifies the mounting and maintenance of the system. The structure of the section is shown in Fig. 4.

Prior to developing main high voltage supply system, we developed a prototype of high-voltage section, on which we made preliminary tests of all systems of the section and debugged the feedback of the power supplies. In addition, we tested resistance to electrostatic discharges. This prototype was designed in 19 inch rack and used as power supply for electrostatic plates. This part of power supply system was delivered to IMP one year earlier than main high voltage column, tested as main power supply for the low voltage cooler at CSRm, and used in recombination experiments [4].

ISBN: 978-3-95450-218-9 ISSN: 2226-0374 doi:10.18429/JACoW-COOL2019-TUPS05

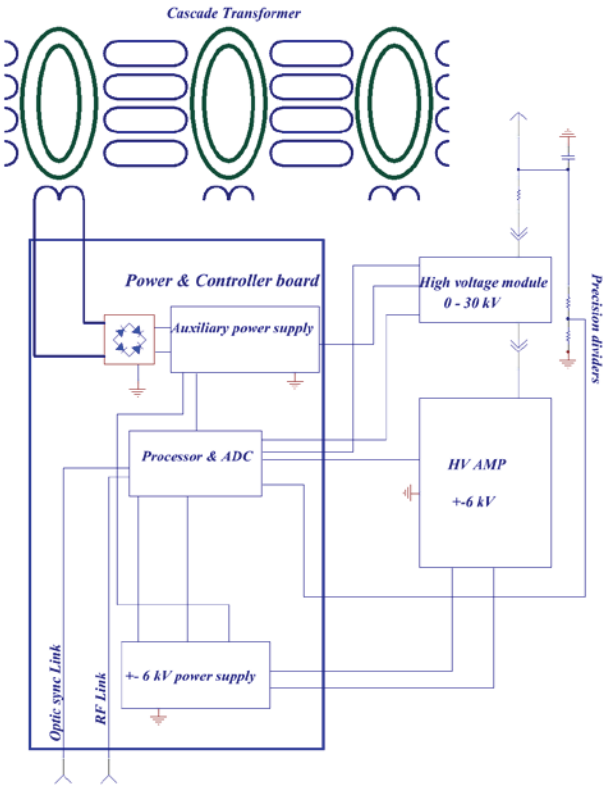

Figure 4: The structure of the high voltage section.

A set of programs with graphical interface were developed for control and monitor of the high voltage power supply system. A screenshot of the graphical interface of the program is shown in Fig. 5.

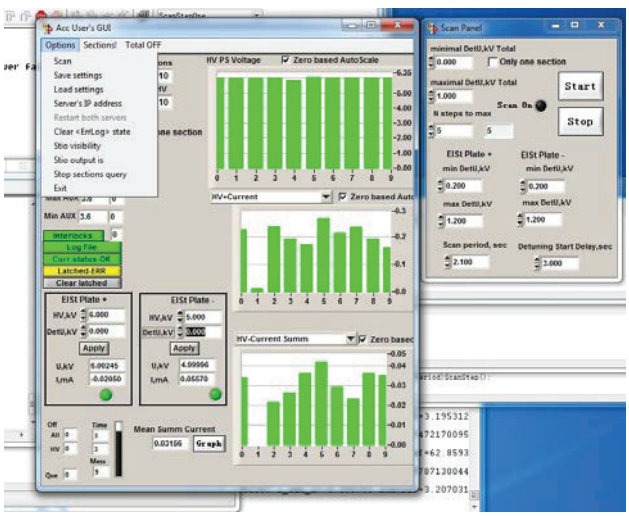

Figure 5: A screenshot of the graphical interface of the supply system control software. An accelerating voltage of 60 kV, a high voltage of about 250 μA presented.

The entire power supply system and individual units of the installation were tested at BINP in the summer and autumn of 2018. High-voltage tests were carried out at voltages in the column of up to 120 kV and detuning voltage up to ±20 kV. Numerous high-voltage breakdowns at voltage of 100 kV in air allowed us to identify and eliminate trouble spots in the power supply system. At the spring of 2019 power supply system was shipped to Lanzhou, and at summer was installed and tested on the CSRe ring.

CONCLUSION

High voltage power supply system for CSRe cooler was designed and produced in BINP. First testing electronic units and all system carried out in BINP before shipping to IMP. The final high-voltage tests of the power supply system and cooler system as a whole performed in IMP after installation on CSRe at summer of 2019 showed that the power supply system of the high-voltage column in general meets all the requirements of the electron cooler.

ACKNOWLEDGEMENTS

Special thanks to Alexander Semenov and Valery Isachenko for the careful assembling of the sections and cascade transformer.

REFERENCES

[1] J. Dietrich *et al.,* "Status of 2 MeV electron cooler for COSY-Julich/HESR" *in Proc. Of PAC'11* New York, NY, USA, paper WEP229, p.1918-1920, 2011.

[2] V. Reva *et al.,* "The first commission results of the high voltage magnetized cooler for COSY" *in Proc. Of COOL'11* Alushta, Crime, paper THIOA02, p.37-42, 2011.

[3] "ETRX357 ZigBee module product manual" https://www.silabs.com/documents/public/data-sheets/TG-PM-0516-ETRX35x.pdf

[4] W.Q. Wen *et al.,* "Dielectronic recombination at low energy range with Boron - like Ar^{13+} at the CSRm", *X-Ray Spectrometry* 2019, 10.1002/xrs.3077.

ISBN: 978-3-95450-218-9 ISSN: 2226-0374 doi:10.18429/JACoW-COOL2019-TUPS06

ELECTRON COOLING SIMULATION BENCHMARKING

B. Veglia†, J. Resta-Lopez, V. Rodin, C. P. Welsch University of Liverpool, Liverpool, UK
D. Gamba, N. Biancacci, A. Latina CERN, Geneva, Switzerland

Abstract

Electron coolers are commonly used in storage rings to reduce the phase space volume of heavy particles such as protons, antiprotons and ions. Their effect depends on the Coulomb interactions between the circulating beam and the cold electrons at small relative velocities. The cooling process can be modelled through different approaches and the behaviour of the cooling force, can be described by various formulas, which include different parameters. The aim of the present study is to compare the accuracy of the cooling simulations performed by two distinct beam-tracking codes: Betacool and RF-Track. Being based on different models and formulas, the two simulation tools require different parameters in order to realistically describe electron cooling. In this contribution, the impact of these parameters is discussed, and simulation predictions are compared with experimental data from LEIR (Low Energy Ion Ring) at CERN and ESR (Experimentier-Speicher-Ring) at GSI. Furthermore, the friction force is calculated for the new antimatter storage ring ELENA (Extra Low Energy Antiproton) at CERN.

INTRODUCTION

Electron cooling is an effective technique to reduce the phase space volume of a circulating beam of heavy particles [1] such as protons, antiprotons and ions in a storage ring [2-4]. The working principle is basically the following: a charged particle beam and an electron beam are overlaid in a small section of the machine and whilst moving at small relative velocities interact by means of electromagnetic forces. However, the simplicity of the concept is side by side with the complexity of the related physics. The phenomena involved fall into the realms of charged particle beam dynamics and plasma physics.

The resulting cooling force can be derived through two different approaches: dielectric theory and the binary collision model [5]. Unfortunately, neither of them can provide a closed form solution in case of a finite-strength magnetic solenoidal field. In order to be able to predict the parameter of the circulating beam after interacting with the electron cooler, it is then necessary to make approximations or to perform numerical evaluations.

* Work supported by the European Union's Horizon 2020 research and innovation programme under the Marie Skłodowska-Curie grant agreement No 721559

† bianca.veglia@liverpool.ac.uk

To take into account the finite value of the solenoidal magnetic field, a semi-empirical expression of the cooling force was proposed by Parkhomchuk [6].

An alternative approach is to use the analytical formula directly and carry out a numerical evaluation as opted by Nersisyan in his study of the stopping force [7]. In this contribution, simulation results using these two different approaches are compared in the context of the following facilities: LEIR and ELENA at CERN, and ESR at GSI.

SIMULATION CODES

Simulations of the cooling force in an experiment are important to determine the physical conditions in which the cooling process takes place and hence to optimise the parameters of the cooling system. Several tracking codes have been developed to simulate beam dynamics under different conditions. Betacool [8] and RF-Track [9] are two of them, both designed to simulate cooling processes. In this contribution, both codes are compared and contrasted against one another and measured data of the cooling force from existing electron coolers.

Betacool

The code has been developed since 1994 at JINR (Joint Institute of Nuclear Research, Dubna, Russia) electron cooling group and benchmarked against many experiments [10, 11]. The program represents the ion beam as an array of model particles which undergo a transformation of coordinates when interacting with the cooler. The cooling processes involved in the simulation lead to changes in the particle momentum components, which are calculated using a linear matrix for random phase advance. The cooling force can be chosen from a library of formulas or user written. For the purpose of this study the formula applied by Betacool simulations is the semi-empirical Parkhomchuk formula:

$$\vec{F} = -\vec{V}\frac{4Z^2e^4N_eL_p}{m_e}\frac{1}{\left(V^2+\Delta_{eff}^2\right)^{3/2}}, \quad (1)$$

where V is the relative ion-electron velocity, L_P is the Coulomb logarithm, N_e is the electron density per squared meter, m_e is the electron mass and Δ_{eff} is the longitudinal effective velocity spread of the electrons. Betacool uses an effective temperature $T_{eff} = m_e\Delta_{eff}^2$ as an input parameter that can be chosen to fit experimental data. Moreover, the electron beam can be described by different

ISBN: 978-3-95450-218-9 ISSN: 2226-0374 doi:10.18429/JACoW-COOL2019-TUPS06

models (uniform cylinder, Gaussian cylinder, hollow, parabolic). In this paper, a uniform cylindrical distribution of the electrons is considered in the cooler.

RF-Track

The approach used to develop RF-Track is different; the cooling force formula is based on Nersisyan treatment in which the integrals are solved numerically using a Monte Carlo technique and tabulated in appropriate 2D meshes (to be interpolated linearly at run time). In this case the cooling force formula is described in Eq. (2).

$$\vec{F} = -\frac{4\pi N_e K^2}{\mu}\left\{\iiint\left[L_F\frac{\vec{V}}{V^3}\right]f(\vec{v}_e)d\vec{v}_e + \int\left[L_M\frac{V_\perp^2}{V^5}\left(\vec{V}_\parallel + \frac{\vec{V}_\perp}{2}\left(1-\frac{V_\parallel^2}{V_\perp^2}\right)\right)\right]f(v_{e\parallel})dv_{e\parallel}\right\} \quad , \qquad (2)$$

whereby K is the coupling constant of the Coulomb interaction, μ is the reduced mass expressed in MeV, and are Coulomb logarithms, V represents the relative velocity of ions and electrons, is the transverse component of the velocity of the ions in the presence of a magnetic field, is the relative longitudinal velocity in the presence of magnetic field and is the electron velocity distribution.

In the program, the ion beam is represented as an ensemble of macro particles in 6D phase space in order to provide an accurate tracking and capturing non-linearities. The electron beam is represented as a fluid (plasma) on a 3D cartesian mesh that enables to consider arbitrary electron densities and velocity distributions. The evolution of the electrons is performed following the Euler equation of fluid dynamics.

BENCHMARKING RESULTS

LEIR

The Low Energy Ion Ring [12] at CERN is part of the accelerator complex that provides LHC with short dense bunches of lead ions. In this case, the cooling force has been calculated as the ratio of the momentum variation over time with increasing electron velocities.

An evaluation of the effect of the Parkhomchuk empirical parameter has been done in order to find the correspondent value to be tuned with the parameters requested by RF-Track and the Nersisyan formula. A scan over various values of the free parameter was performed setting the other variables of the simulations on the values corresponding to the LEIR electron cooler specifications. The variation of results in both, a horizontal and vertical shift of the peak of the force, strongly affecting the predicted performance of the machine (Fig. 1 a).

The other simulation tool, RF-Track, does not require such an empirical parameter. The formula implemented in the code to calculate the cooling force depends on the electron thermal velocity spread (longitudinal and transversal), having a temperature $T_e = m_e\Delta_e^2$. Since also Δ_{eff} is related to the thermal motion of the electrons, it is interesting to observe how tuning the two temperatures in RF-Track (Fig. 1 b) it is possible to replicate the scan in Betacool.

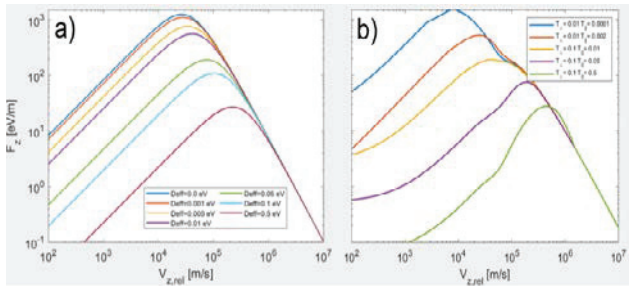

Figure 1: Scan of the LEIR Cooling Force under varying simulation parameters: a) with Betacool b) with RF-Track.

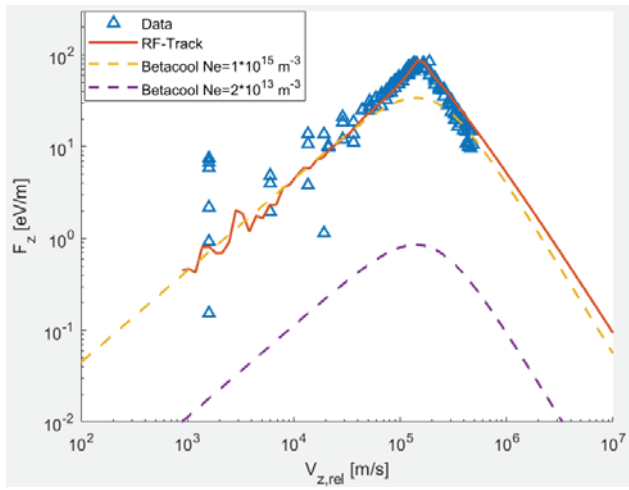

Figure 2: The longitudinal cooling force acting on Pb ions in LEIR electron cooler.

As can be observed in Fig.2 in order to obtain a simulated force with Betacool (dotted lines) that agrees with the data (triangles) and RF-Track simulation results (orange line) is necessary to include a factor of 100. This could be accounted for by the underestimation of L_P due to the very low value of the magnetic field (B= 0.07 T). Further analysis to verify this hypothesis will be performed.

ESR

Measurements of the cooling force have extensively been performed in the past on other storage rings equipped with electron coolers. One of them is the ESR [13], which is part of the GSI accelerator complex, where different kinds of heavy ions are cooled by magnetised electrons. In this experiment, fully stripped Xenon ions circulate in the ring. The cooling force is extracted by averaging the forces over the ion distribution in the beam. Two different methods have been used to determine the force. At low ion velocities the cooling force is extracted from the equilibrium between cooling and longitudinal heating with RF noise. At high relative velocities between

ISBN: 978-3-95450-218-9 ISSN: 2226-0374 doi:10.18429/JACoW-COOL2019-TUPS06

the rest frames of the beams the cooling force is deduced from the momentum drift of the ion beam after a rapid change of the electron energy. Details of these methods are given in [14, 15]. Figure 3 plots the measured data (triangles) along with the simulated forces obtained from Betacool (dotted yellow line) and RF-Track (orange line). Parkhomchuk expression appears to better imitate the behaviour of the real cooling force but diverges for high relative velocities.

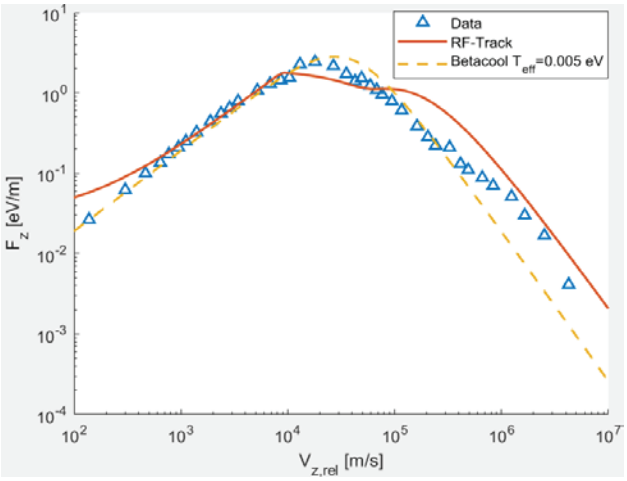

Figure 3: The longitudinal cooling force acting on Xe54+ ions in the ESR ring

ELENA

Last year the antimatter factory at CERN has been upgraded with the commissioning of the Extra Low ENergy Antiproton storage ring [16]. This facility is equipped with an electron cooler, which operates at extremely low energies reducing the emittance of the antiproton beam, thus increasing the trapping efficiency of the antimatter experiments. With the aim of having a well defined framework for the performance of this novel machine, simulations of the expected force have been computed as seen in Fig. 4. A good agreement is obtained between both codes.

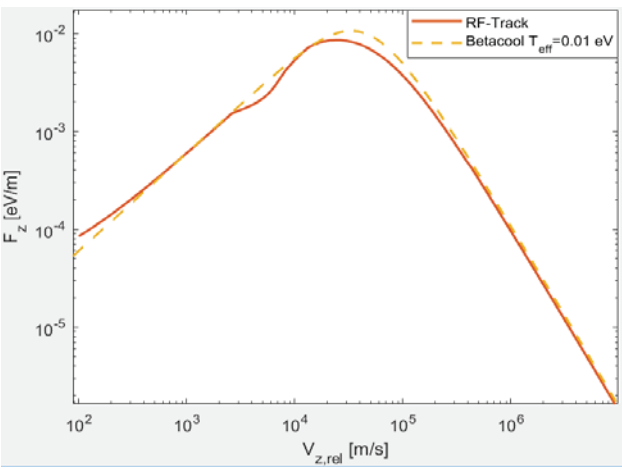

Figure 4: The longitudinal cooling force for the antiproton beam in ELENA.

OUTLOOK

Two beam dynamics simulation codes applying different models for the cooling force have been used to model the interaction of different ions and antiprotons within electron coolers operating at distinct conditions for different storage rings. A general good agreement is achieved between the two codes. However, for the case of the LEIR electron cooler there are some discrepancies, which require further investigations. A comprehensive understanding of the friction force models will allow more realistic predictions in the case of new facilities. Eventually, ELENA cooling performance simulations will be compared with experimental data after the CERN Large Shutdown 2.

ACKNOWLEDGEMENT

Special thanks to the work of the late Dr. Alexander Smirnov (In Memoriam). We would also like to thank our colleagues at CERN for their helpful input and collaboration.

REFERENCES

[1] G. I. Budker, in *Proc. Int. Symp. on Electron and Positron Storage rings*, Saclay, 1966, p. II-I-I; Atomnaya Energia, 22 (1967) 346.

[2] S. Nagaitsev, L. Prost, and A. Shemyakin "Fermilab 4.3 MeV electron cooler", JINST, vol. 10, 2015.

[3] H. Danared, "Studies of electron cooling with a highly expanded electron beam", *Nucl. Instrum. Methods Phys. Res.*, Sect A 441 (2000) 123-133.

[4] L. Hermansson, D. Reistad, "Electron cooling at CELSIUS", *Nucl. Instrum. Methods Phys. Res.*, Sect. A 441 (2000) 140-144.

[5] O. Boine-Frankenheim and J. D'Avanzo, "Stopping power of ions in a strongly magnetized plasma", *Phys. Plasmas 3*, 792 (1996), and references therein.

[6] V. Parkhomchuk, "New insights in the theory of electron cooling", *Nucl. Instrum. Methods Phys. Res.*, Sect. A 441, 1-2 (2000).

[7] H. Nersisyan, C. Toepffer and G. Zwicknagel, *Interactions Between Charged Particles in a Magnetic Field*, Springer (2007).

[8] BETACOOL program for simulation of beam dynamics in storage rings, http://lepta.jinr.ru/betacool/betacool.htm

[9] RF-Track, https://gitlab.cern.ch/alatina/rf-track-2.0

[10] K. Hedblom, L. Hermansson, "Measurements on transverse cooling time and beam profiles in CELSIUS", *Nucl. Instrum. Methods Phys. Res.*, Sect. A 391, 1 (1997)

[11] A. Smirnov *et al.*, "Simulation of pellet target experiments with betacool code", in *Proc. RuPAC 2008*, Zvenigorod, Russia, pp. 9-11

[12] M. Chanel, "LEIR: the low energy ion ring at CERN", in *Proc. EPAC 2002*, Paris, France, pp. 563-566

[13] B. Franzke, "The heavy ion storage and cooler ring project ESR at GSI", *Nucl. Instrum. Methods Phys. Res.*, Sect. B 24-25, 1, 1987

ISBN: 978-3-95450-218-9 ISSN: 2226-0374 doi:10.18429/JACoW-COOL2019-TUPS06

[14] T. Winkler *et al.*, "Electron cooling forces for highly charged ions in the ESR", *Nucl. Instrum. Methods Phys. Res.*, Sect. A, 391, 1 (1997)

[15] T. Winkler: Untersuchungen zur Elektronenkuehlung hochgeladener schwerer Ionen, Thesis, University Heidelberg, Heidelberg (1996)

[16] Wolfgang Bartmann *et al.*, "The ELENA facility", *Philosophical Transactions of the Royal Society A*: Mathematical, Physical and Engineering Sciences, Volume 376, Issue 2116 (2018)

ISBN: 978-3-95450-218-9 ISSN: 2226-0374 doi:10.18429/JACoW-COOL2019-TUPS07

WINSAM AND WINMAG – NEW PROGRAM PACKAGES FOR SIMULATION OF ELECTRON-OPTICAL SYSTEMS

A.V. Ivanov, The Budker Institute of Nuclear Physics, Novosibirsk, Russia

Abstract

In BINP new program packages WinSAM and WinMAG have been developed. The main goal of WinSAM program is the simulation of axially symmetric electron optical systems with space charge consideration. This program is the further development of SAM code with greatly improved interface and enhanced scope of considered tasks. WinMAG is developed to solve 3D non-linear magnetostatic tasks, direct integral method is used in this code. Several types of coils including user-defined coils can be entered, magnetic volumes can be described by several basic volumes.

INTRUDUCTION

Over the years, software packages for modeling electron-optical systems are developed in BINP SB RAS. These software packages, along with well-known commercial programs such as COMSOL Multiphysics or OPERA, are widely used in the Institute for the development of various elements of accelerators and other physical installations. Especially intensively these programs are applied at development of electron coolers. The peculiarity of some of these software packages, considered below, is the use of integral methods of calculation, allowing to maintain accuracy with relatively small number of mesh cells, which leads to a significant reduction in the calculation time.

The first of the programs considered in the article is the SAM complex, which is designed for simulation of axially symmetric electron optical systems with space charge consideration [1, 2]. These systems can include electrodes, dielectrics, coils, permanent magnets, linear ferromagnetics. Tasks with space charge can also be simulated with help of SAM program, that allows calculation of electron guns and collectors. Another program under consideration is the MAG3D complex for solving problems of nonlinear 3D magnetostatics [3].

Despite the wide application of these programs, there was a need for their further serious modernization. The most serious problem is their outdated interface. This makes it difficult for existing users to work with these programs, and prevents the attraction of new users. In addition, a confusing interface can lead to errors when specifying the geometry of the problem and the choice of calculation parameters. It is especially necessary to have a simple and intuitive interface in the program MAG3D, performing three-dimensional calculations. Updating the interface is also required for the efficient operation of the postprocessor, facilitating the output of the results of calculations. In addition, the accumulated experience with these programs allowed us to identify those areas of the computational part that need further development to improve the accuracy of calculations.

WINSAM

Basic Calculation Methods

The SAM software package is based on the method of boundary integral equations. This method uses a general solution of the Poisson equation to solve electrostatics problems:

$$\phi(\vec{r}_0) = \int\limits_{S_e+S_d} \frac{\sigma(\vec{r})\, dS}{|\vec{r}_0 - \vec{r}|} + \int\limits_{V_b} \frac{\rho(\vec{r})\, dV}{|\vec{r}_0 - \vec{r}|},$$

where S_e and S_d – surfaces of electrodes and dielectrics, V_b – volume occupied by beam space charge. Substituting this solution into boundary conditions on the surface of electrodes and dielectrics results in a system of integral equations for an unknown surface charge distribution:

$$\int\limits_{S_e+S_d} \sigma(\vec{r}) \frac{1}{|\vec{r}_e - \vec{r}|} dS = \varphi_e - \int\limits_{V_b} \frac{\rho(\vec{r})\, dV}{|\vec{r}_e - \vec{r}|},$$

$$2\pi \frac{\varepsilon_2 + \varepsilon_1}{\varepsilon_2 - \varepsilon_1} \sigma(\vec{r}_d) - \int\limits_{S_e+S_d} \sigma(\vec{r}) \frac{\partial}{\partial n_d} \left(\frac{1}{|\vec{r}_d - \vec{r}|} \right) dS = \int\limits_{V_b} \rho(\vec{r}) \frac{\partial}{\partial n_d} \left(\frac{1}{|\vec{r}_d - \vec{r}|} \right) dV,$$

where $\vec{r}_e$ and $\vec{r}_d$ – points on the surfaces of electrodes and demarcation boundaries of dielectrics respectively. If an axially symmetric problem is considered, these equations must be integrated with respect to the angle, and the integral over the surface becomes the integral over the contours of the electrodes and dielectrics. Consideration of the problem of linear magnetostatics leads to an integral equation, similar to the second of the above, with respect to the surface density of effective magnetic charges, which describe the field induced by magnetized magnetic materials.

To solve these integral equations a collocation method with spline interpolation of the solution is used in the SAM package. A set of points is placed on the surface of the elements under consideration, the surface charge density is described by linear spline interpolation from the density values at these points. The requirement is put forward – the integral equations must be exactly fulfilled at these points. Due to these conditions, the integral equations are transformed into a system of linear algebraic equations that can be easily solved.

When calculating electron guns and collectors, the right parts of the integral equations describing the effect of the space charge are unknown in advance. In this case, a complete solution of the self-consistent problem is required, which is performed by an iterative method. At

ISBN: 978-3-95450-218-9 ISSN: 2226-0374 doi:10.18429/JACoW-COOL2019-TUPS07

the beginning of the iterative process, some simple initial volume charge distribution is assumed. Integral equations are solved, surface charges are found, and it is possible to calculate the electric field at any point in space by numerical calculation of the corresponding integrals. The emission density is calculated in accordance with the given model, the trajectory analysis of the beam macroparticles is carried out. Based on the results of this trajectory analysis, the volume charge distribution is refined and a new iteration begins.

New Interface

The SAM package was originally DOS-based program. To edit the geometry of the considered task or its calculation parameters, user must make changes by outer text editor in special text file with complex structure, and then start SAM preprocessor to read this file. The calculated geometry and obtained results are shown in small fixed-sized window. All this make difficult the work with SAM program and provokes the user to make mistakes.

It was decided to create a new package with a completely changed interface, which would be similar to the interfaces of modern CAD programs. This program package was named WinSAM. The window of this program with the entered geometry of the electron gun, the calculated trajectories of the beam particles and the parameters of the formed beam at the exit of the gun are shown in Fig. 1.

In the WinSAM program, the entire workspace is divided into two windows, the left window shows the main elements of the problem geometry, the right window shows the geometry itself and the calculation results. One can create new geometry elements and edit existing ones using the structure in the left window or directly in the right one.

The possibilities for the output of the calculation results are expanded – all the obtained data are recorded in a text file, and the resulting image can be saved in a vector format.

It is now possible to export task geometry from files of various CAD formats, as well as import the entered geometry into such files.

Increase of Accuracy of Calculations

Our experience in using SAM software has allowed us to identify areas that significantly affect the accuracy of calculations. First, it is a description of thermal emission in the presence of a strong magnetic field. In the WinSAM complex, the effect of this field has been refined.

The second problem is the insufficient accuracy of the biquadratic interpolation of the eigenfield of the beam in the mesh cells. This leads to an erroneous increase in the current density at the edges of the beam. To eliminate this effect, the approximation of the beam field on the mesh cells occupied by the beam boundary was developed.

WINMAG

Basic Calculation Methods

To solve 3D non-linear magnetostatic problems, another integral equation must be used. To obtain this equation, it is necessary to divide the magnetic field into the field of currents and the field induced by magnetized magnetic materials:

$$\vec{H} = \vec{H}_c + \vec{H}_m .$$

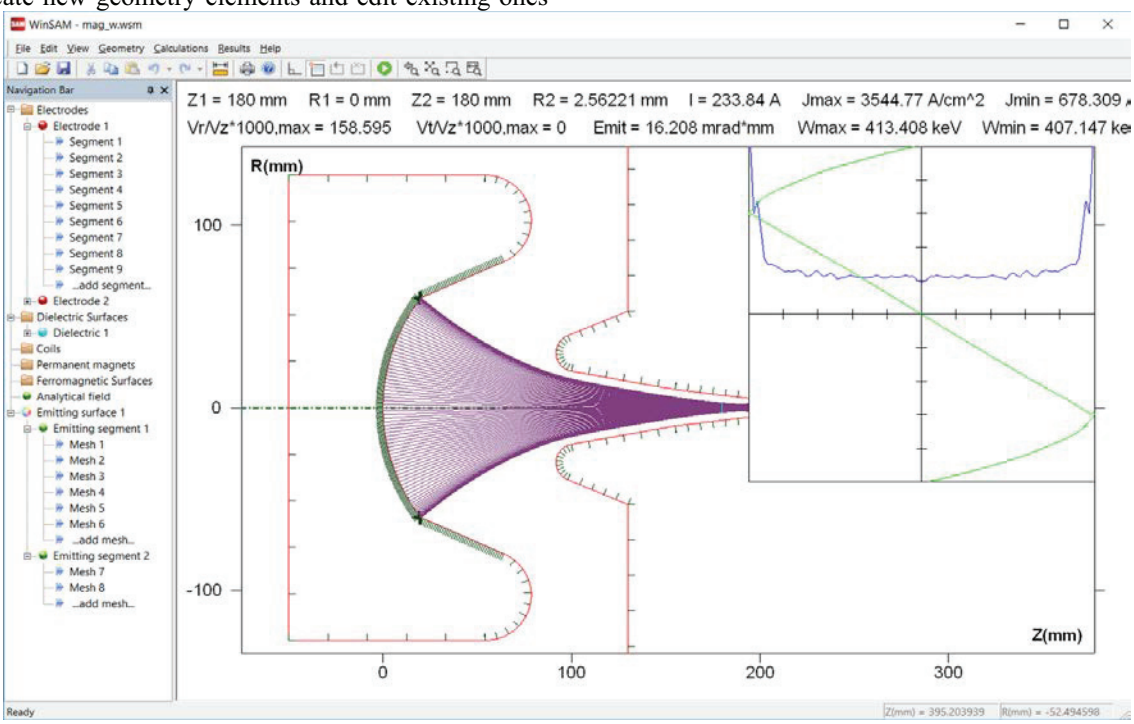

Figure 1: Example of the electron gun simulation in WinSAM. Geometry of electrodes, trajectories of particles and beam parameters are shown.

ISBN: 978-3-95450-218-9 ISSN: 2226-0374 doi:10.18429/JACoW-COOL2019-TUPS07

The field of currents can be directly found according to Biot-Savart law, the other field can be represented as a gradient of scalar potential, that can be found according to following expression:

$$\vec{H}_c(\vec{r}) = \frac{1}{c}\sum_{n=1}^{N_c}\int_{V_{cn}} \frac{\left[\vec{j}(\vec{r}')\times(\vec{r}-\vec{r}')\right]}{\left|\vec{r}-\vec{r}'\right|^3} dV',$$

$$\vec{H}_m(\vec{r}) = -\nabla\psi(\vec{r}),\ \psi(\vec{r}) = \frac{1}{4\pi}\int_{V_m} \frac{\vec{M}(\vec{r}')\cdot(\vec{r}-\vec{r}')}{\left|\vec{r}-\vec{r}'\right|^3} dV',$$

$$\vec{M} = \chi(H)\cdot\vec{H}\ .$$

Combining these two fields, we obtain the following integral equation for unknown magnetic field:

$$\vec{H}(\vec{r}) + \frac{1}{4\pi}\nabla\int_{V_m}\chi\left(H(\vec{r}')\right)\frac{\vec{H}(\vec{r}')\cdot(\vec{r}-\vec{r}')}{\left|\vec{r}-\vec{r}'\right|^3} dV' = \vec{H}_c(\vec{r})\,.$$

In the MAG3D program the entire volume occupied by magnetic materials is divided into triangular prisms (see Fig. 2). The magnetization within each prism is assumed to be constant. The integral equation obtained above is written at the central points of these prisms. Thus, integral equation turns to a system of nonlinear algebraic equations, that can be solved. Following types of coils are implemented: a round solenoid, an O-type coil and a user-defined coil made up of straight and curved sections. Examples of these coils are shown in Fig. 3.

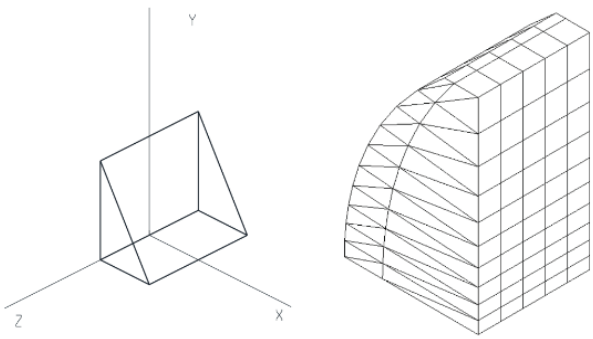

Figure 2: Baisc triangular prizm and division of iron volume into basic prizms.

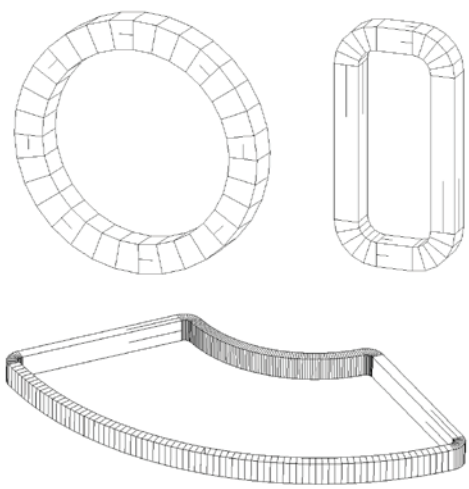

Figure 3: Types of coils imlemented in MAG3D package.

New Interface

As in the WinSAM program, in the WinMAG program the entire workspace is divided into two windows, the left window shows the main elements of the problem geometry, the right window shows the geometry itself and the calculation results. One can create new geometry elements and edit existing ones using the structure in the left window or directly in the right one. The geometry of the bending magnet for an ion beam source, entered in the WinMAG program, is shown in Fig. 4.

While working with the WinMAG program all the obtained data are recorded in a text file, and the resulting image can be saved in a vector format.

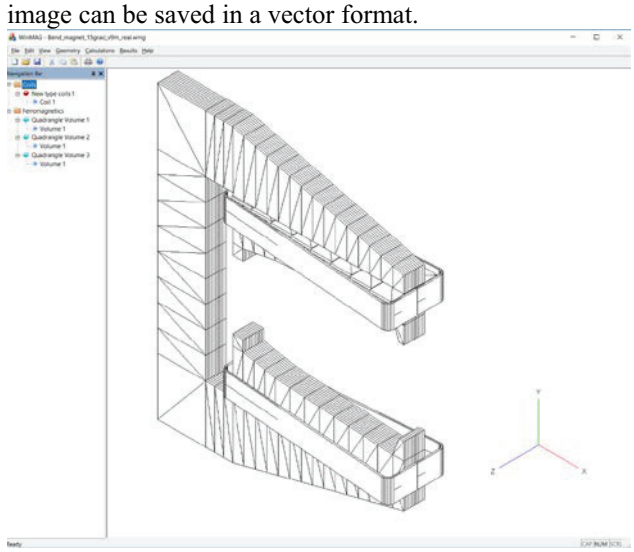

Figure 4: The geometry of the bending magnet in the WinMAG program.

CONCLUSION

In BINP for calculation of electron-optical systems on the basis of integrated methods the programs WinSAM and WinMAG were developed. These programs are based on previously created programs – SAM and MAG3D respectively. The main point of development is a qualitatively new interface, similar to the interface of modern CAD programs. In addition, the accuracy of calculations was improved and the range of tasks was expanded. New programs have been successfully applied in the development of electron coolers in the Institute [4].

REFERENCES

[1] B. Fomel, M. Tiunov, V. Yakovlev, "Computer-aided electron gun design", *in Proceedings of the XIII International Conference on High Energy Accelerators*, Novosibirsk, 1987, v.1, p.353-355.

[2] A. Ivanov, M. Tiunov, "ULTRASAM - 2D Code for Simulation of Electron Guns with Ultra High Precision", *in Proc. Of EPAC'02*, Paris, June 2002, paper WEPRI050, p. 1634, 2002.

[3] MAG3D User's Guide, Novosibirsk, Russia, 2006.

[4] A.V. Ivanov *et al.,* "Simulation of electron-optical systems of electron coolers", presented at the COOL'19 Workshop, Novosibirsk, Russia, September 2019, paper THB02, this conference.

ISBN: 978-3-95450-218-9 ISSN: 2226-0374 doi:10.18429/JACoW-COOL2019-TUPS08

BEAM POSITION MONITOR SYSTEM FOR HIGH VOLTAGE ELECTRON COOLER FOR NICA COLLIDER

E.A. Bekhtenev[1], G.V. Karpov, V.B. Reva[1]
Budker Institute of Nuclear Physics, Novosibirsk, Russia
[1]also at Novosibirsk State University, Novosibirsk, Russia

Abstract

The high voltage (2.5 MV) electron cooler for NICA collider is now designing in BINP. Beam position monitor (BPM) system for orbit measurements has been developed at BINP. The system contains 16 BPMs inside the cooling sections, 4 BPMs inside the high voltage vessels and 22 BPMs in transport channels. Continuous electron beam is modulated with 10 MHz sinusoidal signal for capability to get signals from pickup electrodes. The beam current modulation can be varied in the range of 0.3-5 mA. The modulation signal may be supplied to each sector of the control electrode. So, the position of one quadrant sector of the electron beam can be measured by BPM system. Comparing the positions of each sectors from BPM to BPM it is possible to analyse the shape of the electron beam in the transport channel and cooling section. The BPMs inside the cooling section can measure both electron and ion beams. It is achieved by means of switching the reference signals inside the BPM electronics. The prototypes of new BPM electronics have been fabricated and tested. The BPM electronics provides highly precise beam position measurements. Position measurement error doesn't exceed a few micron. Design features of the BPM system, its parameters and testing results are presented in this paper.

INTRODUCTION

The high voltage (2.5 MV) electron cooler for NICA collider is now designing in BINP [1]. Beam position monitor (BPM) system consists of 42 BPMs and electronics. 16 BPMs are located inside the cooling sections, 4 BPMs are installed inside the high voltage vessels and 22 BPMs are installed in transport channels. Continuous electron beam current is modulated with a ~10 MHz signal for capability to get signals from BPM electrodes. Some parameters of cooler and main BPM system requirements are presented in Table 1.

Table 1: Main Requirements to BPM System

Electron current	0.1-1 A
Modulation amplitude of electron current	0.3-1.5 mA
NICA collider revolution frequency F_0	523-586 kHz
Number of ion bunches N_b	22
Position measurement error	< 100 μm
Measurement rate	0.1-1 sec

To achieve the best cooling effectiveness electron and proton beams must be aligned inside the cooling section with accuracy better than 100 μm. This condition requires simultaneous measurements of electron and proton beams position by 16 BPMs located inside the cooling sections. 22 BPMs in the transport channels and 4 BPMs inside the high voltage vessels measure only electron beam position. A feature of the gun four-sector control electrode using before in the COSY cooler allows measuring not only electron beam position but the beam shape and rotation [2].

SYSTEM STUCTURE

The structure chart of the BPM system is presented in Fig. 1.

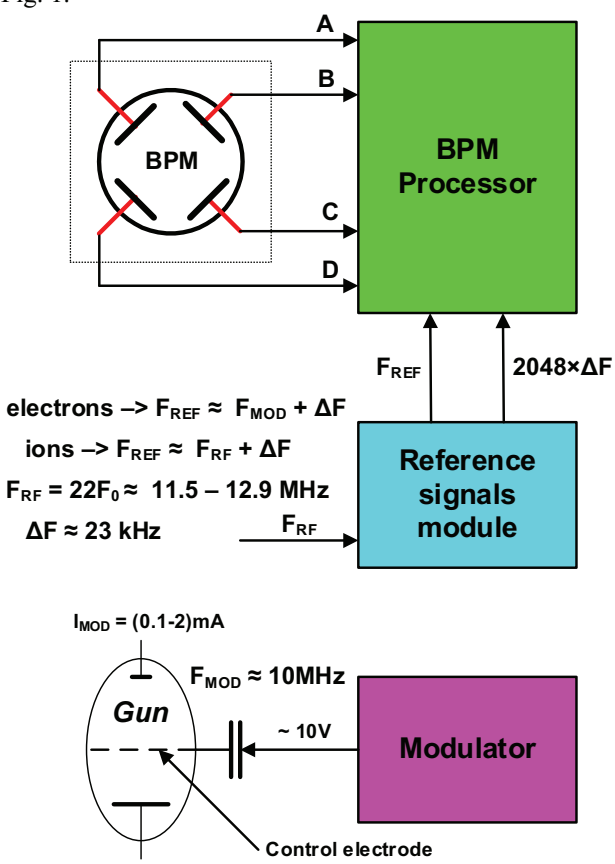

Figure 1: The structure of the BPM system.

The system consists of 42 BPMs, Signal Processing Electronics, including 21 BPM Processors and 38

ISBN: 978-3-95450-218-9 ISSN: 2226-0374 doi:10.18429/JACoW-COOL2019-TUPS08

Preamplifiers, 2 Modulators, 1 Reference signals generator and 1 Reference signals distributor.

Modulator provides electron beam current modulation with frequency $F_{MOD} \approx 10$ MHz. Signal Processing Electronics measures the beam signals amplitude at each of four BPM electrodes. The measurement is based on synchronous detecting of the BPM signal with frequency F_{SIGN}. For BPMs inside the cooling sections F_{SIGN} equals F_{MOD} for electron beam and F_{RF} for ion beam, where $F_{RF} = 22F_0$. Revolution frequency F_0 is changed from 523 kHz to 586 kHz during acceleration in the NICA collider. For BPMs in the transport channels and guns F_{SIGN} equals F_{MOD}. The sinusoidal signal with frequency $F_{REF} \approx F_{SIGN} + \Delta F$ generated by Reference signals module is used as reference signal.

The simultaneous measurements of electron and ion beams position inside the cooling sections is achieved by means of switching the reference signal between $F_{MOD} + \Delta F$ and $F_{RF} + \Delta F$.

ELECTRONICS

Modulator

The system contains 2 Modulators – one modulator for each Gun. A functional diagram of the Modulator is presented in Fig. 2.

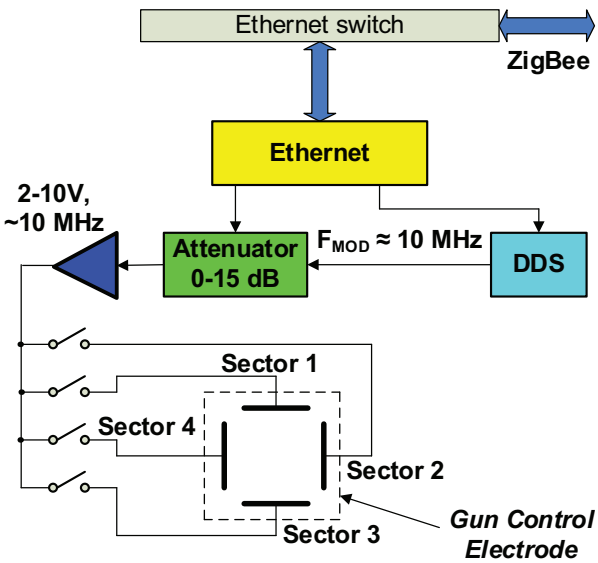

Figure 2: Functional diagram of the Modulator.

Gun Control electrode consists of four sectors. Modulation voltage can be applied both to all sectors and to one of them. In the last case only a part of electron beam in transverse cross-section will be modulated. By switching on different sectors in turn one can get information about the beam shape and beam precession due to longitudinal field in different BPM locations [2].

Modulator is located inside the High Voltage (HV) tank at potential of up to 2.5 MV. Modulation signal with frequency $F_{MOD} \approx 10$ MHz is generated by DDS. An amplitude of modulation voltage can be set in the range 2-10 V with help of programmable attenuator.

Signal Processing Electronics

Functional diagram of the Signal Processing Electronics for BPMs inside the cooling sections and transport channels is presented in Fig. 3.

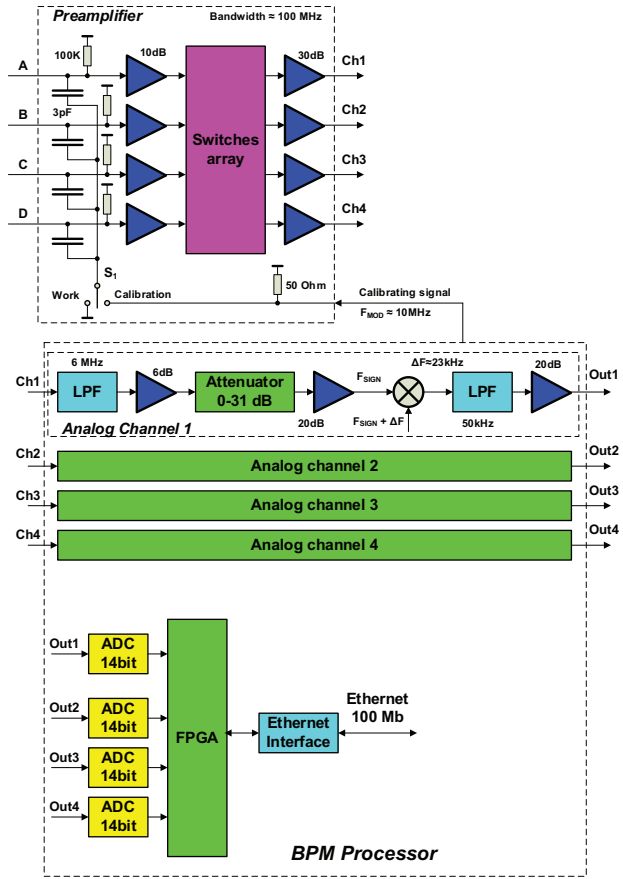

Figure 3: Functional diagram of the Signal Processing Electronics for BPMs inside the cooling sections and transport channels.

Signal Processing Electronics for each BPM inside the cooling sections and transport channels consists of Preamplifier with high input impedance located near BPM and BPM Processor. Preamplifier is connected with BPM via four 75 Ohm cables with length ~1 m. BPM Processors are placed in the rack located in the electronics room. Switches array used in Preamplifier provides 4 connection combinations between 4 BPM electrodes and 4 signal processing channels. Use of the Switches array allows to eliminate measurement error caused by inequality of the channels transmission coefficients.

After amplification the BPM signals with frequency F_{SIGN} are mixed with reference frequency $F_{REF} \approx F_{SIGN} + \Delta F$. Then the signals with frequency $\Delta F \approx 23$ kHz after low pass filtering and amplification are sampled by 14 bit ADC. The signals in digital form come to FPGA where digital processing is performed. This digital signal

ISBN: 978-3-95450-218-9 ISSN: 2226-0374 doi:10.18429/JACoW-COOL2019-TUPS08

processing includes synchronous detecting and accumulation. The frequencies F_{MOD} and F_{REF} are generated by different modules. So, for electrons F_{REF} value is not exactly equaled to $F_{MOD} + \Delta F$. A difference between the reference frequency F_{REF} and $F_{MOD} + \Delta F$ for proper synchronous detecting must be less than 1 kHz. To achieve this a tracking of the reference frequency F_{REF} to $F_{MOD} + \Delta F$ is implemented. The tracking procedure includes measurement of the difference between F_{REF} and $F_{MOD} + \Delta F$ values on base of spectrum of ADC data.

In calibration mode special calibrating signal with frequency $F_{CAL} \approx 10$ MHz comes through the switch S_1 and capacitances to each Preamplifier input (see Fig. 3).

BPM Processor occupies one 1U 19" chassis (Fig. 4). Each BPM Processor can serve two BPMs.

Figure 4: BPM processor prototype.

Signal Processing Electronics for BPMs inside the guns is fully located within one module BPM Processor (1U 19" chassis). It has not the Preamplifiers in separate bodies. Reference signal F_{REF} and calibrating signal F_{CAL} are generated inside the BPM Processor.

EXPERIMENTAL RESULTS

Prototypes of all BPM electronics modules have been fabricated and tested. Main accuracy parameters have been measured with using of the signal generator. A sinusoidal test signal with frequency ~10 MHz was applied via four-way splitter to four Preamplifier inputs. Signal amplitude was changed in the range 0.2-1 mV which corresponds to beam current modulation range 0.3-1.5 mA. Three measured main parameters of accuracy (for $K_X \approx K_Y \approx 40$ mm) are presented in Table 2.

Table 2: Main Accuracy Parameters of the BPM System

Dependence of the result on beam modulation current (I_{MOD} = 0.3-1.5 mA)	~4 μm
Resolution (I_{MOD} = 0.3-1.5 mA)	< 1 μm
Dependence of the result on the temperature	~2 μm/°C

An accuracy achieved with prototypes satisfies all cooler requirements.

STATUS

All BPMs and electronics are fabricating now in BINP. It is planned to complete fabrication and testing all the BPM electronics modules in 2020 year.

REFERENCES

[1] M. Bryzgunov *at al.* "The status of the electron cooling system for the NICA collider", presented at the COOL'19 Workshop, Novosibirsk, Russia, September 2019, paper TUX01, this conference.

[2] V. Reva *at al.,* "The first commission results of the high voltage magnetized cooler for COSY", *in Proc. of COOL'11* Alushta, Crime, September 2011, paper THIOA02, p.37-42, 2011.

ISBN: 978-3-95450-218-9 ISSN: 2226-0374 doi:10.18429/JACoW-COOL2019-TUPS09

ELECTRON COOLER INTRODUCED PERTURBATIONS ON ION BEAM

Y. J. Yuan†, Peng Li
Institute of Modern Physics, CAS, 730000, Lanzhou, China
School of Nuclear Science and Technology, University of CAS, 100049, Beijing, China

Abstract

The influence of electron cooler on stored ion beams in heavy ion synchrotron has been studied for many years. Usually, only the influence on lattice from the magnetic field of solenoid and toroids were considered, in addition to the cooling effect from Coulomb Scattering. However, electron cooling experiments show that there exist limits on intensity of electron beam and the stored ion beams. Meanwhile, experiments of cooling with pulsed e-beam show structure instability that should be explained. The influence of electron beam induced electromagnetic field on ion beams was studied in this paper by means of Lie Algebraic method. The combined transport matrix of solenoid and e-beam field focusing is given. Application of the matrix may help to understand the above phenomena.

INTRODUCTION

As is well known, the general requirements for an e-cooler includes:

1.Parallel and similar velocity of e-beam and ion-beam;
2.Lower electron beam temperature;
3.Adequate cooling force (electron density n_e and length L_e);
4. Compensable or Neglectable influence on ion beam.

In order to satisfy these requirements, solenoid with high uniformity field is introduced to constrain the electron beam and keep its temperature, toroids and/or electrostatic inflectors are introduced to guide the e-beam orbit. The magnetic field of solenoid and toroids will affect the ions passing through it, and usually these effects will be compensated for. The coupling effects of solenoid field can be compensated by a pair of additional solenoids or skew quadrupoles, but the focusing effects are usually neglected. The bending effects of toroid field can be compensated by dipole correctors.

Another source may come from the space charge and current focusing of electron beam, which was usually neglected in practice.

In this paper, we will focus on the study of the e-cooler introduced focusing effects of solenoid and the e-beam field. The combined transport matrix of solenoid and e-beam field will be deduced by means of Lie Algebraic method [1].

Application of the matrix may help to understand why high current e-beam not be used to cool low energy ion beam, why in pulsed e-beam cooling the electron bunches should have the same pulse frequency of ion bunch pulse and cover the ion bunches, and how to get higher deceleration efficiency.

† yuanyj@impcas.ac.cn

EFFECTS OF ELECTRON BEAM

In addition to the cooling effect from Coulomb Scattering, the electron beam also affects the ion beam by its self-field.

For a round uniformly distributed electron beam, its space charge electric field is given by the following formula:

$$\bar{E}(r) = -\frac{n_e e}{2\varepsilon_0} r \quad (1)$$

where n_e is the electron density, e is the electron charge. From Eq.(1), the focusing strength can be given as:

$$K_E = \frac{n_e e}{2\varepsilon_0\, \beta c\, B\rho} \quad (2)$$

where βc is the velocity of ion/electron, $B\rho$ is the magnetic rigidity of the ion beam.

For a round uniformly distributed electron beam, its current induced magnetic field is given by the following formula:

$$\bar{B}(r) = \frac{\mu_0}{2\,\pi\, r^2} I \times r = \frac{\mu_0 n_e\, e\, c}{2\, r} \beta \times r \quad (3)$$

From Eq.(3), the focusing strength can be given as:

$$K_B = -\frac{\mu_0 n_e\, e\, \beta c}{2\, B\rho} = -\beta^2 K_E \quad (4)$$

The total focusing strength of electromagnetic field of electron beam can be given as:

$$k = K_E + K_B = (1-\beta^2)\frac{n_e\, e}{2\varepsilon_0\, \beta c\, B\rho} \quad (5)$$

For the stand-alone electron beam, its transport matrix can be written as:

$$R_{ef} = \begin{bmatrix} \cos(\sqrt{k}L) & \frac{1}{\sqrt{k}}\sin(\sqrt{k}L) & 0 & 0 \\ -\sqrt{k}\sin(\sqrt{k}L) & \cos(\sqrt{k}L) & 0 & 0 \\ 0 & 0 & \cos(\sqrt{k}L) & \frac{1}{\sqrt{k}}\sin(\sqrt{k}L) \\ 0 & 0 & -\sqrt{k}\cdot\sin(\sqrt{k}L) & \cos(\sqrt{k}L) \end{bmatrix} \quad (6)$$

From Eq.(5) we noticed that the focusing strength of electron beam induced field will decrease along with the beam energy.

DEDUCING OF COMBINED TRANSPORT MATRIX

To deduce the combined transport matrix of solenoid and electron beam, Lie Algebraic method is adopted [1]. The simplified combined Hamiltonian for transversal movement is:

$$H = \frac{1}{2}\left(\left(x' + \frac{1}{2}k_s y\right)^2 + \left(y' - \frac{1}{2}k_s x\right)^2\right) + \frac{k}{2}\cdot(x^2+y^2) \quad (7)$$

where $k_s = \frac{B_s}{2B\rho}$ is the strength of solenoid field, B_s is the magnetic field of solenoid, and k is the strength of e-beam field.

As well known, the Lie transformation associated with $f(x,x',y,y') = -L\cdot H$ will give out the polynomial representation of the elements of transport matrix. It's not convenient and not precise to use the truncated polynomial in

ISBN: 978-3-95450-218-9 ISSN: 2226-0374 doi:10.18429/JACoW-COOL2019-TUPS09

beam transport calculation. We tried to guess out the representations of the elements using elementary functions, which will be easily used in 1st order transport calculations.

$$R = \begin{bmatrix} \cos(KL)cos(k_sL) & \sin(KL)\cos(k_sL)/K & \cos(KL)\sin(k_sL) & \sin(Kz)\sin(k_sz)/K \\ -K\sin(KL)\cos(k_sL) & \cos(KL)cos(k_sL) & -K\sin(KL)\sin(k_sL) & \cos(KL)\sin(k_sL) \\ -\cos(KL)\sin(k_sL) & \sin(Kz)\sin(k_sz)/K & \cos(KL)cos(k_sL) & \sin(KL)\cos(k_sL)/K \\ K\sin(KL)\sin(k_sL) & -\cos(KL)\sin(k_sL) & -K\sin(KL)\cos(k_sL) & \cos(KL)cos(k_sL) \end{bmatrix} \quad (8)$$

$$= \begin{pmatrix} \cos(KL) & \sin(KL)/K & 0 & 0 \\ -K\sin(KL) & \cos(KL) & & \\ 0 & 0 & \cos(KL) & \sin(KL)/K \\ & & -K\sin(KL) & \cos(KL) \end{pmatrix} \begin{pmatrix} \cos(k_sL) & 0 & \sin(k_sL) & 0 \\ 0 & \cos(k_sL) & 0 & \sin(k_sL) \\ -\sin(k_sL) & 0 & \cos(k_sL) & 0 \\ 0 & -\sin(k_sL) & 0) & \cos(k_sL) \end{pmatrix}$$

where $K = \sqrt{k + {k_s}^2}$ is the combined focusing strength, L is the length of the solenoid and the electron beam. As can be seen, when $k = 0$, R is transformed into the transmission matrix of the solenoid; when $k_s = 0$, it returns to that of e-beam field, R_{ef}. The transmission matrix R can be rewritten as two parts as in Eq.(8), the left part is the focusing matrix in both transversal plane, and the right part is cyclotron rotation matrix.

APPLICATIONS OF THE MATRIX

Usually the rotation effect of R is easily compensated by introducing of additional solenoids or skew quadrupoles, but meanwhile additional focusing is introduced. The focusing strength of electron cooler and the compensation solenoids/skew quadrupoles usually should be considered in ring lattice design.

As an example to show the combined influence of solenoid and e-beam field to the HIRFL-CSRm[2,3]. In CSRm, the solenoid of e-cooler usually working at a field of 395 G, which is much smaller than the designed 1500 G. Using the parameters of e-cooler: length L=2.56 m, radius of e-beam r_e =3 cm, mean betatron amplitude function of $\langle\beta\rangle$ =10 m, and a supposed electron current of I_e=330 mA, the focusing strength of e-cooler on ion beam can be calculated as shown in Table 1.

Table 1: Example of Electron Cooler Focusing Effects

Ion	E(MeV/u)	k(m^{-2})	k_s^2(m^{-2})	$\Delta Q_{x,y}$
$^{238}U^{30+}$	1.0	0.03	0.0003	0.061
$^{12}C^{6+}$	7.0	0.0064	0.0007	0.013

As shown in Table 1, the focusing strength varies in large range for different conditions, and the contribution of electron beam field domains the contribution. This may help to understand why only tens of mA electron beam current were usually used in practice.

Still for CSRm, we calculated the tune shifts and maximum betatron amplitudes of lattice at different e-beam field focusing strength, as shown in Table 2. As shown in the table, not only the tune shifts are large enough (Fig.1) to be considered seriously, but also the significant change on betatron oscillation amplitude function will significantly change the transverse acceptance of the storage ring and must be fully considered.

And finally, we found the combined transport matrix of solenoid and e-beam field as:

Table 2: Influence of e-cooler to CSRm Lattice

k	Q_x	Q_y	Max β_x (m)	Max β_y (m)
0	3.630	2.624	14.99	30.16
0.01	3.679	2.695	16.95	53.89
0.02	3.709	2.736	19.53	66.81
0.03	3.735	2.773	22.15	81.35

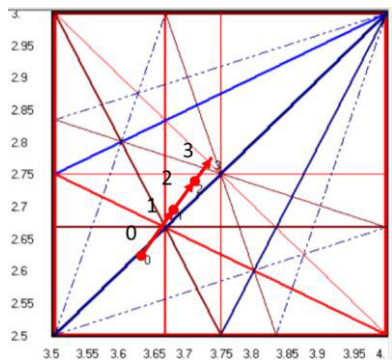

Figure 1: Tune shifts induced by solenoid and e-beam field at CSRm

Recently, electron cooling with pulsed electron beam was studied as HIRFL-CSR[3-5]. The dependence of lifetime on a synchronization between ion and electron pulses (see Figure 2) was found in experiments.

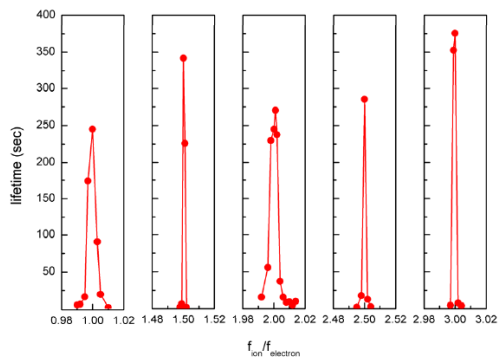

Figure 2: The dependence of lifetime on synchronization between ion and electron pulses[4].

One explanation of this phenomena is the barrier-like electric field at both ends of the e-beam bunch, but it's not sufficient. From the point view of transverse motion, considering the fast varying focusing strength of e-cooler on

ISBN: 978-3-95450-218-9 ISSN: 2226-0374 doi:10.18429/JACoW-COOL2019-TUPS09

the ion beam when the bunches of two beams are not synchronized, it's easy to "naturally" explain the experiment results. The ring lattice will change turn-by-turn according to the coverage condition of ions by electrons and it introduces variation of acceptance and super-period instabilities.

From Eq.(5,6,8), it's clear that the focusing strength will change during the de/acceleration, if the magnet field of solenoid and the current and energy of electron beam are fixed.

For a normal cooling accumulation and acceleration period of the synchrotron, the cooler parameters were usually kept for the injection and cooling accumulation. The tune shift varies smoothly during acceleration. A suitable condition can be found to get high acceleration efficiency if the e-cooler focusing strength is relatively low, as the transverse geometric emittance of ion beam will decrease during acceleration. But if the initial strength is high, crossing of low order resonant lines during acceleration will create significant beam loss.

Deceleration of ion beam is more complicated, as the transverse geometric emittance of ion beam will increase during deceleration. As an example, for the deceleration of Ni^{28+} ion beam from 400 MeV/u to 4 MeV/u at ESR/GSI[6], the efficiency is only 1/6 of the theoretic value. A better consideration of the e-cooler introduced influence on ion beams may help to improve this condition.

CONCLUSION

The combined transport matrix of solenoid and eletron beam field was deduced by Lie Algebraic method for the 1st order study convenience. The transverse perturbation of e-beam field of electron cooler on ion beam is ***not*** neglectable, especially for low energy ion beam cooling, pulsed e-beam cooling and especially when pulsed e-beam used before de/accelerations.

REFERENCES

[1] F. Christoph Iselin, "The MAD Program (Methodical Accelerator Design) Version 8.13 Physical Methods Manual, CERN/SL/92-?? (AP) (1994).

[2] J.W. Xia *et al.*, "The heavy ion cooler-storage-ring project (HIRFL-CSR) at Lanzhou", Nucl. Instr. Meth. A 488(1–2), 11–25 (2002), DOI:/10.1016/S0168-9002(02)00475-8

[3] Y. J. Yuan *et al.*, "Status of the HIRFL–CSR complex", Nucl. Instr. Meth. Phys. Res. Sect. B, 317:214-217, DOI:10.1016/j.nimb.2013.07.040

[4] H. Zhao *et al.*, "Electron Cooling of Bunched Ion Beam in a Storage Ring", *Phys. Rev. Accel. Beams*, 21, 023501, DOI:10.1103/PhysRevAccelBeams.21.023501

[5] H. Zhao *et al.*, "Simulation of Ion Beam Cooling with a Pulsed Electron Beam", *Nucl. Instr.. Meth. Phys. Res., Sect. A*, DOI:10.1016/j.nima.2018.03.048

[6] Frank Herfurth, "Slow, Exotic, Ions at GSI/FAIR", Symposium - IMP & GSI, 40 Years of Cooperation, Beijing, China,2017.

ISBN: 978-3-95450-218-9 ISSN: 2226-0374 doi:10.18429/JACoW-COOL2019-TUPS10

POWER SUPPLIES FOR CORRECTORS OF THE 2.5 MeV ELECTRON COOLING SYSTEM FOR THE COLLIDER NICA

O.V. Belikov, M.I. Bryzgunov, V.R Kozak, V.V. Parkhomchuk, V.B. Reva and D.S. Vinnik,
BINP, Novosibirsk, Russia

Abstract

To achieve the design luminosity of 10^{27} $cm^{-2}s^{-1}$ in the collider NICA [1] on colliding high-intensity ion beams with energy of up to 4.5 GeV/nucleon in the center-of-mass system, it is necessary to form short bunches with small transverse emittance. That will be done using electron cooling of ion beams at the energy of the experiment, which corresponds to an electron energy of 0.2 to 2.5 MeV. For simultaneous cooling of both ion beams, an electron cooling system consisting of two independent coolers has been designed [2].

INTRODUCTION

Each cooler of the electron cooling system includes the gun, where the electron beam appears, the accelerating/decelerating electrostatic tube, the transport beam line, and the cooling section. For correction of electron beams, both coolers use 144 correcting electromagnets (correctors), which need separate power supplies. All the power supplies of the correctors have been developed and produced at BINP.

The correction system includes six types of correctors:

- Correctors of beam position in the transport beam line and cooling section.
- Correctors for alignment of the force line straightness in the cooling section.
- Correctors for alignment of beam shape in the bends.
- Correctors for reducing the Larmor beam gyration (dipole mode and galloping mode).
- Correctors of the section for coordination of the transition from the electrostatic accelerator to the transport beam line.
- Correctors of the section for coordination of the transition from the transport beam line to the cooling section.

According to the power supply type, all the correctors can be divided into two groups:

- Correctors controlled by current of up to 6 A: 112 pcs.
- Correctors controlled by current of up to 20 A: 32 pcs.

However, correctors relating to the group with power sources of up to 6 A differ greatly in the total winding resistance (from 0.7 to 16 Ω, excluding the resistance of the leads). Therefore, the power supplies within the group have different output voltages.

Table 1 shows the numbers of different power supplies used for correction of the electron beam of the electron cooling system. The magnetic system of the electron cooling includes sections where longitudinal field correction is required, but the design makes it impossible to place free-standing correctors. The longitudinal magnetic field is formed by several series-connected sections, energized from a common power supply. For correction of the magnetic field, each section is connected in parallel with an additional, galvanically isolated, power supply, which produces an additional current of up to 20 A, which corresponds to 15% of the main power source current. In total, there are 16 additional current sources. They use the same power supply as the correctors.

Table 1: Power Supplies of Correctors

Type of power supply	Quantity, pcs.	Output current range, A	Maximum output voltage, V
MPS-6-24	32	-6 ÷ 6	24
MPS-6-60	32	-6 ÷ 6	60
MPS-6-140	48	-6 ÷ 6	140
MPS-20-50	48	-20 ÷ 20	50

STRUCTURE OF POWER SUPPLIES

Correctors with current of up to 6 A are powered by multichannel modular power supplies. Figure 1 shows a block diagram of eight-channel module of power supply MPS-6.

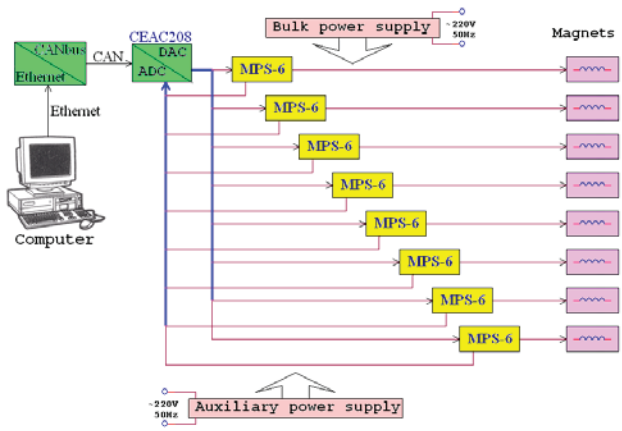

Figure 1: Structure of power module MPS-6.

The module includes 1 to 8 converters of the bulk power supply voltage to DC current. Each of these blocks supplies constant current to the respective load. The MPS-6 converters are monitored and controlled by means of analog signals. All MPS-6 converters within a module have common buffer and auxiliary power supplies, as well as common controller comprising digital-to-analog and analog-to-digital converters. Such a structure has the following advantages:

- The maximum output voltage of all MPS-6 converters within a module is determined by the voltage of the buffer power supply, and thus all the MPS-6 converters can be produced identical, which reduces the number of different blocks.

ISBN: 978-3-95450-218-9 ISSN: 2226-0374 doi:10.18429/JACoW-COOL2019-TUPS10

- Using a common buffer power supply for a multi-channel module improves the reliability of the power system as compared with single-channel devices, where each power supply has an individual buffer power supply.
- Using common devices in a module lowers its cost.

The multi-channel modular system of power supply has the following disadvantage: all outputs of constant voltage converters are galvanically connected with the buffer power source output. Therefore, these power supplies are not suitable as additional 16 current sources.

The correctors with current of up to 20 A are powered by single-channel power sources MPS-20. In contrast to MPS-6, an MPS-20 unit includes a converter of constant voltage to direct current. Converters for MPS-6 and MPS-20 differ in design because of different output powers, but they have a common block diagram (see Fig. 2).

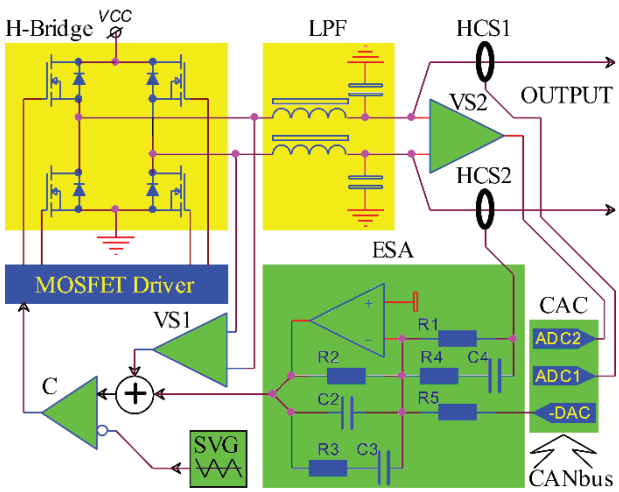

Figure 2: Block diagram of converter of constant voltage to DC. VCC – Bulk power supply voltage: H-Bridge – H-Bridge inverter; LPF – Low-pass filter; HCS – Hall Current Sensors; VS – Voltage sensor; ESA – Error-signal amplifier; CAC – External controller with CANbus interface; ADC – Analog-to-digital converter; DAC – Digital-to-analog converter; C – Comparator; SVG – Sawtooth-voltage generator.

A bridge inverter controls the output current by means of PWM of the buffer supply voltage. A low-pass filter LPF suppresses the fundamental frequency of the invertor and its harmonics. Two independent non-contact sensors HCS1 and HCS2 measure the output current. One sensor regulates the output current and the other is for independent measurements in the monitoring system.

The required quality of regulation is ensured due to application of a dual-feedback system. The first circuit of the current feedback includes elements with integral and differential characteristics. This circuit provides a high open-loop gain of the current feedback of over 10^3. The second circuit of the voltage feedback has zero DC amplification. It is introduced to suppress the bulk power supply ripples in a frequency band up to 1 kHz.

Table 2 shows parameters of the power sources MPS-6 and MPS-20.

Table 2: Parameters of Power Supplies

Parameter	MPS-6	MPS-20
Output current accuracy	$\leq 10^{-3}$	
Output current drift (24 h)	10^{-4}	
Temperature coefficient of output current drift, 1/°K	$4 \cdot 10^{-5}$	
Conversion frequency, kHz	50	
Cooling	Air Natural	Air Forced
Overall dimensions, mm^3	51×227 ×266	432×355 ×133

DESIGN OF THE POWER SUPPLIES

All the power supplies are made in the Eurocard format. Figure 3 presents a photograph of single-channel source MPS-20-50.

Figure 3: Power supply MPS-20-50.

The power supply is structurally designed as a 3U-subunit (432×355×133mm^3) made by Schroff. Monitoring and control are performed by CANbuses using the integrated controller CEAC124 [3], developed at BINP.

Figure 4 presents a photograph of eight-channel module MPS-6.

Figure 4: Eight-channel module MPS-6.

ISBN: 978-3-95450-218-9 ISSN: 2226-0374 doi:10.18429/JACoW-COOL2019-TUPS10

The module is designed as a 6U-subunit (432×415×266 mm^3) made by Schroff. Monitoring and control of the module are performed from the CEAC208 controller [4], developed at BINP.

The design of the power system for the correctors has been completed; all the necessary power supplies are in production. All the equipment will be located in 10 Varistar cabinets (600 × 800 × 1800 mm^3) made by Schroff; the electrical design of connection of the power system for correctors on the collider NICA is being prepared.

REFERENCES

[1] G. Trubnikov *et al.,* "The NICA project at JINR", *in Proc. of 7th International Particle Accelerator Conference IPAC'16*, May 2016, BEXCO, Busan Korea, pp. 2061-2065, 2016.

[2] V. V. Parkhomchuk *et al.,* "Design of the 2.5 MV Electron Cooling System and the Potential for Increasing NICA Collider Luminosity", *Physics of Particles and Nuclei Letters*, Dec. 2018, Vol. 15, Iss. 7, pp. 793-797.

[3] V.R. Kozak *at el., "*CEAC Controllers Family for Control of Power Supplies of Accelerator Facilities", *Vestnik NSU. Series: Physics.* 2012. V7, i 4, pp. 43-48.

[4] V. Kozak, M. Romakh, "Devices with CANBUS interface for automation systems of physical installations (Modules CAC208, CURVV)", Budker INP preprint 2004-68, Novosibirsk (2004).

ISBN: 978-3-95450-218-9 ISSN: 2226-0374 doi:10.18429/JACoW-COOL2019-TUPS13

THE CASCADE TRANSFORMER FOR THE HIGH-VOLTAGE ELECTRON COOLING SYSTEM FOR THE NICA COLLIDER

A. P. Denisov, M. I. Bryzgunov, A. D. Goncharov, V. V. Parkhomchuk, V. B. Reva,
D. N. Skorobogatov, Budker Institute of Nuclear Physics, Novosibirsk, Russia

Abstract

The 2.5 MeV electron cooling system for the NICA collider (JINR, Dubna) will use cascade transformers for distributing the power among the sections of the high-voltage column and for transferring power to the high-voltage terminal. The design of the cascade transformer and the measurements of its prototype are described.

INTRODUCTION

The NICA collider is designed to operate ion beams with energies up to 4.5 GeV/u [1]. In order to increase the ions accumulation efficiency and ions lifetime in the collider the electron cooling system must provide 2.5 MeV electron beams [2]. The designed electron cooling system uses the guiding magnetic field along the entire transport channel of the electron beam, including the high-voltage column. Magnetic coils and the power supply for electron collector constitute the major power consumption of the high-voltage column.

There are several common ways to transfer the electrical power to high-voltage regions, described in [3]. Methods involving the transmission of mechanical energy are not suitable for the new electron cooler, as some of them require larger space, entail the power consumption overhead or tend to be unstable. Instead, the electron cooling system will use a cascade transformed with high coupling coefficient between cascades, which transfers power from section to section through electrically isolated windings (Fig. 1).

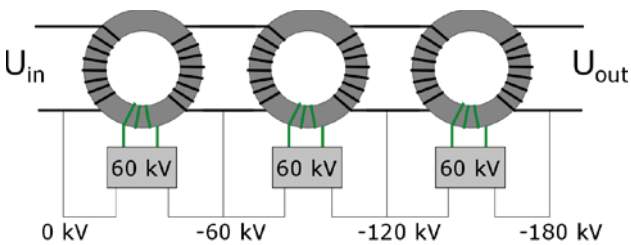

Figure 1: The schematic diagram of a power transferring cascade transformer.

A single high-voltage column includes two cascade transformers with 42 sections each: for transferring power to the high-voltage terminal and for distributing the power among the column sections.

POWER CONSUMPTION OF THE HIGH-VOLTAGE COLUMN

Each section of the high-voltage column (Fig. 2) has two coils for creating 500 G longitudinal magnetic field for focusing the electrons. The power consumption of a single coil is about 100 W. The electronics in a section together with high-voltage power supplies takes additional 220 W. Another consumer is the high-voltage terminal. It includes a 10 kW power supply for the collector rectifier and a 5 kW solenoid for focusing a low energy electron beam. The design parameters of the high-voltage column related to power consumption are presented in Table 1.

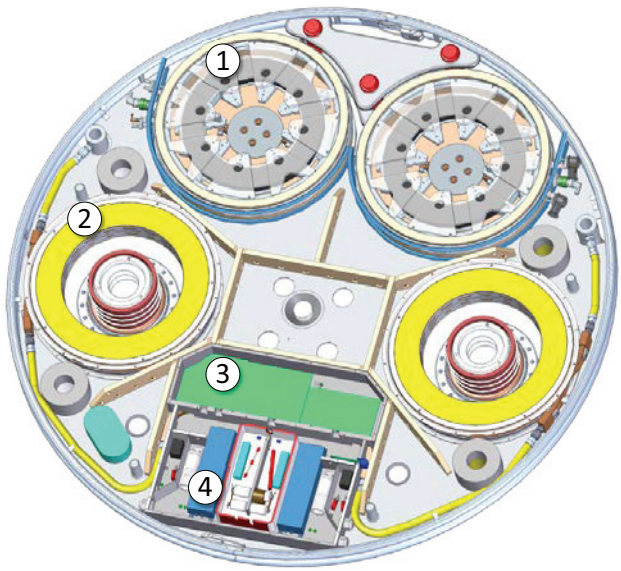

Figure 2: Section of the high-voltage column: (1) a single ring of the cascade transformer, (2) a magnetic coil for creating a guiding magnetic field in the accelerating tube, (3) control electronics, (4) high-voltage power supplies.

Table 1: Power Consumption of the High-Voltage Column

Consumer	Power
Magnetic coils of a section	200 W
HV power supply per a section	120 W
Control electronics per a section	100 W
Collector rectifier	10 kW
Control electronics of the HV terminal	700 W
Magnetic coils in the HV terminal	5 kW
Sections of the HV column	17.6 kW
HV terminal	15.7 kW

DESIGN OF THE CASCADE TRANSFORMER

The cascade transformer consist of 42 sections stacked one onto another with 6.4 cm period. To prevent overheating of the transformer during its operation, it is placed inside an oil-cooled tank (Fig. 3). As voltage between adjacent sections of the transformer reaches 60

ISBN: 978-3-95450-218-9 ISSN: 2226-0374 doi:10.18429/JACoW-COOL2019-TUPS13

kV, the tank is a set of alternating shielding metal and insulating ceramic rings.

Each section includes a ring-shaped magnetic core, power transferring windings and a set of capacitors for compensating the leakage inductance. One set of windings is used to receive electrical power from the previous section of the cascade transformer, and another is for transferring power to the next section. As voltage between these two set of windings is 60 kV, it is necessary to add an insulating gap between these set of windings as well as between windings and the magnetic core (Fig. 4). These gaps leads to the presence of leakage inductance that can be compensated by adding capacitors to the power transferring windings.

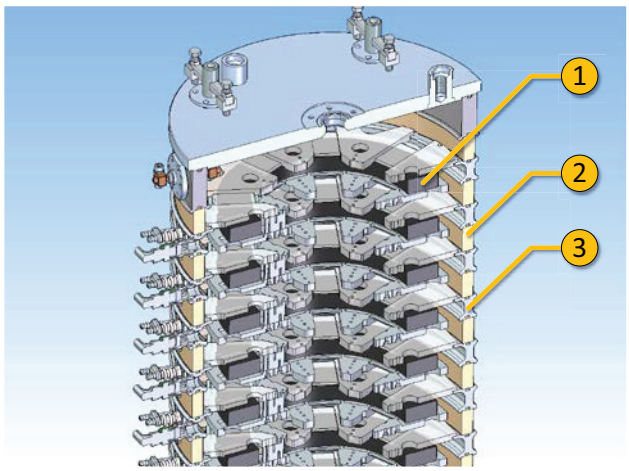

Figure 3: The design of the cascade transformer (for simplicity, windings and other electronic components are not shown): (1) a section of the cascade transformer, (2) ceramic rings for insulating adjacent sections, (3) duralumin shields.

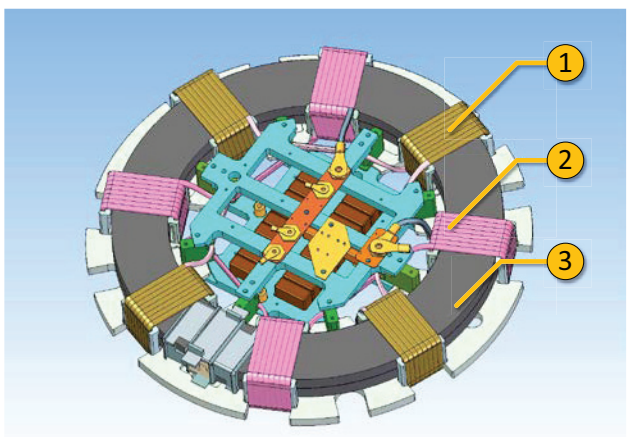

Figure 4: The design of the section of the cascade transformer: (1) windings for receiving electrical power from the previous section of the transformer, (2) windings for transferring power to the next section, (3) a magnetic core of the transformer section.

The similar cascade transformer design were used in the COSY electron cooler [4]. The main difference is that the windings are split into more groups and connected in series (the transformer section of the COSY cooler has two groups of winding connected in parallel). The design parameters of the new cascade section are listed in Table. 2.

Table 2: Parameters of the Cascade Transformer Section

Parameter	Value
Magnetic core shape	Ring
Magnetic core inner radius	10 cm
Magnetic core outer radius	14 cm
Magnetic core thickness	2 cm
Magnetic core material	5BDCP
Number of windings	2
Winding wire type	Litz wire AWG38
Number of winding turns	7×4
Height of a wind turn	3 cm
Width of a winding turn	6 cm
Winding length	6.3 m
Wire electrical resistivity	$17.24 \cdot 10^{-6}$ Ohm·mm
Wire section	5.7 mm^2

MEASUREMENTS OF THE PROTOTYPE

For verifying the design parameters of the cascade transformer, a three-section prototype was tested (Fig. 5). The parameters of interest are the remagnetization losses, which describe the amount of heat produced by the transformer in the idle regime, the section efficient pass-through resistance, and the leakage inductance of the transformer sections affecting the transformer efficiency.

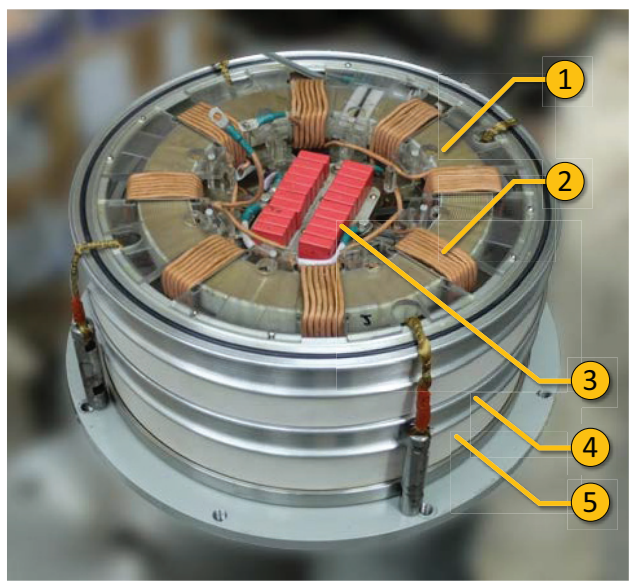

Figure 5: A three-sections prototype of the cascade transformer: (1) a magnetic core, (2) windings, (3) capacitors for compensating the leakage inductance, (4) duralumin shielding rings for decreasing the leakage inductance, (5) ceramic rings for insulating adjacent sections.

The cascade transformer can be represented using its equivalent circuit (Fig. 6). The working frequency of the transformer is chosen so that the capacitors connected to

ISBN: 978-3-95450-218-9 ISSN: 2226-0374 doi:10.18429/JACoW-COOL2019-TUPS13

the winding of the transformer section compensate the reactive impedance caused by the presence of leakage inductance. The capacitors placed after each section in order to lower the voltage drop from one section to another.

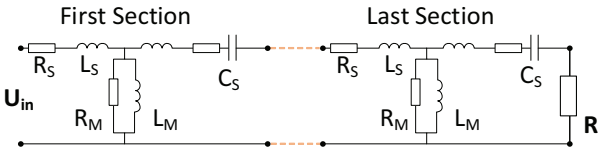

Figure 6: The equivalent circuit of the cascade transformer: (L_M) magnetization inductance, (R_M) load representing the remagnetization losses of a magnetic core, (R_S) losses in the windings, (L_S) leakage inductance, (C_S) capacity for compensating the leakage inductance, (U_{in}) input signal, (R) active load of the transformer.

As the transformer efficiency varies with the working frequency, the frequency response measurements can be used to retrieve the parameters of the transformer. We used frequency response of the transformer pass-through impedance by feeding the transformer with harmonic signal and measuring the output signal on the active load of the transformer. Given the active load and the shape of the input and output signals, one can calculate the impedance of the cascade transformer. At some frequency, the leakage inductance is compensated by the capacitors, and the transformer impedance reaches its minimum corresponding to the active losses in windings. To get a more accurate estimation of the transformer parameters we can fit the measure frequency response function with the curve, calculated with assumption that all transformer sections have similar parameters (Fig. 7). The measured leakage inductance of a single winding is approximately 25 μH. The magnetization inductance was measured the similar way, but with capacitors connected in parallel to the windings and was about 40 mH.

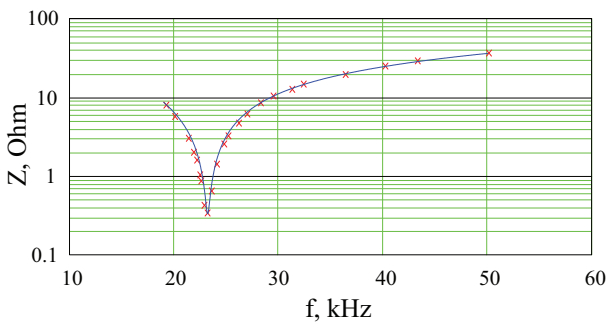

Figure 7: The frequency response of the prototype pass-through impedance (three sections): the red points are measured values of the pass-through impedance and the blue curve is the fit.

Another way to measure losses, which occur during the transformer operation, is to measure the amount of heat that transformer produces. Such experiment was conducted by measuring the heating of the oil, which was used for cooling the transformer loaded to 8 Ohm resistor (Fig. 8). The input voltage is 500 V (rms), input current is 44 A. Given the oil flow 0.1 l/s and its temperature grows about 5.5 degrees, the estimated amount of heat is 240 W per section. At idle, the heating, measured the same way, is about 40 W. So, the pass-through impedance of the transformer can be calculated as (240W - 40W) / $(44A)^2$ ≈ 0.1 Ohm. Electrical parameters of the transformer sections are listed in Table 3.

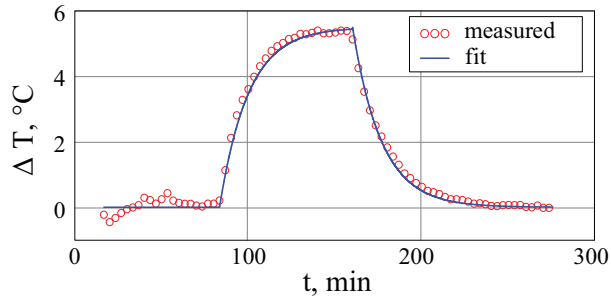

Figure 8: The heating curve of the oil used to cool the sections of the transformer. The current in the transformer windings is 44 A. The input voltage is 500 V. Oil flow is 0.1 l/s.

Table 3: Electrical characteristics of a single section of the cascade transformer.

Parameter	Value
Working frequency	23.2 kHz
Pass-through active impedance	0.11 Ohm
Magnetization inductance	40 mH
Leakage inductance	50 μH
Remagnetization losses	2.5 kOhm
Capacity of compensating conductors	0.94 μF

CONCLUSION

The new cascade transformer with distributed power transferring windings is designed for the high-voltage electron cooling system of the NICA collider. Thermal and electrical tests conducted on the 3-section transformer prototype shows that a single 42 sections cascade transformer is capable of providing more than 18 kW or 16 kW for distributing power along the sections of the high-voltage column or transferring the power to the high-voltage terminal correspondingly.

REFERENCES

[1] A. Kovalenko *et al.*, “Status of the NICA project at JINR”, *EPJ Web Conf*, vol. 191, p. 01003, Oct. 2018.

[2] V. B. Reva *et al.*, “High voltage cooler NICA status and ideas”, in *Proc. 11th International Workshop on Beam Cooling and Related Topics (COOL17)*, Bonn, Germany, January 2018, paper TUM21, pp. 25-27.

[3] A. P. Denisov *et al.*, “Cascade transformer based on the volume coil for power transmission under high voltage”, *Technical Physics*, vol. 63, no. 8, pp. 1212-1222, 2017.

[4] V. B. Reva *et al.*, “Energy transfer in the high-voltage electron cooler for the COSY synchrotron ring”, *Instruments and Experimental Techniques*, vol. 58, no. 2, pp. 181-189, 2015.

ISBN: 978-3-95450-218-9 ISSN: 2226-0374 doi:10.18429/JACoW-COOL2019-TUPS14

ELECTRON COOLING APPLICATION FOR HADRON THERAPY

V. A. Vostrikov†, V. B. Reva, V. V. Parkhomchuk
Budker Institute of Nuclear Physics, 630090 Novosibirsk, Russia
and Novosibirsk State University, 630090 Novosibirsk, Russia

Abstract

The project of synchrotron for hadron therapy with electron cooling is developing in the Budker Institute of Nuclear Physics. The main goal of the project is design of the effective and low cost hadron therapy facility. The electron cooling is applied for an ion beam accumulation, cooling and preparation for slow extraction. The high quality cooled ion beam with an extreme small emittance and energy spread allows significantly decrease the synchrotron and beam transfer lines apertures. Moreover, the electron cooling can be applied for accumulation of short-lived radioactive isotopes that can be used for online visualization of treatment.

INTRODUCTION

Cancer is now the origin of death in one out of every four lives. Overcoming this scourge is a common goal for all of humanity. The common treatment for cancer includes surgery, chemotherapy and radiation therapy. The radiation therapy is one of the effective methods for cancer treatment and is prescribed to more than 50% of all patients. It is based on delivering high doses of ionizing radiation to localized tumours in the body. The goal is to destroy all the tumour cells with acceptable damage effects to the surrounding normal tissue, which is unavoidably irradiated.

Photons are used for most patients treated with a conventional radiotherapy. They deposit most of energy upstream of the tumour in healthy tissue. Special irradiation system from many directions and intensity modulation are used to increase the ratio of tumour to healthy tissue dose. The conventional therapy by photons is relatively inexpensive and wide world use.

Beams of protons and ions offer important advantages over conventional radiotherapy. The protons and ions power does not decrease exponentially with penetration in the body. Instead, they deposit more energy as they slow down, culminating in a Bragg peak. The depth at which the peak occurs can be operated by the value of particles energy are given by the accelerator. The proton and ion beams have little lateral scattering and can be precisely controlled. Therefore, the beam energy can be delivered accurately to the treatment volume without seriously damage of surrounding tissues or adjacent critical organs.

The hadron beam therapy has been shown to be effective in such cases as relatively large tumours of the esophagus and lung, liver, prostate and rectum, tumours of the head and neck, and eye.

For physical as well as for biological reasons, the light ions yield better clinical results than protons. Light ions, such as carbon, have a higher RBE than protons and provided treatment that is more effective for certain, deep-seated tumours that are often radio-resistant.

The clinical success of carbon therapy at the NIRS, Chiba, Japan and GSI, Darmstadt, Germany has led to the establishment of 10 more carbon ion therapy centres in Japan, Germany, Italy, Austria and China [1-3]. Several other centres are planned or are under construction in Europe and Asia. However, the high capital and operating costs limit the wide application of ion therapy. The development of robust, effective, and low costs ion therapy system is a paramount task to increase the availability of treatment to the patients.

ELECTRON COOLING APPLICATION

The idea of electron cooling was proposed and developed at BINP [4]. The electron and ion beams are converged inside the cooling section and during the particles co-moving the heat energy transfers from ions to electrons. Thus, the electron cooling reduces the spread in the longitudinal and transverse ion velocities, which means a decrease in the momentum spread and transverse emittance of the ion beam. Now, the low energy electron cooling is a routine and effective technique wide used in the high energy and nuclear physics. In particular, electron coolers are installed at the leading centres were methods of ion therapy was developed and continues to develop [5, 6]. However, at developing of standard design for ion therapy facility the electron cooling technology was not in demand. Usually, this is argued that the electron cooling is expensive and very complex equipment, redundant for therapy facility. The main goal of present article is the demonstration that electron cooling application helps design robust and not expensive medical accelerator.

The accumulated at BINP experience allows transferring the electron cooling technology to the application field. The ion therapy is the most favourable application. The ion beam energy range required for the cancer therapy is fully overlapped by the standard design of the BINP electron cooler (Fig. 1). This base design demonstrates the effective and robust long time operation at GSI (Darmstadt), IMP (Lanzhou) and LEIR (CERN) with success [7,8].

The cooled high intensity ion beam with extreme small energy spread and transverse emittance is a superior therapeutic instrument allowing irradiate tumour with high accuracy. Certainly, the size of beam spot on the tumour is determined primary by multiple scattering and fluctuations of ionization losses during the path in depth of tissues. Nevertheless, the electron cooling eliminates the beam spot broadening due to the inherent beam emittance and energy spread.

† e-mail: V.A.Vostrikov@inp.nsk.su

ISBN: 978-3-95450-218-9 ISSN: 2226-0374 doi:10.18429/JACoW-COOL2019-TUPS14

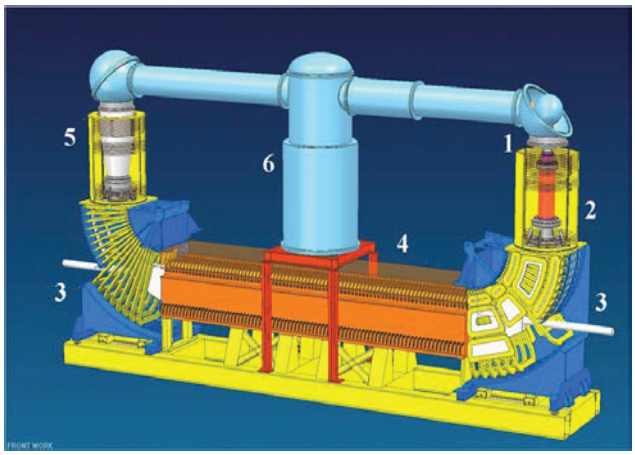

Figure 1: Layout of EC-300. 1 -electron gun, 2 - acceleration tube, 3 - ion beam vacuum chamber, 4 - cooling section, 5 - collector, 6 - high voltage generator.

The electron cooling allows accumulating the beam with high intensity that is important for increasing of the patient throughput. The suppression of beam losses due to space charge and IBS decreases influence of the radiation to the accelerator components and provides more safety of the treatment.

However, the insertion of electron cooler into the ion medical synchrotron with traditional design does not allows to fully revealing all possibilities. The most effective way is design the ion accelerator built around the key element - electron cooler.

The optimal structure for synchrotron with electron cooling has a racetrack mirror-symmetry lattice with achromatic arcs and long straight sections. One straight section is occupied by electron cooler. The set of quadrupole magnets should provide flat and equal betatron functions of high enough value, to achieve the optimal cooling decrements. In the opposite straight section the RF resonator, injection and extraction elements are installed.

In addition, the lattice shall include equipment for a transverse coupling compensation, caused by the cooling solenoid. The longitudinal magnetic field in the main cooling solenoid is constant for all range of the ion beam energies. Thereby at injection energy, the coupling influence is significant. The effective and compact solution is based on the application of sqew quadrupoles that ramping in synchronization with the beam energy.

Clear that the circumference of the synchrotron with electron cooling will be larger than for machine with traditional design. This circumstance contradicts the current trend towards the compaction of medical accelerators. Nevertheless, the resulting increasing in the synchrotron dimensions is insignificant especially in comparison with the area occupied by the total facility.

The small emittance of ion beam gives the possibility to decrease the apertures of synchrotron and HEBT elements significantly. It leads to decrease the weight, power consumption and cost of the synchrotron and the beam transfer lines. To be fair, it should be noted that the energy consumption of the electron cooler partially hides the positive effect. The most suitable would be the application of superconducting technologies in the implementation of the electron cooler magnetic system.

The advantages of small beam size are most evident at the design of a superconducting rotating ion gantry and beam scanning system. Application of the helium free magnets with maximum field about 4 T and small aperture about 15 mm allows design the compact rotating ion gantry with low weight. The small aperture of bend magnets leads to decrease the stored energy. The cooled beam using reduces the thermal load of the magnet assembly caused by particle losses.

The decrease of scanning magnets aperture gives possibility to increase the scanning rate. This seems important to reduce the total time of treatment and can be effective at irradiating of movable organs.

The minimum beam emittance at cooling is depends on the beam intensity and energy. At injection energy the beam emittance limited by the space charge phenomena, at extraction energy by IBS. For minimizing of synchrotron apertures, the injection energy of carbon beam with the intensity 10^{10} particles per pulse should be increased up to 20 MeV/u. For these purposes, the fast cycling booster in combination with the low energy injector (for example electrostatic tandem) can be applied. High repetition rate of booster allows accumulating and cooling the high intensity beam at the main synchrotron. The total cost of booster and injector is comparable with cost of the traditional ion linear accelerator with energy 6-7 MeV/u. This scheme is flexible and can be used for the production of different types of ions.

The two-stage acceleration scheme with electron cooling allows easy production and accumulation of the short-lived PET isotopes (as C^{11}, N^{13}, and O^{15}). The short-lived radioactive isotopes are produced in result of interaction of ion beam from booster with nuclei of gaseous target. The radioactive isotopes beam is injected into the main synchrotron for accumulation, cooling, and acceleration. The irradiation of tumour by short-lived radioisotopes in the treatment room equipped by PET tomography gives the possibility to build the online therapy. The possibility to observe the irradiation process in time is very promising for solving problem of movable tumours. As the rate production of PET isotopes is not so high, the treatment time for whole tumour will be increased. Therefore, the optimal scenario is the tumour marking by the radioactive labels in amount enough for online tracking and then irradiation the target volume by carbon beam.

Also for irradiation of movable tumours, the operative beam energy changing by the cooling friction force can be used.

EXTRACTION

In the synchrotron with electron cooling, few extraction schemes can be arranged. First is the traditional resonance extraction. The electron cooling leads to significant decrease of beam losses at extraction.

ISBN: 978-3-95450-218-9 ISSN: 2226-0374 doi:10.18429/JACoW-COOL2019-TUPS14

Recombination of ions traveling through the cooling section is another option of the slow extraction scheme. An extremely low relative velocity of the ions and the electrons increases the recombination cross-section. Available and fast control of the transverse profile and current of electron beam allows fine adjustment of the $^{12}C^{5+}$ ion beam intensity and spot size. This type of extraction provides high level of the patient safety from over irradiation during treatment (see Fig. 2).

The small emittance and narrow momentum spread enables realize original scheme of extraction by small portions with the low-aperture pulsed high repetition kicker application. This scheme was proposed and applied in the COSY facility [9].

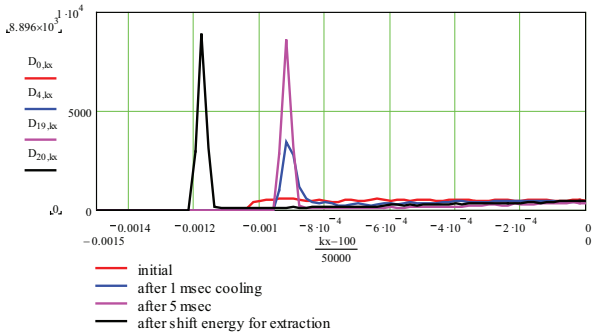

Figure 2: Computer simulation of portion extraction.

The circulating cooled ion beam can be split by cooling force with the well-controlled intensity in the portion.

The beam is shifted close to the septum by the local distortion of orbit. The flat momentum distribution of ions is prepared by the fast scanning of electron beam energy ($\pm 1.5 \cdot 10^{-3}$). After that, the electron beam energy is shifted to the edge of distribution. The neighbour ions cooled to the new energy and forming the portion of required intensity. Due to nonlinearity of friction force, the most part of beam is not affected. After that, the beam as whole fast shifted by the betatron core. The formed portion of beam comes into the kicker aperture, kicked out over septum and extracted. The circulated beam is slowly shifted back as whole by the betatron core reverse. The system is ready to start the forming of new portion. The proposed repetition rate of portion extraction 200 Hz is in good agreement with simulations [10].

EXPERIMENTS WITH COOLING

For demonstration of the electron cooling in action the results of recent experiments in CSRe (IMP, Lanzhou, China) and LEIR, CERN are presented [8, 10, 11].

At Fig. 3, the standard operation cycle of CSRe including the accumulation with cooling at injection energy and next acceleration of carbon beam is shown.

At Fig. 4, the evolution of ion beam profile in LEIR cycle is presented. The cycle starts from two injections with cooling, and then Pb^{54} ion beam is accelerated from 5 MeV/u to 71 MeV/u.

At Fig. 5, the Schottky signal of carbon beam with energy 400 MeV/u during cooling at CSRe is presented.

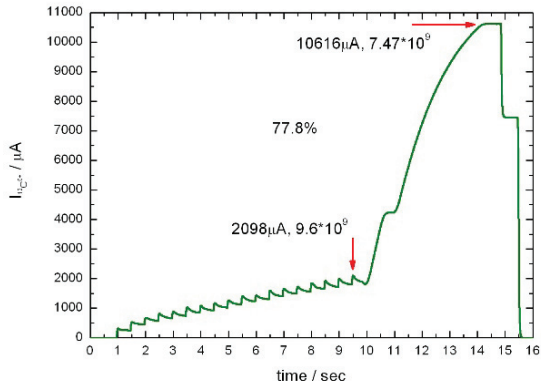

Figure 3: Beam current at single cycle: accumulation at CSRe with electron cooling $9.6 \cdot 10^9$ carbon ions beam on energy 7 MeV/u, then acceleration up to 600 MeV/u.

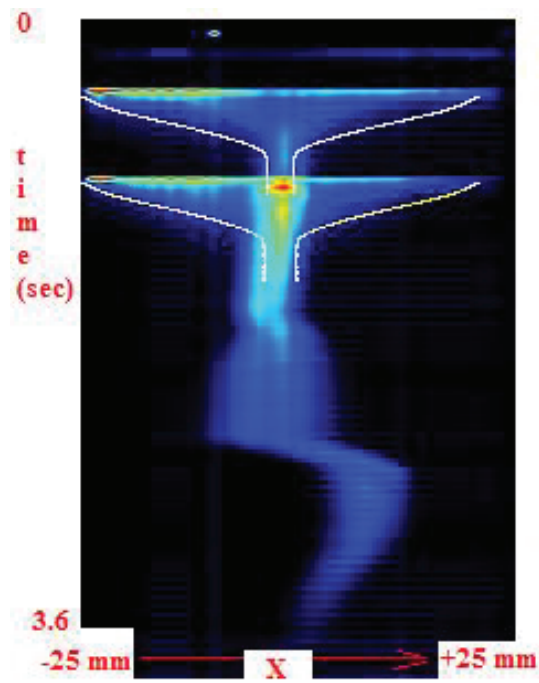

Figure 4: Pb^{54} ion beam profile at LEIR (CERN) cycle.

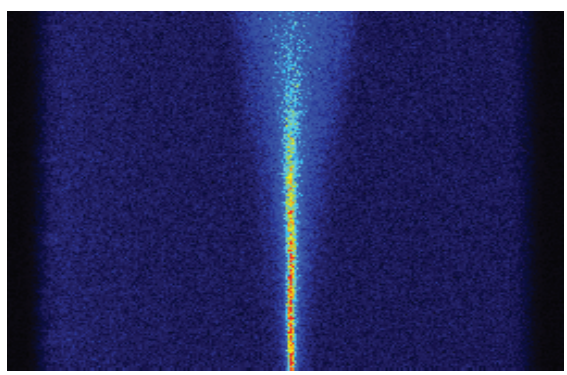

Figure 5: Cooling of carbon beam with energy 400 MeV/u at CSRe (IMP, Lanzhou).

ISBN: 978-3-95450-218-9 ISSN: 2226-0374 doi:10.18429/JACoW-COOL2019-TUPS14

BINP PROJECT

Base on the described above conception the carbon ion medical accelerator is developed in BINP [12, 13]. The accelerator includes the tandem accelerator, the rapid cycling booster, and the main synchrotron with electron cooling. The synchrotron provides $^{12}C^{6}$ ions beam with the average intensity of 10^{10} particles per pulse in the energy range from 140 MeV/u to 430 MeV/u.

The comparison of main parameters of accelerator with PIMMS [14] is presented in Table 1. The main parameters of electron cooler for medical synchrotron are listed in Table 2.

Table 1: Main Parameters of Accelerator

Parameter	BINP	PIMMS
Injector	Tandem & rapid cycling booster	Linac
Injection energy	30 MeV/u	7 Mev/u
Intensity	10^{10} per cycle	10^{9} per cycle
Circumference	83 m	75 m
Electron cooling	EC-300	-
Synchrotron bend magnet gap	36 mm	72 mm
Synchrotron quad. bore diameter	70 mm	170 mm
HEBT bend magnet gap	20 mm	62 mm
HEBT quad. bore diameter	38 mm	80 mm
Extraction	Resonance, recombination, portion extraction	Resonance
Ion gantry	SC rotating	-

Table 2: Main Parameters of Electron Cooler

Parameter	Value
Electron beam energy	Up to 300 KeV
Total length	7.5 m
Cooling length	4.8 m
Magnetic field	0.1 – 0.15 T
Field quality	10^{-4}

CONCLUSION

BINP develops the hadron therapy facility based on the synchrotron with electron cooling. The robust design allows to decrease both capital and operation costs of the facility. The electron cooling allows significantly decrease the apertures of synchrotron, HEBT, gantry, and scanning system. Application of the short lived radioactive isotopes, and the energy scanning can help to solve the movable tumours problem. The electron cooling allows application different types of extraction for both raster and spot scanning simultaneously.

REFERENCES

[1] T. Kamada *et al.,* "Carbon ion radiotherapy in Japan", *Lancet Oncol*. 2015.

[2] G. Kraft, "History of the heavy ion therapy at GSI" https://three.jsc.nasa.gov/articles/Krafts_GSI.pdf

[3] Hongwei Zhao, "Carbon Ion Therapy at Lanzhou", presented at the Workshop "Ideas and technologies for a next generation facility for medical research and therapy with ions", Archamps, June 19-21, 2018.

[4] G. I. Budker, *Soviet Atomic Energy* 22(5): 438–440, 1967.

[5] K. Noda *et al.,* "Commissioning of electron cooler for medical and other application at HIMAC", in *Proc. EPAC' 2000,* pp. 1259-1261.

[6] M. Steck *et al.,* "Beam accumulation with the SIS electron cooler", *Nucl. Instr. Meth., Section* A, vol. 441, pp. 175-182, 2000.

[7] V. Parkhomchuk *et al.,* "Commission of electron cooler EC-300 for HIRFL-CSR", in *Proc. EPAC'04*, pp. 1419-1421, 2004.

[8] A. Bubley *et al.,* "Commissioning of the LEIR electron cooler with Pb^{+54} ions", in *Proc. RuPAC'06*, pp. 25-27, 2006.

[9] J. Dietrich *et al.*, "Fast kicker extraction at COSY-Juelich", in *Proc. EPAC 2000*, pp. 1708-1710, 2000.

[10] V. V. Parkhomchuk *et al.*, "Electron cooling for the therapy accelerator complex", in *Proc. COOL'09*, pp. 168-172, 2009.

[11] XiaoDong Yang *et al.*, "Electron cooling experiments in CSR", *Sci. China Phys. Mech. Astron.* Vol. 54 (Suppl 2), pp. 274-278, 2011.

[12] E. B. Levichev *et al.*, "Carbon ion accelerator facility for cancer therapy", in *Proc. RuPAC'06*, pp. 363-365, 2006.

[13] V. A. Vostrikov *et al.*, "A project for synchrotron with electron cooling for cancer therapy", *Physics of Particles and Nuclei Letters*, Vol. 9, No. 4–5, pp. 429-432, 2012.

[14] P. J. Bryant *et al.*, "Proton-Ion Medical Machine Study (PIMMS), 2", CERN, Geneva, Switzerland, Rep. CERN-PS-2010-007-DR, 2010.

ISBN: 978-3-95450-218-9 ISSN: 2226-0374 doi:10.18429/JACoW-COOL2019-TUPS15

THE MAGNETIC SYSTEM OF ELECTRON COOLERS OF COLLIDER NICA

V. Panasyuk, M. Bryzgunov, A. Bubley, V. Parkhomchuk, V. Reva,V. Konstantinov, V. Korchagin, N. Kremnev, S. Pospolita, S. Ruvinskii, BINP SB RAS, Novosibirsk, Russia

Abstract

The complex of electron cooling is created in the BINP SB RAS. Complex is duplex of electron coolers. According to technical specifications total power consumption of the complex should not exceed 500 kW, electron energy from 0.2 to 2.5 MeV, magnetic field in solenoids of cooling up to 2kG, and distance between the centers of solenoids should be 320mm. In general, the layout of this complex is similar to the layout of the cooler created in BINP for COSY [1], but its production due to the above specifications is much more complicated.

LAYOUT OF MAGNETIC SYSTEM. POWER SUPPLIES.

Magnetic system of coolers complex is shown on Fig. 1. The units of upper cooler of this system marked counter-clockwise from gun to collector: **1**–gun, **2**–accelerating tube, **3**–match-1, **4**–bend-1, **5**–line08-1, **6**–bend-2, **7**–insert-1, **8**–transport channel-1, **9**–insert-2, **10**–tor90-1, **11**–ion dipole-1, **12**–ins&match-1, **13**–solenoid, **14**–ins&match-2, **15**–ion dipole-2, **16**–tor90-2, **17**–insert-3, **18**–transport channel-2, **19**–insert-4, **20**–bend-3, **21**–insert-5, **22**–transport channel-3, **23**–line08-2, **24**–bend-4, **25**–match-2, **26**–decelerating tube, **27**–collector.

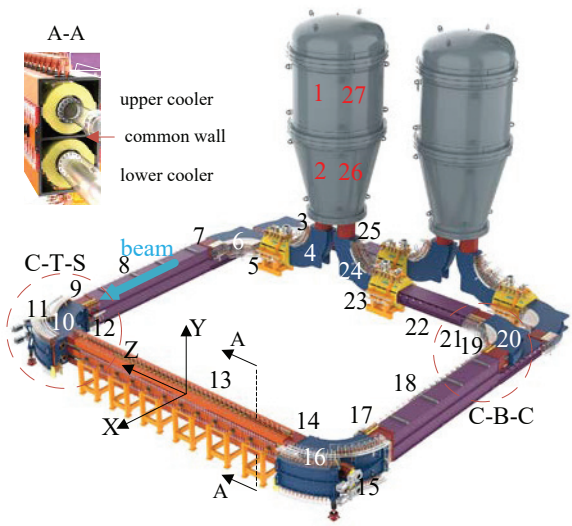

Figure 1: Layout of magnetic system. C-B-C – reference segment, C-T-S – multifunctional segment.

The same units of the lower cooler are placed clockwise from gun to collector (on direction of electron beam). Total length of transport channels here is 1.4 times greater.

The power consumption is determined by the specified value of longitudinal field B_s in units of system and permissible winding height in their coils. The radial or vertical dimensions of the vacuum elements determine inner radius r_{in} of the round coils or inner size on Y of the toroidal coils: ≥87 mm. The common wall of the magnetic shields of electron coolers with a thickness of 15mm and the distance between the beams (320 mm) limit the outer radius of round coils: r_{out}=150mm. To minimize the power loss, it was necessary to implement the maximum possible winding height in round coils: $r_{out} - r_{in}$ = 63mm. In this case, the losses per 1 m in the solenoid (at 2 kG) are equal to 10 kW/m. Coils of bending field (B_b) are locates above and below coils of longitudinal field (B_s) in toroids and bends. Minimal thickness of the bending coil is 17mm. As a result, winding height of these coils is reduced by 17 mm. Such restrictions on the winding height determine the value of the B_s field in these and other units of the magnetic system: no more than 1kG. For this reason, short units of field matching (ins&match **12**, **14**) are inserted into each gap between the solenoid (**13**, 2 kG) and the toroids (**10**, **16**, 1 kG).

Each cooler will use twelve high-current power sources (PS). PS of upper cooler are show in Table 1. IST-9up and IST-5up are PS of bending field B_b. IST-10up and IST-11up are PS of ion dipoles. Others IST-s are PS of longitudinal field B_s of the rest units.

Table 1: PS of Upper Cooler

PS	Magnetic system units	I(A)	P(kW)
IST-1up	solenoid (**13**)	221	61
IST-2up	tor90-1 (**10**)	710	19.8
IST-12up	tor90-2 (**16**)	710	19.8
IST-9up	∑Btor90 (**10**,**16**)	295	3.72
IST-3up	∑bend (**4**,**6**,**20**,**24**)	195	31.5
IST-5up	∑Bbend (**4**,**6**,**20**,**24**)	295	7.45
IST-4up	∑line08 (**5**,**23**)	250	19.3
IST-7up	∑channel(**8**,**18**,**22**)	135	30.1
IST-6up	∑ins(**7**,**9**,**12**,**14**,**17**,**19**,**21**)	320	21.9
IST-8up	∑ins&match (**12**,**14**)	440	7.56
IST-10up	ion dipole-1 (**11**)	440	4.93
IST-11up	ion dipole-2 (**15**)	440	4.93

Full power of upper cooler is 232kW. Power of lower cooler is 244kW (more due to the length of channels).

REFERENCE SEGMENT: CHANNEL– BEND – CHANNEL

Properties of turn of electrons by 90° in the case, when centrifugal force compensates by Lorentz force only on average, studied when creating a COSY cooler [1]. Let's consider the a similar variant adapted to NICA cooling complex. Calculations performed using proven MAG3D code [1]. Sizes of coils and ferromagnets as close to real as possible. Radius of turn is R=1m. The longitudinal field B_s=1kG. The electron passage of the bend is resonant in

ISBN: 978-3-95450-218-9 ISSN: 2226-0374 doi:10.18429/JACoW-COOL2019-TUPS15

energy. At resonant energy, electrons entering a bend without transverse energy leave it without "heating". Some of these energies are equal to 4.865, 2.5, 1.65, 1.185 and 0.905 MeV. The oscillations of electrons $y_i(s)$ across bending plane (y=0) at these energies are shown on Fig. 2.

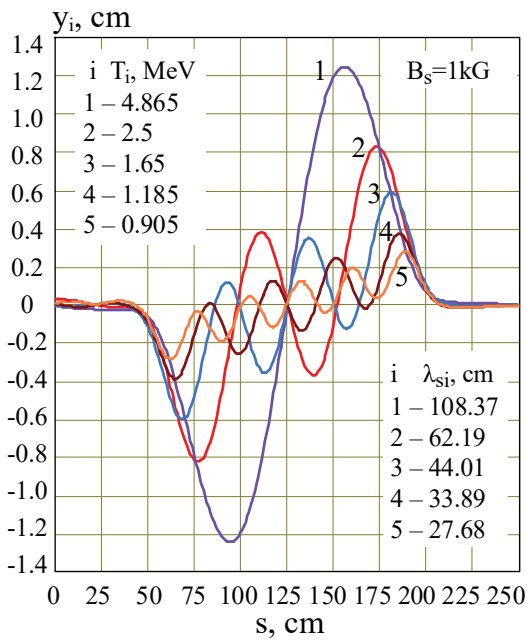

Figure 2: Reference oscillations of electrons yi(s).

The characteristic longitudinal size in this calculation is pitch of Larmor spiral $\lambda_s=2\pi\rho_s$, where $\rho_s = \beta c/\omega_H$ - Larmor radius, $\omega_H = (eB_s)/(\gamma mc)$ - Larmor frequency. Further, K(s) is the curvature of axial force line of longitudinal field B_s. Width at half maximum of K(s) equal $\Lambda \approx (\pi/2)\cdot R$ = 157cm. Note that the ratios Λ/λ_{si} are not integers: 1.45, 2.52, 3.57, 4.63 and 5.67.

For the intermediate energy T_n, we can choose the appropriate y_i (s) (see Fig. 2). For T_{n1}=1.0 and T_{n2}=1.5MeV oscillations $y_3(s)$ are suitable (T_3=1.65MeV).

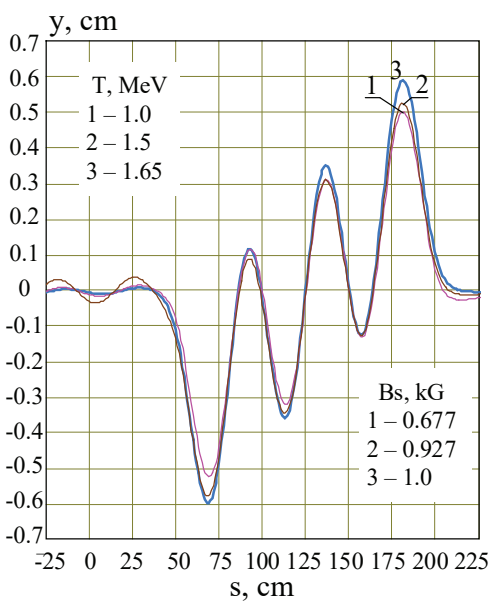

Figure 3: oscillations $y_3(s)$, $y_{n1}(s)$ and $y_{n2}(s)$.

Oscillations $y_{n1}(s)$ and $y_{n2}(s)$ are obtained using verified program for $y_3(s)$. For this, the coils currents in this program were multiplied by corresponding ratio $(\gamma_n\beta_n/\gamma_3\beta_3)$. Such a procedure follows from $\lambda_{s3}=\lambda_{sn1}=\lambda_{sn2}$ and bending fields $B_{b3}(s) \sim \gamma_3\beta_3$, $B_{bn1}(s) \sim \gamma_{n1}\beta_{n1}$, $B_{bn2}(s) \sim \gamma_{n2}\beta_{n2}$. Results of such calculations are given in Fig. 3.

Calculations performed for ferromagnetic shields with nonlinear magnetic permeability from ST-10. This causes some discrepancies in oscillations.

Profiles of the centrifugal force Fc(s) and the Lorentz force FL(s) are shown on Fig. 4. Here $Fc(s) = \gamma\beta^2\mathcal{E}_0K(s)$, where $\mathcal{E}_0$=512keV, K(s) in cm^{-1}, and $FL(s) = -0.3\beta\cdot B_b(s)$, where $B_b(s)$ in G.

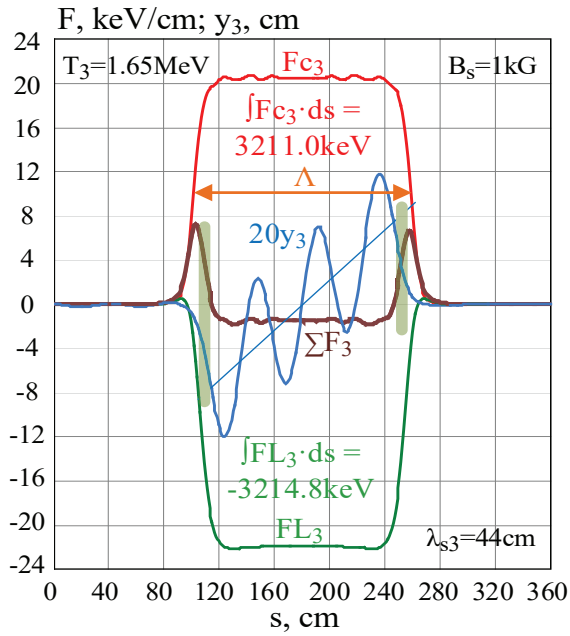

Figure 4: Profiles of $Fc_3(s)$, $FL_3(s)$ and $\sum F_3(s) = Fc_3(s) + FL_3(s)$ along axial force line.

Note that integrals of these forces along the longitudinal coordinate quite well compensate each other.

Dependencies of bending fields B_b in the center of the bend on y and on radius ΔR=r-R are shown on Fig. 5.

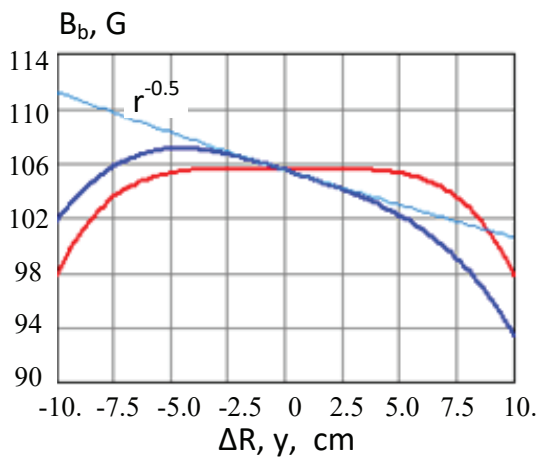

Figure 5: Profiles of bending fields $B_b(y)$ and $B_b(\Delta R)$.

ISBN: 978-3-95450-218-9 ISSN: 2226-0374 doi:10.18429/JACoW-COOL2019-TUPS15

The field index (~0.5) is provided by the shape of bending coils located on the side walls of magnetic shields. Note that correct profile of $B_b(\Delta R)$ is limited by interval -2.5cm <ΔR <2.5cm.

Electrons moving in the channel after passing through the bend are shown on Fig. 6. View of the trajectories from the end of the channel is presented.

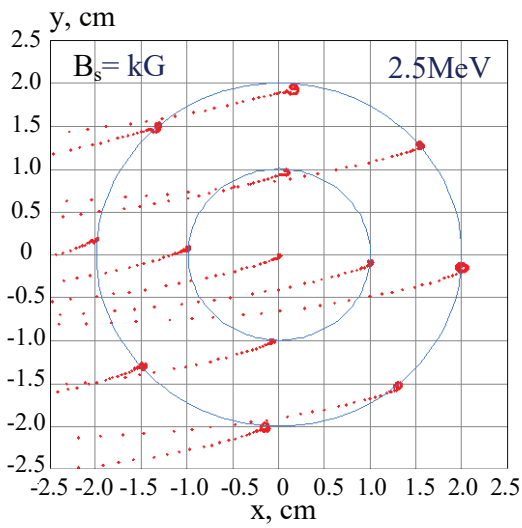

Figure 6: View on trajectories from the end of channel.

Coordinates of the axial electrons x=0 and y=0. A noticeable transverse Larmor radius arises at periphery of considered electrons ensemble.

Bends and toroids are units with similar properties. Considered algorithm for changing fields (coils currents) with a change in electron energy is also suitable for toroids. In addition, there is a sufficient number of tools to configure the field: additional PSU, various correctors etc.

MULTIFUNCTIONAL SEGMENT: CHANNEL – TOROID – SOLENOID

Layout of this segment is shown on Fig. 7. Inserts and ins&matches are multifunctional units that provide the possibility of mounting and repairing of the whole complex.

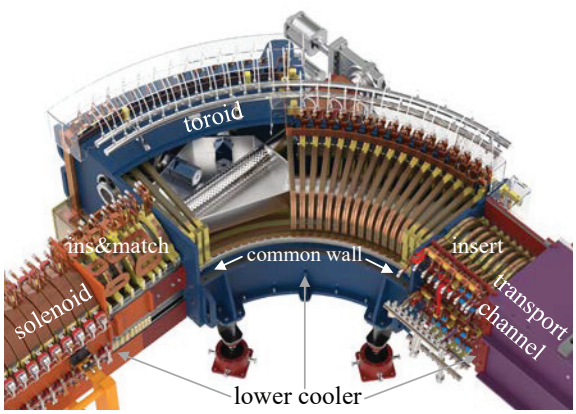

Figure 7: Layout of segment **C**–**T**–**S**.

The inner radius of the insert coils of these units is 2 cm larger than the radius of the coils of adjacent units. Field inhomogeneity occurs at the junction of coils of different inner radius. Inhomogeneity is minimized by order of insert coils location.

Dipoles of the transverse fields (see Fig. 8) are located in obtained radial gap of insert. Radius of uniform field region is ~ 3cm. These dipoles are tools to reduce "heating" of electrons.

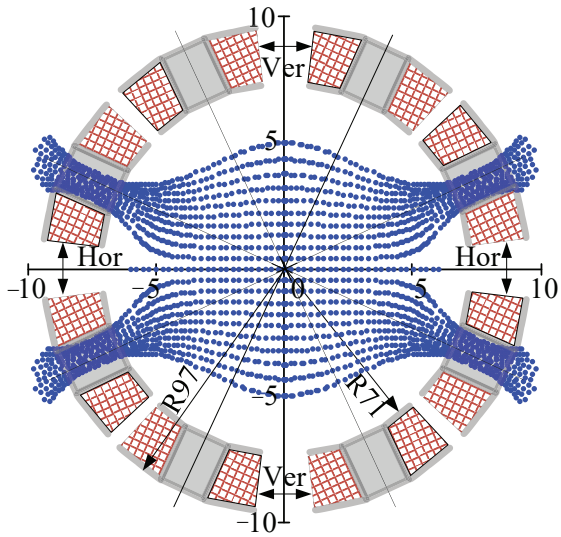

Figure 8: Dipoles of transverse fields. Force lines of horizontal field.

The pancake coils of the solenoids almost touch the common wall of the magnetic shields. Because of this, the magnetic fluxes of the solenoids axially symmetrical in the center of the solenoids to their edges lose symmetry, shifting to a common wall. In addition, about half of the flux of each solenoid is closed on magnetic shields of units ins&matchs (**12**, **14**) and again asymmetrically. Accordingly, vertical field $B_y(z)$ appears along the axis of each solenoid, changing the sign in its center. In principle, this field can be compensated by correctors of ins&match unit and by means of precise turns of solenoid coils around horizontal axis X and vertical axis Y [2]. But the strength of these compensation tools is limited, and additional steps are needed to reduce the value of this BY(z) field.

Field matching units of segment are shown on Fig. 9.

According to the calculations, the end plates at the joints of the solenoids with units **12** and **14** (ins&matcht) redistribute the fluxes so that the vertical field decreases to $B_{Y0}(z)$. Then above tools compensate the field to $B_{Y1}(z)$ (see Fig. 10). Plates 15mm thick have holes coaxial with coils. The calculation made with a shortened solenoid: only 34 pancake coils (whole solenoid has 84 coils).

ISBN: 978-3-95450-218-9 ISSN: 2226-0374 doi:10.18429/JACoW-COOL2019-TUPS15

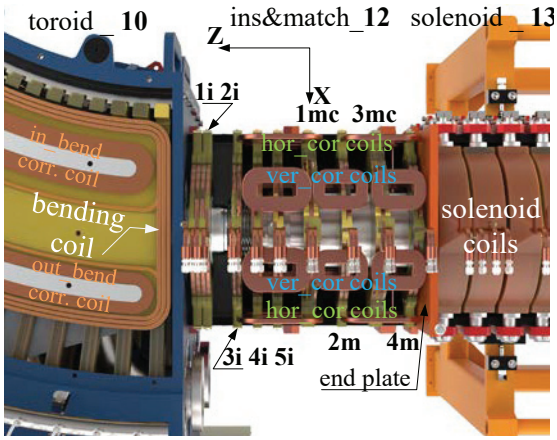

Figure 9: Magnetic elements of units **10**, **12** and **13**.

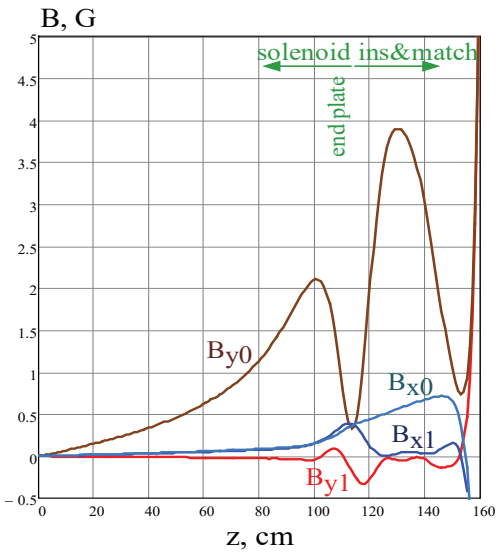

Figure 10: Transverse fields along solenoid axis before (B_{x0}, B_{y0}) and after (B_{x1}, B_{y1}) compensation.

In units **12** and **14** (ins&match), the field $B_z(z)$ should be not only axisymmetric but also have a certain profile along Z axis: $B_{z1}(z, T, B1, B2)$ [3]. The basic profile $B_{z2}(z)$ is given by the arrangement of round coils 1mc – 4m. Adjustment of profile $B_{z3}(z)$ for selected parameters T, B1, B2 is carried out using the correcting turns of the coils 1mc and 3mc. Profiles for the following parameters: T=2.5MeV, B1=1kG, B2=2kG, are shown in Fig. 11.

Calculation of electrons passage through segment **C–T–S** is considered. The electrons start in the channel (**8**) along magnetic field B1=1kG. They must enter the field B2=2kG of the solenoid **13** without "heating". Field B2 itself must be uniform with an accuracy of 10^{-5}. View of trajectories from the end of solenoid (**13**) is shown on Fig. 12.

Coordinates of the axial electrons x=0.14cm and y=0. After passing ins&match-1 (**12**), the electron radius $\sqrt{x^2+y^2}$ decreases by $\sqrt{2}$ times.

To obtain an acceptable result, we used:

- Six PS, four of them with individually adjustable currents: in solenoid (**13**), in 1mc - 4m coils of ins&match (**12**), in coils of longitudinal field of toroid (**10**) and in coils of bending field of toroid (**10**).
- Three correctors of vertical and two horizontal fields in ins&match (**12**).
- Precise turns of solenoid coils around a horizontal axis X
- Adjustment of $B_{z3}(z)$ profile using correcting turns of the 1mc and 3mc coils.
- Dipoles of the transverse fields in insert-2 (**9**).

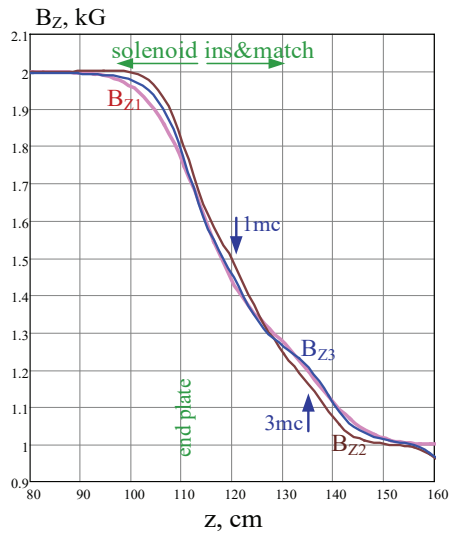

Figure 11: Profiles $B_{z1}(z)$ – theoretical, $B_{z2}(z)$ – basic, $B_{z3}(z)$ – adjusted by coils 1mc and 3mc.

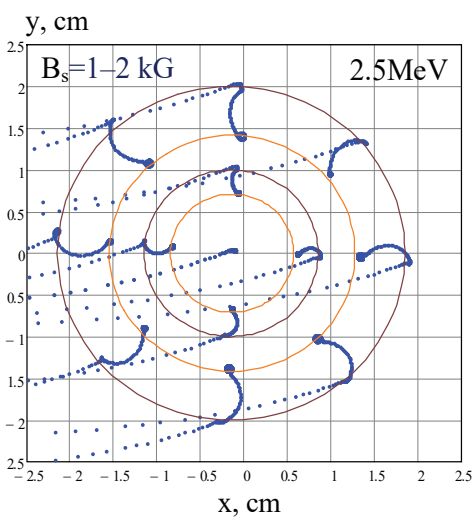

Figure 12: View on trajectories from the end of solenoid.

REFERENCES

[1] M. Bryzgunov, A. Bubley, *et al.* "Magnetic system of electron cooler for COSY", *inProceedings of COOL'11*, Alushta, Crime, September 2011, paper TUPS10.

[2] A. Bubley, V. Bocharov, S. Konstantinov, V.Panasyuk, V. Parkhomchuk, "Precision Measurements and Compensation for the Transversal Components of the Solenoids' Magnetic Field", *Instrum. Exper. Techn.* Vol. 48, № 6, 2005, pp.772-779.

[3] M.I. Bryzgunov, V.M. Panasyuk, V.B. Reva, "Calculation of electron beam motion in electron cooling system for COSY", *in Proceeding of COOL-09 Workshop*, Lanzhou, China, August 31-September 4, 2009.

ISBN: 978-3-95450-218-9 ISSN: 2226-0374 doi:10.18429/JACoW-COOL2019-TUPS17

PARAMETER OPTIMISATION OF RING SLOT COUPLER PICKUP AND KICKER FOR NICA STOCHASTIC COOLING SYSTEM

K. Osipov#, I. Gorelyshev[1], V. Filimonov, A. Sidorin[1], JINR, Dubna, Russia
[1]also at Saint Petersburg State University, Saint Petersburg, Russia

Abstract

Pickup and kicker structures for the NICA stochastic cooling system are supposed to be based on ring slot couplers proposed in [1]. However, it differs from the original design by the insertion of a ceramic vacuum chamber that shifts frequency of the structure down to 1-1.5 GHz. Possible design solution of the rings was proposed to shift frequency of the structure to the desired 2 – 4 GHz.

INTRODUCTION

Ring slot coupler structures proposed for HESR stochastic cooling system (SCS) [1] were successfully used for the beam cooling at Nuclotron and COSY [2, 3]. The demonstrated performance within 2-4 GHz frequency band satisfies to requirements of the NICA collider SCS. In the ring structure with octagonal arrangement of shorted electrodes (Fig. 1) the total image current passes the surrounding uninterrupted gap formed by two adjacent rings.

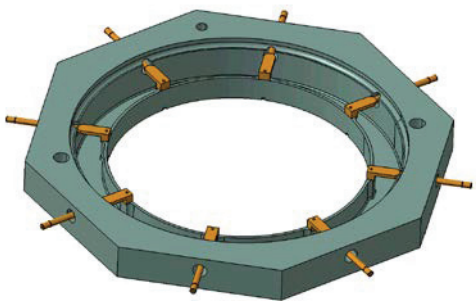

Figure 1: Schematics of single ring of the ring slot coupler structure.

However, the external sealing used in the systems mentioned above makes it problematic to achieve ultra-high vacuum of 10^{-11} Torr which is essential for NICA. Therefore, strict vacuum requirements force us to produce pickups and kickers with internal sealing. In this case, pickup and kicker is assembled over the cylindrical ceramic tube made of Al_2O_3 material (Fig. 2). The ceramic tube shifts frequency of the structure down to 1-1.5 GHz. The goal of this work is to demonstrate possibility to modify design of the pickup and kicker for effective work in the same 2 – 4 GHz band – so in this case we can use the other elements of the system without changes.

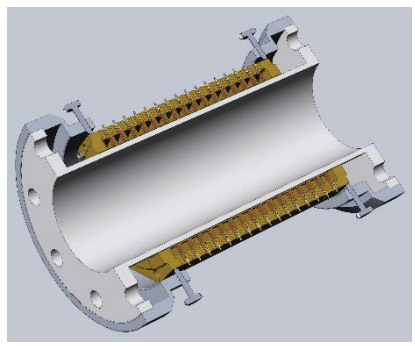

Figure 2: Schematics of pickup (kicker) with internal sealing using ceramic vacuum chamber.

MODELING

Parameters of the Model

The study and design optimisation was done in CST Microwave Studio. The goal was to qualitatively evaluate the field of optimal structure parameters. So maximal simplification of model and calculation settings were done – to make faster calculations even to the detriment of accuracy. Lumped elements and ports were used; the form of feeding loop was not taken into account, lose free materials so as maximal mesh step were used.

Model Benchmarking

To estimate the accuracy of modelling method the original structure was modelled (Fig. 3) and the results were compared with the same obtained earlier [4].

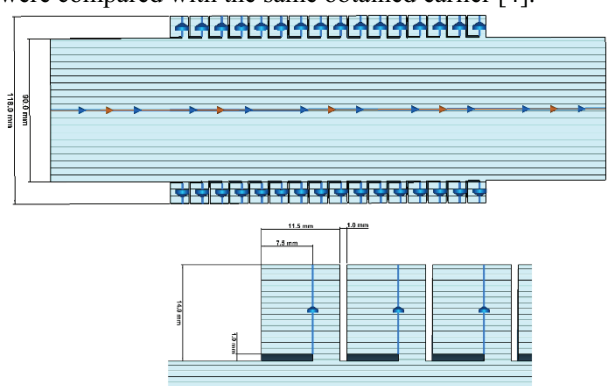

Figure 3: Dimensions of the model.

Electrical field of structure on different frequencies for infinite number of cells and for 17 cells was calculated. The results are given in Fig. 4.

Oskos82@mail.ru

ISBN: 978-3-95450-218-9 ISSN: 2226-0374 doi:10.18429/JACoW-COOL2019-TUPS17

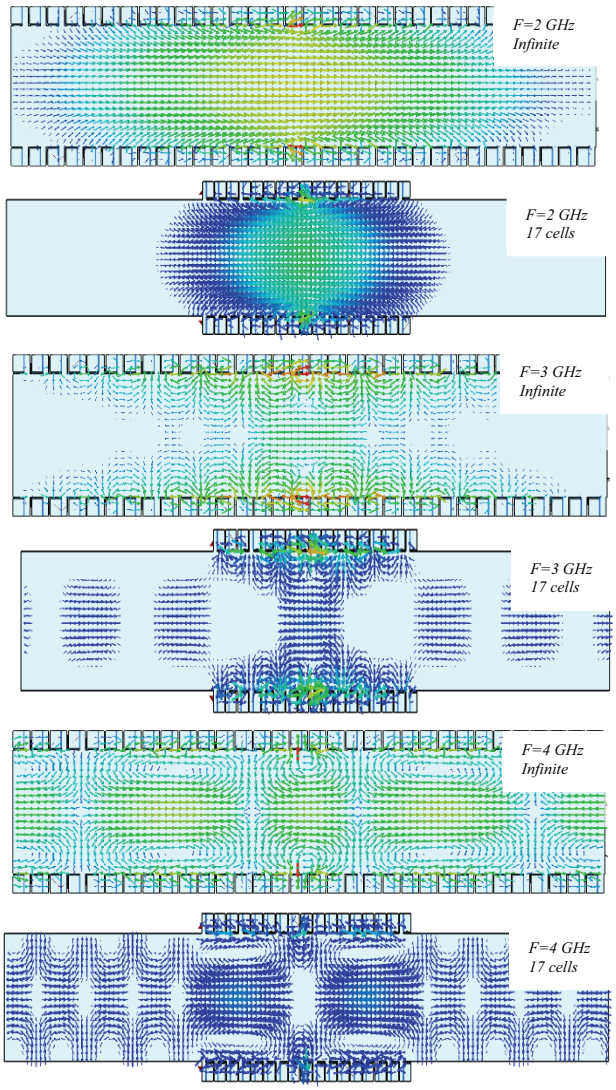

Figure 4: Electrical field on different frequencies for infinite and 17-cell structure.

Also longitudinal wake impedance of finite structure (17 cells) was calculated (Fig. 5).

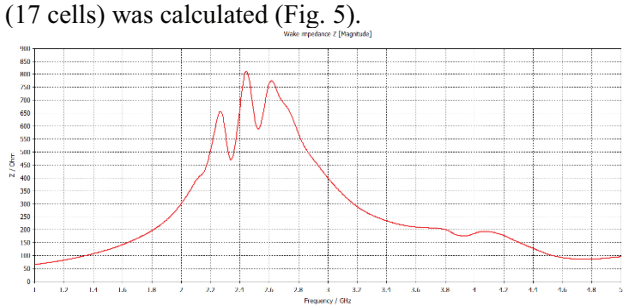

Figure 5: longitudinal wake impedance of 17-cell structure.

Comparison of the results with [5] shows that it is possible to use simplified model for qualitative estimation of structure characteristics and parameters.

Modelling Structure with Ceramic Tube

Minimum internal diameter of NICA vacuum pipe is 98mm – it differs from that on COSY and Nuclotron. Minimal thickness of ceramic tube used for sealing is about 5mm. Dielectric constant of ceramic (Al_2O_3) ε=10.

The list of model optimization parameters (Fig. 6):

Tube_b – width of tube wall (≥5mm).
gap_b – air gap between tube and rings.
Res_b – ring width.
Res_h – ring depth.
Res_gap – distance between rings

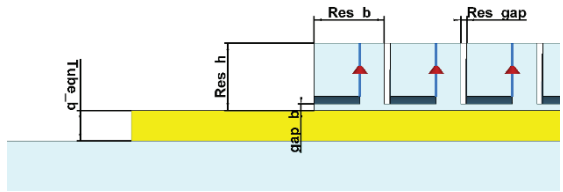

Figure 6: Optimisation parameters.

The results of modelling shows significant influence of a ceramic tube on the structure frequency response (Figs. 7 and 8). The goal of modelling was to optimize the frequency response of structure for working in 2-4 GHz band. Optimization results shows that it is impossible to obtain the required behaviour by parameter optimization of the structure without changes in the design.

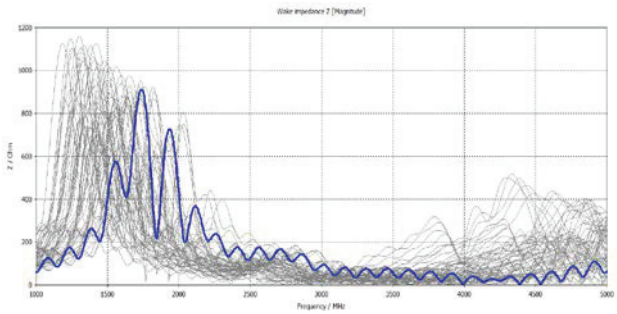

Figure 7: Longitudinal wake impedance of the structure for different parameters.

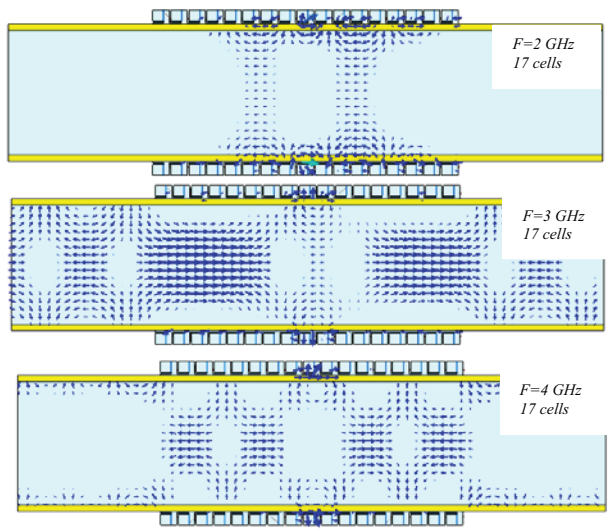

Figure 8: Electrical field on different frequencies.

Design Modification

To compensate frequency decreasing due to ceramic tube influence it is proposed to insert shorts symmetrically

ISBN: 978-3-95450-218-9 ISSN: 2226-0374 doi:10.18429/JACoW-COOL2019-TUPS17

between electrodes (Fig. 9). The shorts can be made during ring milling or added as separate inserting segments to the original structure. Variation of the short geometry can smoothly tune the resonant frequency of individual rings and the whole structure itself.

List of model optimization parameters:

Short_fi – angular dimension of the short
Short_b – width of short
Tube_D – ceramic tube diameter
Ring_Din – internal ring diameter
Ring_Dout – external ring diameter

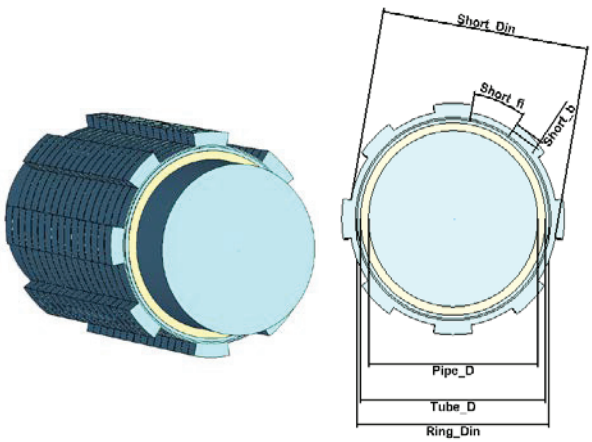

Figure 9: The ring slot coupler structure with additional shorts and optimized parameters.

Optimization was done for maximization of longitudinal wake-impedance in frequency band (2-4 GHz) of the structure consisting of 16 rings (Fig. 10). Length of structure was not changed during optimisation (200 mm) and some dimensions like ring slot width (4 mm) too.

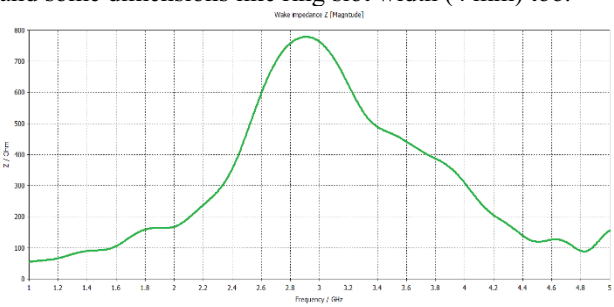

Figure 10: longitudinal wake-impedance of optimised structure.

As a result of optimization the reasonable response of longitudinal wake-impedance was obtained. Therefore, we can make conclusion that it is possible to compensate influence of high dielectric constant ceramic tube insertion by rather simple redesign of ring-slot coupler and make it work in the desired band of 2 – 4 GHz.

CONCLUSIONS

- Ring-slot coupler pickup and kicker can be used in NICA cooling system with internal Al_2O_3 ceramic tube sealing.
- Simple modification of the ring design can compensate ceramic tube influence on frequency of coupler.
- The modification is including shorts in the rings.
- Shorts parameters can smoothly control the design frequency response to get best performance of pickup/kicker.

REFERENCES

[1] R. Stassen *et al.,* "Recent development for the HESR stochastic cooling system", *in Proc. Of COOL'11*, Bad Kreuznach, Germany, Sept. 2011, p. 191.

[2] N. Shurkhno *et al.,* "Study for stochastic cooling at nuclotron", *in Proceedings of COOL2013*, Murren, Switzerland, Sept. 2013, p. 73.

[3] R. Stassen, B. Breitkreutz, and N. Shurkhno, "Recent Results of HESR Original Stochastic Cooling Tanks at COSY", in *Proc. 9th Int. Particle Accelerator Conf. (IPAC'18)*, Vancouver, Canada, Apr.-May 2018, pp. 913-915. doi:10.18429/JACoW-IPAC2018-TUPAF078

[4] B.Breitkreutz, *et al.,* "Design of pick-up and kicker for HESR", GSI/FAIR Workshop on Stochastic Cooling 2019, https://indico.gsi.de/event/8237/session/2/-contribution/10

[5] G.Zhu, *et al.,* "HIAF SRing stochastic cooling", GSI/FAIR Workshop on Stochastic Cooling 2019, https://indico.gsi.de/event/8237/session/4/contribution/14

ISBN: 978-3-95450-218-9 ISSN: 2226-0374 doi:10.18429/JACoW-COOL2019-TUPS18

PHASE STEP METHOD FOR FRICTION FORCE MEASUREMENT IN FILTER STOCHASTIC COOLING

I. Gorelyshev[1*], V. Filimonov, A. Shemchuk, A. Sidorin[1], JINR, Dubna, Russia
[1]also at Saint Petersburg State University, Saint Petersburg, Russia
N. Shurkhno, R. Stassen, Forschungszentrum Jülich, Jülich, Germany

Abstract

Voltage step method for friction force measurement in electron cooling is well known. The similar method for friction force measurement in longitudinal stochastic cooling with comb filter is provided. First test of the method during the run at COSY has been implemented.

INTRODUCTION

Stochastic cooling systems (SCS) for High Energy Storage Ring (HESR) and Nuclotron-based Ion Collider fAcility (NICA) are under development in GSI Helmholtz Centre for Heavy Ion Research [1] and in Joint Institute for Nuclear Research [2] respectively. The preparatory experimental work on stochastic cooling for HESR and NICA is carried out at COoler SYnchrotron (COSY) at Forschungszentrum Jülich [1]. During this work hardware solutions and automation techniques for system adjustment had been worked out and tested. The automation technique is based on the cooling process simulation which is described by Fokker-Planck equation (FPE) [3]. One of the notions defining the evolution of the cooling process is drift term of the FPE which is also known as friction force. The measurement of friction force may be fruitful for fine tuning of cooling systems. The approach for friction force measurement in filter stochastic cooling is discussed below.

DESCRIPTION OF THE METHOD

Procedure

Originally the method of longitudinal friction force measurement was widely used in electron cooling [4 – 7]. Cold electrons interchange their temperature with hot ions during the electron cooling process. Cathode voltage of the electron cooler defines energy of electrons. If the mean energy of electrons is slightly different than the one of ions the ion energy distribution evolves to the new equilibrium.

The experimental procedure is the following: at first the mean electron energy is equal to the ion one, then after a rapid voltage step on the cooler cathode the friction force shifts along the energy as shown in Fig. 1 and ion energy distribution starts to evolve as shown in Fig. 3. By the evolution of maximum and/or mean values of ion energy distribution one can evaluate the actual friction force. The evaluation is described in details in the next section.

Similar procedure where the shift of the friction force is provided for momentum stochastic cooling can be done with a comb filter. Such technique is simpler for filter stochastic cooling due to comb filter has more parameters to adjust (see Fig. 2) in comparison with other methods for momentum stochastic cooling. Simulation based on FPE approach [2] shows that proper shift of the friction force along the energy is performed by adding extra delay Δt_{filter} in the long leg of the comb filter and proportional system delay

$$\Delta t_{sys} = \frac{T_{P\to K}}{T_0}\Delta t_{Filter},$$

where $T_{P\to K}$ is time of flight between pickup and kicker for the reference particle and T_0 is the revolution period. So the only difference in procedures for friction force measurement between electron and filter stochastic cooling is that instead of changing one parameter of cathode voltage for electron cooling there are two proportional parameters Δt_{filter} and Δt_{sys} which should be stepped simultaneously.

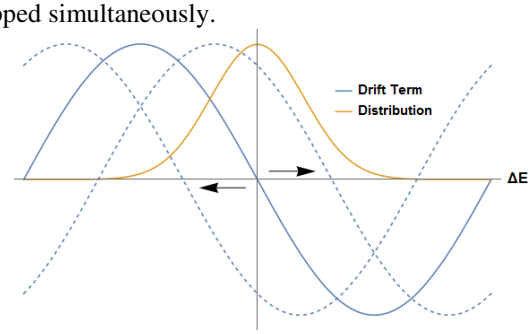

Figure 1: FPE drift term a.k.a. friction force (blue): initial (solid) and shifted to the left or to the right (dashed) in comparison with distribution function (orange).

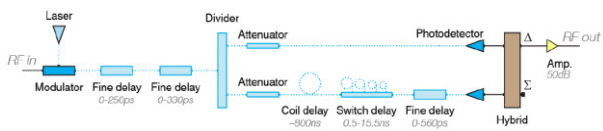

Figure 2: Scheme of optical comb filter

The friction force of the momentum stochastic cooling is alternating and during the adjustment several possible delay combinations lead to cooling. The optimal combination of delay parameters is when system delay is equal to the reference particle's transit time between pickup and kicker and filter delay is equal to the revolution period. If SCS has optimal adjustment the friction force is close to an odd function. In our case we intentionally chosen not optimal adjustment of the system by adding extra system delay in order to have asymmetric friction force. The transfer function of the SCS which is proportional to the friction force is shown in Fig. 4.

* gorelyshev@jinr.ru

ISBN: 978-3-95450-218-9 ISSN: 2226-0374 doi:10.18429/JACoW-COOL2019-TUPS18

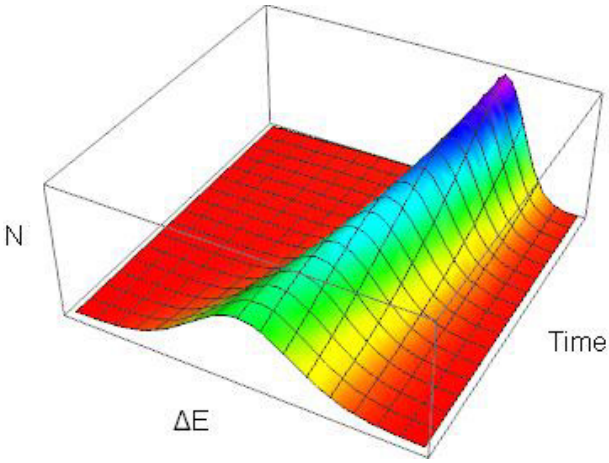

Figure 3: Evolution of ion beam energy distribution due to shift of the friction force.

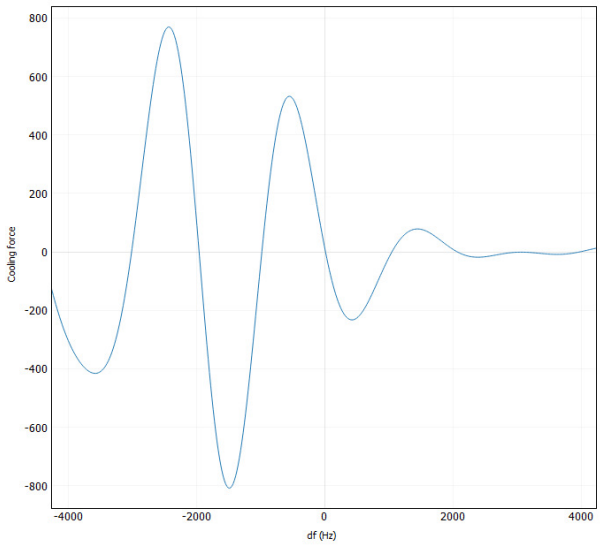

Figure 4: Transfer function of the COSY SCS during the experiment.

Measurements

The first implementation of the method described above has been done at COSY. The parameters of COSY and its stochastic cooling system are given in Table 1.

Table 1: Parameters of Stochastic Cooling at COSY

Parameter	**Value**
Circumference	184 m
Ions	p^+
Energy	2.285 GeV/u
Revolution frequency	1 559 493 Hz
Slip-factor, η	-0.1
Intensity	$3 \cdot 10^9$ ions
$\Delta p / p_0$	$3 \cdot 10^{-4}$
Bandwidth	2-4 GHz
Output Power	0 W

Measurements were carried out at the 1400th harmonic of the revolution frequency. Spectrum analyzer saved one spectrum per second. Two measurements are given as an example in the paper. During the first measurement the proton beam was initially accelerated by the filter stochastic cooling phase step, and when the beam reached the new equilibrium energy it decelerated back to the initial state. The spectrogram of the first measurement is shown in Fig. 5 (top) During the second measurement the beam was initially decelerated and then accelerated back. The spectrogram of the second measurement is shown in Fig. 5 (bottom). The difference between measurements is that system gain in the second one is 3 dB higher.

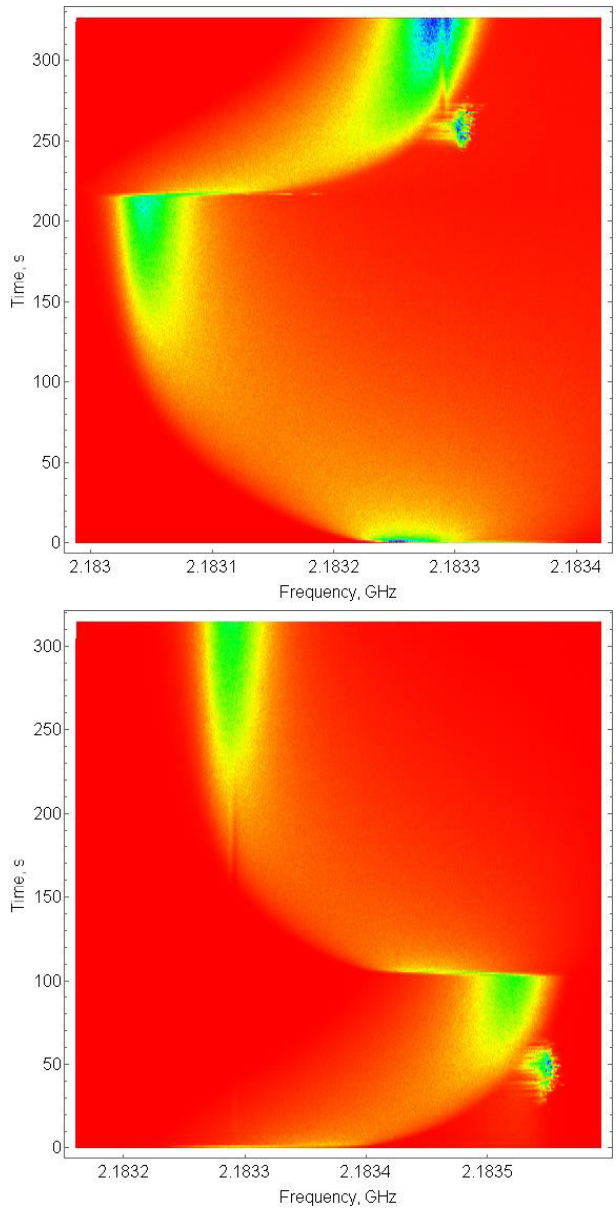

Figure 5: Waterflow spectrogram of the first (top) and second (bottom) measurements.

Processing

Before we started the friction force evaluation we filtered out the outlying noise signal which is clearly seen (in Fig.5 both top and bottom) as a blob right to the signal distribution during the accelerating phase. The noise was filtered by the combination of low pass and minimum

ISBN: 978-3-95450-218-9 ISSN: 2226-0374 doi:10.18429/JACoW-COOL2019-TUPS18

filters. The frequencies of filters were searched by the rule of thumb in a trade-off between noise reduction and signal loss. Also before the evaluation the spectrograms of schottky noise power vs frequency was converted into the energy distribution functions.

The FPE for the preprocessed energy distribution function Ψ, friction force F and diffusion D is written in the form [3]

$$\frac{\partial\Psi(E,t)}{\partial t}+\frac{\partial}{\partial E}\left(F(E)\Psi(E,t)\right)-\frac{\partial}{\partial E}\left\{D(E)\frac{\partial\Psi(E,t)}{\partial E}\right\}=0$$

Following only the distribution maximum value E_M for which distribution function satisfies the condition

$$\Psi(E_M,t)\Leftrightarrow\left.\frac{\partial\Psi(E,t)}{\partial E}\right|_{E_M}=0$$

we obtain the reduced equation without a diffusion term

$$\frac{\partial\Psi(E_M,t)}{\partial t}+\frac{\partial F(E_M)}{\partial E}\Psi(E_M,t)=0$$

and finally we can trace the exact value of the friction force up to the equilibrium point Eq

$$F(Eq-E)=-\int_E^{Eq}\frac{1}{\Psi(E_M,t)}\frac{\partial\Psi(E_M,t)}{\partial t}dE_M$$

Another characteristic value of the distribution is its mean as known as first raw moment M. Its evolution is written as

$$\frac{dM}{dt}=\int E\left[-\frac{\partial}{\partial E}\left(F(E)\Psi(E,t)\right)+\frac{\partial}{\partial E}\left\{D(E)\frac{\partial\Psi(E,t)}{\partial E}\right\}\right]dE$$

The first term is transformed as follows

$$\int -E\frac{\partial}{\partial E}\left(F(E)\Psi(E,t)\right)dE=\int F(E)\Psi(E,t)dE=\langle F\rangle_\Psi$$

and if we assume that the diffusion is approximately an even function we obtain the second term of the mean evolution is almost zero. So the evolution of distribution mean corresponds to the friction force averaged over the energy distribution function which tends to actual value of the friction force as the distribution function approaches to Dirac δ-function

$$\frac{dM}{dt}\approx\langle F\rangle_\Psi\xrightarrow{\Psi\to\delta}F(M)$$

It means that the evolution of mean value for relatively narrow distributions is also applicable for approximate estimation of the friction force.

The evolution of mean and maximum energy distribution function values for first and second measurements is given in Fig. 6.

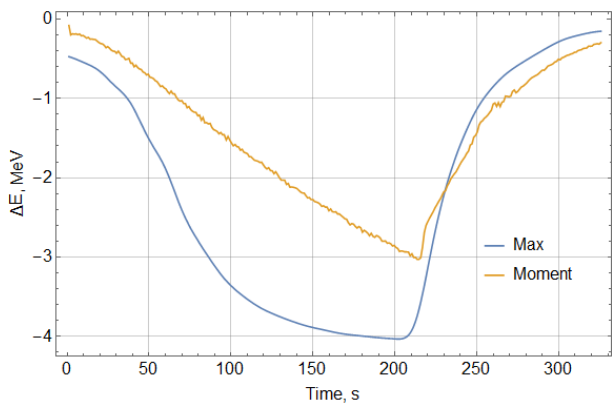

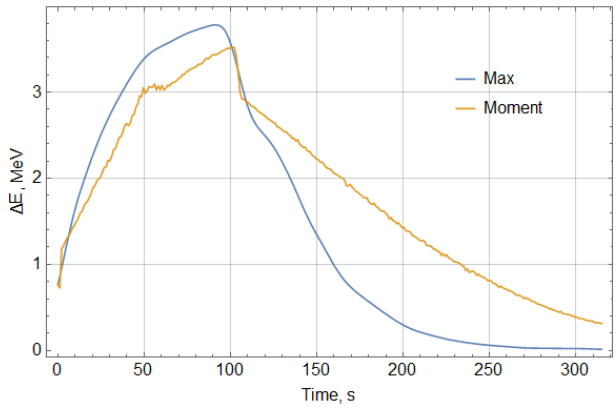

Figure 6: Evolution of maximum (Max) and mean (Moment) energy distribution function values for first and second measurements.

RESULTS

The estimated friction force for both measurements in comparison with theoretical one proportional to the system transfer function is given in Fig. 7. The asymmetry of the theoretical friction force is repeated for both experimental estimations. The 3dB gain difference between two measurements is seen as well. As we suppose the estimation of friction force based on the evolution of the distribution maximum is more precise than the mean evolution. But for approximations the mean evolution can be also used.

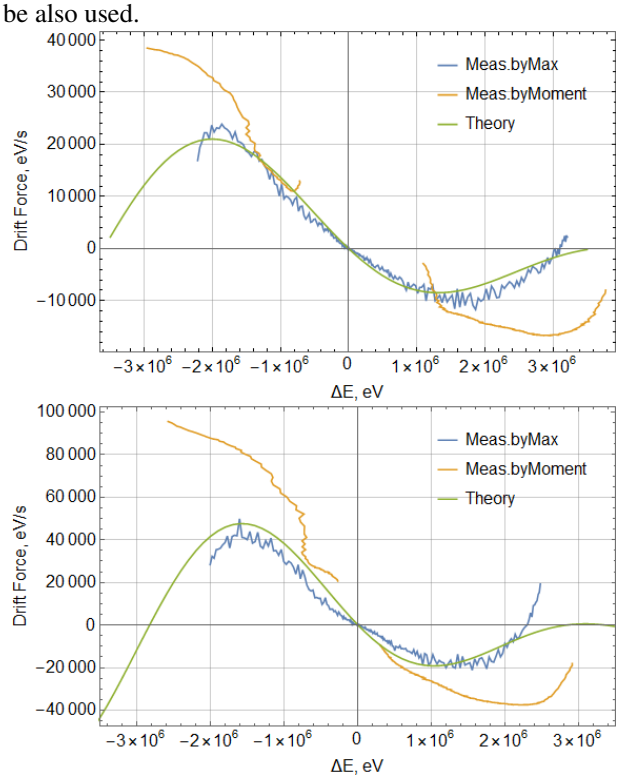

Figure 7: Comparison of theory and measurements for first (top) and second (bottom) measurements.

ISBN: 978-3-95450-218-9 ISSN: 2226-0374 doi:10.18429/JACoW-COOL2019-TUPS18

CONCLUSION

The presented approach allows one to evaluate the friction force of filter stochastic cooling based on the experimental measurements. First tests of the method were performed at COSY and demonstrated an agreement with the theory.

ACKNOWLEDGMENTS

Authors are sincerely grateful to the COSY team for smooth and steady operation of the machine during the experiment.

REFERENCES

[1] R. Stassen, B. Breitkreutz, and N. Shurkhno, "Recent Results of HESR Original Stochastic Cooling Tanks at COSY", IPAC'18, Vancouver, BC, Canada, Apr. 4,, pp. 913-915, doi:10.18429/JACoW-IPAC2018-TUPAF078

[2] E. Syresin *et al.*, "NICA Accelerator Complex at JINR", IPAC'19, Melbourne, Australia, May 2019, pp. 452-454. doi:10.18429/JACoW-IPAC2019-MOPMP014

[3] T. Katayama, N. Tokuda, "Fokker-Planck Approach for the Stochastic Momentum Cooling with a notch filter", Part. Accel. 1987. V. 21. P. 99.

[4] G.I. Budker et al., Preprint IYaF 76-32 (1976), URL: http://cdsweb.cern.ch/record/118046/files/CM-P00100706.pdf

[5] M. Steck et al., "Electron Cooling of Heavy Ions at GSI", PAC93, Washington D.C., USA. 1993, pp. 1738-1740

[6] L. Prost et al., "Electron Cooling of 8 GeV Antiprotons at Fermilab's Recycler: Results and Operational Implications", ICFA-HB'06, Tsukuba, Japan, WEAY02 p. 182 (2006)

[7] L. Mao et al., "Longitudinal Cooling Force Measurements in HIRFL-CSRm", IMP & HIRFL Annual Report, 2008

ISBN: 978-3-95450-218-9 ISSN: 2226-0374 doi:10.18429/JACoW-COOL2019-TUPS19

STOCHASTIC COOLING SIMULATION OF RARE ISOTOPE BEAMS ON THE SPECTROMETER RING OF THE HIGH ENERGY AND HIGH INTENSITY ACCELERATOR FACILITY*

X. J. Hu†, J.X.Wu, G.Y.Zhu,Y.J.Yuan
Institute of Modern Physics, Chinese Academy of Sciences, Lanzhou, China

Abstract

Among various cooling methods, stochastic cooling is an effective way of cooling low intensity beams with larger size[1]. For the HIAF (High energy and high Intensity Accelerator Facility) project, stochastic cooling will be built on the SRing (Spectrometer Ring). This paper mainly concerns on cooling effects based on different stochastic cooling methods, aiming at finding the optimal cooling method and cooling parameters for different physical experiment purposes. Besides, TOF cooling combined with filter cooling was also studied. Simulation analysis will provide theoretical reference and support for the engineering construction.

INTRODUCTION TO HIAF STOCHASTIC COOLING SYSTEM

The High Intensity heavy ion Accelerator Facility (HIAF) is high intensity facility in nuclear physics and related research fields, and stochastic cooling system will be built on the Spectrometer Ring (SRing) of the HIAF project. For the SRing stochastic cooling, 2 pickup tanks and 2 kicker tanks will be performed for both transverse and longitudinal cooling. The cooling electrodes will be installed in the straight section without dispersion, and it is advantageous to prevent the coupling between phase subspaces. For transverse cooling, the designed betatron phase advances between pickup and kicker are almost 90 deg.

The momentum spread of the radioactive beam injected into SRing is almost ±1.5e-2. Stochastic cooling is not suitable for cooling this kind of hot beam, because the cooling frequency would be designed relatively smaller, which will greatly reduce the performance. Fortunately, it is planned to decrease the momentum spread to ±4.0e-3 firstly by using bunch rotation, and then stochastic cooling combined with electron cooling will further decrease the momentum spread to the desired value.

For the SRing stochastic cooling system, the beam energy is 740 MeV/u, bandwidths are different based on the different initial momentum spreads. With bunch rotation, the initial momentum spread for stochastic cooling is ±4.0e-3, but without bunch rotation, the initial momentum spread is ±1.5e-2. Therefore, bandwidth is designed differently in order to involve initial momentum spread with the cooling acceptance.

For longitudinal cooling on SRing, TOF cooling [2,3] will be used for cooling of hot beam firstly, and filter cooling [4] will be used for continuous cooling to further reduce the momentum spread subsequently.

LONGITUDINAL STOCHASTIC COOLING SIMULATION ON SRING

Cooling with Bunch Rotation

Table 1: Longitudinal Stochastic Cooling Parameters

Physical parameters	values
Ion	$^{132}Sn^{50+}$
Kinetic energy	740 MeV/u
Total number of RI	1.0e5
Initial Δp/p	±4.0e-3/±1.5e-2 (TOF Cooling) ±7.0e-4/±2.0e-3 (Filter Cooling)
γt	3.37
Local γt	2.752
Bandwidth	0.6-1.2 GHz/0.2-0.6 GHz
Number of slot rings for Pickup/Kicker	64/64
Temperature	300 K
Lpk	92.01 m

The SRing stochastic cooling parameters are listed in Table 1. Slot ring coupler is adopted for the pickup and kicker structure, for the shunt impedance per meter of the slot ring structure is higher compared to other structures such as Faltin structure. The shunt impedance response per cell is shown in Fig. 1.

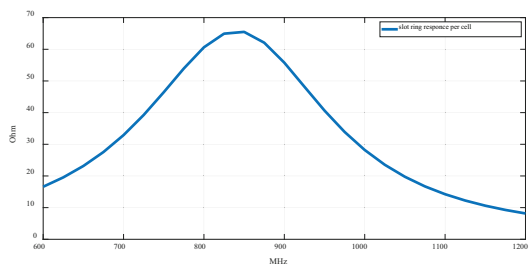

Figure 1: Shunt impedance response of slot ring structure per cell.

* Work supported by National natural science foundation of China (Y862010GJ0)
† E-mail: huxuejing@impcas.ac.cn.

ISBN: 978-3-95450-218-9 ISSN: 2226-0374 doi:10.18429/JACoW-COOL2019-TUPS19

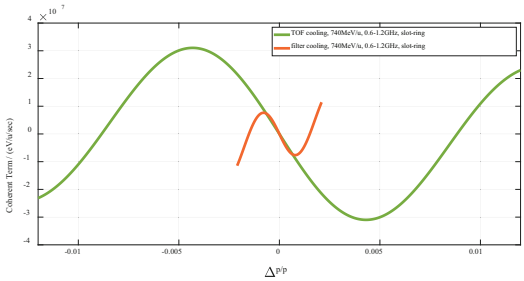

Figure 2: Coherent terms of TOF cooling and filter cooling.

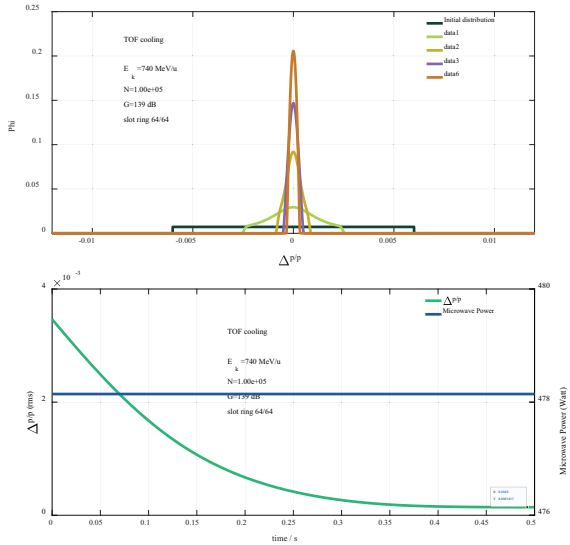

Figure 3: Results of TOF cooling simulation (Ek=740 MeV/u, 0.6GHz≤f≤1.2GHz). (up)Beam distribution during cooling. (down) Evolution of momentum spread (rms) and microwave power.

In Fig. 2 it is obviously that TOF cooling acceptance is much larger than filter cooling acceptance, therefore, TOF cooling is used for longitudinal stochastic cooling simulation at first. When the particle number is 1e5, cooling bandwidth is from 0.6 to 1.2 GHz, number of slot ring coupler is 64 both for pickup and kicker and the amplifier gain is 139 dB, the total cooling time is about 0.5 second which is shown in Fig. 3. From the simulation results, it is clearly that TOF cooling has the ability of cooling the beam to the equilibrium momentum spread of 1e-4 when the amplifier gain is 139 dB.

If the equilibrium momentum spread is expected to be smaller, then the amplifier gain should be decreased which can lead to slower cooling subsequently. As is shown in Fig. 4, cooling with amplifier gain of 125 dB is much slower than that of 139 dB, but the equilibrium momentum spread is smaller than the other.

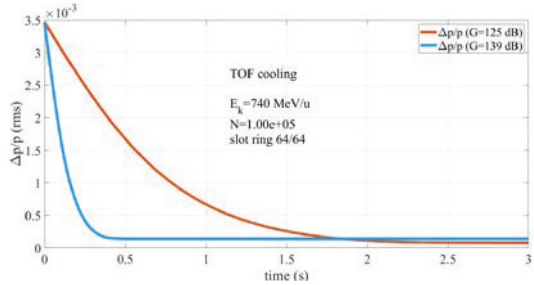

Figure 4: cooling comparisons between different amplifier gains.

When the momentum spread is decreased which can fit inside the filter cooling acceptance, it is better to use filter cooling method for subsequent cooling process. Similar to TOF cooling, filter cooling has the ability of cooling beam to the equilibrium momentum spread of 1e-6, which is smaller than the TOF cooling equilibrium value. Result is shown is Fig. 5.

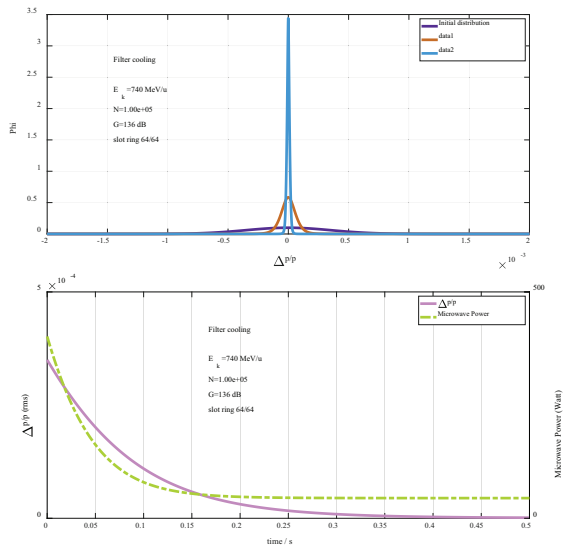

Figure 5: Results of filter cooling simulation (Ek=740 MeV/u, 0.6GHz≤f≤1.2GHz). (up) Beam distribution during cooling. (down) Evolution of momentum spread (rms) and microwave power.

In order to obtain less cooling time and smaller equilibrium momentum spread, it is better to use TOF cooling combined with filter cooling. For TOF cooling combined with filter cooling, it should be very careful to decide the switch time from TOF to filter cooling. When the kinetic energy is 740 MeV/u, particle number is 1e5 and number of slot ring cell are 64 for both pickup and kicker, the switch time from TOF to filter should be longer than 0.3 s from simulation.

ISBN: 978-3-95450-218-9 ISSN: 2226-0374 doi:10.18429/JACoW-COOL2019-TUPS19

The results are clearly as shown in Fig. 6. When the switch time is at 0.2 sec, heating is obvious. When the switch time is 0.25 sec, although it is not obvious, heating also occurs slightly as seen in the middle part of the Fig.6. Therefore, the suitable switch time from TOF to filter cooling should be larger than 0.3 sec. Besides, switch from TOF to filter at 0.35 sec is also studied, but the cooling effect is not good enough. Therefore, the optimum switch time t_{opt} from TOF to filter should be 0.25 sec<t_{opt}<0.3 sec. after TOF cooling is switched to filter cooling, the higher the gain, the faster the cooling will be, as is obvious in the down part the Fig. 6.

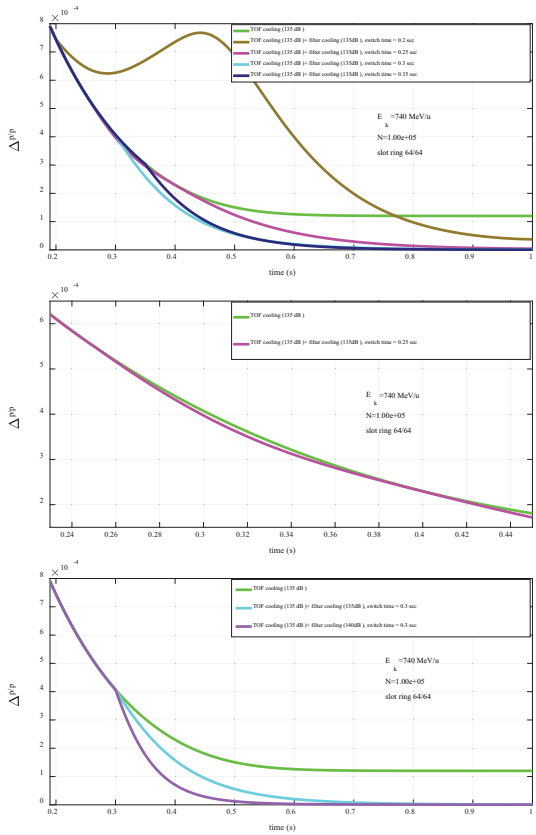

Figure 6: Simulation of different switch times from TOF cooling to filter cooling.

However, it should be noticed that the switch time 0.3 s is not fixed. The optimum switch time from TOF cooling to filter cooling is at the time when the momentum spread is decreased to fit just inside the filter cooling acceptance, and the cooling acceptance of filter method relies on many factors, such as the beam kinetic energy, bandwidth, the distance between pickup and kicker and the circumference of the storage ring, as shown in Eq. (1)-Eq. (6) [5].

$$2m\left|2x\eta_{pk}+\eta\right|\left|\frac{\delta p}{p}\right|<1. \quad (1)$$

Here x is the ratio of paths between pickup and kicker and the closed orbit circumference C.

$$m=\frac{f_{min}+f_{max}}{2f_{rev}} \quad (2)$$

$$x=\frac{s_k-s_p}{C} \quad (3)$$

The frequency slip factor is

$$\eta_{pk}=\gamma^{-2}-\alpha_{pk} \quad (4)$$

With the relativistic Lorentz factor γ and the local momentum compaction factor

$$\alpha_{pk}=\frac{1}{s_k-s_p}\int_{s_p}^{s_k}\frac{D(s)}{\rho(s)}ds \quad (5)$$

$D(s)$ is the dispersion function, and $\rho(s)$ is the local orbit curvature. s_p and s_k are the azimuthal coordinates of pickup and kicker.

Here η stands for the usual frequency slip factor for one revolution around the ring, calculated using Eq. (5) with the usual momentum compaction factor

$$\alpha_P=\frac{1}{C}\int_0^C\frac{D(s)}{\rho(s)}ds \quad (6)$$

Cooling without bunch rotation

Without bunch rotation, the initial beam spread should be ±1.5% instead of ±0.04%, therefore cooling bandwidth should be reduced to 0.2-0.6 GHz in order to accept the initial beam spread. Compared to 0.6-1.2 GHz, cooling acceptance is much larger for the frequency from 0.2-0.6 GHz, as is shown in Fig. 7. Cooling results are shown is Fig. 8. Cooling comparisons between with and without bunch rotation is shown in Fig. 9. It is clearly that it is better to use bunch rotation before the stochastic cooling process, for the cooling time is much shortened when bunch rotation is used. Filter cooling result is shown in Fig. 10 and the shunt impedance response for the frequency from 0.2-0.6 GHz is shown in Fig. 11.

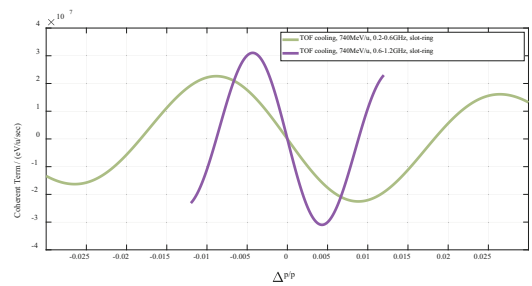

Figure 7: comparisons of cooling acceptances.

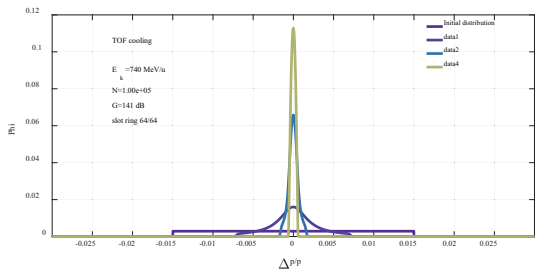

ISBN: 978-3-95450-218-9 ISSN: 2226-0374 doi:10.18429/JACoW-COOL2019-TUPS19

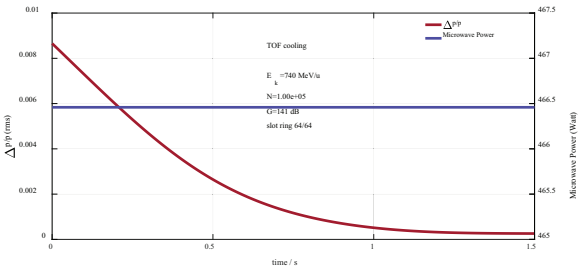

Figure 8: Results of TOF cooling simulation (Ek=740 MeV/u, 0.2GHz≤f≤0.6GHz). (up)Beam distribution during cooling. (down) Evolution of momentum spread (rms) and microwave power.

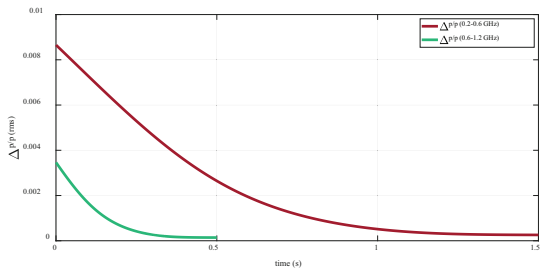

Figure 9: cooling comparisons between different bandwidths.

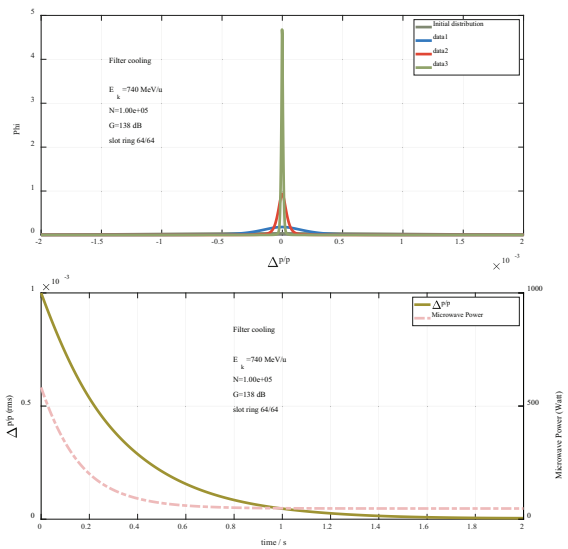

Figure 10: Results of filter cooling simulation (Ek=740 MeV/u, 0.2GHz≤f≤0.6GHz). (up)Beam distribution during cooling. (down) Evolution of momentum spread (rms) and microwave power.

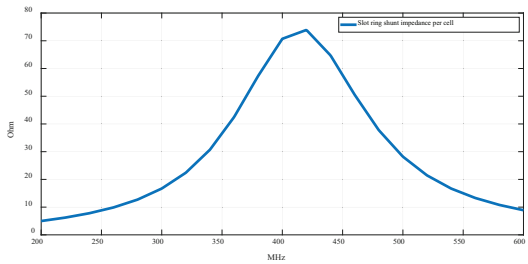

Figure 11: slot ring shunt impedance per cell for the cooling frequency from 0.2 GHz to 0.6 GHz.

CONCLUSION

Stochastic cooling simulation is investigated in this paper, and both TOF and filter cooling method are studied at the same time. From simulation results analysis, it is better to switch from TOF cooling to filter cooling at an appropriate time during the whole cooling process. This is because after switches, cooling is obviously faster than before.

Without bunch rotation, the initial beam spread should be $\pm 1.5\%$ instead of $\pm 0.04\%$, therefore cooling bandwidth should be reduced to 0.2- 0.6 GHz, in order to accept the initial beam spread. With the new system bandwidth, cooling is slower than previous system which has bandwidth of 0.6-1.2 GHz. Slot ring structure is adopted for the pickup and kicker structure, for the shunt impedance is higher compared to other structures such as Faltin structure.

REFERENCES

[1] Dieter Möhl, Andrew M. Sessler, "Beam Cooling: Principles and Achievements", *Nucl. Instr. and Meth. in Physics Research Section A: Accelerators, Spectrometers, Detectors and Associated Equipment,* Volume 532, Issues 1–2, 11 October 2004, pp. 1-10.

[2] H. Stockhorst, R. Stassen, R. Maier, *et al,*. "Experimental Test of Momentum Cooling Model Predictions at COSY and Conclusions for WASA and HESR", *AIP Conference Proceedings*, 2007, 950:239-255.

[3] T. Katayama, C. Dimopoulou, A. Dolinskii, *et al.,* "Simulation Study of Stochastic Cooling of Heavy Ion Beam at the Collector Ring of FAIR", in *Proc. Int. Workshop on Beam Cooling and Related Topics (COOL'13)*, Mürren, Switzerland, Jun. 2013, paper TUAM1HA04, pp. 52-54.

[4] John Marriner, "Stochastic Cooling Overview" https://arxiv.org/ftp/physics/papers/0308/0308044.pdf

[5] F. Nolden, I. Nesmiyan, C. Peschke, "On stochastic cooling of multi-component fragment beams", in *Nuclear Instruments and Methods in Physics Research* A 564 (2006) 87-93.

ISBN: 978-3-95450-218-9 ISSN: 2226-0374 doi:10.18429/JACoW-COOL2019-TUPS21

ADJUSTING UNIT OF LONGITUDINAL FIELD COILS FOR NICA HV ELECTRON COOLER'S SOLENOID

N.S.Kremnev[1], M.I. Bryzgunov, A.V. Bubley, V.V. Parkhomchuk[1], V.M. Panasyuk, V.B. Reva[1], A.A. Putmakov, S.V. Shiyankov, Budker Institute of Nuclear Physics of SB RAS, Novosibirsk, 630090 Russia
[1] also at Novosibirsk State University, Novosibirsk, 630090, Russia

Abstract

Adjusting unit of longitudinal field coils is necessary element used to obtaining a rectilinear longitudinal field in cooling solenoids of electron cooling machines. Due to limited distance between cooling channels of HV electron cooler (320 mm) previously used adjusting unit for longitudinal coil couldn't been applied. Possible orientation of adjusting unit is 90 degrees rotated and gravity force could not load longitudinal field coil mounting to make adjusting unit working. New design of preloaded coil mounting unit, made by BINP, solves this problem and provides necessary adjusting range and adjusting precision of longitudinal field coils for NICA HV electron cooler's solenoid.

DESCRIPTION

Electron cooling systems with magnetized electrons have high requirements for magnetic field quality, i.e. $\Delta B_{\perp}/B=\theta<10^{-5}$ [1]. Other words, for good cooling it is necessary to have strait magnetic field lines in longitudinal axis area of cooling solenoid.

The design of cooling solenoid of the NICA collider is based on a set of discreet coils used to obtain longitudinal magnetic field. Procedures for measuring and adjusting of such solenoids are described in the article [2]. Briefly, the field can be tuned by tilting and rotation of separate coils in solenoid. Usually used in BINP adjusting unit shown on schematic diagram (Fig. 1) consists of longitudinal field coil (1), coil mounting with ball bearing (2) and adjusting screws (3). Unfortunately, this mechanics works only when gravity force loads coil mounting by the coil weight and could not been used in other positions.

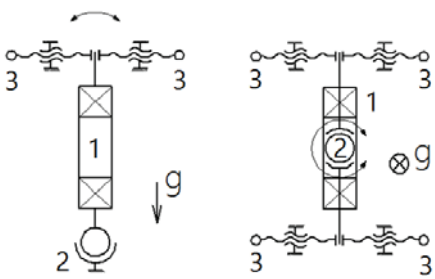

Figure 1: Schematic diagram of coil tilting (left) and rotation (right).

Cooling solenoid of NICA collider is a duplex of lower and upper cooling cannels with distance at 320 mm between cannels axes shown on Fig. 2 and consists of six separated sections. Each section have a length of about 1 meter. Totally, each solenoid have 90 longitudinal field coils placed with a pitch of 66.5 mm [3]. Coil cross-section area is $61.2x56^{+2}$ mm, and outer radius of the coil are $146^{+1.5}$ mm. Under this dimensions of the coil and distance between cooling cannels the gap between the coil and body wall (magnetic shield wall) at a bottom of upper cannel is about only of 5 mm. And this does not allow to use normal spherical bearing mounting for this coils in upper solenoid. Founded solution is to rotate coil mounting at 90 degrees, and use the Belleville spring to preload spherical bearing unit. Mounting unit shown on the right side of solenoid body on Fig. 2.

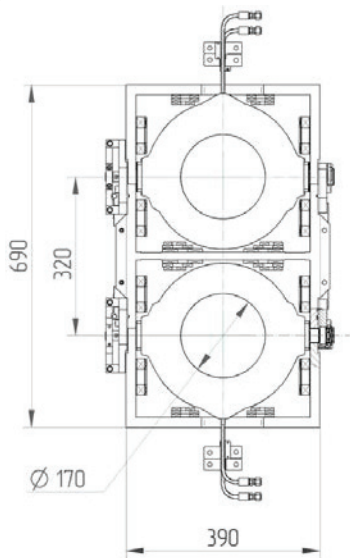

Figure 2: Cooling solenoid cross-section.

This solution shown on Fig. 3 have several parts: ball bearing (2) mounted in case (5) and coil semiaxle (1) is loaded with Belleville spring assembly (3) throw small ball (4) to keep coil tilting and suppress clearances, all this parts are installed in mounting body (6) which is fixed to solenoid section body (7), mark placed in tilting center. In addition, case (5) with bearing can be moved along semiaxle direction to compensate displacement of the coil center.

ISBN: 978-3-95450-218-9 ISSN: 2226-0374 doi:10.18429/JACoW-COOL2019-TUPS21

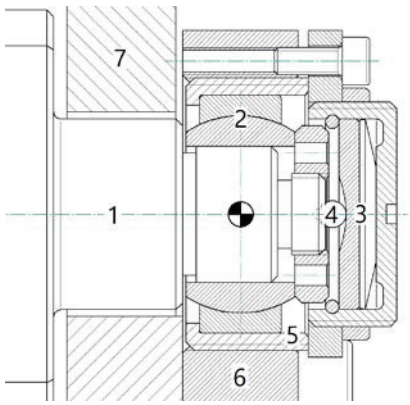

Figure 3: Belleville spring loaded mounting.

On the left side of body (Fig. 2) is the adjusting unit sown on Fig. 4 where: driving arm (3) clamped on coil semiaxle (1) moves by micrometric screws (2) which could be blocked by lock screws, mark placed in rotation center. Adjusting unit body (4) fixed on solenoid section body and prepositioned there by key (5). Same key used on coil mounting.

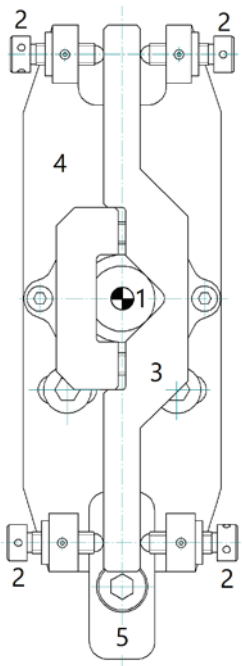

Figure 4: Adjusting unit of the coil.

To provide alignment of coil center and rotation center it is necessary to provide coil semiaxles collinearity. Therefore, accurate machined surfaces are needed for the semiaxles installation. Our solution is to use bronzial inserts with internal cylindrical surfaces, which are pre-positioned (centered) in mould before and precisely machined after coil compounding impregnation. The collinearity tolerance of semiaxles are 50 μm with the same value of parallelism for face surfaces of inserts.

CONCLUSION

This "rotated design" of adjusting unit, coil dimensions and their disposition, allows to having adjusting range not less than ±10 mrad for coil tilting and rotation about of ±20 mrad, at half of the longitudinal gap. For precise tuning this unit have a micrometric drive screws placed on a distance of 66.5 mm from coil axle and about of 430 mm from spring loaded mounting, which provides tuning accuracy in 1 mrad per turn for tilting and 7 mrad per turn for coil rotation. We consider it enough to obtain a rectilinear field in cooling solenoid for NICA experiments.

REFERENCES

[1] M. Bryzgunov, A. Bubley, V. Gosteev, V. Panasyuk, V. Parkhomchuk, V. Reva, "Magnetic system of electron cooler for COSY", *in Proc.* of COOL'11, paper TUPS10, Alushta, Crime, September 12-16, p. 114-117, 2011.

[2] A. Bubley, V. Bocharov, S. Konstantinov, V.Panasyuk, V. Parkhomchuk, "Precision Measurements and Compensation for the Transversal Components of the Solenoids' Magnetic Field", *Instrum. Exper. Techn*. Vol. 48, № 6, pp.772-779, 2005.

[3] V. B. Reva *et al.,* "High Voltage Cooler NICA Status and Ideas", *in Proc.* 11th Workshop on Beam Cooling and Related Topics (COOL'17), Bonn, Germany, Sep. 2017, pp. 25-27. doi:10.18429/JACoW-COOL2017-TUM21

ISBN: 978-3-95450-218-9 ISSN: 2226-0374

List of Authors

Bold papercodes indicate primary authors; ~~crossed out~~ papercodes indicate 'no submission'

ISBN: 978-3-95450-218-9 ISSN: 2226-0374

ISBN: 978-3-95450-218-9 ISSN: 2226-0374

ISBN: 978-3-95450-218-9 ISSN: 2226-0374

Institutes List

BINP SB RAS
Novosibirsk, Russia
- Bainazarova, A.
- Bekhtenev, E.A.
- Belikov, O.V.
- Bryzgunov, M.I.
- Bubley, A.V.
- Chekavinskiy, V.A.
- Denisov, A.P.
- Goncharov, A.D.
- Gusev, I.A.
- Ivanov, A.V.
- Karpov, G.V.
- Kondaurov, M.N.
- Konstantinov, V.M.
- Korchagin, V.Ya.
- Kozak, V.R.
- Kremnev, N.S.
- Mityanina, N.V.
- Panasyuk, V.M.
- Parkhomchuk, V.V.
- Petrov, V.M.
- Polukhin, V.A.
- Pospolita, S.
- Putmakov, A.A.
- Repkov, V.V.
- Reva, V.B.
- Rotov, E.
- Ruvinsky, S.I.
- Senkov, D.V.
- Shiyankov, S.V.
- Skorobogatov, D.N.
- Skrinsky, A.N.
- Tribendis, A.G.
- Vinnik, D.S.
- Vinokurov, N.A.
- Vostrikov, V.A.
- Zharikov, A.A.

BNL
Upton, New York, USA
- Altinbas, Z.
- Brutus, J.C.
- Di Lieto, A.
- Fedotov, A.V.
- Gassner, D.M.
- Hayes, T.
- Inacker, P.
- Jamilkowski, J.P.
- Jing, Y.C.
- Kayran, D.
- Kellermann, R.
- Litvinenko, V.
- Ma, J.
- Mahler, G.J.
- Mapes, M.
- Michnoff, R.J.
- Mihara, K.
- Miller, T.A.
- Minty, M.G.
- Narayan, G.
- Paniccia, M.C.
- Phillips, D.
- Pinayev, I.
- Roser, T.
- Seberg, S.K.
- Severino, F.
- Skaritka, J.
- Smart, L.
- Smith, K.S.
- Sorrell, Z.
- Than, R.
- Tuozzolo, J.E.
- Wang, E.
- Wang, G.
- Wu, Y.H.
- Xiao, B.P.
- Xin, T.
- Zaltsman, A.

Brunel University
Middlesex, United Kingdom
- Brown, C.

CERN
Meyrin, Switzerland
- Arnaudon, L.
- Biancacci, N.
- Bjorsvik, E.
- Carli, C.
- Caspers, F.
- Cenede, J.
- Deschamps, S.
- Eriksson, T.
- Frassier, A.
- Gamba, D.
- Höfle, W.
- Jørgensen, L.V.
- Latina, A.
- Louwerse, R.
- Myklebust, V.R.
- Petrenko, A.V.
- Ponce, L.
- Saá Hernández, Á.
- Thorndahl, L.
- Tranquille, G.

Cockcroft Institute
Warrington, Cheshire, United Kingdom
- Resta-López, J.
- Veglia, B.
- Welsch, C.P.

Fudan University
Shanghai, People's Republic of China

ISBN: 978-3-95450-218-9 ISSN: 2226-0374

- Chen, C.Y.

FZJ
Jülich, Germany
- Halama, A.J.
- Kamerdzhiev, V.
- Niedermayer, P.J.
- Shurkhno, N.
- Stassen, R.

GSI
Darmstadt, Germany
- Aulenbacher, K.
- Dimopoulou, C.
- Hess, R.
- Joseph, R.
- Litvinov, S.A.
- Lorentz, B.
- Roßbach, J.
- Steck, M.
- Winters, D.F.A.

HIM
Mainz, Germany
- Aulenbacher, K.
- Beiser, Th.
- Bruker, M.W.
- Dietrich, J.
- Klag, W.

HZDR
Dresden, Germany
- Bussmann, M.H.

Illinois Institute of Technology
Chicago, Illinois, USA
- Kaplan, D.M.

IMP/CAS
Lanzhou, People's Republic of China
- Dou, L.J.
- Du, Z.
- Hai, B.
- Hu, X.J.
- Huang, Z.
- Khan, N.
- Li, J.
- Li, P.
- Li, X.N.
- Lu, H.J.
- Ma, X.M.
- Ma, X.
- Mao, L.J.
- Mao, R.S.
- Tang, M.T.
- Wang, H.B.
- Wang, S.X.
- Wen, W.Q.
- Wu, J.X.
- Yan, K.M.
- Yang, J.C.
- Yang, X.D.
- Yin, D.Y.
- Yuan, Y.J.
- Zhao, D.
- Zhao, H.W.
- Zhao, L.X.
- Zhao, T.C.
- Zhou, Y.B.
- Zhu, G.
- Zhu, X.

Imperial College of Science and Technology, Department of Physics
London, United Kingdom
- Long, K.R.

ISP
Novosibirsk, Russia
- Terekhov, A.S.

JINR
Dubna, Russia
- Filimonov, V.V.
- Kobets, A.G.
- Melnikov, S.A.
- Meshkov, I.N.
- Orlov, O.
- Semenov, S.V.
- Sergeev, A.S.
- Shemchuk, A.V.
- Sidorin, A.A.
- Sidorin, A.O.
- Smirnov, A.V.
- Syresin, E.

JINR/FLNR
Moscow region, Russia
- Grigorenko, L.V.

JINR/VBLHEP
Dubna, Moscow region, Russia
- Gorelyshev, I.V.
- Osipov, K.G.
- Philippov, A.V.
- Sidorin, A.O.

JLab
Newport News, Virginia, USA
- Bruker, M.W.
- Derbenev, Y.S.
- Krafft, G.A.
- Lin, F.
- Morozov, V.S.
- Zhang, Y.

ISBN: 978-3-95450-218-9 ISSN: 2226-0374

MPI-K
Heidelberg, Germany
- Grieser, M.
- Krantz, C.
- KÃ¡losi, A.
- Novotny, O.
- Paul, D.
- Wilhelm, P.
- Wolf, A.

Nihon University
Narashino, Chiba, Japan
- Katayama, T.

NSU
Novosibirsk, Russia
- Bekhtenev, E.A.
- Reva, V.B.
- Vinokurov, N.A.
- Vostrikov, V.A.

ODU
Norfolk, Virginia, USA
- Delayen, J.R.
- Dhital, B.

RadiaSoft LLC
Boulder, Colorado, USA
- Bruhwiler, D.L.
- Eidelman, Y.I.
- Pogorelov, I.V.

Saint Petersburg State University
Saint Petersburg, Russia
- Gorelyshev, I.V.
- Sidorin, A.O.

SBU
Stony Brook, New York, USA
- Shih, K.

St. Petersburg University
St. Petersburg, Russia
- Sidorin, A.O.

Stony Brook University
Stony Brook, USA
- Kayran, D.

SUNY SB
Stony Brook, New York, USA
- Petrushina, I.

The University of Liverpool
Liverpool, United Kingdom
- Resta-López, J.
- Welsch, C.P.

TU Darmstadt
Darmstadt, Germany
- Kiefer, D.
- Klammes, S.
- Walther, T.

University of Glasgow
Glasgow, United Kingdom
- Nugent, J.C.
- Soler, P.

University of Leicester, Department of Physics and Astronomy
Leicester, United Kingdom
- Preval, S.

USTC
Hefei, Anhui, People's Republic of China
- Ma, W.L.
- Wang, S.X.
- Zhu, L.F.

USTRAT/SUPA
Glasgow, United Kingdom
- Badnell, N.R.

Xidian University
Xi'an, People's Republic of China
- Chen, D.Y.
- Zhang, D.
- Zhang, H.Y.

ISBN: 978-3-95450-218-9 ISSN: 2226-0374

Participants List

— A —

Kurt **Aulenbacher**
Helmholtz Institut Mainz
Mainz, Germany

— B —

Thomas **Beiser**
Helmholtz Institut Mainz
Mainz, Germany

Evgeniy **Bekhtenev**
BINP
Novosibirsk, Russian Federation

Oleg **Belikov**
BINP
Novosibirsk, Russian Federation

Dmitriy **Berkaev**
BINP
Novosibirsk, Russian Federation

Maxim **Bryzgunov**
BINP
Novosibirsk, Russian Federation

Alexander **Bubley**
BINP
Novosibirsk, Russian Federation

— C —

Fritz **Caspers**
CERN
Geneve, Switzerland

— D —

Andrey **Denisov**
BINP
Novosibirsk, Russian Federation

Jürgen **Dietrich**
Helmholtz Institut Mainz
Mainz, Germany

Nikolay **Dikansky**
BINP
Novosibirsk, Russian Federation

Christina **Dimopoulou**
GSI
Darmstadt, Germany

— G —

David **Gamba**
CERN

Ivan **Gorelyshev**
JINR
Dubna, Russian Federation

Leonid **Grigorenko**
JINR
Dubna, Russian Federation

Igor **Gusev**
BINP
Novosibirsk, Russian Federation

— H —

Zhongkui **Huang**
Institute of Modern Physics of CAS
Lanzhou, China

Xuejing **Hu**
Institute of Modern Physics of CAS
Lanzhou, China

— I —

Andrey **Ivanov**
BINP
Novosibirsk, Russian Federation

— J —

Lars **Jørgensen**
CERN
Geneve, Switzerland

— K —

Vsevolod **Kamerdzhiev**
Forschungszentrum Jülich
Jülich, Germany

Daniel **Kaplan**
Illinois Institute of Technology
Chicago, IL, USA

Takeshi **Katayama**
Nihon University
Narashino, Japan

Alexey **Kondakov**
BINP
Novosibirsk, Russian Federation

Nikolay **Kremnev**
BINP
Novosibirsk, Russian Federation

Maksim **Kuzin**
BINP
Novosibirsk, Russian Federation

— L —

Jie **Li**
Institute of Modern Physics of CAS
Lanzhou, China

Vladimir **Litvinenko**
Stony Brook University
Stony Brook, NY, USA

Sergey **Litvinov**
GSI
Darmstadt, Germany

— M —

Lijun **Mao**
Institute of Modern Physics of CAS
Lanzhou, China

Xinwen **Ma**
Institute of Modern Physics of CAS
Lanzhou, China

Igor **Meshkov**
JINR
Dubna, Russian Federation

Natalya **Mityanina**
BINP
Novosibirsk, Russian Federation

ISBN: 978-3-95450-218-9 ISSN: 2226-0374

— N —

Philipp **Niedermayer**
Forschungszentrum Jülich
Jülich, Germany

— O —

Konstantin **Osipov**
JINR
Dubna, Russian Federation

— P —

Vitaly **Panasyuk**
BINP
Novosibirsk, Russian Federation

Vasily **Parkhomchuk**
BINP
Novosibirsk, Russian Federation

Alexey **Petrenko**
BINP
Novosibirsk, Russian Federation

Ilya **Pogorelov**
RadiaSoft LLC
Boulder, CO, USA

Andrey A. **Prokopenko**
BINP
Novosibirsk, Russian Federation

— R —

Vladimir **Reva**
BINP
Novosibirsk, Russian Federation

Adriana **Rossi**
CERN
Geneve, Switzerland

Evgeny **Rotov**
BINP
Novosibirsk, Russian Federation

— S —

Sergey **Sadovich**
CERN
Geneve, Switzerland

Dmitriy **Senkov**
BINP
Novosibirsk, Russian Federation

Sergey **Shiyankov**
BINP
Novosibirsk, Russian Federation

Nikolay **Shurkhno**
Forschungszentrum Jülich
Jülich, Germany

Dmitry **Skorobogatov**
BINP
Novosibirsk, Russian Federation

Alexander **Skrinsky**
BINP
Novosibirsk, Russian Federation

Rolf **Stassen**
Forschungszentrum Jülich
Jülich, Germany

Markus **Steck**
GSI
Darmstadt, Germany

— T —

Alexey **Tribendis**
BINP
Novosibirsk, Russian Federation

— V —

Bianca **Veglia**
University of Liverpool
Liverpool, United Kingdom

Vladimir **Vostrikov**
BINP
Novosibirsk, Russian Federation

— W —

Hanbing **Wang**
Institute of Modern Physics of CAS
Lanzhou, China

Weiqiang **Wen**
Institute of Modern Physics of CAS
Lanzhou, China

Andreas **Wolf**
Max Planck Institute for Nuclear Physics
Heidelberg, Germany

— Y —

Xiaodong **Yang**
Institute of Modern Physics of CAS
Lanzhou, China

Youjin **Yuan**
Institute of Modern Physics of CAS
Lanzhou, China